Coherent Secondary Radiation from Femtosecond Laser Filaments

Sergey Mitryukovskiy

Thèse de doctorat de l'École Polytechnique

Spécialité : Optique non-linéaire

Présentée par

Sergey Mitryukovskiy

pour l'obtention du grade de
Docteur ès sciences, mention physique

Rayonnements Secondaires Cohérents Émis lors de la Filamentation Laser Femtoseconde

Soutenue le 15 septembre 2014 devant la commission d'examen formée de :

Yi Liu	Directeur de thèse
André Mysyrowicz	Co-directeur de thèse
François Amiranoff	Président du jury
Olga G. Kosareva	Rapporteur
Erik T. J. Nibbering	Rapporteur
Vladimir T. Tikhonchuk	Examinateur
Jean-Louis Coutaz	Examinateur

Thèse préparée au Laboratoire d'Optique Appliquée UMR 7639

ÉCOLE POLYTECHNIQUE

Ph.D. Thesis

Coherent Secondary Radiation from
Femtosecond Laser Filaments

by Sergey Mitryukovskiy

Acknowledgments

This work resumes the last three years, which I have spent at the Laboratoire d'Optique Appliquée. It was a great, priceless and the most useful experience for me. This time was also very enjoyable and interesting, it will rest forever in my memory.

I am grateful to all the people who have helped me during these years and contributed in one way or another in the realization of the thesis work.

First of all I would like to thank my thesis supervisors and mentors: Yi Liu and André Mysyrowicz for showing me the way to progress. I deeply appreciate your help and support both scientific and human. Your optimism, sympathy, dynamism and thirst to know and to do always more and more serve for me as an ideal example. Thank you André! Thank you Yi!

I thank extremely warm the "Interaction Laser-Matière" group, our chief Aurélien Houard and all the team, particularly: Bernard Prade, Yves-Bernard André, Amélie Jarnac, Pengji Ding, Yohann Brelet, Guillaume Point, Jérôme Carbonnel, Leonid Arantchouk, the members of our research group who have helped me in different ways and provided solutions to numerous problems during all my work. It is a real pleasure and honor to be a part of the ILM team. Thank you and good luck my friends!

I also thank Arnaud Couairon who has helped us with calculus and numerical simulations and who is always ready to give a valuable advice.

Special thanks to François Amiranoff for accepting to be a president of the Jury at my thesis defense, as well as to my two reviewers Olga Kosareva and Erik Nibbering, who have taken their time to examine the manuscript and to come to the defense despite all the difficulties. I also warmly thank Vladimir Tikhonchuk and Jean-Louis Coutaz for participating in the Jury and for their valuable suggestions concerning the manuscript. I am grateful to all the Jury members for their interest, their comments and concerns.

At the Laboratoire d'Optique Appliquée of the École Polytechnique where I spend these three years many people have assisted me. I thank Antoine Rousse, director of the laboratory, for the hospitality and the secretaries for the great assistance with all the administration issues. I thank Magali Lozano, Gilles Cheriaux, Joinel Cheleux, Adrien Hervy for helping me with experiments in Salle Orange and Salle Verte. Even if they did

not turn to publications, still they gave us important experience and knowledge, which will be useful in the future. Thanks to our informatics technicians, Pierre Zaparucha and Maxence Le Sourd, as well as to our magician of mechanics Jean-Lou Charles. I also thank Natalia Naumova, Evgeny Chelnokov, Igor Andriyash, Sergey Stremoukhov, Asad Hussain and Lu Li for interesting talks we had about science and life.

I am also grateful to all the friends which I have met on this long way to the PhD in Physics, particularly the "SHG lab", the "group 105, extended", as well as all the members of football teams "A P International" and "Red Alert" for their presence, their useful advises, our football matches, our evenings and parties.

Finally, all my love and gratitude goes to my girlfriend Nadia, my parents, my brother and my grand-parents.

Contents

Preface

Laser filamentation is a nonlinear optical phenomenon which appears spontaneously during the propagation of an intense ultrashort laser pulse in a transparent medium, when the pulse peak power exceeds a material dependent critical value (several Gigawatts in air). At such intensity level the beam tends to collapse due to the optical Kerr self-focusing effect until the intensity is high enough to ionize the medium, giving rise to a defocusing plasma. Thereafter, a dynamic competition between these two effects takes place leaving a thin and weakly ionized plasma channel in the wake of the pulse. Such channel is called a filament. The first demonstration of femtosecond laser filamentation in air was reported by Braun and coworkers in 1995 [Braun 95], and reproduced over longer distances shortly later at the Laboratoire d'Optique Appliquée (LOA) [Nibbering 96]. Since that time, femtosecond laser filamentation in air attracts considerable interest not only because of the rich physics involved, but also its wide range of applications in remote sensing, light frequency conversion, laser-based weather control, Terahertz generation, *etc.*

The author's work is mainly devoted to the secondary emission from femtosecond laser filaments: Ultraviolet luminescence, coherent stimulated lasing and Terahertz radiation emitted by filaments. The PhD thesis consists of three parts which are further divided into several chapters.

In the opening part of the thesis, we first recall the basics of the filamentation process and then present a simple technique to determine experimentally the laser fluence and intensity inside filaments. Up to now, a direct measurement of the laser intensity inside filaments is very difficult because any device used for this purpose would be easily damaged due to the very high intensity level inside filaments ($10^{13} - 10^{14}$ W/cm^2). Our method is based on the measurement of the laser energy transmitted through a variable diaphragm fabricated by the filament itself on a thin metallic foil by cumulative laser irradiation. We thus can directly determine the laser fluence inside the filament. With an additional measurement of the pulse duration, the intensity can be estimated. The obtained value of the laser intensity inside filaments allowed us to explain our findings in the following chapters.

The second part of the thesis is devoted to the ultraviolet (UV) emission from plasma filaments in nitrogen gas and in air. The luminescence of plasma is one of the most spectacular phenomena associated with filamentation and is identified as due to the optical transitions of the excited neutral and ionic nitrogen molecules inside the plasma

[Talebpour 99, Martin 02]. In the first chapter of this part, we report a strong dependence of the luminescence from both molecular and ionic nitrogen on the incident laser polarization. The results point to the important role of electron collision excitation for circularly polarized laser, where energetic electrons are generated after the passage of the laser pulses.

In the second chapter of this part, we demonstrate that an intense backward stimulated radiation at 337 nm from filaments in nitrogen gas can be achieved with circularly polarized 800 nm femtosecond laser pulses at atmospheric pressure. Existence of the stimulated radiation is confirmed by the distinct dependence of the backward UV spectrum on the incident laser polarization and intensity, by the emission profile and polarization properties. We attribute the population inversion inside the plasma to inelastic collisions between the electrons liberated by the pump laser and surrounding neutral ground state nitrogen molecules. The dependence of the lasing effect on the incident laser pulse polarization is explained by the fact that a circularly polarized laser produces more energetic electrons than a linearly polarized one.

Next, a further enhancement of the ASE is shown when an external 337-nm seeding pulse is launched in the backward direction. At the same time, the divergence angle of the seeded lasing is found to be significantly reduced compared to that of the ASE. Moreover, the seeded lasing radiation inherits the polarization property of the seed pulse. These three observations confirm unambiguously the assumption of population inversion between the relevant nitrogen molecular states. The critical role of pump laser ellipticity was also observed in this seeded backward lasing scheme, which supports the hypothesis that inelastic collision between the energetic electrons with neutral nitrogen molecules is at the origin of population inversion.

The work presented in the third part concerns the Terahertz generation by femtosecond laser filaments in air. Electromagnetic radiation in the Terahertz (THz) domain has received much attention in the past two decades. THz spectroscopy is ideally suited for various research and diagnostics. Applications of THz radiation range from medicine, security concerns to telecommunication, *etc.* Unfortunately, many applications that require illumination of a distant target are hampered by the poor transmission of THz radiation through atmosphere, due to the strong attenuation posed by water vapor. Recently, significant progress has been achieved in remote THz generation. To alleviate the strong attenuation in air, one produces a THz emitting source close to the distant target. This can be readily achieved using femtosecond laser filaments. A possible scheme consists in simply launching a short intense laser pulse to create a plasma filament near the target object.

In this last part of the thesis we describe the coherent synthesis of the THz radiation from N individual single-color filaments organized in an array. We experimentally demonstrate a strong mutual coherence between the THz radiation pulses emitted by filaments created independently in air. We find that the THz intensity scales up with N^2 provided that proper filament separation and laser pulse temporal delays are chosen. Moreover, the THz radiation pattern can be controlled, which is a useful property for many applications. Calculations based on the transition-Cherenkov model of THz emission by filaments agree well with our experimental observations. We further consider the THz radiation from fil-

aments forming an analogue of a "Vee-antenna". We show an interesting possibility for 'V-oriented' filaments to produce circularly polarized THz emission. At the same time, a method of effective enhancement of a THz radiation at a selected frequency is discussed. It consists in optimizing the angle between two 'V-oriented' filaments. In the last chapter of this part we consider the effect of an external electric field on the coherent THz emission from multiple filaments in air. A strong enhancement of a broadband THz radiation in the forward direction is found, scaling like E_{ext}^2 in the presence of a static transverse electric field and scaling like N^2, where N is a number of filaments organized in an array. There is also a possibility to direct the THz emission along preferential directions by tuning the temporal delay between the filamentary laser pulses.

Part I

Properties of a plasma filament

Chapter 1

Filamentation of a femtosecond laser pulse in air

1.1   Introduction to laser filamentation

High power laser pulses undergo nonlinear propagation in transparent media. Nonlinear self-action leads to strong evolution of the properties of the laser pulse as well as that of the propagation medium, which is partially ionized by the laser beam [Keldysh 65]. Such phenomena as self-focusing [Kelley 65, Askar'yan 74, Shen 75], self-reflection [Roso-Franco 85], self-phase modulation [Alfano 70], self-steepening [Yang 84], pulse splitting [Ranka 96], *etc.* have been studied extensively since the mid-1960s−1970s. They were mostly restricted to condensed matter media, where the damage associated with laser nonlinear propagation prevented application.

Since 1985, the development of the chirped pulse amplification (CPA) technique [Strickland 85, Maine 88] permitted to produce ultrashort laser pulses with intensities as high as 10^{20} W/cm^2 and hence to observe highly nonlinear propagation even in atmospheric pressure gases and the atmospheric air itself. The first demonstration of the femtosecond laser pulse nonlinear propagation in air was reported in 1995 [Braun 95]. Braun, *et al.* have observed a significant increase of the peak intensity of a femtosecond laser pulse propagating in air. For instance, it reached sufficiently high values to provoke micro-burns on a hard coated mirror 10 m away from the laser. At the same time, the mirror was undamaged if placed immediately close to the laser output, before propagation in air. The authors explained their observation by the nonlinear effect of the laser beam self-focusing. The damage tracks subsisted if the mirror was displaced several meters along the propagation axis. The beam therefore remained focused over an extended distance. This type of propagation was called **filamentation** or self-guided propagation. Shortly after, femtosecond laser filaments of more than 50 meters in length were produced in the Laboratoire d'Optique Appliquée [Nibbering 96]. Further studies have shown the possibility of femtosecond laser filamentation to occur over several hundreds of meters and even several kilometers [La Fontaine 99, Méchain 04a, Méchain 05]. With multi-terawatt lasers, continuous plasma strings extending over more than 50 m have been obtained at a distance of 1 km from the laser system [Durand 13].

7

Filamentation aroused a great interest and during the past 15-20 years many interesting phenomena and applications have been revealed. One can adduce the following examples: the white light continuum generated during self-guided propagation can be used for the detection of pollutants in the atmosphere by LIDAR technique [Kasparian 03, Bourayou 05]; the creation of plasma channels in a filament can trigger and guide high-voltage discharges and could be used to control lightning [Comtois 00, Rodriguez 02, Ackermann 04]; high local intensities can be used to identify targets at a distance by laser-induced ablation spectroscopy (LIBS) [Stelmaszczyk 04]; the filament plasma can also deliver broadband THz radiation at long distances [D'Amico 07c, Houard 08c]. The high intensity inside filaments leads to emission of characteristic fluorescence spectra which can be used for the sensing purposes in the propagation media [Dai 06, Xu 11b].

In the following the discussion will be restricted to the basic principles of filamentation and its properties peculiarly connected to the reported PhD study. More detailed survey of filamentation process and its applications is presented in a number of review papers [Couairon 07, Bergé 07, Kasparian 08, Chin 10].
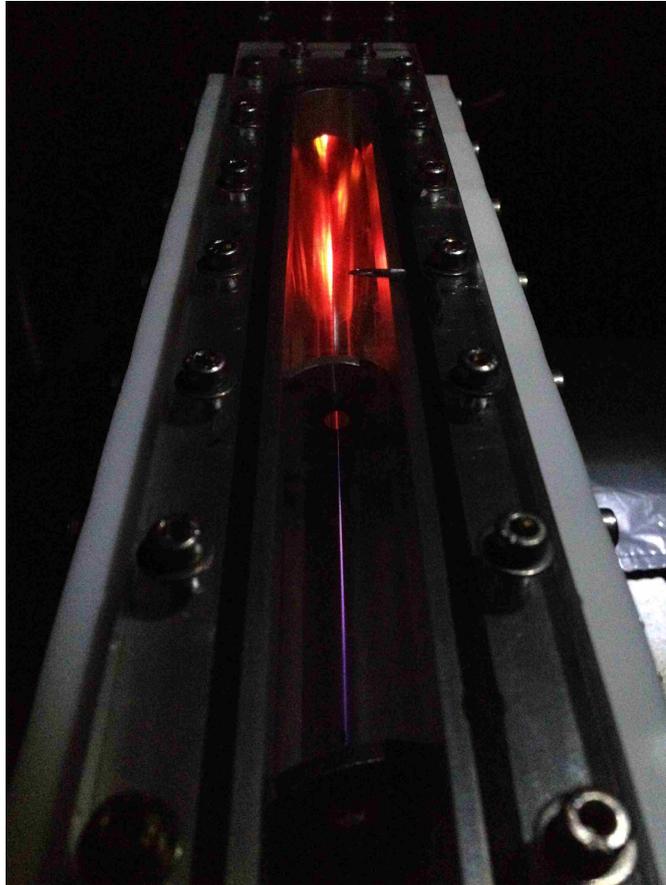

Figure 1.1: Photo of a 4-cm-long plasma filament induced by 800 nm femtosecond laser pulses in a gas chamber filled with nitrogen (1 bar). The violet light corresponds to fluorescence of excited nitrogen molecules inside the filamentary plasma.

1.2 Basic principle of femtosecond laser filamentation

As it was mentioned, many physical effects come into play during the propagation of an intense laser pulse in transparent media. The filamentation process can be described as a dynamic competition mainly between two nonlinear physical effects: the optical Kerr self-focusing effect and the beam defocusing by the induced plasma.
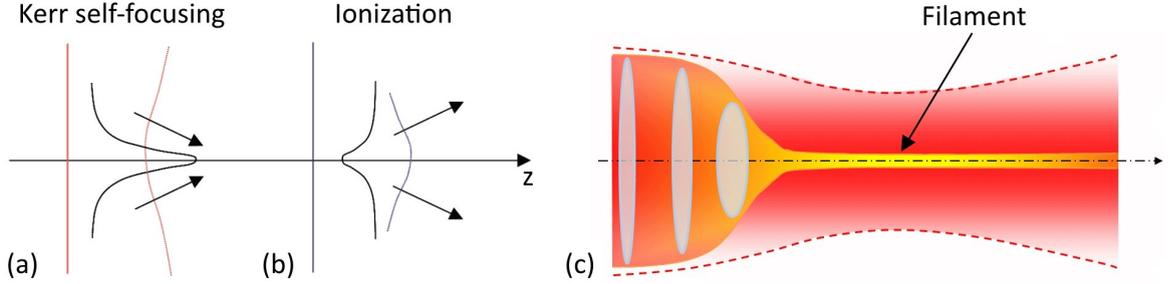
Figure 1.2: Schematic illustration of the filamentation process. (a) Self-focusing of a laser beam by optical Kerr effect. (b) Defocusing of the beam by the plasma. (c) Illustration of the collapse of the beam on itself by the Kerr effect leading to the ionization of the media with the following formation of a filament.

Kerr self-focusing effect

Optical Kerr self-focusing was first predicted in the 1960s [Askar'yan 62, Chiao 64, Kelley 65] and experimentally verified by studying the interaction of ruby lasers with glasses and liquids [Lallemand 65, Garmire 66]. At high powers, the refractive index of air n in the presence of an intense electromagnetic field is modified by the Kerr effect [Shen 84]:

$$n = n_0 + n_2 I_L(\vec{r}, t), \tag{1.1}$$

where n_0 and n_2 are the linear and non-linear components of the refractive index, and $I_L(\vec{r}, t)$ is the laser intensity. The coefficient of the non-linear Kerr index n_2 is related to the third order susceptibility as $\chi^{(3)} = 4\varepsilon_0 c n_2 n_0^2/3$, where ε_0 is the permittivity of vacuum. Since the coefficient n_2 is positive in most materials, the total refractive index increases in the presence of intense radiation. The spatial intensity distribution of a laser beam leads to an effect of curvature of the wavefront similar to that of a lens, with the difference that here the effect is cumulative and can lead, in the absence of other saturating effects, to a catastrophic collapse of the beam on itself [Gaeta 00]. This effect is represented schematically in Figure 1.2.

The characteristic length of self-focusing (L_{SF}) is defined as the length over which the cumulated nonlinear phase, measured by the B-integral ($B \equiv k_0 \int_o^z n_2 I dz$), varies by a factor of one. It is expressed as a function of the peak intensity I_0:

$$L_{SF} = \frac{1}{n_2 k_0 I_0}, \tag{1.2}$$

where $k_0 = 2\pi/\lambda_0$ is the wavenumber in vacuum.

The significant parameter for self-focusing is the initial power of the laser beam. Self-focusing overcomes diffraction and leads to collapse of the beam only if the input peak power (P_{in}) exceeds a critical threshold [Marburger 75, Fibich 00]:

$$P_{cr} \equiv \frac{\alpha \lambda_0^2}{4\pi n_0 n_2},$$
(1.3)

where λ_0 is the radiation wavelength in vacuum and α is a constant which depends on the initial spatial distribution of the beam. Although there is no general analytical expression for α, its value has been derived numerically for many beam profiles [Fibich 00]. The lower limit is $\alpha \approx 1.86225$, which corresponds to Townes beams, whereas for a Gaussian beam $\alpha \approx 1.8962$. For a $\lambda_0 = 800$ nm laser pulse propagating in air ($n_0 \approx 1$, $n_2 \approx 4 \times 10^{-19}$ cm^2/W [Nibbering 97]) the critical power is $P_{cr} \approx 3.2$ GW.

Plasma defocusing

With the accumulative self-focusing of the laser beam its intensity becomes so high that it ionizes the medium. The generation of a plasma leads to a local reduction in the refraction index [Feit 74], according to the law:

$$n \simeq n_0 - \frac{\rho(\vec{r}, t)}{2\rho_c},$$
(1.4)

where $\rho(\vec{r}, t)$ is the density of free electrons and ρ_c is the value of the critical plasma density above which the plasma becomes opaque:

$$\rho_c \equiv \varepsilon_0 m_e \frac{\omega_0^2}{e^2},$$
(1.5)

where m_e and e are the electron mass and charge, respectively. $\rho_c \approx 1.7 \times 10^{21}$ cm^{-3} at 800 nm laser wavelength.

One can define the characteristic length (L_{PL}) for plasma defocusing as the length over which the B-integral ($B \equiv k_0 \int_o^z \rho/(2n_0\rho_c)dz$) changes by a factor of one for a fully-ionized plasma ($\rho = \rho_{at}$, where ρ_{at} is the neutral atom density). L_{PL} is expressed as a function of the neutral atom density:

$$L_{PL} = \frac{2n_0\rho_c}{k_0\rho_{at}}.$$
(1.6)

For a weakly ionized medium of density ρ, the length scale for plasma defocusing is therefore $\sim L_{PL} \times \rho_{at}/\rho$. For a gas density $\rho_{at} = 2 \times 10^{19}$ cm^{-3}, and an electron density $\rho = 10^{16}$ cm^{-3}, one obtains $L_{PL} \approx 22$ μm, and $L_{PL}\rho_{at}/\rho \approx 44$ cm. The reduction in the refraction index acts as a divergent lens, preventing the complete collapse of the beam on itself. This effect is schematically shown in Figure 1.2(b).

The self-focusing and plasma defocusing compete each other along the laser pulse propagation inside the medium. As a result, a long plasma channel, a filament, is formed.

1.3 Theoretical description of laser nonlinear propagation during filamentation

In order to model the physics of filamentation of ultrashort laser pulses in gases, solids and liquids, many teams have developed various unidirectional propagation equations and the propagation codes for the numerical simulations [Moloney 07, Couairon 07, Chin 10]. The first numerical simulations in this field started with a basic model in the form of a nonlinear Schrödinger equation describing the pulse propagation. The influence of various physical effects can be studied by the addition of the corresponding source terms to this model.

In 1997, Brabec and Krausz [Brabec 97] proposed an envelope equation modeling the propagation of a laser pulse of a few optical cycles. The main idea of this approach, the derivation of the equation called the nonlinear envelope equation, consists in assuming that the pulse envelope is slowly varying in the propagation direction z, but not in time. This introduces additional terms corresponding to optical shocks [Zozulya 98, Gaeta 00]. An equivalent formulation in the frequency domain was proposed by Bespalov, *et al.* [Bespalov 02]. The high order dispersive terms can be retained in the propagation equation when it is written in the frequency domain [Gaeta 00, Couairon 02a, Sprangle 02]. For the laser pulse linearly polarized along the x-axis, the electric field can be decomposed into a carrier wave and an envelope as $\vec{E}(x, y, z, t) = \frac{1}{2}\mathcal{E}(x, y, z, t) \exp[i(kz - \omega_0 t)]\vec{e_x} + c.c.$, where z is the propagation direction, k and ω_0 are the central wavenumber and frequency of the laser pulse. The extended nonlinear Schrödinger equation can be written as [Couairon 07]:

$$U\frac{\partial\hat{\mathcal{E}}}{\partial z} = \frac{i}{2k}\left[\Delta_\perp + \frac{n^2(\omega)\omega^2}{c^2} - k^2 U^2\right]\hat{\mathcal{E}} + \mathcal{F}\{N(|\mathcal{E}|^2, \rho)\mathcal{E}\}. \tag{1.7}$$

Here $\hat{\mathcal{E}}(x, y, z, \omega)$ represents the Fourier transform of $\mathcal{E}(x, y, z, t)$. The operator $\Delta_\perp$ denotes the transverse Laplacian and $\mathcal{F}$ denotes the Fourier transform from the time to the frequency domain. The operator U is given by $U \equiv \left(1 + \frac{\omega - \omega_0}{kv_g}\right)$, where ω_0 is the pulse central frequency and k is the wavevector. The function N includes self-focusing, plasma defocusing and photoionization effects, and is given by:

$$N(|\mathcal{E}|^2, \rho) = T^2 N_{Kerr}(|\mathcal{E}|^2) + N_{plasma}(\rho) + T N_{MPA}(|\mathcal{E}|^2), \tag{1.8}$$

where $T \equiv \left(1 + \frac{i}{\omega_0}\frac{\partial}{\partial t}\right)$ accounts for space-time focusing and self-steepening of the pulse. It also takes into account the deviations from the slowly varying envelope approximation.

The Kerr effect term $N_{Kerr}(|E|^2)$ results from the intensity dependent refractive index and includes both instantaneous and retarded contributions [Ripoche 97]:

$$N_{Kerr}(|\mathcal{E}|^2) = ik_0 n_2 \left[(1 - f)|\mathcal{E}(x, y, z, t)|^2 + f \int_{-\infty}^{t} \mathcal{R}(t - t')|\mathcal{E}(x, y, z, t')|^2 dt'\right], \tag{1.9}$$

where n_2 is the nonlinear index of refraction, f is the ratio of the fraction of the delayed contribution and $\mathcal{R}$ represents the molecular response of the gas. The delayed contribution

is important for simulation in air, as rotational coherence of oxygen and nitrogen molecules are excited by femtosecond laser pulses [Ripoche 97, Nibbering 97].

The plasma and multi-photon absorption (MPA) terms in eq. (1.8) read, respectively:

$$N_{plasma}(\rho) = -\frac{k_0}{2n_0\rho_c}\frac{\omega_0\tau_c}{(1+\omega^2\tau_c^2)}(1+i\omega\tau_c)\rho = -\sigma(1+i\omega\tau_c)\rho, \qquad (1.10)$$

and

$$N_{MPA}(|\mathcal{E}|^2) = -\frac{W(|\mathcal{E}|^2)U_i}{2|\mathcal{E}|^2}(\rho_{at}-\rho). \qquad (1.11)$$

where, τ_c is the electron collision time, ρ is the electron density in the plasma, ρ_c is the critical plasma density, σ is the cross section of inverse Bremsstrahlung, following the Drude model [Yablonovitch 72], U_i is the ionization potential, ρ_{at} is the density of the neutral atoms and W is the photoionization rate, including multi-photon ionization (MPI) and tunnel ionization contributions.

Note that eq. (1.7) can only be solved numerically. For instance, Figure 1.3 shows the beam width during the filamentation process in air calculated by the nonlinear propagation code developed by A. Couairon and coworkers [Couairon 02b]. Similar (2+1)D simulation results that show the space-time reshaping of infrared laser pulses undergoing filamentation in air can also be found in several publications [Kandidov 97, Chiron 99]. A detailed guide to simulation and models of laser pulse propagation has been published recently [Couairon 11].
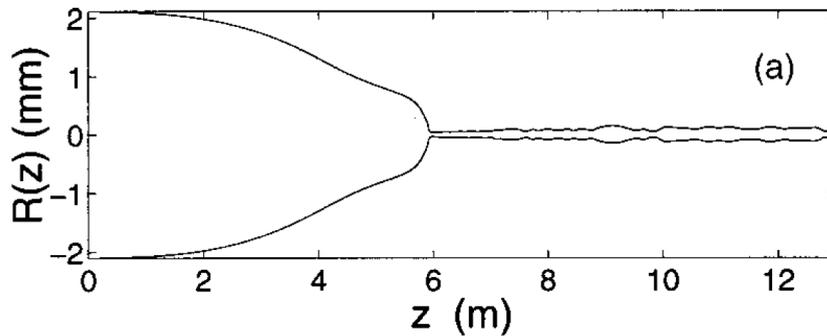
Figure 1.3: Evolution of the laser beam width along the propagation direction (result of computer simulation). The Figure is taken after [Couairon 02b]. The laser pulse is 5 mJ, 50 fs, 800 nm. The laser beam self-collapses on its axis due to the Kerr effect, subsequently the laser intensity becomes high enough to ionize the gas. Therefore, a long filament is formed due to the competition of the Kerr effect and plasma defocusing.

1.4 Properties of filaments

Laser filamentation reveals many remarkable features, which are useful for a variety of applications. Several of them are particularly important in the frame of this PhD work and will be briefly introduced in the following paragraphs.

Length of self-focusing

Diffraction of a laser beam occurs always, even while its propagation in vacuum. For the typical length for diffraction of a laser beam one can use the Rayleigh length (the width of a Gaussian beam with a flat spatial phase is increased by a factor of $\sqrt{2}$ when the beam propagates over this length). The Rayleigh length is defined as

$$L_{DF} = \frac{kw_0^2}{2} = \frac{\pi n_0 w_0^2}{\lambda_0}, \tag{1.12}$$

where w_0 is the beam waist, λ_0 the laser wavelength in vacuum, n_0 the refraction index of the medium at this wavelength, $k \equiv n_0 k_0$ and $k_0 \equiv 2\pi/\lambda_0$, the wavenumbers in the medium and in vacuum, respectively. For example, the Rayleigh length of a beam with $w_0 = 100\ \mu m$ at $\lambda_0 = 800$ nm in vacuum ($n_0 = 1$) is $L_{DF} = 3.9$ cm.

The propagation length of the self-focusing beam until its collapse may be approximated by a semi-empirical formula [Dawes 69, Marburger 75]:

$$L_c = \frac{0.367 L_{DF}}{\sqrt{((P_{in}/P_{cr})^{1/2} - 0.852)^2 - 0.0219}}. \tag{1.13}$$

This equation is valid for the collapse of Gaussian beams with moderate input powers in purely Kerr media. For a collimated beam, at a pulse wavelength of 800 nm, with a power $P_{in} = 10 P_{cr}$ and a waist of $w_0 = 0.5$ cm, the distance to collapse L_c is approximately 15.6 m. At higher input powers (100 P_{cr}), the validity of eq. (1.13) breaks down due to modulational instabilities.

In the case of a convergent (or divergent) beam focused by a lens of a focus length f, the position of the collapse $L_{c,f}$ moves before the position of the linear focus of the lens according to:

$$\frac{1}{L_{c,f}} = \frac{1}{L_c} + \frac{1}{f}. \tag{1.14}$$

Plasma density

The published values of the mean plasma density in filaments vary over a big range (between 10^{14} and 10^{18} cm^{-3}) [Tzortzakis 99, Schillinger 99, Yang 02, Ting 05a]. For instance, Tzortzakis, *et al.* obtained the value of the plasma density of 10^{16} - 10^{17} cm^{-3} from the measurement of the conductivity of a filament generated by a 120 fs, 800 nm laser pulse [Tzortzakis 99]. Employing pump–probe back longitudinal diffractometry, Liu, *et al.*

have investigated the electron density and decay dynamics of a plasma channel generated by a 2-cm-long filament in air [Liu 05]. From an analytical reconstruction method of electron density which is sensitive to the phase shift and channel size, the electron density in the weak plasma channel generated by 800 nm, 50 fs laser pulses, was extracted to be about 4×10^{16} cm^{-3} and the diameters of the plasma channel and light filament were estimated about 50 and 150 μm, respectively. Théberge, *et al.* have shown that the plasma density in a filament, characterized by side imaging fluorescence and longitudinal diffraction techniques, is highly dependent on the focal length of the lens and slightly dependent on the pulse power [Théberge 06]. The density was found to increase from 10^{15} to 2×10^{18} cm^{-3} with a decrease of the focal length from 4 m to 10 cm.

Plasma lifetime

After the filamentation process in the atmosphere the self-guided laser pulse leaves a plasma channel in its wake. The density of free electrons drops off rapidly due to recombination and attachment processes, therefore the lifetime of the plasma channel is limited to a few nanoseconds [Zhao 95]. The temporal evolution of the density of free electrons generated in the wake of a filament have been characterised in several experiments [Schillinger 99, Tzortzakis 00, Ladouceur 01]. For instance, the plasma decay presented in Figure 1.4 was obtained by means of time resolved diffraction, where the contrast of fringes observed in the far field is measured as a function of a temporal delay between the filamentary pulse and the probe pulse [Tzortzakis 00].
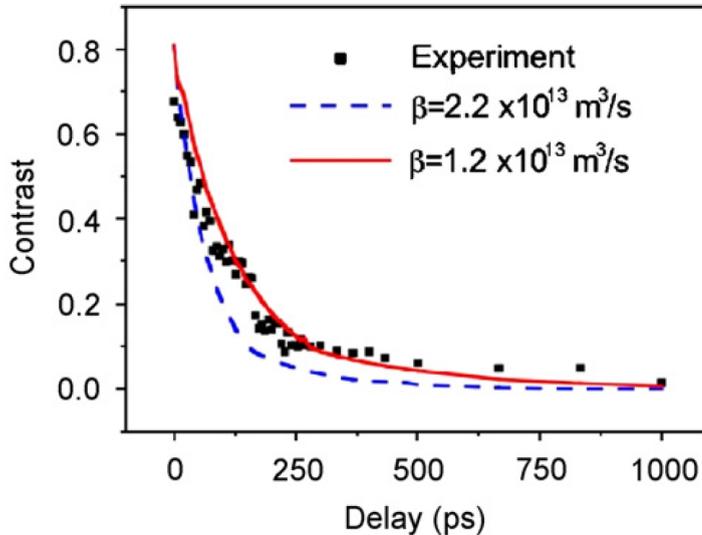
Figure 1.4: Optical contrast of the probe wave front central fringe as a function of the delay between the probe and the filamentary pulses. Black squares - experimental data, lines - result of simulations. From [Tzortzakis 00].

A fast initial and slow secondary decay was observed (see Figure 1.4). The rapid decay in the first phase indicates that the capture of electrons on the parent ions dominates the initial evolution of the plasma during the first few hundreds of picoseconds.

For the latter evolution, when free electron density $\rho_e < 10^{15}$ cm^{-3}, the attachment of electrons on the neutral oxygen molecules becomes the main recombination process. It yields in an exponential decay of the electron density with a characteristic time $\tau \sim 150$ ns [Ladouceur 01].

Terahertz radiation

During filamentation process a plasma string is left behind the moving laser pulse. The interaction between free electrons born near the laser intensity peak with the remaining of the pulse leaves the plasma in an excited state of oscillations [Sprangle 04, D'Amico 07c]. Predominant are transverse electron oscillations induced by the transverse component of the laser field. However, for a pulse of many optical cycles ($\tau > 10$ fs at 800 nm), the net radial current is zero, so that no THz emission results. There is also a small longitudinal oscillation due to the Lorentz force. Since the density of the plasma is on the order of 10^{16} cm^{-3}, the corresponding electron plasma frequency $\omega_{pe} = \sqrt{e^2 n_e / m_e \varepsilon_0}$ is around 1 THz. This longitudinal oscillation is damped quickly by collisions with neutral molecules, so that the duration of the plasma oscillation and the corresponding THz pulse duration are on the order of a few picoseconds. In other words, only the leading moving part of the plasma string contains longitudinal oscillations that are responsible for THz emission. One has therefore the equivalent of a longitudinal dipole-like structure moving at the speed of light over a finite length and emitting therefore a transition-Cherenkov type THz radiation [D'Amico 07c, D'Amico 08a].

A laser filament as a THz source has several unique advantages comparing to the traditional techniques for THz generation including photoconductive antenna and optical rectification with electro-optic crystal. Being a femtosecond filament a THz source can be positioned far away from the laser system, thereby avoiding the absorption of the THz field by water vapor during propagation in ambient air. At the same time, high-energy laser pulses can be employed for THz generation without damage to the emitter, which is impossible with the traditional techniques.

Multifilamentation

When the input peak power is far above the critical power for self-focusing, the modulational instability splits the beam to a large number ($N \simeq P_{in}/P_{cr}$) of filaments [Vidal 96]. These multiple filaments interact with each other in a complex way: they can merge and slip during the laser pulse propagation, particularly for collimated TW beams.

In high-power laser beams filaments are born from inhomogeneities of the wavefront, which are generally produced by the noise in the laser system and are then amplified by the air turbulence during the propagation. This process is named the modulational instability [Couairon 07]. The control over multifilamentation is possible by deformation of the wavefront with a phase-mask or with a deformable mirror [Méchain 04b]. For example, it has been demonstrated that one can organize filaments in a matrix [Rohwetter 08] or in a cylinder [Châteauneuf 08].

Conical emission of white light

The white light beam generated during filamentation in gases or condensed media generally consists of a white central part surrounded by a rainbow-like conical emission (see Figure 1.5). The radial order of the spectral components is inverse of diffraction with bluer frequencies appearing on the outside rings. This phenomenon is a signature of filamentation. Several mechanism have been proposed to explain this phenomenon: Cherenkov radiation [Golub 90, Nibbering 96], self-phase modulation [Kosareva 97], four-wave mixing [Luther 94], formation of X-waves in the spatiotemporal domain [Conti 03, Faccio 06].
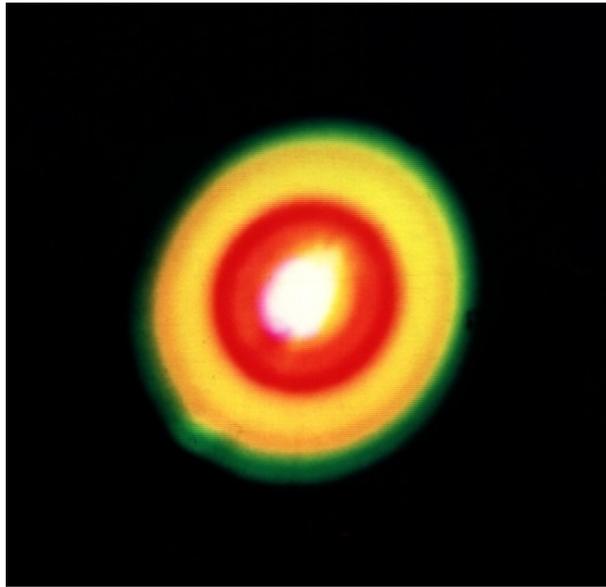
Figure 1.5: Photo of the conical white light emission accompanying a filamentary pulse in air, recorded at a distance of 30 m after the onset of filamentation [Nibbering 96]. A central white core (the filament) is surrounded by a ring structure.

Ultraviolet fluorescence

During filamentation a bright plasma channel left after the passage of the laser pulse is often visible for a human eye. Spectral analysis of plasma filaments in air has been performed by several groups and the luminescence was identified as due to the optical transitions of the excited neutral and ionic nitrogen molecules inside the filamentary plasma [Talebpour 99, Martin 02]. This plasma luminescence has been widely used for various purposes, like remote sensing of the atmosphere [Xu 11b], experimental measurements of the length and width of a laser filament, the electron temperature and the laser intensity inside laser filaments [Filin 09, Xu 12], *etc.* The plasma luminescence was observed to be sensitive to the external electric field, this has opened up important applications for the remote measurements of DC electric field or intense THz radiation [Sugiyama 09, Liu 10].

Coherent stimulated emission

Stimulated radiation of air plasma pumped by ultrashort intense laser pulses has attracted growing attention in recent years. Both backward and forward stimulated emissions have been observed in experiments. In particular, the backward stimulated emission is very interesting, because it can be potentially employed for remote sensing applications. The advantage lies in the fact that it can bring information about pollutants towards the ground observer with a well defined directionality. This has to be compared to the omni-directionality of the fluorescence or scattered optical signal from the same pollutants. The employment of backward stimulated lasing radiation for remote sensing is expected to bring about tremendous improvement of the measurement precision and sensitivity.

Chapter 2

Measurements of laser intensity inside femtosecond plasma filaments

2.1 Introduction

Femtosecond laser filamentation in air attracts considerable interest because of a rich physics involved in the process, as well as due to a long list of possible applications. The precise knowledge of parameters such as the fluence or intensity distribution inside filaments is important. However, due to the very high intensities inside a filament (at least 10^{13} W/cm^2), direct measurements are difficult because any device placed in the filament path, whether a detector, a reflector or an attenuator, is easily damaged. Nowadays, the information about laser intensity during filamentation relies on numerical simulations to a large extent [Mlejnek 99, Nurhuda 02, Kandidov 03, Méchain 04b, Couairon 07, Kosareva 08, Kandidov 11, Couairon 11].

Several indirect measurements of laser intensity inside filaments are possible and have been performed. They are "indirect" in the sense that they rely on theoretical models which link laser intensity to some measurable physical quantities. The first experimental measurement of the filamentary laser intensity was mentioned in the paper by H. R. Lange, *et al.* devoted to high-order harmonic generation [Lange 98]. A laser filament was formed with an $f = 1000$ mm lens, 70 cm after the geometrical focus the filamentary pulse entered into a cell containing a noble gas (xenon). For intensities of about 10^{13} - 10^{14} W/cm^2, the atoms generate a large number of odd high-harmonics [Salières 99]. The order (q) of the highest harmonic is given by simple and well established relation [Krause 92, Corkum 93]:

$$qh\omega = U_i + 3.2U_p, \tag{2.1}$$

where U_i is the ionization potential of the atom (12.13 eV for Xe) and U_p is the pondero-motive energy (the mean kinetic energy of free electrons oscillating in the field of the laser pulse), which is directly proportional to the peak intensity:

$$U_p = \frac{1}{2}m_e\langle v^2 \rangle = \frac{e^2 E^2}{4m_e\omega^2} = 9.33 \times 10^{-14} I\lambda^2. \tag{2.2}$$

Here, the laser intensity I is expressed in W/cm^2, wavelength λ in μm, U_p in eV. Harmonics up to the 15rd order was measured. The authors deduced an intensity of 4.5×10^{13}

W/cm^2. Recently, D. S. Steingrube, *et al.* used the same approach to measure the intensity at different distances along the filament. They found a laser intensity plateau along the filament but also the presence of higher intensity spikes predicted in simulations [Steingrube 11].

A peak intensity value of 4×10^{13} W/cm^2 during filamentation of a 100-fs laser pulse in air have been semi-empirically estimated by J. Kasparian, *et al.* [Kasparian 00], under the assumption of a steady state balance between self-focusing and multi-photon ionization.

In 2005 A. Ting *et al.*, presented a method to use an helium gas interface for characterization of femtosecond laser filaments in air without perturbing the measurement by the introduction of an optical element [Ting 05b]. Because of its low Kerr index, helium allowed beam expansion before attenuation by reflection on the surface of a glass plate. The authors found a fluence between 0.23 and 0.67 J/cm^2 in a single filament and estimate a peak intensity between 0.45 and 1.3×10^{13} W/cm^2.

Recently, S. Xu, *et al.* proposed another method based on the measurement of the ratio of two nitrogen fluorescence lines [Xu 12]. These lines, namely, 337 nm and 391 nm, are assigned to the second positive band of N$_2$ ($C^3\Pi_u \rightarrow B^3\Pi_g$) and the first negative band system of N$_2^+$ ($B^2\Sigma_u^+ \rightarrow X^2\Sigma_g^+$), respectively [Lofthus 77, Talebpour 01]. Because of distinct excitation mechanisms (although they are still not clear), the authors proposed that the signals of the two fluorescence lines increase with the laser intensity at different orders of nonlinearity. The value of the intensity inside filament was deduced to be 3.5×10^{13} W/cm^2 for conditions close to our experiment, which will be discussed further (focal length of the lens 1000 mm, laser pulse energy 1 mJ). In a subsequent paper, using the same technique, the authors also found intensity spikes reaching 10^{14} W/cm^2.

2.2 Our method: results and discussion

We have recently proposed a simple technique to determine experimentally the laser fluence/intensity inside a filament in air. Our method is based on the measurement of the laser energy transmitted through diaphragms of increasing sizes (40 μm – 150 μm). These diaphragms are fabricated by the filament itself on a thin metallic foil by cumulative laser irradiation. The transmitted laser energy measured as a function of the diaphragm size yields a spatially resolved laser fluence distribution. If the pulse duration is known, the radial intensity distribution can be deduced. By displacing the metallic foil along the filament propagation axis and repeating this procedure, one can then reconstruct a 2-dimensional distribution of the laser intensity along the filament.

The method is illustrated in Figure 2.1. Femtosecond laser pulses (wavelength: 800 nm, pulse duration: $\tau_p \approx 46$ fs) propagate in air, with an initial laser beam width of $d_0 \approx 15$ mm. The spatial profile of our laser beam is not perfect. We thus installed an aperture of $d_a = 10$ mm to the center of the beam to select its uniform part. After passing through the aperture, laser pulses with an energy of 1.1 mJ are focused by a convex lens ($f = 1000$ mm) to create single filaments in air. Employment of the aperture leads to formation of a more stable filament [Cook 05]. An aluminium foil with thickness of 45 μm is placed perpendicular to the laser propagation axis around the filamentation area. The

metallic foil is mounted on a 3-dimensional translation stage for a scan along the filament. A laser Joulemeter (model: Gentec SOLO 2, QE50SP-H-MB-D0) is placed far behind the metallic foil to measure the transmitted laser energy once a micrometric pinhole has been drilled by the filament itself.
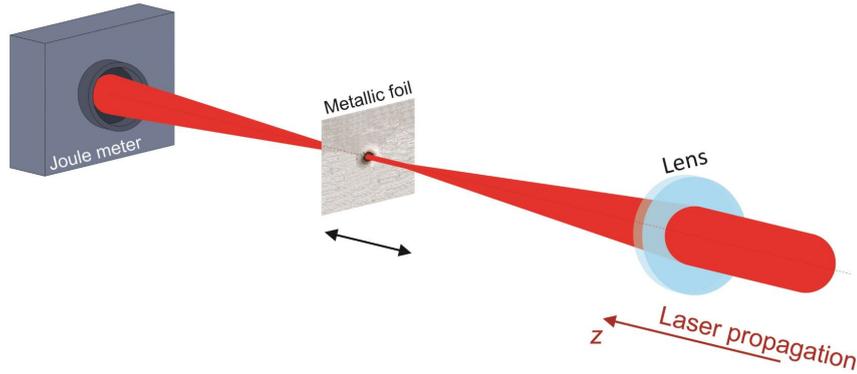
Figure 2.1: Scheme of the experiment. The intense laser filament drills a micrometric diaphragm on the aluminum foil and the transmitted energy is measured by the laser energy meter.

In our experiments, successive filament-forming laser shots progressively drilled a pinhole in the metallic foil. In Figures 2.2(a)-(f), these pinholes are presented as a function of the number of laser shots (N). In this case, the metallic foil was placed 1 cm after the geometrical focus of the lens ($z = 1$ cm). It is seen that the pinhole diameter increases gradually with increasing number of laser shots.
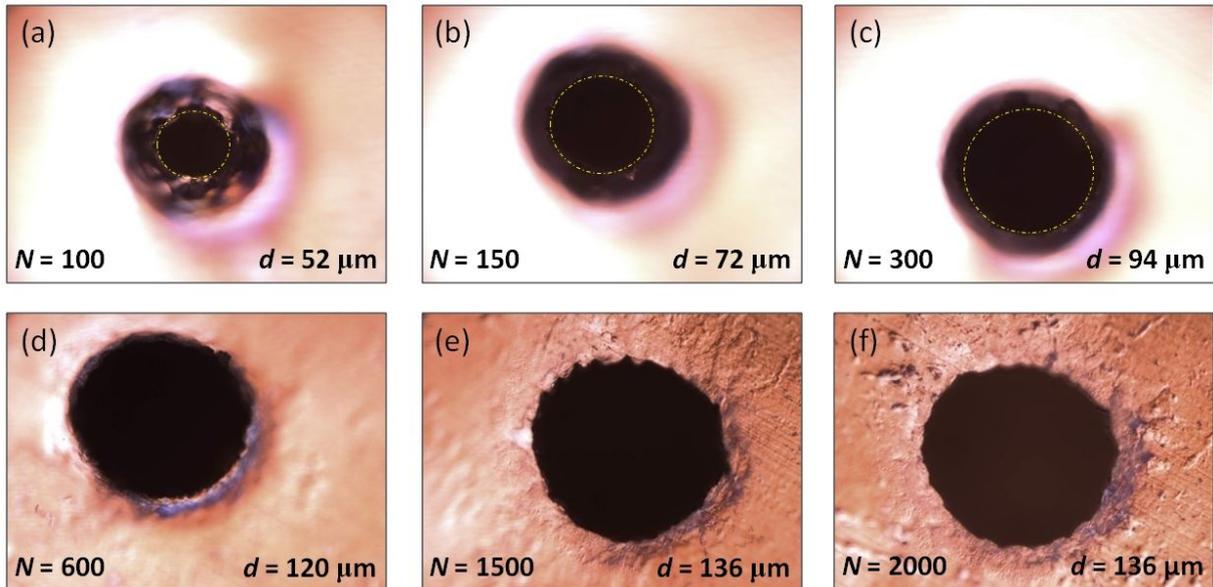
Figure 2.2: The micrometric pinholes created by the laser filament as a function of the number of laser shots. The 1.1 mJ femtosecond laser pulses are focused by a convex $f = 1000$ mm lens in air.
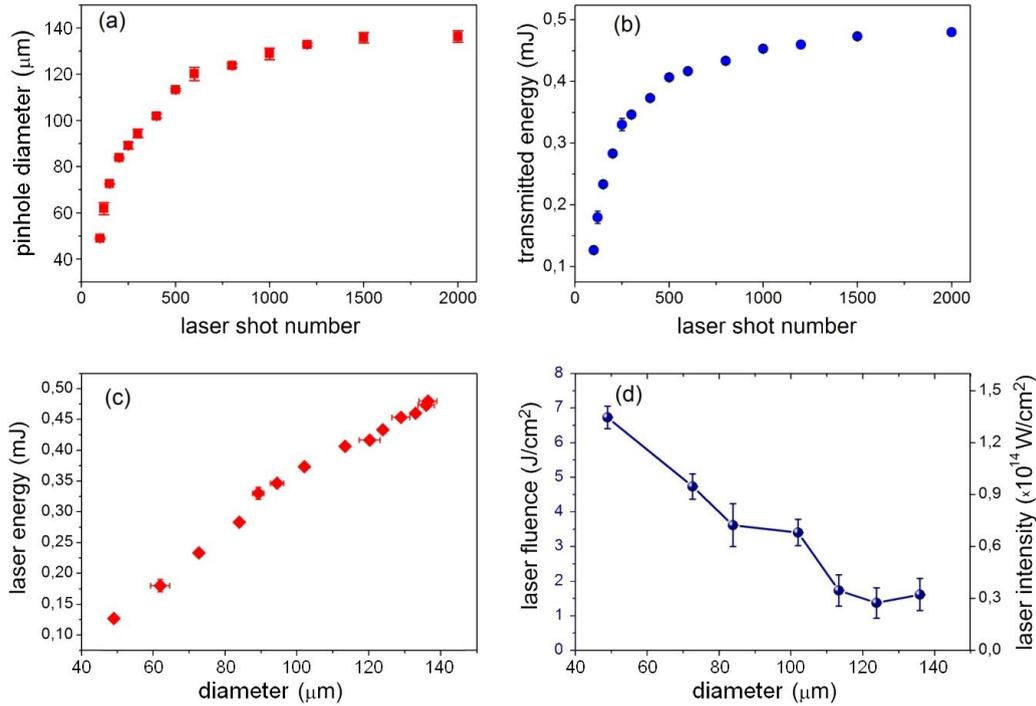
Figure 2.3: (a) and (b), diameter of the micrometric pinholes and the corresponding transmitted laser energy as a function of the laser shot number. (c), Transmitted laser energy as a function of the pinhole diameter. (d), Calculated laser fluence (left scale) and laser intensity (right scale) as a function of the pinhole diameter.

In Figure 2.3(a), the diameter of the drilled pinholes is presented as a function of the number of laser shots. It is seen that the pinhole diameter increases from ≈ 50 μm after 100 shots to a stable value of ≈ 130 μm after 1000 laser shots. The laser energy transmitted through the pinhole is also presented in Figure 2.3(b) as a function of the laser shot number. For $N = 2000$, the transmitted energy was around 0.48 mJ. In Figure 2.3(c), the transmitted laser energy is plotted against the size of the diaphragms. Knowing the transmitted laser pulse energy and the corresponding diaphragm area, one can calculate the laser fluence directly. For two adjacent diaphragms with diameter d_1 and $d_2 > d_1$, the laser fluence in the zone $d_2 > d > d_1$ is given by:

$$F = \frac{E_2 - E_1}{\frac{\pi}{4}\left(d_2^2 - d_1^2\right)}, \tag{2.3}$$

where E_1 and E_2 are the measured laser energy contained in the diaphragm of d_1 and d_2, respectively. The results are presented in Figure 2.3(d), where a maximum laser fluence of ≈ 7 J/cm^2 is observed.

To estimate the laser intensity, one needs to know the laser pulse duration τ_p. Once τ_p is measured or estimated, the maximum laser intensity can be deduced as $I \approx 0.94F/\tau_p$, assuming a Gaussian temporal profile. However, it is known that during the filamentation process the pulses may experience complicated temporal transformations such as pulse

splitting [Ranka 96, Bernstein 02] and pulse shortening [Kosareva 07, Odhner 10]. As a result, sharper temporal structures compared to the initial laser pulse duration of the incident laser can occur and have been observed. Consequently, taking the initial pulse duration unchanged is likely to underestimate the filament peak intensity.

We measured the pulse duration of the central part of the laser beam after filamentation with a Frequency Resolved Optical Gating (FROG) apparatus by Swamp Optics [Trebino 00]. A 1-mm-diaphragm was installed 60 cm after the zone of filamentation, where the beam size was about 10 mm. For a pulse energy below 2 mJ, the measured pulse duration in the central part of the filament was ≈ 46 fs and remained rather stable with successive laser shots (see Figure 2.4). For laser pulse energy beyond 3 mJ, the measured pulse duration became unstable from shot to shot, indicating the emergence of complicated temporal structures. Assuming the pulse duration of 46 fs, we calculated the laser intensity distribution inside the filament, as presented in Figure 2.3(d). Note that the maximum laser intensity inside the filament is $\approx 1.44 \times 10^{14}$ W/cm^2. This value is 2-3 times higher than previously reported for conditions close to those of our experiment [Lange 98, Kasparian 00, Xu 12]. We believe this translate the fact that we are able to measure the intensity of a small central area of the filament. If we consider the laser energy in a larger section of the filament (corresponding to the diaphragm of the largest size), we extract a value of $\approx 5.5 \times 10^{13}$ W/cm^2, close to previous results.
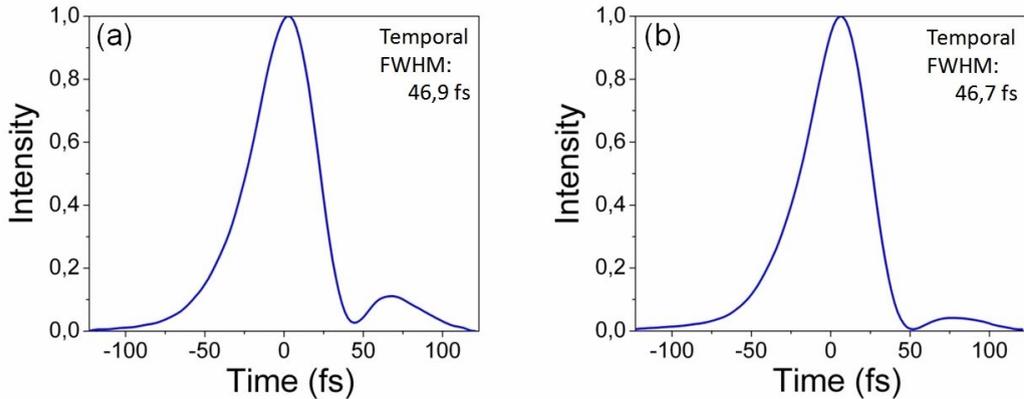
Figure 2.4: Laser pulse temporal profile measured by FROG apparatus 60 cm after the zone of filamentation: (a) with the laser pulse energy $E_{pulse} = 200$ μJ (under the threshold of filamentation) and (b) with $E_{pulse} = 1.1$ mJ (our experimental conditions).

The above measurements were performed 1 cm after the geometrical focus of the laser beam. By repeating the same measurement along the filament propagating axis at different z positions, we obtained the laser intensity distribution around the entire filamentation zone. Combining all measurements, we construct a 2-dimensional distribution of the laser intensity of the filament. This "intensity map" is presented in Figure 2.5. Two laser intensity peaks are observed around $z = -3$ cm and $z = 1$ cm, signaling the occurrence of re-focusing [Talebpour 99, Liu 03]. We also present in Figure 2.5(a) the luminescence of the plasma channel taken with a CCD camera.
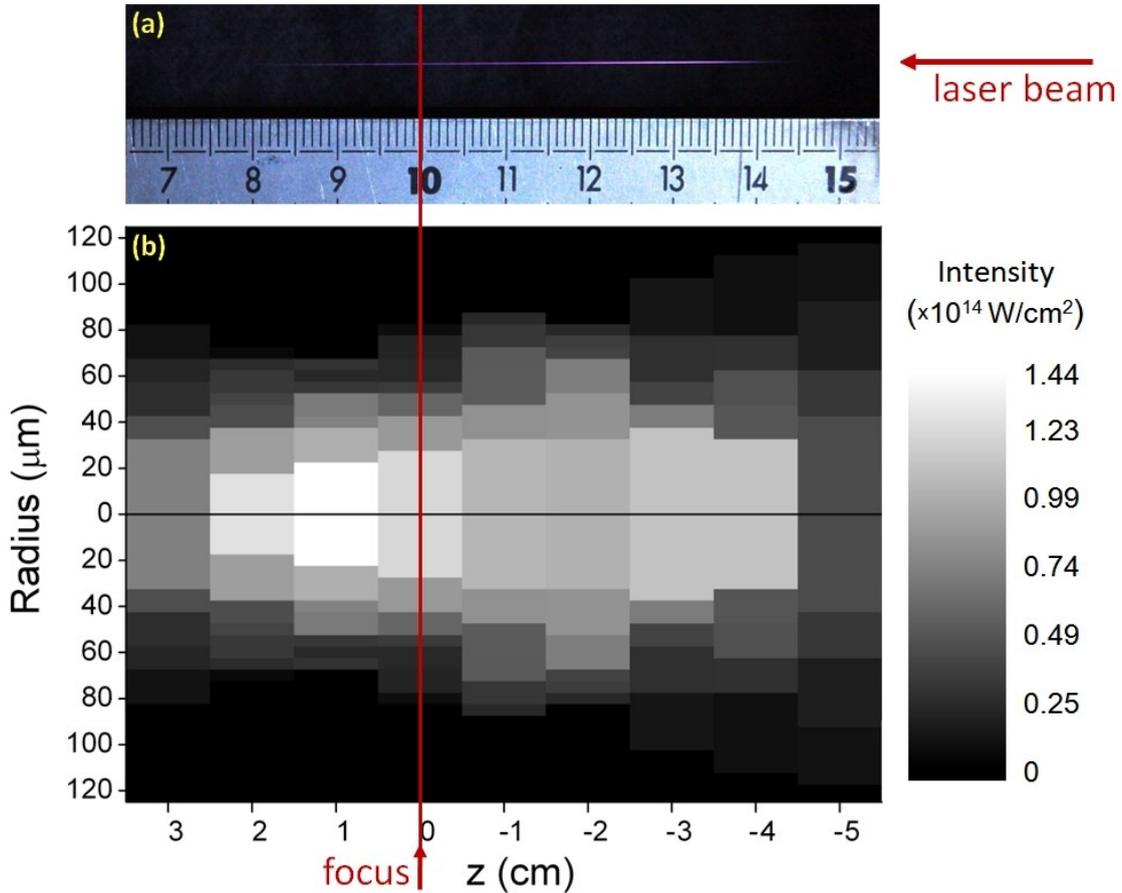
Figure 2.5: (a) Image of the filament luminescence taken by a CCD camera. (b) Measured laser intensity distribution along the filamentation area. The laser comes from the right side of the figure.

2.3 Conclusion

In summary, we demonstrated a simple and direct method to measure the laser fluence/intensity distribution inside an intense femtosecond laser filament in air. This method exploits the destructive capacity of a filament to fabricate a variable diaphragm on a metallic foil. The laser intensity is obtained from the measured diaphragm size, the corresponding transmitted laser energy and the laser pulse duration. A longitudinal scan along the filament provides a 2-dimensional characterization of the laser intensity of the filament. For a laser pulse energy of ~ 1 mJ the maximum intensity inside filament is measured to be $\sim 1.44 \times 10^{14}$ W/cm^2, 2-3 times larger than previously reported for similar experimental conditions. We attribute this higher value to a spatial resolution (≈ 50 μm) better than the filament diameter (≈ 150 μm). This simple method could find application in other intense laser-matter interaction experiments where measurement of laser intensity distribution is highly desired, such as in high order harmonic generation in gases or laser surface ablation.

Part II

Ultraviolet emission from femtosecond plasma filaments

Chapter 3

Ultraviolet fluorescence from plasma filaments in air

3.1   Introduction

Intense femtosecond laser pulses launched in transparent media experience filamentary propagation, which has been observed to be a generic phenomenon in solids, liquids, and gases. One of the most spectacular phenomena associated with filamentation is the formation of a long, bright plasma channel after the passage of the laser pulse, which extends from a few centimeters to hundreds of meters in air depending on experimental conditions [Couairon 07, Chin 10]. Spectral analysis of the plasma channel in air has been performed by several groups and the fluorescence was identified as due to the following two main processes [Talebpour 99, Martin 02]:

- the $C^3\Pi_u \rightarrow B^3\Pi_g$ transition of the second negative band of excited triplet state ($C^3\Pi_u$) of neutral N_2 molecules,

- the $B^2\Sigma_u^+ \rightarrow X^2\Sigma_g^+$ transition of the first positive band of the excited cation state N_2^+ ($B^2\Sigma_u^+$).

These bands of ionic and neutral molecular nitrogen is schematically shown in Figure 3.1. A typical filament fluorescence spectra in air is presented in Figure 3.2.

The spectroscopy of molecular nitrogen has been extensively studied since the middle of the XIX century [Lofthus 77]. At that time the second negative band of N_2 and the first positive band of N_2^+ have been observed and described for the first time. In the 1920s the rotational structure of these systems became a subject of systematic study. The complete "identification atlas" of the two bands was presented in the mid-1960s by Tyte and Nicholls [Tyte 64, Tyte 65]. As the names indicate, these systems were observed in the positive and negative columns of a discharge through nitrogen, but it is also readily produced in various sources such as transformer-excited discharges through gases containing traces of nitrogen, in discharges produced by microwaves, in hollow cathode tubes, *etc.* In the late-1970s−1980s the spectroscopic investigation of laser-initiated plasmas in atmospheric gases has begun. At that time mostly a neodymium (wavelength: 1.06
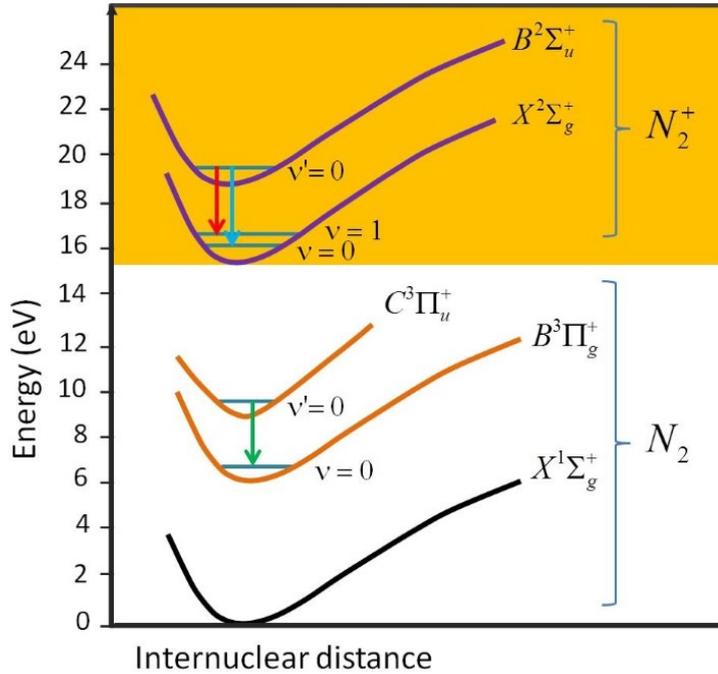
Figure 3.1: Schematic potential energy diagram of the neutral and ionic nitrogen molecules. The $C^3\Pi_u \to B^3\Pi_g$ of the neutral N_2 was historically named as the second positive band of nitrogen molecules, the $B^2\Sigma_u^+ \to X^2\Sigma_g^+$ transition of N_2^+ as the first negative band.

μm, pulse duration: 10-20 ns, intensity: 10^{10} - 10^{12} W/cm^2) laser was used. Emission measurements of plasmas produced in low pressure air (~ 100 torr) reveal molecular lines of the second negative system of N_2 and the first positive system of N_2^+ [Armstrong 83]. Measurements in pure nitrogen (100 - 800 torr) reveal Stark broadened N^{3+} lines and molecular N_2^+ lines [Alam 90]. At higher pressure in air the continuum emission peaked around 200 nm was observed [Radziemski 83, Borghese 98]; there was no line or band emission detected. In 1999, Talebpour, *et al.* presented a spectral measurements of filamentary plasmas produced in atmospheric air using a 60 mJ, 220 fs, Ti:Sapphire laser, showing nitrogen molecular lines [Talebpour 99]. The spatial distribution of line emission presents an evidence of multiple re-focusing during filamentation.

Applications of filament-induced nitrogen fluorescence

The plasma fluorescence has been widely used for various purposes. Potential use of femtosecond laser-induced fluorescence for remote sensing in the atmosphere was demonstrated in 2004 [Luo 04, Gravel 04]. Later, simultaneous detection and identification of gas pollutants mixed with air at atmospheric pressure were performed using filament-induced nonlinear spectroscopy (FINS) [Xu 07]. The high intensity inside a filament can dissociate the gas molecules into small fragments which emit characteristic fluorescence. The authors have demonstrated the generic algorithm to identify the unknown spectra. The FINS technique has been applied for remote sensing of hydrocarbons, ethanol va-
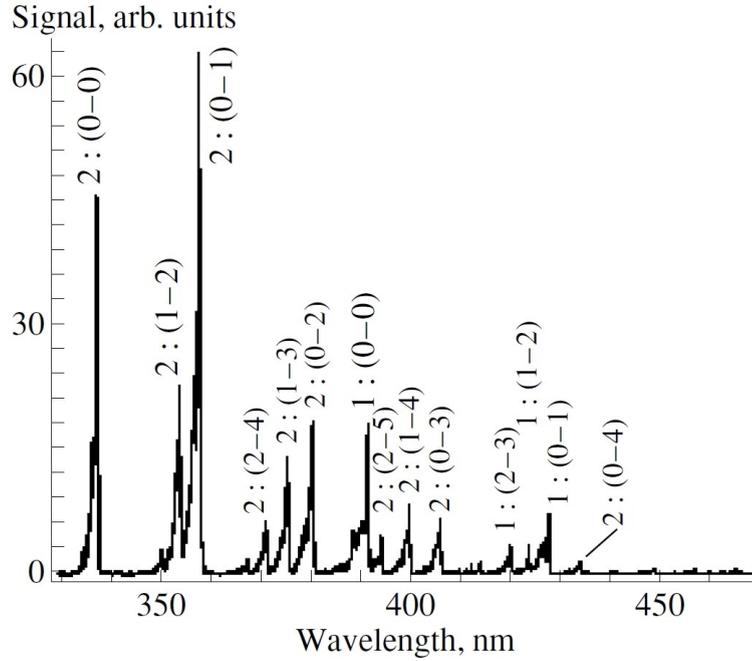
Figure 3.2: The emission spectra of air in atmospheric pressure interacting with a 200 fs laser pulse, taken from [Talebpour 01]. The lines marked by 1 are assigned to the first negative band system of N_2^+ ($B^2\Sigma_u^+ \rightarrow X^2\Sigma_g^+$ transition) and those marked by 2 are assigned to the second positive band system of N_2 ($C^3\Pi_u \rightarrow B^3\Pi_g$ transition). In the transitions ($\nu - \nu'$), ν and ν' denote the vibrational levels of upper and lower electronic states, respectively.

por and smoke [Xu 06, Luo 06, Daigle 08, Kamali 09, Chin 09, Xu 11b]. Recently, water vapor condensation induced by femtosecond laser filamentation has been observed in a cloud chamber [Rohwetter 10] and in the atmosphere [Petit 11, Henin 11]. Remote humidity measurements using filament-induced fluorescence spectroscopy have been performed. Clear fluorescence emission from OH radical at 308.9 nm [Wang 12] and the stronger one from NH radical at 336 nm [Yuan 14] were observed in air. The linear dependence of the fluorescence signal intensity with the relative humidity around the filament region was reported.

The fluorescence of nitrogen molecules from plasma filaments has been used for characterisation of filaments. The length and width of laser filaments in air have been experimentally measured mainly based on the plasma fluorescence trace left in air after the intense laser pulse [Kasparian 03, Hosseini 03, Iwasaki 03, Luo 05, Théberge 06, Bernhardt 08, Owada 13, Point 14]. The fine structure of the fluorescence spectrum has been exploited to extract the electron temperature inside an intense laser filament [Filin 09]. Recently, Xu, *et al.* proposed a simple method for the measurement of laser intensity inside femtosecond laser filaments [Xu 12]. It is based on an empirical dependence between the laser peak intensity and the strength ratio of two nitrogen fluorescence signals at 337 nm and 391 nm from femtosecond filament in air. Because of distinct excitation mechanisms, the signals of these fluorescence lines increase with the laser intensity at different orders of nonlinearity.

In the presence of external electric field, the plasma fluorescence was observed to increase, which has opened up important applications for the remote measurement of DC electric field [Sugiyama 09] or intense Terahertz radiation [Liu 10]. In the later work, J. Liu and coworkers introduced an optical technique of broadband THz wave detection by coherently manipulating the fluorescence emission of a gas plasma interacting with THz waves. The coherent THz wave detection was demonstrated at a distance of up to 10 m.

Mechanisms of nitrogen fluorescence

There is still controversy about the physical mechanisms that achieve population in the $(C^3\Pi_u)$ and $(B^2\Sigma_u^+)$ states inside laser filaments in air.

Direct photon excitation into the excited triplet state $(C^3\Pi_u)$ of neutral N_2 molecules is a spin forbidden process and therefore unlikely. Up to now, two indirect processes to achieve population in this state have been suggested. It was first proposed that dissociative recombination through the two processes: $N_2^+ + N_2 + N_2 \Rightarrow N_4^+ + N_2$, followed by $N_4^+ + e \Rightarrow N_2 (C^3\Pi_u) + N_2$ is responsible at atmospheric pressure [Xu 09, Xu 11a]. At the mean time, recent experiments indicates that intersystem crossing from an excited singlet state is the dominant path to produce the triplet state and dissociative recombination was shown to be a minor contributor [Arnold 12].

The formation of the excited cation state N_2^+ $(B^2\Sigma_u^+)$ results from the removal of an inner-valence electron from the $(\sigma_u 2s)$ orbit of neutral N_2 molecule, where the ground state electronic configuration is $KK(\sigma_g 2s)^2(\sigma_u 2s)^2(\pi_u 2p)^4(\sigma_g 2p)^2$ [Talebpour 00, Talebpour 01].

Stimulated UV emission from plasma filaments

The understanding of the plasma luminescence is also important in the context of recently discovered stimulated emission from filaments in air and other gas mixtures. The backward and forward stimulated emissions from filaments have attracted attention due to their potential for applications to remote sensing [Kocharovsky 05, Hemmer 11, Kartashov 13, Yao 13, Chu 14b]. It was revealed that the stimulated emissions were rooted in the same electronic transitions corresponding to the luminescence, i. e., the $C^3\Pi_u \to B^3\Pi_g$ transition of neutral N_2 molecules, and the $B^2\Sigma_u^+ \to X^2\Sigma_g^+$ transition of the first positive band of the excited cation state N_2^+ [Kartashov 12, Yao 13, Mitryukovskiy 14]. Therefore, the plasma luminescence and stimulated emission are actually two sides of the same coin.

In 2011, Yao, *et al.* reported a forward stimulated radiation in ambient air or pure nitrogen pumped by short and intense mid-IR laser pulses [Yao 11]. The lasing effect corresponded to the $B^2\Sigma_u^+ \to X^2\Sigma_g^+$ transition between the excited and ground cation states. It could be triggered by fine tuning of the wavelength of a femtosecond Optical Parametric Amplification (OPA) laser system operating in the mid-IR (wavelength: 1.2 μm - 2.9 μm). Lasing radiation was initiated by a seeding effect of the 3rd or 5th harmonic of the driving pulse overlapped with specific spectral positions of the above transitions. The authors attributed the lasing effect to the amplification of the weak harmonic pulse in the presence of population inversion [Yao 11, Ni 12, Chu 12]. The mechanism responsible

for population inversion is still a subject of controversy. Later, the same group showed that lasing action of N_2^+ could also be activated with 800 nm femtosecond laser pulses, but required injection of a seed pulse around 400 nm [Ni 13, Yao 13]. This external 400 nm pulse is the counterpart of the 3rd or 5th harmonic in the case of mid-IR pumping. Lasing obtained with a pump at 800 nm is particularly interesting because of the wide availability of femtosecond lasers at this wavelength. Very recently, three independent groups reported self-seeded lasing action from N_2^+ in air or pure nitrogen pumped by just one single pulse at 800 nm [Liu 13, Wang 13, Chu 14a]. The seeding was provided by the generation of second harmonic and supercontinuum white light inside the gas. Subsequently, the lasing action in atmospheric air pumped by 800 nm laser pulses with peak power up to 4 TW was obtained [Point 14]. The maximum lasing radiation energy was 2.6 μJ, corresponding to an emission power in MW range. The maximum conversion efficiency of 3.5×10^{-5} is measured at moderate pump pulse energy.

Q. Luo and coworkers were the first to suggest the existence of a backward stimulated emission from femtosecond laser filaments in air, based on an exponential increase of nitrogen fluorescence with filament length [Luo 03]. In 2012, Kartashov, *et al.* reported a strong backward lasing emission at 337 nm and 357 nm in high-pressure (2 - 5 bar) mixture of nitrogen and argon pumped by powerful mid-IR lasers (wavelength: 3.9 μm or 1.03 μm), due to a collision-induced population inversion between the $C^3\Pi_u^+$ and $B^3\Pi_g^+$ states of the excited N_2 molecule [Shneider 11, Kartashov 12].

In 2013-2014 our group achieved a backward stimulated emission at 337 nm under atmospheric pressure [Mitryukovskiy 14, Ding 14]. Our findings will be presented in detail in the Chapter 4 of this manuscript. Interestingly, it was observed that backward 337 nm stimulated emission associated with the neutral N_2 molecules can only be achieved with circularly polarized laser pulses, while the forward 391 nm and 428 nm radiation originated from the excited nitrogen cation exists just for linear laser polarization [Zhang 13, Mitryukovskiy 14, Ding 14].

3.2   Plasma fluorescence of femtosecond laser filaments in air

In this chapter, we present and discuss the strong dependence of the luminescence from both the N_2 and N_2^+ molecules on the incident laser polarization. It reveals a new non-radiative route of populating excited neutral and ionic molecular levels through electron collision.

Scheme of the experiment

In the experiment (see Figure 3.3 for the scheme of our setup), femtosecond laser pulses with pulse energy up to 10 mJ (46 fs, 800 nm) from a commercial laser system were focused by a convex lens in ambient air. A quarter-wave plate ($\lambda/4$) was installed before the focal lens to change the laser polarization from linear to circular. Plasma channels with length varying from a few millimeters to several centimeters were created, dependent on the incident pulse energy. In order to detect the spontaneous luminescence in the direction orthogonal to the laser propagation axis, an $f = 25$ mm lens was employed to collimate the luminescence emitted at its geometrical focus and a second lens of $f = 100$ mm was used to focus the collected emission onto the entrance slit of a monochromator (Jobin-Yvon H-20 UV). The two lenses are made of fused silica. The luminescence signal from the monochromator was measured by a photomultiplier tube (Hamamatsu, model: H10722). In order to resolve longitudinally the luminescence signal along the filament, a 1 mm × 6 mm rectangular diaphragm was placed 1 mm away from the filament.
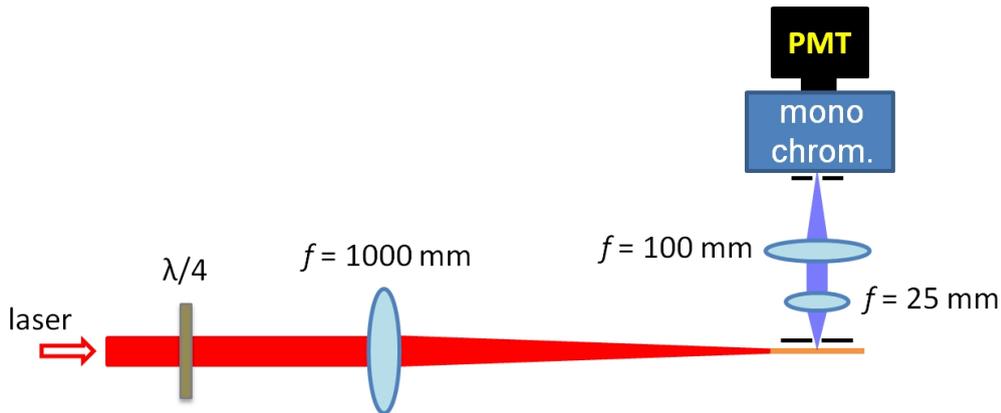
Figure 3.3: Scheme of the experimental setup. The incident femtosecond pulses are focused by an $f = 1000$ mm lens to create a filament in air. The luminescence from the filamentary plasma is collected by a system of two fused silica lenses into the slit of a monochromator. The signal is measured with a photomultiplier tube (PMT). A 1 mm × 6 mm rectangular diaphragm was placed 1 mm away from the filament to resolve longitudinally the luminescence signal along the filament.

Experimental results

We first measured the luminescence spectrum for linearly and circularly polarized laser pulses at different incident energies. Detection was performed at the middle position of the filaments in each case. In Figures 3.4(a) and (b), we present the results for E_{in} = 250 μJ, with a power just at the threshold for filamentation and for E_{in} = 10 mJ, where the peak power is 30 times higher than the critical power for self-focusing. The corresponding peak laser intensities were obtained from measurements of the laser flux through circular diaphragms of 60 μm diameter fabricated by a single filament formed with pulses of 1 mJ energy (this method is presented in detail in the Chapter 2). The intensities were estimated to be around 3×10^{13} W/cm^2 and 1.45×10^{14} W/cm^2, respectively. The emission peaks around 315, 337, 357, 380, 400 nm have been identified as due to the $C^3\Pi_u \rightarrow B^3\Pi_g$ transition of the third excited triplet state of the neutral nitrogen molecules with different initial and final vibrational quantum numbers. The two peaks around 391 nm and 428 nm correspond to the $B^2\Sigma_u^+ \rightarrow X^2\Sigma_g^+$ transition of the excited ionic N_2^+ molecules. In Figure 3.4(a), a much stronger luminescence emission is observed for all lines with linearly polarized laser pulses. However, at higher laser energy, the neutral N_2 molecular lines become stronger with circular laser polarization (see Figure 3.4(b)). The luminescence signal of the excited ionic molecules at 391 nm and 428 nm is now almost equal for the two pump laser polarization states.
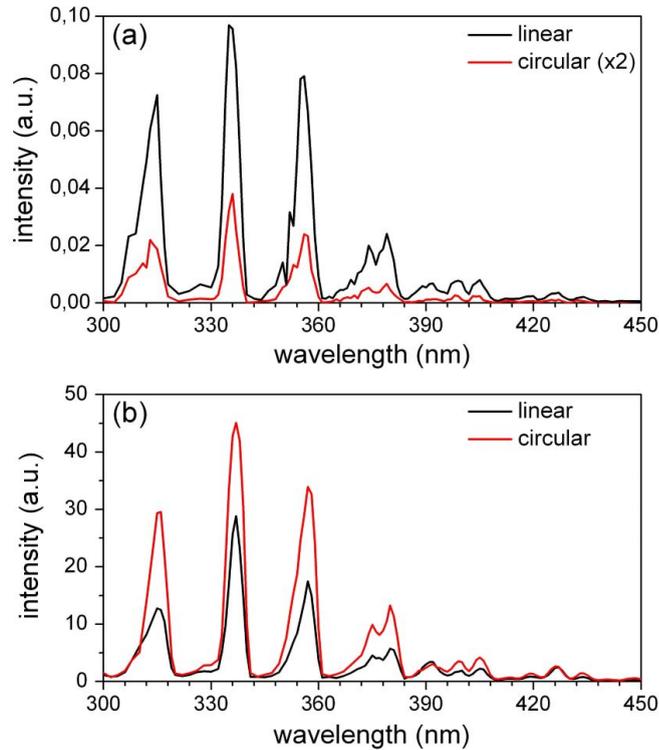
Figure 3.4: Luminescence spectrum of the air plasma filaments for linearly and circularly polarized laser pulses of 250 μJ (a) and 10 mJ (b). In (a), the signal obtained with circular laser polarization is multiplied by a factor of 2 for visibility.

In Figure 3.5, we present the evolution of the 337 nm and 391 nm luminescence signal representative of neutral and ionic nitrogen molecules along the filament axis z for both linear and circular laser polarization, for three different incident laser pulse energies. In Figures 3.5(a) and (a'), where the incident laser energy was 250 μJ, linear laser polarization yields more intense luminescence for both lines along the $\sim$ 25 mm filament. For an incident pulse energy of 10 mJ, however, the 337 nm emission line becomes $\sim$ 1.5 times stronger with circularly polarized laser between $z = -40$ mm to $z = -10$ mm (Figure 3.5(c)). The 391 nm signal is nearly equivalent along the filament for the two laser polarizations, with a slight difference dependent on the position (see Figure 3.5(c')). For intermediate laser pulse energy of 1.1 mJ, the 337 nm and 391 nm signals with circularly polarized laser are found to be comparable to those obtained with linear laser polarization, as presented in Figures 3.5(b) and (b'). We verified that the 357 nm and 428 nm emission lines exhibit similar behavior as those observed for 337 nm and 391 nm.
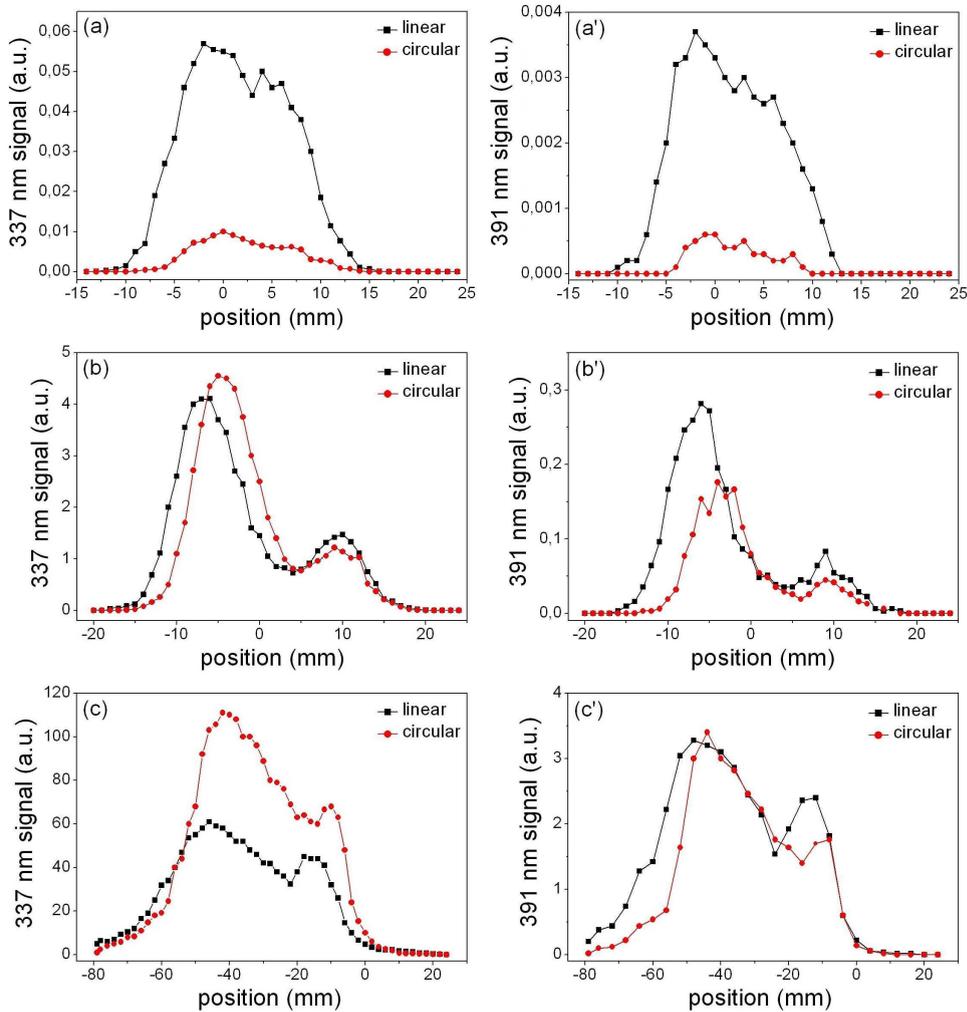

Figure 3.5: Intensity of the 337 nm ((a)-(c)) and the 391 nm ((a')-(c')) luminescence signal measured along the filaments for linearly and circularly polarized laser pulses. The incident pulse energy was 250 μJ for (a) and (a'), 1.1 mJ for (b) and (b'), and 10 mJ for (c) and (c').

The ellipticity ε of the laser can be changed continuously from linear ($\varepsilon = 0$) to elliptical ($0 < \varepsilon < 1$), and eventually circular ($\varepsilon = 1$) by rotating the quarter-wave plate. We therefore measured the dependence of the 337 nm and 391 nm signal as a function of ellipticity. All measurements were performed around the center of the plasma filament. In Figure 3.6, the results are presented for 4 different pulse energies as a function of the rotation angle of the $\lambda/4$ waveplate. The angles $\phi = 90° \times m$ correspond to linearly polarized laser, with m = 0, 1, 2, 3. The angles $\phi = 45° + 90° \times m$ correspond to
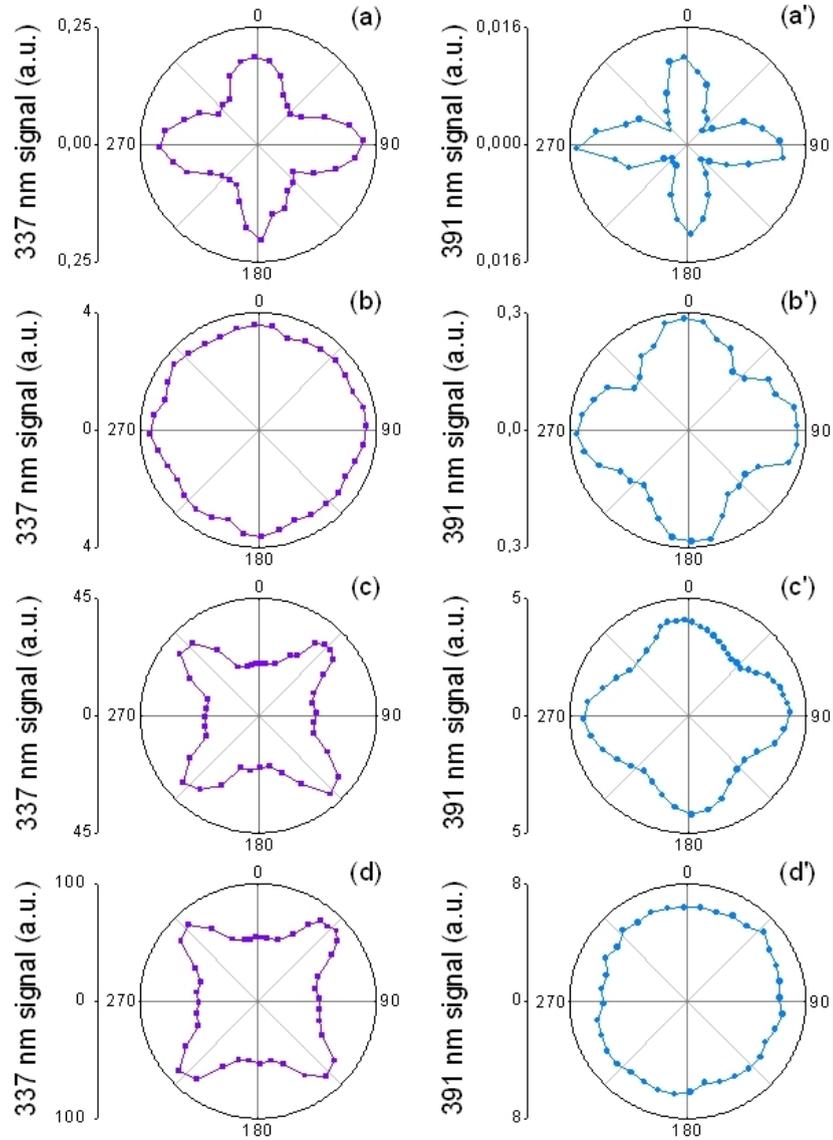
Figure 3.6: The luminescence signals at 337 nm ((a)-(d)) and 391 nm ((a')-(d')) as a function of the rotation angle of the quarter-wave plate. The incident pulse energy was 250 μJ, 600 μJ, 2.7 mJ and 10 mJ for (a) and (a'), (b) and (b'), (c) and (c'), (d) and (d'), respectively. All the measurements were performed around the center of the filament. Angle 0° corresponds to linear polarization of the pump laser.

circular laser polarization. With laser pulse energy of 250 μJ, the dominance of linear laser polarization over elliptical and circular is observed for both 337 nm and 391 nm emissions (Figures 3.6(a) and (a')). With increased pulse energy of 600 μJ, the signal at 337 nm is of same amplitude irrespective of the pump polarization (Figure 3.6(b)). Upon further increase of the pump pulse energy, the signal at 337 nm becomes more intense with a circularly polarized pump (Figures 3.6(c) and (d)). Concerning the emission of N_2^+ at 391 nm, the relative intensity obtained with circularly polarized laser pulses increases (see Figures 3.6(b') and (c')), until almost no dependence on ellipticity is observed for pulses of 10 mJ (Figure 3.6(d')).

Interpretation of the results

How should we understand the dependence of the luminescence with pump laser polarization? For the population of N_2^+ ions in the $(B^2\Sigma_u^+)$ state by inner-valence photon-ionization, linear laser polarization has been shown to be more efficient [Talebpour 00, Becker 01]. For the triplet neutral N_2 $(C^3\Pi_u)$ molecules, both dissociative recombination and intersystem crossing predict that a linearly polarized pump should generate a signal larger than that with a circularly polarized pump. In the case of dissociative recombination, the final density of N_2 $(C^3\Pi_u)$ molecules depends on the density of N_2^+ in the fundamental state after photon-ionization within the duration of the femtosecond laser pulse [Xu 09], which is more effectively produced by linearly polarized laser in the laser regime of 10^{13} W/cm^2 - 10^{15} W/cm^2 [Talebpour 00, Becker 01]. The intersystem crossing mechanism expects a similar dependence on laser polarization, because the transition from the fundamental singlet state of N_2 to an intermediate singlet state is likely more effective with linearly polarized laser pulses. Therefore, the dominance of linear laser polarization on the luminescence (Figure 3.5(a) and Figure 3.6(a)) is compatible with the two mechanisms. Consequently, the dominancy of linear laser polarization in generating both 337 nm and 391 nm luminescence in the lower laser intensity regime is explained by the corresponding higher photonic inner-valence ionization probability. So the question is why circularly polarized laser pulses become more efficient in the higher laser intensity regime, as presented in Figure 3.6(d) and (d')?

An important difference between linear and circular laser polarization in gas plasma generation is the kinetic energy of free electrons generated by the intense laser field [Bucksbaum 86, Corkum 89]. With linearly polarized laser pulses, the electrons are left with low kinetic energy because they experience alternative acceleration and deceleration by the laser field during the pulse duration. In striking contrast, with a circularly polarized laser electrons are always accelerated away from the molecular ion. As discussed below, they acquire an average energy of $\sim 2U_p$ at the end of the laser pulse, where $U_p = e^2/c\varepsilon_0 m_e \times I/2\omega_0^2$ is the ponderomotive energy of the electron in the laser field with ε_0, m_e, I, ω_0 the vacuum permittivity, the mass of the electron, the intensity and the frequency of the laser field. Therefore, a large number of electrons with a kinetic energy around $2U_p = 16.7$ eV is produced inside the filament in the high intensity regime ($I = 1.45 \times 10^{14}$ W/cm^2). The distribution of transverse electron kinetic energies can be predicted by semi-analytical laws: integration of Newton equations leads to a transverse

momentum $\vec{p}(t) = -e\left(\vec{A}(t) - \vec{A}_0\right)$, where $\vec{A}(t)$ denotes the vector potential at instant t and $\vec{A}_0$ denotes its counterpart when the electron is liberated, at rest. After the passage of the pulse, $\vec{A}(t)$ vanishes. The transverse momentum becomes $p(\infty) = -eA_0$, and the transverse kinetic energy reads $E_{kin}(t_0) = e^2 A_0^2 / 2m_e$, where t_0 indicates that the corresponding electron was liberated at the instant t_0 within the pulse. Using an analytical form for the electric field (cosine envelope) allows us to infer the vector potential by integration of $\vec{E} = -\partial\vec{A}/\partial t$. Therefore, all electrons generated between t_0 and $t_0 + \Delta t$ with probability $(\partial n_e / \partial t)_{t_0} \times (\Delta t / n_{e,\infty})$, where $n_e(t)$ denotes the electron density calculated from the rate equations and $n_{e,\infty}$ denotes the total electron density generated by the pulse, will have a kinetic energy between $E_{kin}(t_0)$ and $E_{kin}(t_0 + \Delta t)$, leading to a parametric representation of the distribution of kinetic energies presented as a continuous curve in Figure 3.7. In the case of linear laser polarization most of the electrons are left with an energy below 1 eV, as shown in Figure 3.7(a). By contrast, an almost monoenergetic distribution around 16.7 eV is achieved for circular laser polarization (Figure 3.7(b)). These results were obtained in collaboration with Arnaud Couairon of CPHT, École Polytechnique.
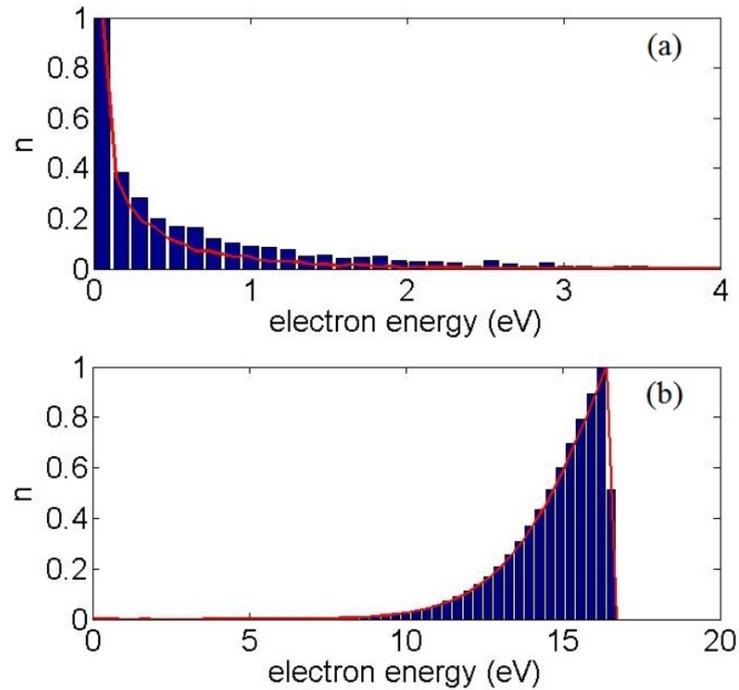
Figure 3.7: Calculated electron energy distribution in the case of linearly (a) and circularly (b) polarized laser pulses. The laser intensity used in the calculation was 1.45×10^{14} W/cm^2. The red lines represent the analytic results and the bars denote that from numerical simulation.

We also calculated the electron energy distribution after the passage of the laser pulses by numerical simulations. In the simulations, we assume that electrons are generated by optical field ionization of oxygen and nitrogen molecules, described by a set of coupled rate equations. At the intensity level considered, we also computed second ionization processes

so as to accurately determine the fraction of oxygen and nitrogen ions which liberate a second electron and found them negligible. Liberated electrons are assumed at rest and are accelerated by the electromagnetic (Lorentz) force mainly in the polarization plane. The acceleration in the longitudinal (propagation) direction is negligible compared to the transverse acceleration. We calculated the classical motion of a set of electrons under the action of the Lorentz force and then performed statistics by weighting each electron by its probability to be liberated at a given instant during the pulse. The results by numerical simulations are presented by the bars in Figure 3.7 and agree very well with that of the semi-analytical analysis.

A collision excitation process of N_2 and N_2^+ is expected to contribute significantly to populate their excited states. This process obviously depends on the electron kinetic energies, which are pump polarization dependent. In particular, electron collision process $N_2(X^1\Sigma_g^+) + e = N_2(C^3\Pi_u^+) + e$ opens up if the electron energy exceeds the threshold energy of ≈ 14 eV, with a cross section of 0.58 Å^2 [Itikawa 06]. As a result, the energetic electrons produced inside the filament plasma with circularly polarized laser pulse leads to efficient population built-up in the $C^3\Pi_u^+$ state, and thus to a stronger luminescence at 337 nm, as observed in Figures 3.5(c) and 3.6(d). In a traditional nitrogen laser pumped by electric discharge, it is actually this inelastic collision that gives rise to population inversion between the $C^3\Pi_u^+$ and $B^3\Pi_g^+$ states [Kunabenchi 84].

In the presence of abundant energetic free electrons, electron collision excitation to populate the excited ionic state is also possible through the following two processes:

$$N_2^+(X^2\Sigma_g^+) + e \rightarrow N_2^+(B^2\Sigma_u^+) + e, \tag{3.1}$$

$$N_2(X^1\Sigma_g^+) + e \rightarrow N_2^+(B^2\Sigma_u^+) + e + e. \tag{3.2}$$
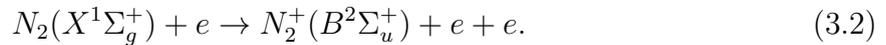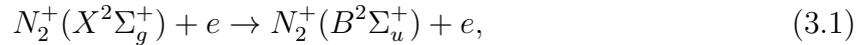
The threshold electron energy of the above two collisions are respectively 3.17 eV and 18.75 eV [Crandall 74, Nagy 03, Itikawa 06]. The effective collision sections of the two processes are ~ 3 Å^2 and ~ 0.01 Å^2 at optimum electron energy [Crandall 74, Nagy 03, Itikawa 06]. With circularly polarized laser pulses, energetic electrons from ionization of O_2 and N_2 experience frequent collisions with neutral air molecules at frequency of $\nu_c \sim 10^{12}$ Hz at standard temperature-pressure conditions. Therefore, population of the $B^2\Sigma_u^+$ state through the above two collision processes is expected to contribute upon an increase of circularly polarized laser energy. We therefore interpret the relative increase of luminescence with circularly polarized pump light presented in Figures 3.6(b')-(d') as resulting from collision excitation channels that gradually compensate the weaker direct inner-valence ionization from the ($\sigma_u 2s$) orbits. The process starting with ions requires electrons with less kinetic energy and is therefore contributing at lower laser energies. The process (3.2) requires higher laser intensities, but the density of collision partners (neutral molecules) is much higher.

3.3   Conclusion

In summary, we have demonstrated that the luminescence emitted by neutral and singly ionized N_2 molecules inside femtosecond laser filaments in air depends strongly on the polarization state of the incident laser pulses. At lower pump laser intensity, the predominance of the luminescence from both species with linearly polarized pump is simply explained by the higher optical field ionization rate. At higher laser intensity, new excitation routes become available, due to the presence of electrons with high kinetic energy left after the laser pulse. This collision-assisted mechanism leads to an increase of population in the excited triplet state through direct collision excitation from neutral molecules in the ground state with energetic electrons. For a laser intensity reaching 10^{14} W/cm^2, it is also believed to increase the population of the excited ionic state. These findings are important for the understanding of the stimulated radiation from filaments and may find applications, such as the remote sensing of electric field or THz radiation.

Chapter 4

Backward lasing of femtosecond plasma filaments

Stimulated radiation in ambient air or its major components (N_2 and O_2) when pumped by an intense ultrashort laser pulse has attracted much attention in recent years [Dogariu 11, Sprangle 11, Kartashov 12, Owada 13]. The generation of coherent radiation with such cavity-less laser sources holds great potential for remote sensing applications. The advantage of the backward stimulated radiation for remote sensing lies in the fact that it can bring information about pollutants towards the ground observer with a well defined directionality (Figure 4.1). The employment of a backward stimulated lasing radiation for remote sensing is expected to bring about tremendous improvement of measurement precision and sensitivity, because coherent detection methods such as Stokes- and anti-Stokes Raman Scattering can be then employed instead of the currently used incoherent detection of laser induced luminescence [Malevich 12].

4.1 Introduction: State of art

Up to now, two different schemes for backward stimulated radiation in air have been demonstrated experimentally, based on population inversion either of O atoms or N_2 molecules. In the first scheme, inversion in the population of oxygen atoms was obtained with an intense UV pulses at 226 nm. The UV pulse served two functions, first to photo-dissociate oxygen molecules, then to pump the oxygen atoms to the $3p^3P$ state via two-photon excitation [Dogariu 11]. Strong stimulated emission at 845 nm, corresponding to the $3p^3P \rightarrow 3s^3S$ transition, was observed in both the backward and forward directions. However, a serious limitation of this scheme is the significant absorption of 226 nm light by atmosphere, preventing its use for remote pollutant sensing.

The second scheme deals with population inversion in neutral N_2 molecules. About 10 years ago, Q. Luo and coworkers suggested the existence of a backward amplified spontaneous emission (ASE) from femtosecond laser filaments in air with linearly polarized 800 nm laser pulses. The evidence was based on the observation of a weak exponential increase of the backward UV luminescence at 357 nm upon filament length [Luo 03]. Filaments offer a favorable geometry for ASE because of the high aspect ratio of the

plasma strings at the origin of the emission. The UV emission corresponded to a transition between the $C^3\Pi_u$ ($\nu' = 0$) and the $B^3\Pi_g$ ($\nu = 1$) triplet states of the N_2 molecules, where ν and ν' are the vibrational quantum numbers. Similar results have been reported recently by S. Owada and coworkers [Owada 13]. In 2012 D. Kartashov, *et al.* reported a strong backward ASE lasing from N_2 molecules. A high power mid-infrared (3.9 μm or 1.06 μm) femtosecond pulses was used to induce a filament plasma column in a high pressure mixture of nitrogen and argon gas. Microjoule amounts of backward ASE from the plasma column were observed with a well-defined spatial profile [Kartashov 12]. The emission at 337 nm and 357 nm have been identified as being due to the transition between the third and second excited triplet states of neutral nitrogen molecules, *i.e.* $C^3\Pi_u \rightarrow B^3\Pi_g$. The population inversion mechanism was attributed to the traditional Bennet scheme, where collisions transfer the excitation energy of argon atoms to molecular nitrogen [Kunabenchi 84]. Unfortunately, this scheme cannot be employed for remote sensing application in atmospheric air, because of its requirement of high pressure argon gas ($p > 3$ bar).

Recently, we demonstrated that an intense backward stimulated radiation from filaments in nitrogen gas can be achieved with circularly polarized 800 nm femtosecond laser pulses at the atmospheric pressure [Mitryukovskiy 14]. The population inversion between the triplet $C^3\Pi_u$ and $B^3\Pi_g$ states was attributed to inelastic collisions between the electrons liberated by the pump laser and surrounding neutral ground state N_2 molecules. Next, we showed that it is possible to enhance this backward UV emission by injecting a weak optical signal in a segment of the filament [Ding 14]. Our simple scheme for backward stimulated emission and amplification from nitrogen gas pumped by the widely available 800 nm femtosecond laser pulse is a significant step towards applications for remote sensing.
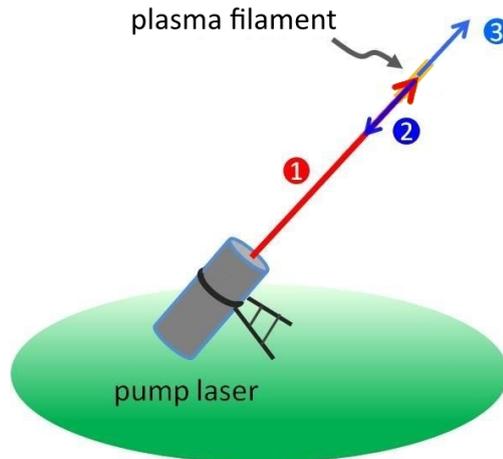
Figure 4.1: Scheme of a "laser in the sky" setup, which is strongly desirable for such remote sensing applications as detection of pollutants, distant humidity measurements and other atmospheric studies. Commercial laser system on the ground (1) creates filaments in the sky, which emit lasing radiation in the backward (2) and the forward (3) directions. Such secondary emission can bring the desired information towards the ground observer.

4.2 Backward stimulated radiation from plasma filaments pumped by circularly polarized femtosecond laser pulses

In this section we present an intense backward stimulated radiation from filaments in nitrogen gas pumped with circularly polarized 800 nm femtosecond laser pulses. Existence of the stimulated radiation is confirmed by the distinct dependence of the backward UV spectrum on the incident laser polarization and by the measured intensity profile of the backward emission. We attribute the population inversion between the triplet $C^3\Pi_u$ and $B^3\Pi_g$ states to inelastic collisions between the electrons liberated by the pump laser and surrounding neutral ground state N_2 molecules. The dependence of the lasing effect on the incident laser pulse polarization is explained by the fact that a circularly polarized laser produces more energetic electrons than a linearly polarized one. We find that the presence of oxygen molecules results in a significant quenching of the lasing action. With our present experimental parameters, significant gain occurs up to an oxygen concentration of $\sim 12\%$.

Experimental setup

In our experiments, a commercial chirped pulse amplification (CPA) laser system (Thales Laser, Alpha 100) was used. Femtosecond laser pulses (duration of 46 fs, repetition rate of 100 Hz) were focused by a convex lens of an $f = 1000$ mm in a gas chamber filled with 1 bar of pure nitrogen gas or a mixture of nitrogen and oxygen. A broadband dielectric beam splitter was used to steer the incident pulses into the gas chamber, while transmitting the backward UV emission from the gas plasma to the detector. A quarter-
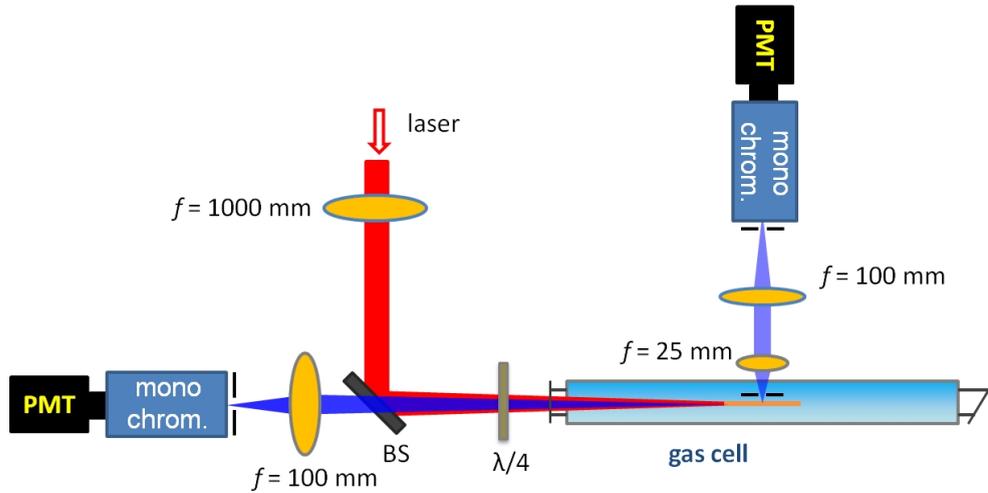
Figure 4.2: Schematic experimental setup. The incident femtosecond pulse is focused by an $f = 1000$ mm lens. The dichromatic beam splitter (BS) steers the 800 nm pulses inside the gas cell filled with nitrogen gas or its mixture with air. The backward radiation from the plasma is collected by an $f = 25$ mm and an $f = 100$ mm fused silica lenses into the slit of a monochromator. The signal is measured with a photomultiplier tube (PMT).

wave plate was inserted before the incident window of the gas chamber to change the laser polarization between linear and circular. The backward emission was focused by an $f = 100$ mm fused silica lens to the slit of a monochromator (Jobin-Yvon H-20 UV, grating: 1200 g/mm) combined with a photomultiplier tube (PMT). Typically, an average over 500 laser shots was performed for each individual measurement. The transverse fluorescence from the plasma channel was also measured. In this case a vertical slit of 1 mm was installed close to the center of the filament in order to limit the investigated plasma length. The fluorescence transmitted through the slit was first collimated by an $f = 2.5$ mm fused silica lens and then focused by another $f = 100$ mm fused silica lens to the incident slit of the same monochromator and PMT (see Figure 4.2).

Spontaneous UV emission from filaments in nitrogen gas

We first examine the spontaneous UV fluorescence emitted by filaments in a pure nitrogen gas. The fluorescence spectra recorded in the transverse detection geometry are shown in Figure 4.3(a) for linearly and circularly polarized pump laser pulses. The emission peaks centered at 315, 337, 357, 380, 405 nm have been previously identified as due to transitions between various vibronic levels of the triplet $C^3\Pi_u$ and $B^3\Pi_g$ states of the neutral N_2 molecule, *i.e.* the second positive band of the N_2 molecules [Kartashov 12]. For all these five spectral lines, the signals are ~ 2 times stronger with circularly polarized laser than with linear laser polarization, which has been discussed in the previous chapter.
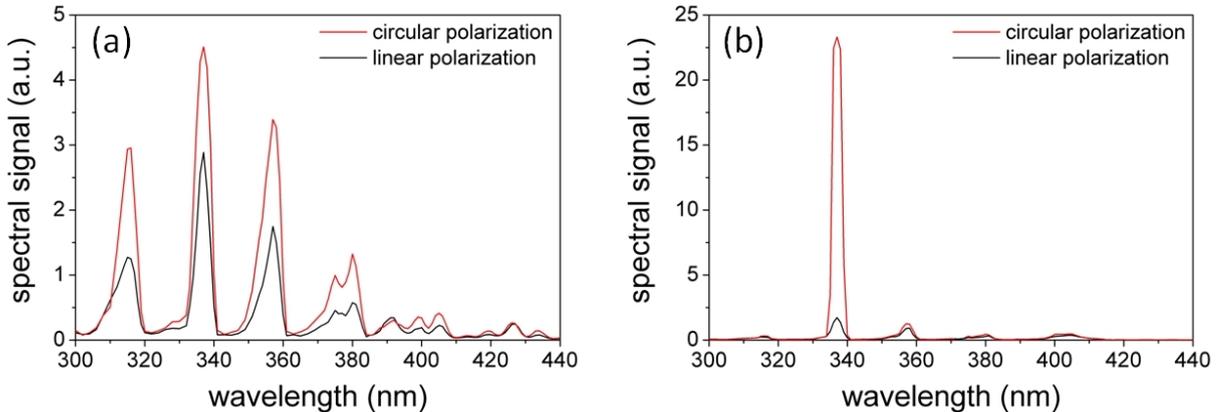
Figure 4.3: Spectra of transverse fluorescence (a) and backward UV emission (b) obtained with circular and linear laser polarization. The incident laser pulse energy is 9.3 mJ.

Before discussing the backward emission at 337 nm with circularly polarized laser, we first examine in more detail the results obtained with linear laser polarization in the backward direction, a geometry where ASE was reported previously [Luo 03, Owada 13]. In Figure 4.4(a), we present the measured backward 337 nm signal as a function of the incident laser pulse energy up to 9.3 mJ. We also measured the length and the width of the plasma channel (defined at $1/e^2$ level) as a function of laser pulse energy (see Figure

4.4(b)). With an increase of the laser energy, the filament length increases linearly, in agreement with a recent observation [Owada 13].
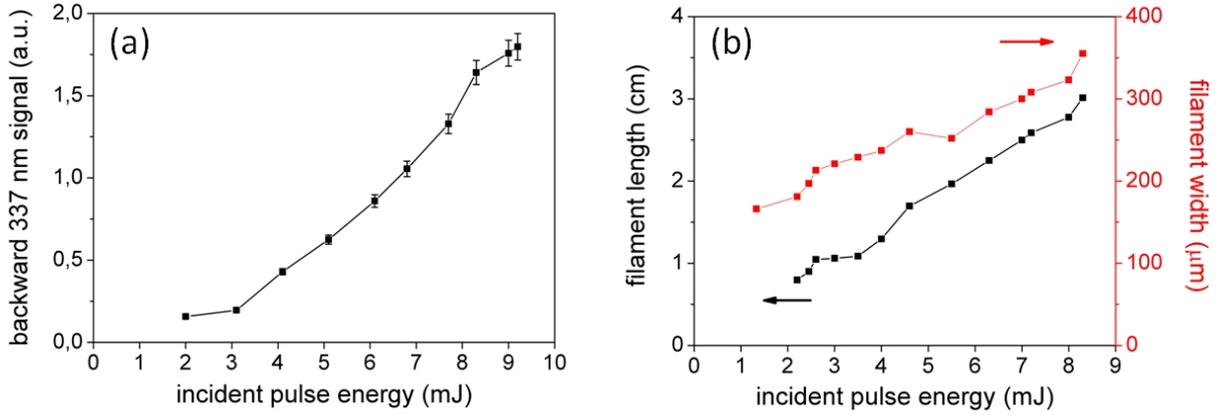
Figure 4.4: (a) Backward 337 nm signal as a function of incident laser pulse energy. (b) Measured length and width of the plasma filament as a function of pump laser energy. In both cases the pump laser is linearly polarized.

In Figure 4.5, we plot the 337 nm signal as a function of the filament length, as it was previously done for identification of ASE [Luo 03, Owada 13]. A weak nonlinear dependence is observed, which is tentatively fitted with an exponential law. We note that a more satisfying procedure consists in plotting the signal as a function of plasma volume, in view of the fact that the filament size increases slightly with pump laser energy (see Figure 4.4(b)). A plot of the backward signal as a function of plasma volume is best fitted by a linear dependence, as shown in Figure 4.5. Therefore, we come to the conclusion that stimulated radiation at 337 nm is not achieved with linearly polarized femtosecond pulses in our experiments. We also performed measurements at 357 nm and observed a similar dependence.
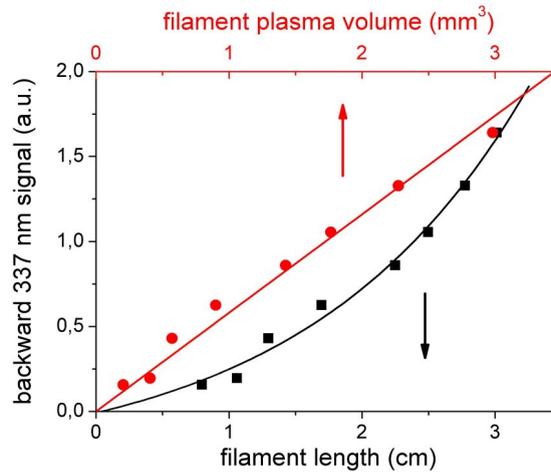
Figure 4.5: Backward 337 nm signal as a function of plasma length (black squares, lower scale) and plasma volume (red circles, upper scale). The curves are best fitted with an exponential or linear law respectively.

Stimulated UV emission from filaments in nitrogen gas

We now concentrate on the backward emission at 337 nm obtained with circularly polarized femtosecond laser pulses. It corresponds to the (0-0) vibronic transition of the second positive band system of N_2 molecule. In Figure 4.3(b), the spectra of the backward UV emission are shown for circular and linear polarization of the laser. The emission intensity at 337 nm is now about 10 times larger with circular pump laser polarization than with linear polarization. Others lines at 315, 357, 380, and 405 nm increase by a factor of ~ 1.5, an increase similar to that of the spontaneous fluorescence presented in Figure 4.3(a). The remarkable behavior of the 337 nm signal suggests that backward stimulated emission is initiated for this particular line with circularly polarized laser pulses.

In Figure 4.6, the backward emission intensity at 337 nm is plotted as a function of incident laser energy. The 337 nm signal displays a superlinear dependence on incident laser energy.
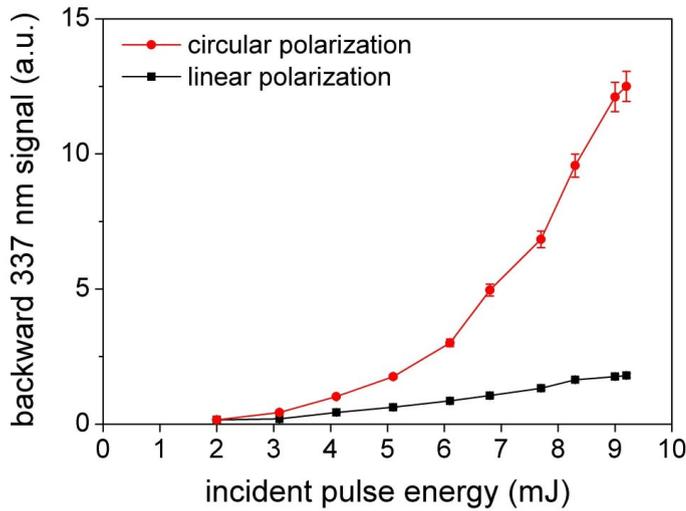
Figure 4.6: Measured backward signal at 337 nm as a function of incident laser pulse energy, for both circular and linear laser polarization.

To get further insight into the distinct pump polarization dependence presented in Figure 4.6, we measured the backward radiation intensity at 337 nm as a function of the incident laser ellipticity. In Figure 4.7, the measured signals are presented as a function of the rotation angle of the quarter-wave plate for different incident laser energies. The angles $\phi = 90° \times m$ correspond to linearly polarized laser, with $m = 0, 1, 2, 3$. The angles $\phi = 45° + 90° \times m$ correspond to circularly polarized laser. For a low pulse energy of 300 μJ, linearly polarized pulses generate a UV radiation with an intensity twice that obtained with circular polarization (Figure 4.7(a)). For an increased incident energy of 660 μJ, an octagon-shaped dependence is observed (Figure 4.7(b)), indicating the onset of a new mechanism for the emission at 337 nm. In the case of $E_{in} = 9.3$ mJ, the signal obtained with circular laser polarization totally dominates and decreases rapidly when the laser polarization deviates slightly from circular (Figure 4.7(c)). This critical dependence of the emission signal at 337 nm with laser polarization reinforces the hypothesis that backward stimulated emission at 337 nm occurs inside the filamentary plasma.
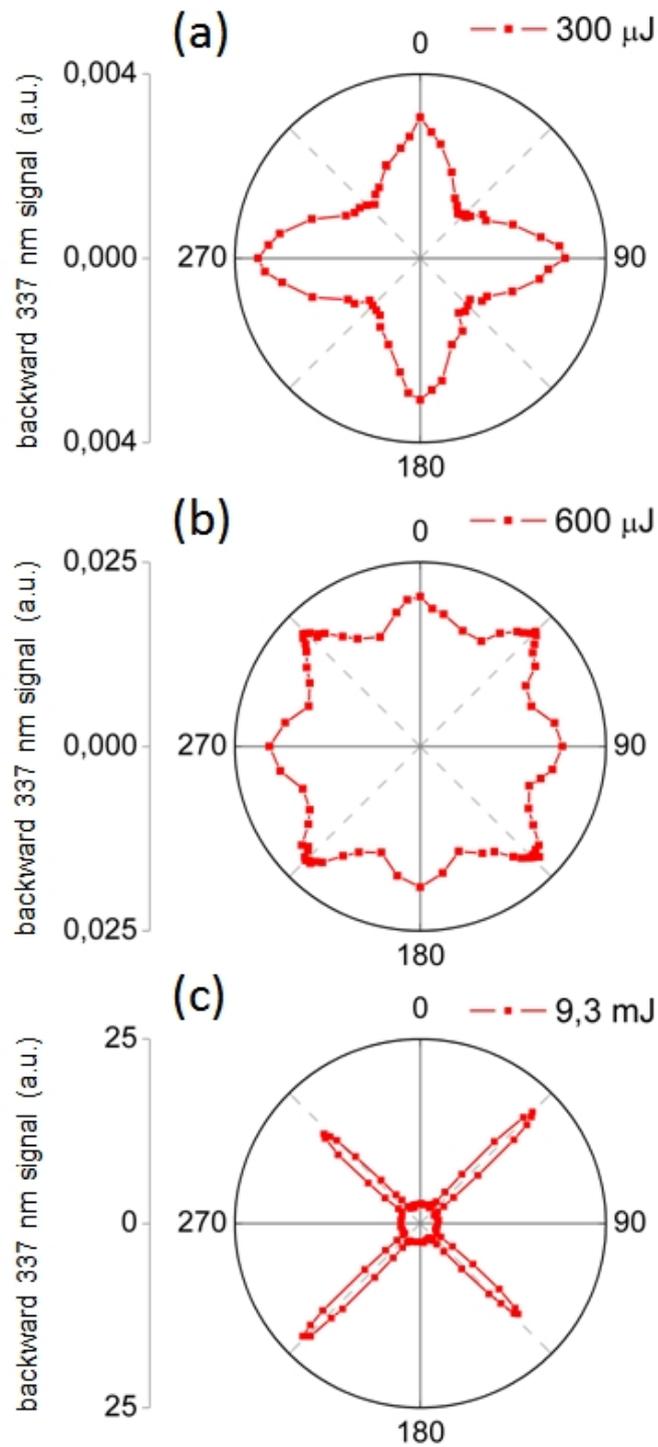
Figure 4.7: Backward emission signal at 337 nm as a function of the rotation angle of the quarter-wave plate. The incident laser energy for (a), (b), (c) are 0.3 mJ, 0.6 mJ, and 9.3 mJ, respectively. Angle 0° corresponds to linearly polarized light.

In order to analyse the polarization of this backward emission, we installed a Glan-Taylor prism before the detection system. In the experiment, the intensity of the transmitted 337 nm radiation was measured as a function of the rotation angle of the Glan-Taylor prism. The result for the backward stimulated emission from a filament created with circularly polarized 9.3 mJ pump laser pulses is presented in Figure 4.8. It indicates that the 337 nm backward emission is not polarized.
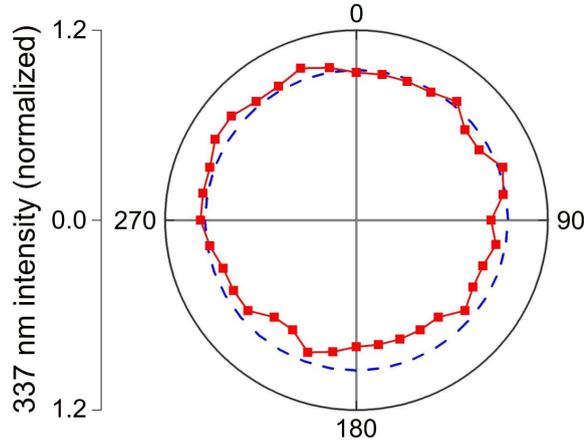
Figure 4.8: Polarization property of the 337 nm backward stimulated emission from a filament induced with circularly polarized 800 nm laser pulses in nitrogen gas. The incident laser energy is 9.3 mJ.

Finally, we performed the measurements of the spatial profile of the backward emission. For this purpose we replaced our detection system with an intensified Charge Couple Device (iCCD) camera (Prinston Instruments, model: PI-MAX). An interference band-pass filter (transmission peak: 340 nm, bandwidth: 10 nm) was placed before the iCCD camera to select the spectrum component around 337 nm. In Figure 4.9, the profiles of the backward emission captured by the iCCD are presented for both circularly and linearly polarized pump pulses. A clear highly directional beam profile, with a divergence
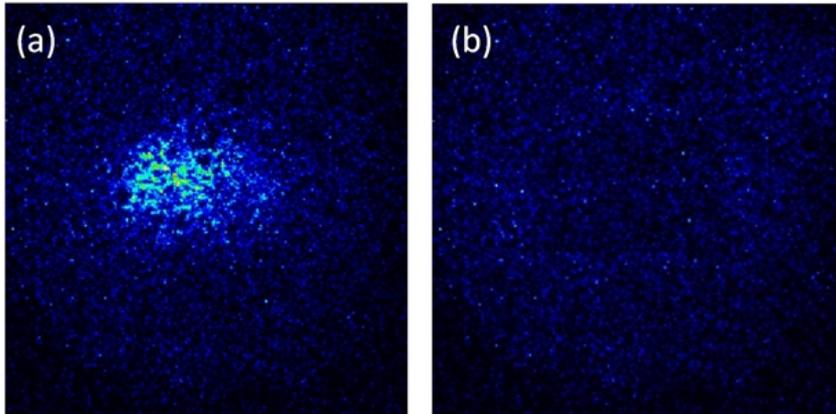
Figure 4.9: Profile of the backward emission at 337 nm, captured with the iCCD camera for (a) circular and (b) linear incident laser polarization. The opening angle of each panel is 24 mrad × 24 mrad.

angle of ~ 10 mrad, can be observed for circularly polarized pump pulses. For linearly polarized pump pulses, no observable beam can be detected by the iCCD. These spatial profile measurements agree with the above spectral results where significant stimulated emission at 337 nm can only be observed with circularly polarized pump pulses.

We also studied the dependence of the backward radiation intensity on the nitrogen pressure. The results for the pressure range from 200 mbar to 1 bar is presented in Figure 4.10. For a low pressure (around 200 mbar) a similar weak signal is detected for both linearly and circularly polarized laser pulses. With an increase of the pressure the signal obtained with circularly polarized laser beam experiences a fast increase, while just a small enhancement is observed for linear polarization. This also indicates that different mechanisms are responsible for the emission at 337 nm.
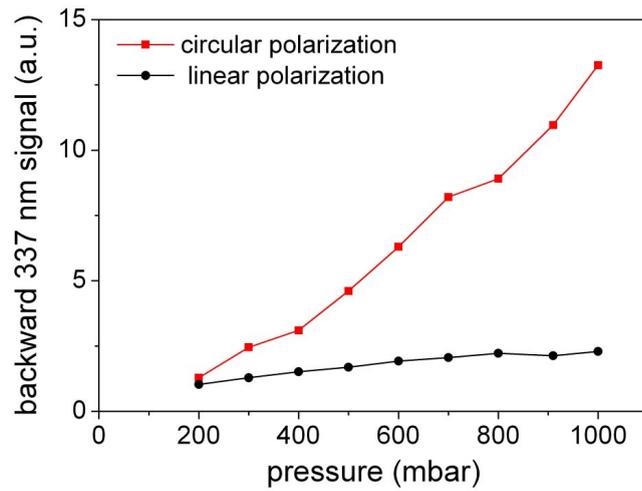
Figure 4.10: Measured backward signal at 337 nm as a function of nitrogen pressure, for both circular and linear laser polarization.

Discussion of the results

We now discuss possible mechanisms for population inversion between the $C^3\Pi_u$ and $B^3\Pi_g$ states of the neutral N_2 molecule, at the origin of the backward stimulated radiation. First, it is worth reminding that a direct population transition between the ground singlet state $X^1\Sigma_u^+$ and the excited triplet $C^3\Pi_u^+$ state is forbidden in the electric dipole approximation. One widely discussed mechanism to populate the $C^3\Pi_u^+$ state inside filaments in air is the following reaction [Xu 09]:

$$N_2^+ + N_2 + N_2 = N_4^+ + N_2,$$

$$N_4^+ + e = N_2(C^3\Pi_u^+) + N_2(X^1\Sigma_g^+).$$
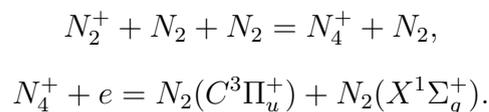
With this mechanism, one expects that a linearly polarized laser produces a stronger fluorescence signal for two reasons. First, it is known that the ionization rate of atoms and molecules is higher for linear polarization both in the multiple photon ionization and

tunneling ionization regime [Kolesik 01]. As a result, the densities of electrons and positive ions N_2^+ are higher in the case of linear laser polarization and should result in a higher density of $N_2^+(C^3\Pi_u^+)$. Second, the nonlinear refractive index of ambient air n_2 is higher for linearly polarized laser [Kolesik 01]. This results in slightly higher laser intensity inside filaments, which should again lead to higher densities of electrons and ions. We therefore assume that this collision-assisted recombination process of the electron on the parent ion is responsible for the fluorescence of filaments at relatively low laser energy, such as that of $E_{in} = 300$ μJ in Figure 4.7(a), but not to the stimulated emission observed at higher pump powers.

Another mechanism for the transition from the ground state to the $C^3\Pi_u^+$ state is the electron-molecule inelastic collision:

$$N_2(X^1\Sigma_g^+) + e = N_2(C^3\Pi_u^+) + e.$$
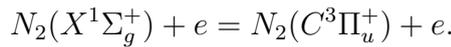
This is actually the main reaction responsible for population inversion in a traditional N_2 laser, where the electrons are accelerated to obtain sufficient energy by the discharge electric field [Kunabenchi 84]. The cross section of the above reaction is sensitive to the kinetic energy of the incident electron. It is nearly zero for electron energy below the threshold kinetic energy $E_{th} \sim 10$ eV, exhibits a resonant peak around 14.1 eV, and then decreases progressively for higher energy electrons [Fons 96]. For electrons born in the intense laser field inside filaments, the distribution of kinetic energies depends strongly upon pump laser polarization. With linear polarization, free electrons are accelerated back and forth along the laser polarization direction at each optical cycle, so that at the end of the pulse most of them have a low kinetic energy, with a weak tail distribution extending to a few eV. For circularly polarized light, where electrons are always accelerated away from the ion core, the final electron distribution is nearly mono-kinetic with a peak at twice the ponderomotive energy, which has been discussed in the previous chapter.

In the current experiment, we estimated the laser intensity inside the filament by the method described in the Chapter 2. An Al foil was placed around the middle of the filament in the case of $E_{in} = 9.3$ mJ, in ambient air. After 300 laser shots the transverse size of the drilled hole became stable and its diameter (d) was measured to be 170 μm. At the same time, the transmitted laser energy E_t was measured to be about 6.6 mJ. The average laser intensity can be estimated as:

$$I = \frac{E_t}{\pi \left(\frac{d}{2}\right)^2 \tau_p} = 1.45 \times 10^{14} \text{ W/cm}^2,$$

where τ_p is the initial laser pulse duration of 50 fs. This corresponds to the electron energy of 17.3 eV in case of circular laser polarization. Therefore the electron energy required for impact excitation of neutral N_2 molecules is well reached in filaments. For linearly polarized laser field, this mechanism is turned off because of the low electron kinetic energy, even with a laser intensity above the clamped value. As a conclusion, we believe that the inversion of population inside the triplet manifold of N_2 is due to impact excitation by electron collisions. The threshold behavior of the inelastic collision cross section with respect to electron energy is reflected in the sharp dependence of the lasing emission with ellipticity [Fons 96].

Backward emission from filaments in ambient air

For applications of this backward stimulated radiation source for remote sensing, operation in ambient air is required. We therefore performed measurements in atmospheric air. We first examined the backward UV emission from filaments formed in ambient air driven by both circularly and linearly polarized laser pulses. Emission spectra similar to those of Figure 4.3(b) were observed, except that the signal at 337 nm increased only by a factor 2 for circular laser polarization. In Figure 4.11, the measured backward 337 nm signal is shown as a function of the rotation angle of the quarter-wave plate. The backward emission intensity at 337 nm as a function of incident laser energy is plotted in Figure 4.12. The signal is ~ 2 times higher for circular polarization of the laser pulses than for linear polarization, indicating the quenching of the backward lasing action.
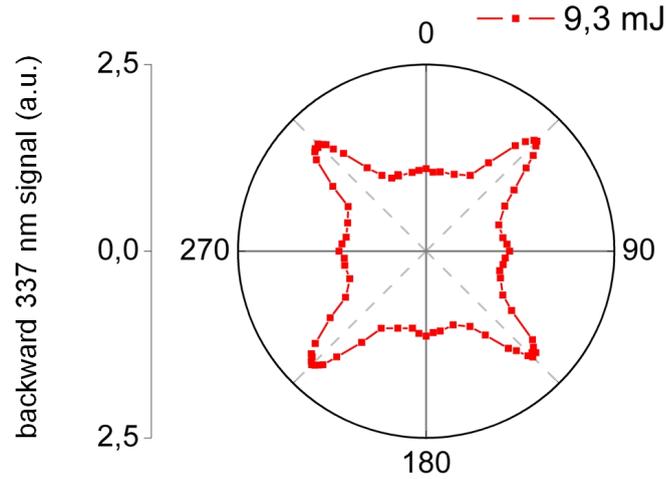
Figure 4.11: Dependence of the backward 337 nm signal obtained from filaments in air as a function of the rotation angle of the quarter-wave plate. The incident laser energy is 9.3 mJ and the focal length is $f = 1000$ mm.

To further assess the influence of oxygen gas for the lasing action, we measured the backward 337 nm signal in different mixtures of nitrogen and oxygen. We present in Figure 4.13 the measured 337 nm signal for both circularly and linearly polarized laser as a function of the percentage of oxygen. A slow decrease of the signal is observed upon increasing oxygen concentration up to 10%. Beyond 10% oxygen, the signal shows a rapid decrease, indicating the termination of significant lasing action. For oxygen concentration more than 13%, the signal obtained with circular laser polarization becomes ~ 2 times larger than that of linear laser polarization, similar to the transverse fluorescence presented in Figure 4.3(a).

The detrimental influence of oxygen molecule for the conventional discharge-pumped nitrogen laser is well documented [Kunabenchi 84]. The underlying physical mechanism is attributed to the collision reaction

$$N_2(C^3\Pi_u^+) + O_2 = N_2(X^1\Sigma_g^+) + O + O,$$
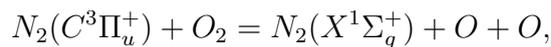
which efficiently reduces the population density in the upper state of the lasing emission [Kartashov 12]. This process has a very high rate constant $\approx 3 \times 10^{-10}$ cm^{3}s^{-1}
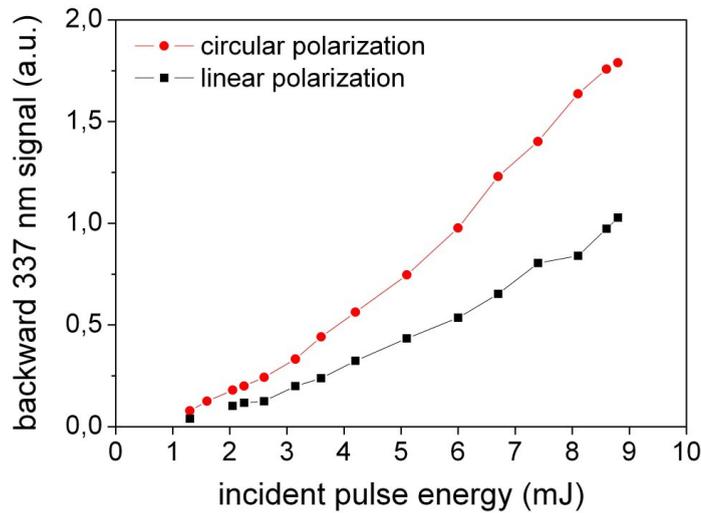
Figure 4.12: Measured backward signal at 337 nm from 800 nm laser-induced filament in air as a function of incident laser pulse energy, for both circular and linear laser polarization.

[Pereira 10], which is more than an order of magnitude higher than the rate constants of quenching in nitrogen-nitrogen collisions and other reactions, like dissociative recombination, three-body recombination, attachment, which would effectively reduce lasing efficiency [Kossyi 92].

To obtain a significant backward stimulated emission in atmospheric air, a higher population inversion density (or a higher gain) is required to overcome the quenching effect of the oxygen molecules. A possible approach to achieve this is to use a pump laser at longer wavelengths, because the kinetic energy of the produced electrons increases like $I\lambda^2$, where I is the laser intensity and λ its wavelength.
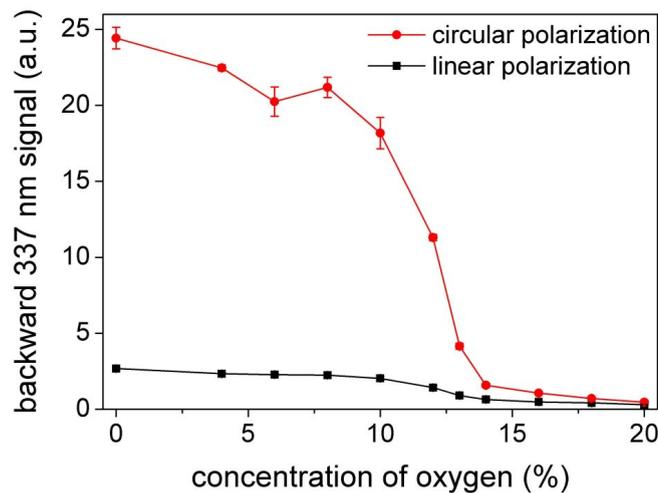
Figure 4.13: Measured backward 337 nm signal from filaments in air as a function of oxygen gas concentration, for both circular and linear polarized laser pulses. The incident pulse energy is 9.3 mJ.

4.3 Externally seeded backward lasing radiation from femtosecond laser filaments

In the further study of the backward ASE, we upgraded the experimental setup to the "pump-probe" scheme, where the counterpropagating probe beam served as a seed. A ~ 16 times enhancement of the backward ASE is observed, when the external seeding pulse around 337 nm is launched in the backward direction. At the same time, the divergence angle of the seeded lasing is found to be significantly reduced compared to that of the ASE. Moreover, the seeded lasing radiation inherits the polarization property of the seed pulse. These three observations confirm unambiguously the assumption of population inversion between the relevant nitrogen molecular states. The critical role of pump laser ellipticity is also observed in this seeded backward lasing scheme, which supports the hypothesis that inelastic collision between the energetic electrons with neutral nitrogen molecules is at the origin of population inversion.

Experimental setup

The scheme of the experimental setup is presented in Figure 4.14. The output laser pulse was split into a main pump pulse and a much weaker second pulse by a 1-mm-thick 5%/95% beam-splitter. The pump pulse passed through a quarter-wave plate and then was focused by an $f = 1000$ mm convex lens. A dichromatic mirror was used to reflect the focused 800 nm pump pulses into a gas chamber filled with pure nitrogen gas at 1 bar pressure. This dichromatic mirror reflects more than 99% of the 800 nm pump pulse and it is transparent to the backward UV emission from the laser plasma situated inside the gas chamber. The second weaker 800 nm pulse first passed through a mechanical delay line and then through a 1-mm-thick type-I BBO crystal in order to generate femtosecond pulses at 400 nm. The 400 nm pulses was linearly polarized in the vertical direction. The obtained 400 nm pulse was further focused by an $f = 200$ mm convex lens (L_2) inside a 20-mm-long fused silica sample to broaden its spectrum through intense nonlinear interaction.
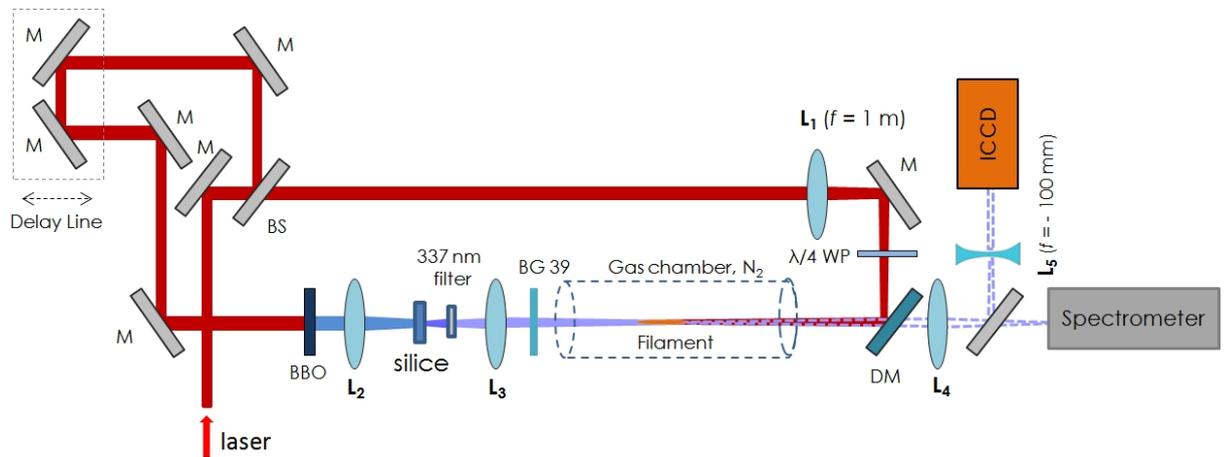
Figure 4.14: Scheme of the experimental setup.

We selected the spectrum component around 337 nm with an interference bandpass filter, which has a transmission peak at 340 nm and a bandwidth of 10 nm. The resulting pulse centered at 340 nm, referred to as seeding pulse in the following, was focused by another $f = 100$ mm lens into the gas chamber from the opposite direction of the pump pulses. The separation between the lenses L_2 and L_3 was adjusted to insure that the geometrical focus of the seeding pulse overlapped with the central part of the long plasma filament in the longitudinal direction. The transverse spatial overlapping between the geometrical focus of the seeding pulse and the center of the plasma filament was carefully assured by translating finely the focal lens (L_3) in the transverse plane. The temporal delay between the 800 nm pump pulses and the seeding pulse at 337 nm could be adjusted by the mechanical delay line. For some of our experiments, we installed a quarter-wave plate for 400 nm radiation after the BBO crystal, so that a circularly polarized seeding pulse could be obtained after filamentation inside the fused silica sample. The backward emission from the laser plasma filaments was detected by either a spectrometer (Ocean Optics HR 4000), an intensified Charge Coupled Device (iCCD) camera (Princeton Instruments, model: PI-MAX), or a calibrated photodiode.

Experimental results

We first measured the spectra of the backward emission from the laser plasma with and without the seeding pulses, for both circularly and linearly polarized pump lasers. The results are presented in Figure 4.15. In the case of circularly polarized pump pulses, a sharp radiation peak at 337 nm can be observed even without external seed pulse, which is referred to as a backward ASE (see Figure 4.3(b)). With the external seed pulse, an enhancement of the peak by a factor of ~ 16 is found (Figure 4.15 (a)). Considering the intensity of the seed pulse at the 337 nm spectral position, we estimated that the seed pulse is amplified by a factor of $2.5 \times 10^5/2000 = 125$ times. In the case of linearly polarized pump pulses (Figure 4.15(b)), no detectable ASE was observed and no amplification of
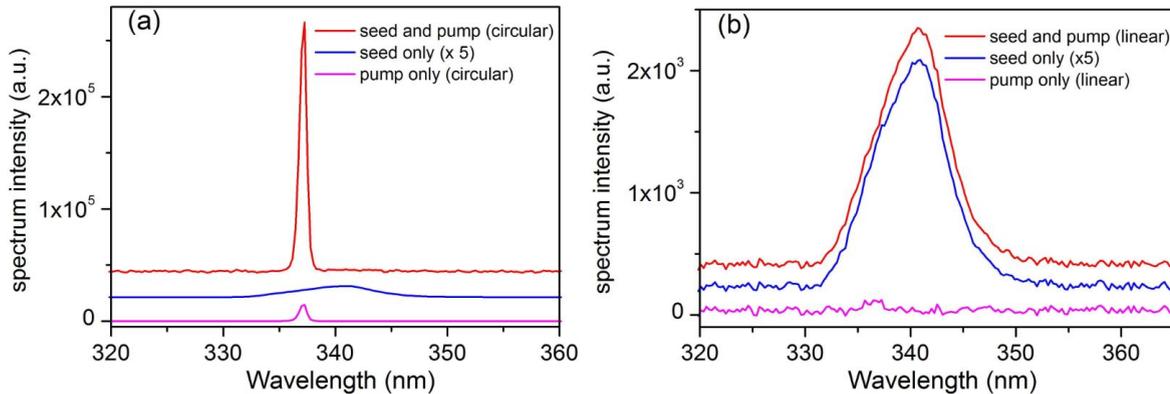

Figure 4.15: Spectra of the backward stimulated emission with circularly (a) and linearly (b) polarized pump pulsed at 800 nm. The spectra of the seed pulses and those of the backward emission from just the pump pulses are also presented for comparison.

the seed pulse could be observed. These observations confirm our previous conclusion that population inversion responsible for the stimulated 337 nm radiation is only established with circularly polarized pump pulses.

We then studied the polarization property of this seeding effect by injecting linearly and circularly polarized seeding pulses inside the plasma filament. To analyse the polarization properties of the lasing radiation, we installed a Glan-Taylor prism before the detecting photodiode. In the experiment, we recorded the intensity of the transmitted 337 nm radiation as a function of the rotation angle of the Glan-Taylor prism. The result for the ASE obtained without seeding pulse is first presented in Figure 4.16(a), indicating that the ASE is not polarized. For linearly polarized seed pulses in the vertical direction, we observed that the amplified lasing signal is also linearly polarized in the same direction (see Figure 4.16(b)), evidenced by the good agreement between the experimental results and the theoretical fit with Malus' law. The result for circularly polarized seeding pulses is presented in Figure 4.16(c), where a circularly polarized amplified emission is also observed. The maintenance of the pulse polarization during the amplification is in agreement with our hypothesis that population inversion is present and responsible for the seeding pulse amplification.
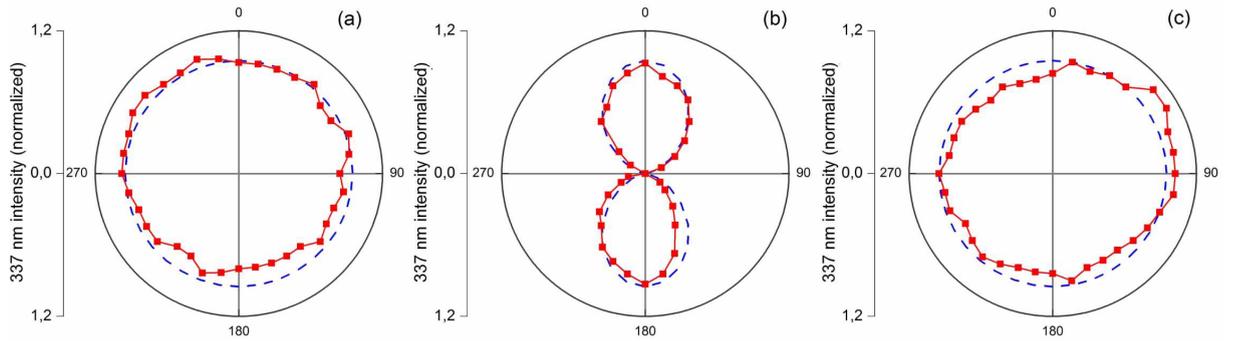
Figure 4.16: Polarization properties of the ASE (a), the seeded backward stimulated emission with linearly (b) and circularly (c) polarized seed pulses at 337 nm. The dots present the experimental results and the dashed lines denote the theoretical fitting.

Next, we measured the spatial profile of the ASE and the seeded lasing emission with the iCCD camera. In Figure 4.17(a), the measured spatial profile of the backward emission without seeding pulse is shown for circularly pump pulses of 800 nm. The ASE exhibits a Gaussian distribution with a divergence of 9.2 mrad (Figure 4.17(a)). We present the spatial profile of the seeding pulse in Figure 4.17(b). This weak pulse exhibits a divergence around 20 mrad in our experiments. In the presence of both pump and seeding pulse, an extremely intense 337 nm radiation was found, as presented in Figure 4.17(c). This amplified stimulated emission shows a divergence angle of ~ 3.8 mrad, much smaller than that of the ASE and the seeding pulse.

We have also measured the laser energy of the seeded backward radiation with a sensitive laser energy meter (model: OPHIR, NOVA, PE9-C). The energy of seeded lasing
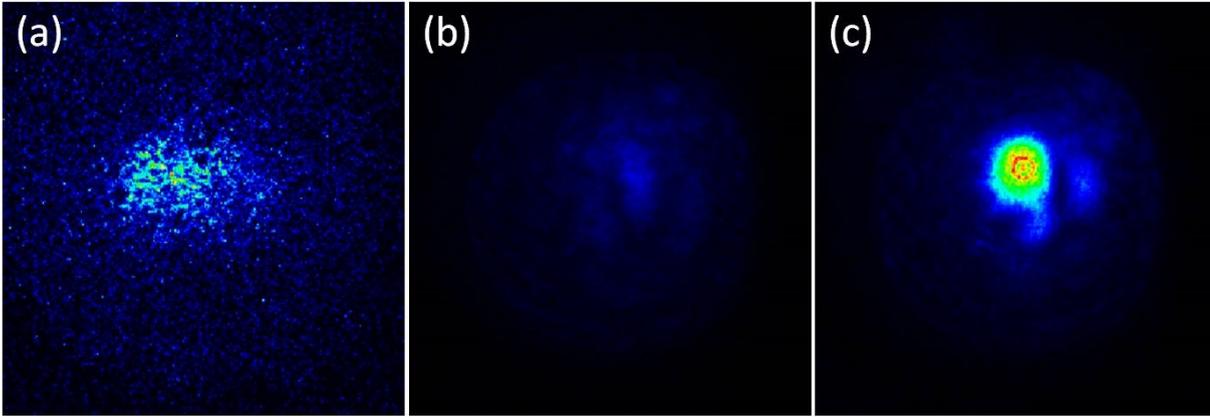
Figure 4.17: Spatial profile of the backward ASE (a), the seed pulse (b), and the seeded stimulated radiation (c). The opening angle of each panel is 24 mrad × 24 mrad.

pulses was measured to be around 5.0 nJ, corresponding to an energy conversion efficiency of 5.1×10^{-7} from 9.8 mJ pump pulses. Therefore, the pulse energy of the ASE was deduced to be 310 pJ with a conversion efficiency of 3.2×10^{-8}.

All the above experimental observations highlight the crucial role of pump laser polarization. To evaluate that, we measured systematically the seeded lasing emission intensity by rotating the quarter-wave plate for the pump pulses. In Figure 4.18(a), the result for the ASE without seeding pulse is first presented as a function of the rotation angle ϕ of the waveplate, which has been reported in the previous paragraph. Intense ASE was observed only with circularly polarized pump pulses and shows dramatic decrease when the ellipticity deviates from $\epsilon = 1$. In the presence of a constant linearly polarized seeding pulse,
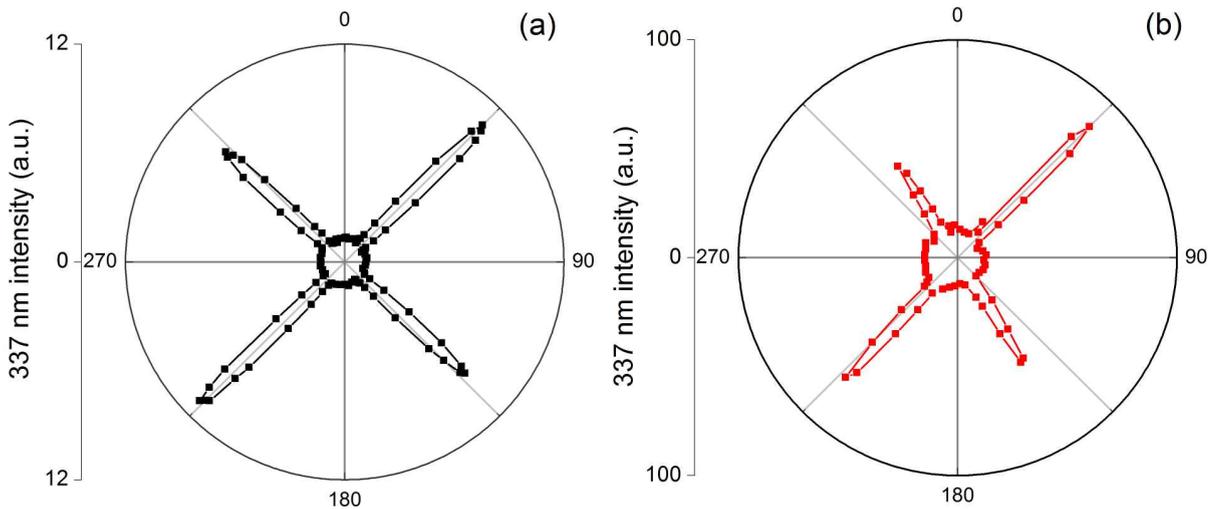
Figure 4.18: Dependence of the backward ASE (a) and the seeded backward stimulated radiation (b) as a function of the rotation angle of the quarter-wave plate.

a similar dependence on laser ellipticity was observed (Figure 4.18(b)). This confirms that population inversion between the $C^3\Pi_u$ and $B^3\Pi_g$ states can be only achieved with circularly polarized pump pulses. The slight asymmetry and the deviation of the peaks from $\phi = 135°$ and $\phi = 315°$ can be due to the fact that the circularly polarized pump pulses reflect on the dielectric dichromatic mirror in this experiment. This mirror has slight different reflectivity for $p-$ and $s-$ polarized light and thus results in a non-perfect circularly polarized pump pulses after reflection.

4.4 Conclusion

In summary, we have shown that a strong stimulated radiation at 337 nm can be achieved in the backward direction from plasma filaments in an atmospheric-pressure nitrogen gas pumped by circularly polarized laser pulses at 800 nm. Existence of the stimulated radiation is confirmed by the distinct dependence of the backward ultraviolet spectrum on the incident laser polarization and intensity, by the observed beam profile and the polarization property of the emission. However, in ambient air, the presence of oxygen molecules suppresses the lasing action to a large extend.

We have obtained a further enhancement of the backward radiation intensity by a factor of ~ 16 by injecting a seeding pulse in the opposite direction of the pump pulse. The amplified lasing radiation inherits the polarization property of the seeding pulse and its divergence angle was found to be around 3.8 mrad, 3 times less than that of the backward ASE. The critical role of pump laser polarization was also observed in the seeded lasing regime, where intense lasing effect was only possible for circularly polarized pump pulses.

We attribute the mechanism responsible for the population inversion to inelastic collisions between electrons liberated by the pump laser and neutral nitrogen molecules, a process which is more efficient with circularly polarized laser pulses. We believe that this simple scheme for backward stimulated emission from nitrogen gas pumped by the widely available 800 nm femtosecond laser pulse is a significant step towards applications for remote sensing.

Part III

Coherent synthesis of Terahertz radiation from femtosecond laser filaments

Chapter 5

Terahertz radiation from femtosecond laser filaments

5.1 Terahertz radiation

Terahertz band

The part of electromagnetic spectrum between the microwave (MW) and infrared (IR) frequencies is named the terahertz (THz) band. As commonly defined, THz range spans from 0.1 THz to 10 THz.
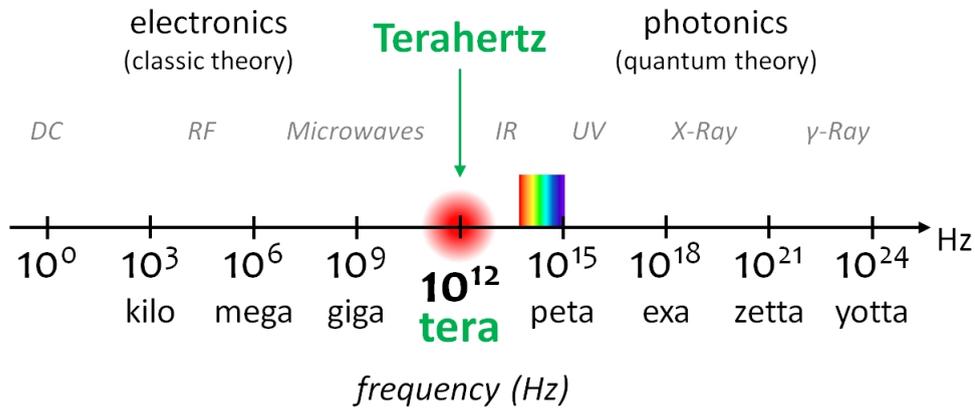
Figure 5.1: The terahertz band in the electromagnetic spectrum.

Until the mid 1970s the study of electromagnetic spectrum (Figure 5.1) was divided into two broad parts. The radio and microwave frequencies (≤ 100 GHz) were accessed by *electronics*, while infrared radiation and above (with frequency higher than ~ 10 THz) were a subject of *photonics*. A large frequency range between the MW and IR has been hardly accessible, because there were neither suitable emitters for sending out controlled THz signal nor efficient sensors to detect it. As a result, this part of the electromagnetic spectrum was called the THz gap. In last 30-35 years, advances in the electronics and photonics fields have provided new materials and devices that made the THz gap accessible.

In different times THz radiation has been involved and studied in different fields of physics, it has found huge variety of applications. Through this it is also called submillimeter radiation, THz waves, terawaves, THz, T-rays, T-light, T-waves, *etc.* Typical values of the THz radiation is presented in Table 5.1.

Table 5.1: Typical values of the Terahertz band.

Frequency:	10^{11} Hz $< \nu < 10^{13}$ Hz	1 THz
Period:	0.1 ps $< T <$ 10 ps	1 ps
Wavenumber:	3 cm^{-1} $< k <$ 300 cm^{-1}	33 cm^{-1}
Wavelength:	30 μm $< \lambda <$ 3 mm	300 μm
Photon energy:	0.4 meV $< W <$ 40 meV	4 meV

The THz band is an area of convergence between the fields of electronics and photonics. The fields are significantly different in the theoretical framework and technical approach. Thus the THz band is a fruitful area for interesting hybrid systems. The main features of THz radiation are as follows:

- **Safety.** Energy of a photon with a THz frequency is on the order of meV, which is a thousand times less than that of a photon at 800 nm. At such energy level excitation of the media is mainly occurs on rotational levels and vibrational levels. It is almost impossible to ionize a media with current THz sources, even in solid state. As a result, THz radiation is safe for both the sample and the operator; this is an advantage versus X-Rays. Due to strong water absorption, THz waves cannot penetrate into the human body like microwaves can. Therefore, even if a very strong THz wave can possibly cause any harm, it is limited to skin level.

- **Transparency of non-polar and non-conducting materials to THz waves.** The wavelength of THz radiation is longer than that of visible and IR range. Thus, THz waves are less affected by Mie scattering. THz radiation can pass through most dry dielectric materials, such as cloth, paper, wood, plastic, ceramics, *etc.* Thus, the THz radiation is considered very promising in nondestructive evaluation applications.

- **Molecular fingerprints reveal in the THz range.** Many molecules, especially organic ones, exhibit strong absorption and dispersion within the THz range due to dipole-allowed rotational and vibrational transitions. These transitions are specific to the molecule and therefore enable spectroscopic fingerprinting in the THz range. Both the profile and composition information of the target can be provided by THz imaging techniques.

- **High resolution of THz imaging.** Because the wavelength of THz radiation is in the range of tens μm to mm, THz images of macroscopic samples provide detailed and localized data. This is an advantage compared to microwaves. Spatial resolution of ~ 10 nm can be achieved using near-field techniques.

- **Absorption by atmospheric water.** THz radiation has limited penetration through fog and clouds and cannot penetrate liquid water or metal. The Earth's atmosphere is a strong absorber of THz radiation in specific water vapor absorption bands. However, at distances up to 10 meters the THz band still allows many useful applications in imaging and construction of high bandwidth wireless networking systems, especially indoor systems.

Brief history

THz radiation has received much attention in last 20 years. Although a great number of publications on generation, detection and various applications appeared recently, research in the THz (or far-infrared) region has a long history [Kimmitt 03].

The first THz sources used glowing objects where the black-body radiation of a heated object emits at THz wavelengths. First experiments on the radiation in the far-IR domain have begun at the end of XIX century. In 1893 Rubens and Snow measured spectra of several minerals in the far-IR region which was described as the "great wavelength" range [Rubens 93]. In 1897 Nichols discovered the "Residual ray" - a wave radiated at 9 μm, reflected from a crystalline quartz [Nichols 97]. This is now known to be due to lattice vibrations. In the following 20 years more than 100 papers on far-IR research were published. In 1911 Rubens and Baeyer showed that the quartz mercury lamp is able to emit long-wavelength radiation (210 μm and 324 μm) [Rubens 11]. In the THz region it has an equivalent black-body temperature of over 4000 K and is still the preferred source in grating spectrometers. At the same time Wood had made the first blazed diffraction grating which allowed the concentration of light into a single order with efficiencies of over 75% for the first order even beyond 100 μm (3 THz) [Wood 10]. Nowadays such blazed gratings are employed in monochromators and tunable lasers.

In 1920s joining of far-IR and microwave ranges has happened: Nichols and Tear obtained wavelengths down to 220 μm using a Hertzian oscillator [Nichols 23]; in 1924 Glagolewa-Arkadiewa showed that a submillimeter radiation of about 90 μm could be generated by exciting small Hertzian oscillators in the form of brass filings immersed in oil [Arkadiewa 24]. In 1930s a number of papers on applications of far-IR region began to increase, with a particular emphasis on absorption bands in gases. In the mid 1930s a complete spectrum of water vapour absorption was presented [Barnes 35, Randall 37].

At that time most usual detector was the bolometer, invented by Langley in 1880 [Langley 81], while a mercury arc or some heated material such as gas mantle were used as a source. Two important inventions were made in the mid 1940s: in 1947 Marcel Golay has presented the pneumatic IR detector ('Golay cell') [Golay 47]; the first cooled bolometer was also invented in the mid 1940s [Andrews 46].

Harmonic generation from a microwave source (klystron) began in the mid 1940s. The far-IR spectra of Oxygen has been measured [Berlinger 46]. This technique was developed by the group of Gordy in 1950s, they reached the frequencies above 300 GHz [Burrus 54]. First backward wave oscillator (BWO) or carcinotron was demonstrated at the same period, it achieved mW power level at 1 THz [Kompfner 53].

The late 1950s and 1960s have been fruitful for mm and sub-mm wave research, with over 1000 publications on this field. The detectors were largely improved: pyroelectric detectors, new bolometers (Carbon, [Boyle 59], n-InSb electron [Putley 60], Germanium [Low 61])), the Ge:Ga photoconductor [Moore 65], a Josephson effect-based detector [Grimes 68]. Dispersive Fourier-Transform Spectroscopy (DFTS) was demonstrated for the first time in 1963 [Chamberlain 63] which allowed to obtain optical coefficients of solids, liquids and gases. But, of course, the main discovery was the laser. It led to the water vapour laser, the first high-power far-IR device, in 1964 [Crocker 64]. Also in this decade the Time Domain Spectroscopy (TDS) has been demonstrated for the first time in the THz regime [Nicolson 68].

In 1970s the group of Shen [Yang 71] and Auston [Auston 73] reported the far-IR generation by electro-optical rectification (EOR) [Bass 62] of a picosecond laser pulse in the nonlinear crystal ($LiNbO_3$, ZnTe). However, this advances had a limited impact since it was still very difficult to detect the radiation. In the mid 1980s Auston has developed the technique of coherent detection of THz waves based on the Pockels effect [Auston 84, Auston 88, Nahata 96]. Probably, this method is the most commonly used nowadays for broadband THz generation and detection. Another highly widespread method is the use of photoconductor (PC) antennas [Fattinger 88, Fattinger 89, Smith 88]. At the same time new powerful sources for THz radiation have appeared: the gyrotron [Flyagin 77], the free electron laser [Elias 84], the quantum cascade laser [Faist 94, Faist 04]. In 1990s Hamster and co-workers demonstrated the coherent THz radiation from plasma in air induced by laser pulses [Hamster 93, Hamster 94]. Such plasma THz sources allows performing experiments with a simple ultra-short pulsed lasers, widely available today.

In 1980s and 1990s a large amount of new applications of the THz radiation have been discovered. This gave rise to a huge interest to the THz science and technology. Annual number of papers on the subject experiences an impressive growth (see Figure 5.2); new techniques, methods and fundamental findings appear regularly.

Applications of Terahertz radiation

An incredible number of applications of THz waves have been proposed up today [Tonouchi 07, Ferguson 02, Dragomar 04, Zhang 10]. The THz band has been studied already for a long time in astronomy and analytical science [Fazio 79, Kulesa 11]. Recent technological innovations in photonics, electronics and nanotechnology have allowed application of THz research in a variety of different areas. The THz spectroscopy is ideally suited for the identification of biological or complex inorganic molecules [Zhong 06], the study of collective excitations in condensed media [Hangyo 05, Kampfrath 11, Suzuki 12] and for plasma diagnostics [Jamison 03]. Applications of THz radiation range from biology and medicine [Fitzgerald 02, Siegel 04, Pickwell 06, Yu 12], to security concerns [Liu 07a],

telecommunication [Federici 10] and earth sciences [Waters 06]. THz waves provide a useful diagnostic tool for quality control [Hu 95], restoration of objects of cultural heritage [Jackson 08, Fillippidis 12], food industry process control [Lee 12], *etc.*

Impressive progress has been achieved in the last few years in the development of intense THz sources. Optical rectification of a short laser pulse in a nonlinear crystal yields THz sources with field amplitude reaching the MV/cm level [Hirori 11, Iwaszczuk 12]. Even the 100 MV/cm level has been obtained via difference-frequency mixing of two parametrically amplified pulse trains from a single white-light seed [Sell 08]. Matsubara, *et al.* reported the two-color mixing of a hollow-fiber compressed 10 fs laser pulses to provide an ultra-broadband radiation ranging from far-IR to 200 THz [Matsubara 12]. Unfortunately, many applications that require illumination of a distant target are hampered by the poor transmission of THz radiation through atmosphere, due to the strong attenuation posed by water vapor. Therefore the propagation of a locally created THz wave to a remote target is difficult. To overcome this drawback the laser plasma can be used as a source of THz radiation. Such plasma can be created far from the laser itself, and thus avoid the THz absorption by water vapor in air.
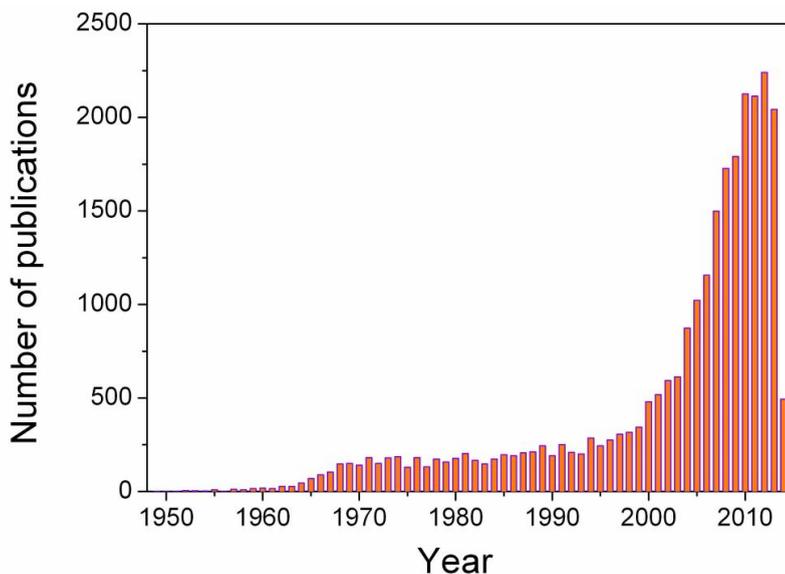
Figure 5.2: Number of publications in a given year in the field of THz radiation. The numbers are taken from ISI Web of Science, using General Search in the SCI-EXPANDED database with the title query 'thz OR terahertz OR 'far infrared' OR 'submillimetre wave*' (the same manner as in [Reimann 07]) on 26 May 2014. This query yields neither all the publications on this subject nor all the publications returned deal exactly with THz radiation. However, the general trend should not be influenced by this.

5.2 Generation of THz radiation by laser-induced plasma in air

In last 20 years, a new class of THz emitters based on laser-generated plasmas has begun to develop. The basic principle is to focus a short high-energy laser pulse in a gaseous medium. If the optical field strength is high enough to ionize the medium a plasma will be formed in the focal region. If we then manage to obtain a net polarization within the plasma, the time-dependent macroscopic dipole-moment will lead to the emission of THz radiation. Such THz sources can be positioned far away from the laser system (and the operator), thereby avoiding the absorption of the THz field by water vapor during propagation in ambient air, a highly desired feature for applications. At the same time, high-energy laser pulses can be employed for THz generation without damage to the emitter, which is impossible with the traditional techniques.

The THz radiation from plasma in air induced by laser pulses was first demonstrated by Hamster and co-workers about 20 years ago [Hamster 93, Hamster 94]. Laser pulses with energy of 50 mJ and duration of 120 fs was tightly focused in a noble gas (helium or argon). With low pressure a strong emission of pulsed radiation at THz frequencies was observed from the resulting plasmas. The mechanism of the THz emission was attributed to the polarization produced by the free electrons accelerated by the ponderomotive force, which is caused by a spatio-temporal optical intensity gradient in the plasma with the propagation of the laser pulses.

It was later demonstrated by Löffler, *et al.* that this THz emission from plasma can be enhanced significantly if the static electric field is applied around the plasma area [Löffler 00]. THz generation was associated with ultrafast screening of the external field within the plasma, so the corresponding displacement current is the source of the induced net polarization. The energy of the resultant THz emission scales quadratically with the external biased field. However, the maximum of the THz emission is limited by the maximal external bias field which can be applied without dielectric breakdown of the gas. It was later demonstrated that the breakdown field, and thus the maximal energy of the THz emission, can be enhanced with an increase of the gas pressure [Löffler 02].

At the same time, Cook, *et al.* reported that with tight focusing of IR laser pulses (800 nm) together with its second harmonic (400 nm) the resulting THz emission is much stronger than that in the case of only IR laser pulses [Cook 00]. The THz wave emission mechanism was attributed to the four-wave mixing (FWM) nonlinear optical process $(\omega + \omega - 2\omega)$ in ionized air plasmas produced by the laser fields themselves. However, it was soon noticed that the third order nonlinearity $\chi^{(3)}$ of gas medium is too small to explain the measured THz field strength [Kress 04, Bartel 05]. Xie, *et al.* presented a THz field amplitude scaling result $(E_{THz} \propto \chi^{(3)} E_{2\omega} E_\omega E_\omega)$ supporting the FWM as the principal mechanism for THz generation. However, in that study, the THz scaling was studied over a limited pump energy range, and the origin of $\chi^{(3)}$ in air remains unclear. Soon after, a transient electron current model was proposed by Kim, *et al.* [Kim 07, Kim 08, Kim 09]. In this model, bound electrons of gas-phase atoms or molecules undergo rapid tunnel ionization as the Coulomb barrier is suppressed by the instantaneous laser field. The electrons, freed from their parent atoms or molecules by the mixed laser field, can form

a directional transverse current. As this electrical current surge occurs on the time scale of photoionization, in the case of ultrafast lasers (< 100 fs), this process can generate electromagnetic radiation at THz frequencies. Although, the physical mechanism remains under debate, the THz generation by the two-color method receives much attention. For a short plasma string in the laboratory, the THz produced in this way was found to be 10^2–10^3 times larger than with a single-color pulse [Löffler 05, Xie 06, Manceau 10, Li 12]. Recently, two groups reported bicolor THz generation at a distance of 16–17 m, with an enhancement by two orders of magnitude with respect to the single-color case [Wang 10, Dai 11]. However, there are difficulties with the production of THz radiation by this method at longer distances [Daigle 12]. The difficulties are tied to the process of filamentation, which appears unavoidably when $P > P_{cr}$ and generates an extended plasma column. In order to produce THz radiation efficiently, proper phase relation and temporal overlap between the ω and 2ω pulses must be maintained over the plasma length [Liu 09, Daigle 12, You 12]. For instance, the THz emission produced by this two-color method at a distance of 55 m was only a small fraction of that at shorter distance, due to walk-off between fundamental and second harmonic pulses [Daigle 12].

THz radiation from femtosecond laser filaments

In 1999, Schillinger and Sauerbrey proved the existence of a plasma during the filamentation, which plays a crucial role in the interplay of diffraction and self-focusing, leading to the formation of long stable channels [Schillinger 99]. The free-electron density inside the filamentary plasma was measured to be of 10^{16} cm^{-3} [Tzortzakis 99] in agreement with the numerical calculations [Chiron 99, Couairon 02b]. The corresponding plasma frequency is around 1 THz. An electric current induced inside the filamentary plasma should thus give rise to the radiation in the THz range.

In 2000, Proulx, *et al.* observed in the near field (several mm from the plasma) a sub-picosecond emission in the direction perpendicular to the filament propagation. The spectrum of the emission lies in the sub-THz domain [Proulx 00]. Next year, Cheng, *et al.* proposed that the plasma column should emit radial THz radiation due to the plasma oscillations induced by the pulse radiation pressure and that the emission is coherent [Cheng 01]. This prediction was experimentally verified in next two years [Tzortzakis 02, Méchain 03]. However, according to Sprangle, *et al.*, the THz emission is due to some components of the pulse ionization front, which have superluminal velocities and give rise to Cherenkov-like radiation [Sprangle 04], the THz emission was also expected to be coherent in this case. In addition to the predicted temporal coherence, D'Amico, *et al.* demonstrated that the radially emitted THz radiation from the filament exhibits good spatial coherence properties [D'Amico 07b].

In 2007 D'Amico, *et al.* demonstrated experimentally that the nature of the THz emission is different from the previously expected. Instead of being emitted radially, the THz radiation is confined to a narrow cone in the forward direction [D'Amico 07c] (see Figure 5.3 for the scheme of the experiment). This forward conical emission was found to be more than two orders of magnitude higher that the radial one. Moreover, the polarization of the THz signal is found to be perpendicular to the emission cone
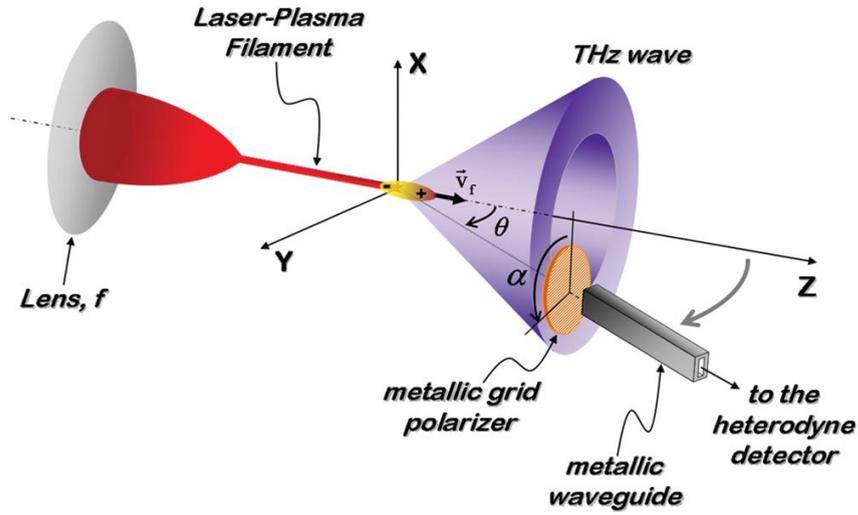
Figure 5.3: Scheme of the experiment demonstrating conical forward THz emission from femtosecond laser filament in air, [D'Amico 07c].

surface and does not depend on the polarization of the laser pulses. Therefore, the THz emission cannot be assigned to a mechanism implying the oscillation of a free electron cloud driven by the linearly polarized electric field of the laser, since one would expect the electric vector of the THz radiation to depend on the laser polarization. One can therefore exclude the mechanism based on the optical rectification via a four-wave or higher order mixing process. The origin of the THz radiation was attributed to a combined "transition-Cherenkov" emission by a dipole-like electric charge oriented along the laser propagation axis, and moving at the light velocity behind the self-guided laser pulse in the medium. This dipole-like charge separation is created by the longitudinal ponderomotive force behind the ionization front during filamentation process. The detailed theoretical model was presented next year [D'Amico 08a].

Unfortunately, this technique has poor energy conversion efficiency from IR to THz, on the order of 10^{-9} per filament [Houard 07]. However, the THz output can be increased by increasing the number of filaments. With a laser pulse of peak power $P \gg P_{cr}$, N parallel filaments are formed, where $N \sim P/P_{cr}$, adding their emission *incoherently*. For instance, a laser with terawatt power led to a THz radiation at 30 m from the laser with 40 times higher power than with a 12 gigawatt laser [D'Amico 07c]. Note that there is no obvious limit to the further scaling up in laser power since there is no optical element susceptible of being damaged in the path of the laser. Recently, we have shown that it is possible to add *coherently* the THz emission from multiple filaments, leading to an increase of the radiated THz energy scaling like N^2, where N is the number of filaments [Mitryukovskiy 13].

5.3 Transition-Cherenkov Terahertz emission from a filament

5.3.1 Physical principle

In 2007 our group experimentally demonstrated that femtosecond laser filaments emit THz radiation to a narrow cone in the forward direction of laser propagation axis [D'Amico 07c]. This is attributed to so-called "transition-Cherenkov" mechanism [D'Amico 07c, D'Amico 08b]. The longitudinal plasma oscillations created inside the filament are considered to be the source of the THz radiation, since the oscillation frequency is equal to the plasma frequency. For an electron density typically obtained in filaments $n_e = 10^{16}$ cm^{-3}, the plasma frequency lies in the THz region. Sprangle, *et al.* highlighted the main role of the ponderomotive force in the THz emission by plasma strings [Sprangle 04].
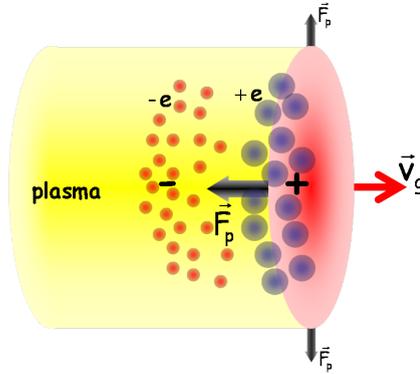
Figure 5.4: Scheme of the electric charge separation induced by the ponderomotive force in the wake of the laser pulse, [D'Amico 07a].

During the initial stage of filamentation, the field-induced increase of refractive index leads to beam self-focusing. The pulse peak intensity increases until it induces high field ionization of air molecules. Beyond the ionization onset, a dynamic competition takes place that maintains a contracted pulse with intensity close to the multi-photon ionization threshold. Therefore a plasma string is left behind the moving pulse. The interaction between free electrons born near the peak of the ionization front with the remaining of the pulse leaves the plasma in an excited state of oscillations [Proulx 00]. Transverse electron oscillations induced by the transverse component of the laser field are predominant. However, for a pulse of many optical cycles ($\tau_p > 10$ fs at 800 nm), the net radial current is zero, so that no THz emission results. There is also a small longitudinal oscillation due to the Lorentz force. This longitudinal oscillation is damped quickly by collisions with neutral molecules, so that the duration of the plasma oscillation and the corresponding THz pulse duration are on the order of a few picoseconds, which corresponds to one or two oscillations. We have, therefore, a very short plasma wave (~ 1 mm) created continuously in the wake of the ionization front, propagating with it at a speed of the laser pulse inside the filament. The electric charge of the plasma rests neutral as a whole,

but the space charge in the wake of the pulse is equivalent to a dipole propagating with a group velocity v_g along the laser pulse propagation direction (see Figure 5.4). This type of an electromagnetic emission from a charged particle propagating with a constant velocity $v_p > c/n$ (there n is the refractive index of the medium) is called Cherenkov radiation. It is localised on the surface of a cone, oriented in the propagation direction. The emission is polarized radially, perpendicularly to the cone surface. The radiation is emitted with an angle θ to the propagation direction, defined by the relation $\cos \theta = 1/n\beta$, where $\beta = v_p/c$.

Note, that there is a difference between this mechanism of THz radiation from a filament and the common Cherenkov emission. The THz emitting charges are moving with the laser pulse at the velocity very close to the velocity of light. This reduces the emission efficiency, but does not suppress it completely, if one takes into account the finite length of the emission. In that sense it resembles transition radiation [Takahashi 00]. Therefore, the discussed mechanism of THz emission from filaments was named transition-Cherenkov radiation [Houard 08a].

5.3.2 Theoretical model

The theoretical development of the model for the transition-Cherenkov THz radiation from a filament can be split into two parts: first, we will calculate the plasma current inside the filament which leads to the THz radiation; second, the THz field induced by this current will be calculated for the far field. Polarization components of the THz field will also be defined. The basis of this theoretical model was developed in collaboration with Prof. Vladimir TIkhonchuk of CELIA, Bordeaux 1 University [Le Bloas 07, Diaw 08].

In the calculations we consider a filament produced in air by femtosecond laser pulses focused by a convex lens. The laser pulse intensity is clamped inside the filament to a value I_0. The duration of the laser pulse is assumed to be constant and equals τ_L. The plasma channel is of a length L and of a diameter $2r_0 \sim 100~\mu$m. The laser polarization was found to have no effect on the THz emission, one can therefore consider the system to be symmetric around the laser pulse propagation axis (z-axis, see Figure 5.5).

We use the following basic ideas to model the mechanism of the THz emission:

- The electrons and the ions created during the ionization experience the influence of the electromagnetic field of the laser pulse: the electrons oscillate in the direction transversal to the laser pulse propagation with an oscillation frequency equal to the laser frequency. At the the same time the electrons acquire a longitudinal movement, one can consider this longitudinal oscillations due to the action of the longitudinal component of the Lorentz force.

- The electrons being much more mobile than the ions, thus a charge separation is induced, giving birth to an electric field which opposes the movement of the electrons.

- The longitudinal oscillation of the electrons can be modeled by an electric current that emits electromagnetic radiation.
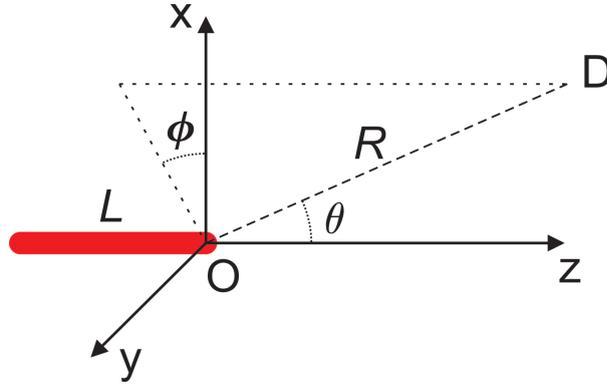
Figure 5.5: Schematic orientation of the filament and the coordinate axes.

Expression of the laser force F_z

The excitation of an electric field in the wake of a filament-forming laser pulse was described by Sprangle, *et al.* [Sprangle 04]. The authors presented the equations for dynamics of the electric field of the charge separation induced by the ponderomotive force inside the plasma. An expression for what we name 'laser force' was obtained. However, no detailed derivation has been presented. Here we will obtain the expression for the laser force driving an electron inside the plasma.

The movement of an electron in the field of the laser pulse is described by the hydrodynamic equation:

$$\frac{\partial \vec{v}_e}{\partial t} + (\vec{v}_e \cdot \vec{\nabla})\vec{v}_e = -\frac{e}{m_e}(\vec{E}_L + \eta \vec{v}_e \times \vec{B}_L) - \nu_e \vec{v}_e, \tag{5.1}$$

where e and m_e are the charge and the mass of the electron, and ν_e is the electron collision frequency. The parameter η is included to keep track of orders of perturbation theory and reflects the fact that the velocity-dependent component of the Lorentz force is of the order $|\vec{v}_e|/c \ll 1$ smaller than the dominant force due to the electric field. Here we also assume that ions inside plasma are heavy and remain stationary.

Let us develop the calculation by using a perturbation solution: $\vec{v}_e = \epsilon \vec{v}_0 + \epsilon^2 \vec{v}_1$. By taking the terms of the first two orders ($\sim \epsilon$ and $\sim \epsilon^2$) one obtains:

$$\epsilon: \quad \frac{\partial \vec{v}_0}{\partial t} = -\frac{e}{m_e}\vec{E}_L - \nu_e \vec{v}_0, \tag{5.2a}$$

$$\epsilon^2: \quad \frac{\partial \vec{v}_1}{\partial t} = -\vec{v}_0 \cdot \vec{\nabla}\vec{v}_0 - \frac{e}{m_e}(\vec{v}_0 \times \vec{B}_L) - \nu_e \vec{v}_1. \tag{5.2b}$$

One can formally solve (5.2a) by using the Laplace transform:

$$p\hat{v}_0 = -\frac{e}{m_e}\hat{E}_L - \nu_e \hat{v}_0, \tag{5.3}$$

and then:

$$\hat{v}_0 = -\frac{e}{m_e}\frac{\hat{E}_L}{p + \nu_e}. \tag{5.4}$$

E_L and B_L are bound by the Maxwell's equation $\vec{\nabla} \times \vec{E} = -\partial \vec{B}/\partial t$. By taking a curl of the equation (5.4), one obtains:

$$\vec{\nabla} \times \hat{v}_0 = -\frac{e}{m_e} \frac{\vec{\nabla} \times \hat{E}_L}{p + \nu_e} = \frac{e}{m_e} \frac{p}{p + \nu_e} \hat{B}_L, \tag{5.5}$$

and finally

$$\hat{B}_L = \frac{m_e}{e}(1 + \frac{\nu_e}{p})\vec{\nabla} \times \hat{v}_0. \tag{5.6}$$

By taking the inverse Laplace transform, one obtains the expression for $\vec{B}_L$:

$$\vec{B}_L = \frac{m_e}{e} \left(\vec{\nabla} \times \vec{v}_0 + \nu_e \int_{-\infty}^{\infty} (\vec{\nabla} \times \vec{v}_0) dt \right). \tag{5.7}$$

The substitution of $\vec{B}_L$ in the equation (5.2b) by the expression (5.7) yields:

$$\frac{\partial \vec{v}_1}{\partial t} + \nu_e \vec{v}_1 = -\vec{v}_0 \cdot \vec{\nabla} \vec{v}_0 - \vec{v}_0 \times (\vec{\nabla} \times \vec{v}_0) - \nu_e \vec{v}_0 \int_{-\infty}^{\infty} (\vec{\nabla} \times \vec{v}_0) dt = $$
$$= -\frac{1}{2}\vec{\nabla}\vec{v}_0^2 - \nu_e \vec{v}_0 \int_{-\infty}^{\infty} (\vec{\nabla} \times \vec{v}_0) dt. \tag{5.8}$$

Let us now consider the x-polarized laser pulse in the form of a slowly varying wave packet multiplied by a rapidly oscillating term: $\vec{E}_L = (E_x(t') \sin(\omega_0 t'); 0; 0)$, where $t' = t - z/c$ is the retarded time. We thus have a system of two equations to solve:

$$\begin{cases} \dfrac{\partial v_{0x}}{\partial t'} + \nu_e v_{0x} = -\dfrac{e}{m_e} E_x(t') \sin(\omega_0 t'), \\ \dfrac{\partial v_{1z}}{\partial t'} + \nu_e v_{1z} = \dfrac{1}{2c} \left(2\nu_e + \dfrac{\partial}{\partial t'} \right) v_{0x}^2. \end{cases} \tag{5.9}$$

Integration of the first equation of (5.9) gives:

$$v_{0x} = -\frac{e}{m_e} e^{-\nu_e t'} \int_{-\infty}^{\infty} E_x(t') e^{\nu_e t'} \sin(\omega_0 t') dt \approx$$
$$\approx -\frac{e}{m_e} E(t') \frac{\nu_0 \sin(\omega_0 t') - \omega_0 \cos(\omega_0 t')}{\nu_e^2 + \omega_0^2}, \tag{5.10}$$

as soon as the wave packet varies slowly in time.

Finally, retaining only the slowly varying terms in v_{0x}^2, one obtains:

$$v_{0x}^2 = \frac{e^2}{2m_e^2} \frac{E^2(t')}{(\nu_e^2 + \omega_0^2)} = \frac{e^2}{2m_e^2 c \varepsilon_0} \frac{I}{(\nu_e^2 + \omega_0^2)}. \tag{5.11}$$

Therefore, the second equation of the system (5.9) turns to:

$$\frac{\partial v_{1z}}{\partial t} + \nu_e v_{1z} = \frac{e^2}{4c^2 m_e^2 \varepsilon_0} \frac{1}{(\nu_e^2 + \omega_0^2)} \left[\frac{\partial I}{\partial t'} + 2\nu_e I \right]. \tag{5.12}$$

Thus, the expression of the laser force reads:

$$F_z = \frac{e^2}{4c^2 m_e \varepsilon_0 (\nu_e^2 + \omega_0^2)} \left[\frac{\partial I}{\partial t'} + 2\nu_e I \right]. \tag{5.13}$$

Note that it consists of two terms: the first one involving the laser intensity gradient is associated with the ponderomotive force, the second is proportional to the collision frequency and corresponds to the radiation pressure. One can write the second term of the expression (5.13) in the following form:

$$F_z = \frac{\hbar \omega_0}{c} \frac{I}{\hbar \omega_0} \frac{e^2 \omega_0 \nu / c}{2 m_e \omega_0 \varepsilon_0} \frac{1}{(\nu_e^2 + \omega_0^2)} = pN\sigma, \tag{5.14}$$

where p is the impulse of a photon, N is the number of photons and σ is the Bremsstrahlung cross section.

Calculation of the 'wake' current inside a filament

The movement of the electrons inside the filamentary plasma is defined by the following equations of hydrodynamics (In further text we omit the arrow labels of the vector quantities to simplify the view of the formulae). For the electrons with the density n_e moving along the z-axis with the speed v_e:

$$\begin{cases} \dfrac{\partial n_e}{\partial t} + \dfrac{\partial n_e v_e}{\partial z} = 0, \\ \dfrac{\partial v_e}{\partial t} + v_e \dfrac{\partial v_e}{\partial z} = -\dfrac{e}{m_e} E + \dfrac{F_z}{m_e} - \nu_e v_e, \\ \varepsilon_0 \dfrac{\partial E}{\partial z} = e(n_i - n_e), \end{cases} \tag{5.15}$$

where n_i is the density of the ions, E is the electric field induced by the charge separation, ν_e is the collision frequency and F is the laser force.

The 'wake' current may be defined as:

$$j = -e n_e v_e. \tag{5.16}$$

Note that the quantities figuring in the system (5.15) are created by the laser pulse and are, therefore, functions of $t - z/c$. Let's thus use the retarded time $t' = t - z/c$. The system (5.15) turns to:

$$\begin{cases} \dfrac{\partial n_e}{\partial t'} - \dfrac{1}{c} \dfrac{\partial n_e v_e}{\partial t'} = 0, \\ \dfrac{\partial v_e}{\partial t'} - \dfrac{v_e}{c} \dfrac{\partial v_e}{\partial t'} = -\dfrac{e}{m_e} E + \dfrac{F_z}{m_e} - \nu_e v_e, \\ -\dfrac{\varepsilon_0}{c} \dfrac{\partial E}{\partial t'} = e(n_i - n_e). \end{cases} \tag{5.17}$$

We now consider a small perturbations of the electron density in respect to the state of equilibrium, as well as the small electron velocities $v_e/c \to 0$. We put $n_e = n_{e0} + \delta n_e$:

$$\begin{cases} \dfrac{\partial \delta n_e}{\partial t'} - \dfrac{n_{e0}}{c}\dfrac{\partial v_e}{\partial t'} = 0, \\[2ex] \dfrac{\partial v_e}{\partial t'} = -\dfrac{e}{m_e}E + \dfrac{F_z}{m_e} - \nu_e v_e, \\[2ex] \dfrac{\varepsilon_0}{c}\dfrac{\partial E}{\partial t'} = e\delta n_e. \end{cases} \qquad (5.18)$$

Integration of the first equation of the system (5.18) gives $\delta n_e = n_{e0}v_e/c$ (for $t' = 0$, $\delta n_e = 0$ and $v_e = 0$). So on, the third equation gives:

$$v_e = \frac{\varepsilon_0}{en_{e0}}\frac{\partial E}{\partial t'}. \qquad (5.19)$$

Substitution of the $\partial v_e/\partial t'$ in the second equation of the system (5.18) by the result of the derivation of the equation (5.19) yields:

$$\frac{\varepsilon_0}{en_{e0}}\frac{\partial^2 E}{\partial t'^2} + \frac{\varepsilon_0 \nu_e}{en_{e0}}\frac{\partial E}{\partial t'} + \frac{e}{m_e}E = \frac{F_z}{m_e}. \qquad (5.20)$$

One can rewrite this equation using the expression (5.13) for the laser force along with the expression for the plasma frequency: $\omega_{pe} = \sqrt{\frac{n_{e0}e^2}{m_e \varepsilon_0}}$. The problem, therefore, turns to the solving of an inhomogeneous differential equation of the second degree with constant coefficients:

$$E'' + \nu_e E' + \omega_{pe}^2 E = \frac{e\omega_{pe}^2}{4c^2 m_e \varepsilon_0 (\nu_e^2 + \omega_0^2)}\left[\frac{\partial I}{\partial t'} + 2\nu_e I\right], \qquad (5.21)$$

with $E = 0$ and $E' = 0$, when $t' = 0$.

The electric current is given now by:

$$j_z = -en_e v_e = -\varepsilon_0 \frac{\partial E}{\partial t'}. \qquad (5.22)$$

Let us solve the equation (5.21) by taking the Fourier transform:

$$(-\omega^2 - i\nu_e\omega + \omega_{pe}^2)E(\omega) = \frac{e\omega_{pe}^2}{4c^2 m_e \varepsilon_0 (\nu_e^2 + \omega_0^2)}\left[-i\omega + 2\nu_e\right]I(\omega), \qquad (5.23)$$

with

$$j_z(\omega) = i\omega\varepsilon_0 E(\omega). \qquad (5.24)$$

Assuming the laser pulse of the duration τ_L to be of the sine form: $I_L(t) = I_0 \sin^2(\pi t/\tau_L)$, like in [D'Amico 08a], one obtains:

$$I(\omega) = I_0 \int_0^{\tau_L} \sin\left(\frac{\pi t'}{\tau_L}\right)e^{-i\omega t'}dt' = \frac{I_0}{\omega\left(\left(\frac{\omega\tau_L}{2\pi}\right)^2 - 1\right)}\sin(\omega\tau_L/2)e^{-i\omega\tau_L/2}. \qquad (5.25)$$

Therefore, using the equation (5.23), we get the following expression for the spectral current amplitude:

$$j_z(\omega) = \varepsilon_0 E_L \omega_{pe} \left(\frac{\omega + 2i\nu_e}{\omega^2 - \omega_{pe}^2 + i\nu_e\omega} \right) \frac{\sin(\omega\tau_L/2)}{1 - (\omega\tau_L/2\pi)^2} e^{-i\omega\tau_L/2}, \tag{5.26}$$

where $E_L = e\omega_{pe}I_0/2m_e\varepsilon_0 c^2\omega_0^2$ is the amplitude of the plasma wave, ω_{pe} is the electron plasma frequency, ω_0 is the laser circular frequency ($\approx 2 \times 10^{15}$ c^{-1}), ν_e is the electron collision frequency ($\approx 10^{12}$ - 10^{14} c^{-1}), and τ_L is the laser pulse duration. Here, we have employed that $\omega_0^2 \gg \nu_e^2$.

5.3.3   Electromagnetic emission from a single filament in the far field

A plasma wave is excited in the wake of a laser pulse inside a filament. This movement of the charge gives rise to the emission of the electromagnetic radiation. In the following the radiated field will be calculated.

First let us recall the Maxwell equations [Jackson 65]:

$$\begin{cases} rot\vec{E} = -\dfrac{\partial\vec{B}}{\partial t}, \\[2mm] div\vec{D} = \rho, \\[2mm] div\vec{B} = 0, \\[2mm] rot\vec{H} = \vec{j} + \dfrac{\partial\vec{D}}{\partial t}, \end{cases} \tag{5.27}$$

and the constitutive equations:

$$\begin{cases} \vec{D} = \varepsilon_0 n^2 \vec{E}, \\[2mm] \vec{B} = \mu_0 \vec{H}. \end{cases} \tag{5.28}$$

Here $\vec{j}$ represents the density of the electric current and is expressed in amperes per square meter.

A simple way to resolve the Maxwell equations is to introduce a vector potential $\vec{A}$ and a scalar potential V defined by

$$\vec{B} = rot\vec{A}, \tag{5.29a}$$

$$\vec{E} = -gradV - \frac{\partial\vec{A}}{\partial t}. \tag{5.29b}$$

$\vec{A}$ and V are the solutions of the following equations:

$$\Delta\vec{A} - \mu_0\varepsilon_0 n^2 \frac{\partial^2\vec{A}}{\partial t^2} + \mu_0\vec{j} = grad[div\vec{A} + \mu_0\varepsilon_0 n^2 \frac{\partial V}{\partial t}], \tag{5.30a}$$

$$\Delta V - \mu_0\varepsilon_0 n^2 \frac{\partial^2 V}{\partial t^2} + \frac{\rho}{\varepsilon_0 n^2} = -\frac{\partial}{\partial t}[div\vec{A} + \mu_0\varepsilon_0 n^2 \frac{\partial V}{\partial t}]. \tag{5.30b}$$

Taking into account the Lorentz gauge

$$div\vec{A} + \mu_0\varepsilon_0 n^2\frac{\partial V}{\partial t} = 0, \tag{5.31}$$

allows to simplify the equations:

$$\Delta\vec{A} - \mu_0\varepsilon_0 n^2\frac{\partial^2\vec{A}}{\partial t^2} + \mu_0\vec{j} = 0, \tag{5.32a}$$

$$\Delta V - \mu_0\varepsilon_0 n^2\frac{\partial^2 V}{\partial t^2} + \frac{\rho}{\varepsilon_0 n^2} = 0. \tag{5.32b}$$

Now let us consider the potentials and the current density $(\vec{A}, V, \text{ and } \vec{j})$ in the form of the Fourier integrals:

$$f(\vec{R}, t) = \int_{-\infty}^{\infty} f_\omega(\vec{R}, \omega)e^{-i\omega t}d\omega, \tag{5.33a}$$

$$f_\omega(\vec{R}, \omega) = \frac{1}{2\pi}\int_{-\infty}^{\infty} f(\vec{R}, t)e^{i\omega t}dt, \tag{5.33b}$$

where f serves for $\vec{A}$, or V, or $\vec{j}$.

Keeping in mind that $k^2 = \mu_0\varepsilon_0 n^2\omega^2 = n^2\omega^2/c^2$, one obtains

$$\Delta A_\omega + k^2 A_\omega + \mu_0 j_\omega = 0, \tag{5.34}$$

together with:

$$div A_\omega = i\frac{k^2}{\omega}V_\omega. \tag{5.35}$$

Let us now consider the electric current inside the filamentary plasma. The current is directed along the z-axis. We assimilate the transverse distribution of the current to the Dirac distribution, thus the current density can be written in the following form:

$$j(t) = j(t - z/c)\delta(x)\delta(y). \tag{5.36}$$

Therefore, by taking the Fourier transform, one obtains:

$$\begin{cases} j_x(\omega) = 0, \\ j_y(\omega) = 0, \\ j_z(\omega) = j(\omega)\delta(x)\delta(y)e^{ikz}. \end{cases} \tag{5.37}$$

Here $j(\omega)$ represents a spectral component of the linear current density.

The solution of the equation (5.34) may be obtained as a convolution of the Green's function with the expression for the current density (5.37). We come to an expression in the form of the Fresnel's diffraction integral:

$$A_\omega(\omega, x, y, z) =$$

$$= \frac{\mu_0}{4\pi}\int_{-\infty}^{\infty}\delta(x')dx'\int_{-\infty}^{\infty}\delta(y')dy'\int_0^L \frac{j(\omega)e^{ikz'}e^{ik\sqrt{(x-x')^2+(y-y')^2+(z-z')^2}}}{\sqrt{(x-x')^2+(y-y')^2+(z-z')^2}}dz'. \tag{5.38}$$

After the integration, one obtains:

$$\begin{cases} A_\omega^{(x)}(\omega, x, y, z) = 0, \\ A_\omega^{(y)}(\omega, x, y, z) = 0, \\ A_\omega^{(z)}(\omega, x, y, z) = \dfrac{\mu_0}{4\pi} \displaystyle\int_0^L \dfrac{j(\omega) e^{ikz'} e^{ik\sqrt{(x)^2+(y)^2+(z-z')^2}}}{\sqrt{(x)^2 + (y)^2 + (z - z')^2}} dz'. \end{cases} \tag{5.39}$$

With the expressions (5.39) for components of the vector potential, one can calculate the components of electric and magnetic fields using the relations (5.29) and (5.35).

Radiation in the far field

The integral in the expression for the z-component of the vector potential (5.39) does not have an analytical solution. However, the approximation of the far field will allow us to simplify (5.39). Assume that the length of the filament (L) is much smaller than the distance to the detector (R) (see Figure 5.5). Let us rewrite (5.39) as

$$A_\omega^{(z)}(\omega, x, y, z) = \frac{\mu_0}{4\pi} j(\omega) \int_0^L \frac{e^{ikz'} e^{ik\sqrt{R^2 - 2zz' + z'^2}}}{\sqrt{R^2 - 2zz' + z'^2}} dz'. \tag{5.40}$$

For $R \gg z'$ (in the far field) or $\frac{z'}{R} \ll 1$ one can express the square root in the form of series before limited by $\frac{z'}{R}$ term:

$$\sqrt{R^2 - 2zz' + z'^2} \simeq R \left(1 - \frac{zz'}{R^2} + ... \right) = R - z' \cos\theta. \tag{5.41}$$

Therefore, the equation (5.40) turns to:

$$A_\omega^{(z)}(\omega, R, \theta) = \frac{\mu_0}{4\pi} j(\omega) \frac{e^{ikR}}{ikR} \int_0^L e^{ikz'(1-\cos\theta)} dz'. \tag{5.42}$$

After the integration we have:

$$A_\omega^{(z)}(\omega, R, \theta) = \frac{\mu_0}{4\pi} j(\omega) \frac{e^{ikR}}{ikR} \frac{e^{ikL(1-\cos\theta)} - 1}{1 - \cos\theta}. \tag{5.43}$$

One can now write the components for the vector potential in the spherical coordinates (R, θ, ϕ) (see Figure 5.5):

$$\begin{cases} A_R = A_\omega^{(z)} \cos\theta, \\ A_\theta = -A_\omega^{(z)} \sin\theta, \\ A_\phi = 0. \end{cases} \tag{5.44}$$

Note that the component A_ϕ equals zero and that A_R and A_θ do not depend on ϕ, thus (see (5.29) and (5.35)) $E_\phi = 0$.

Using the equation (5.35)), one obtains:

$$V_\omega \simeq -i\frac{\omega}{k^2}\frac{\mu_0}{4\pi}j(\omega)\frac{e^{ikR}}{R}\frac{e^{ikL(1-\cos\theta)}-1}{1-\cos\theta}\cos\theta, \tag{5.45}$$

where the terms $\sim 1/R^2$ are neglected. Finally, by using (5.29b) we have the following expressions for the components of the emitted THz electric field, in the far field approximation.

$$\begin{cases} E_R = 0, \\ E_\theta = \dfrac{1}{4\pi}\sqrt{\dfrac{\mu_0}{\varepsilon_0}}j(\omega)\dfrac{e^{ikR}}{R}\sin\theta\dfrac{e^{ikL(1-\cos\theta)}-1}{1-\cos\theta}, \\ E_\phi = 0. \end{cases} \tag{5.46}$$

The expressions for the magnetic field components can be found as well (with the use of the equation (5.29a)):

$$\begin{cases} B_R = 0, \\ B_\theta = 0, \\ B_\phi = -\dfrac{1}{4\pi c}\sqrt{\dfrac{\mu_0}{\varepsilon_0}}j(\omega)\dfrac{e^{ikR}}{R}\sin\theta\dfrac{e^{ikL(1-\cos\theta)}-1}{1-\cos\theta}. \end{cases} \tag{5.47}$$

Therefore, the energy density (the Poynting vector) of the THz emission yields:

$$u = \bar{S} = \frac{1}{128\pi^2}\sqrt{\frac{\mu_0}{\varepsilon_0}}j^2(\omega)\frac{1}{R^2}\frac{\sin^2\theta}{(1-\cos\theta)^2}\sin^2\left(\frac{kL}{2}(1-\cos\theta)\right). \tag{5.48}$$

5.3.4 Conical distribution of the THz radiation

The angular distribution of the THz energy in the far field is given by the function (see (5.48)):

$$f^2(\omega, \theta) = \frac{\sin^2 \theta}{(1 - \cos \theta)^2} \sin^2 \left(\frac{\omega L}{2c} (1 - \cos \theta) \right).$$ (5.49)

The distribution is, therefore, conical. An example of the calculated THz radiation pattern from a single filament is presented in Figure 5.6(a). We have verified the THz intensity angular dependence experimentally using a heterodyne detector operating at ~ 0.1 THz, the corresponding data is presented in Figure 5.6(b) for the detector rotating in the YOZ plane, 30 cm away from a 1-cm-long filament.
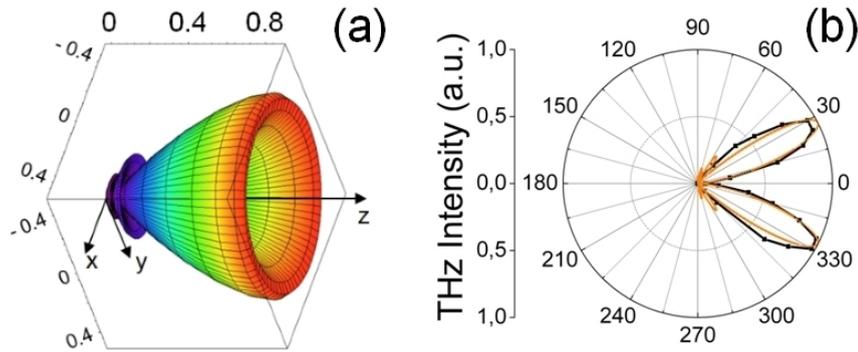
Figure 5.6: (a) Calculated THz radiation pattern at 91 GHz from a single 1-cm-long filament. (b) Emission diagram of the THz radiation in the YOZ plane from a single filament. Black points: experimental results. Solid line: calculation.

Note (see equation (5.49)) that the opening angle of the cone is defined by the filament length L and the frequency of detection $\nu = \omega/2\pi$. The calculation predicts the following dependence of the THz emission cone opening angle (2α) with the filament length and with the detection frequency (see Figure 5.7(a) and 5.7(b), respectively). Increasing of
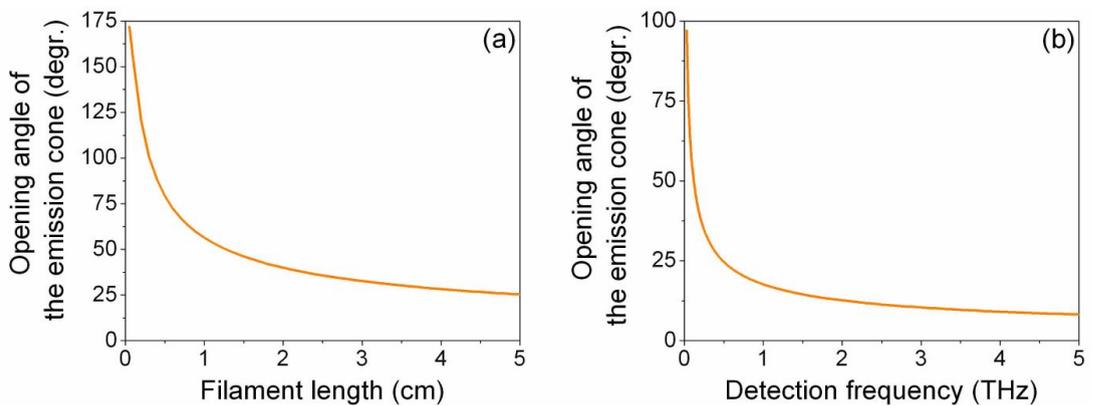
Figure 5.7: Calculated value of the THz emission cone opening angle (2α) as a function of (a) the filament length (for the fixed detection frequency $\nu = 0.1$ THz) and (b) the detection frequency (for the fixed filament length $L = 1$ cm).

the filament length leads to the narrowing of the opening angle of the THz emission cone. In addition, for the fixed filament length, the higher the spectral component of the THz emission, the narrower the opening angle of emission cone (2α). For a 1-cm-long filament it varies from $\sim 60°$ (for 0.1 THz) to $\sim 17°$ (for 1 THz).

Polarization of the THz emission

For better visualization and understanding, the calculated THz radiation patterns for x-, y- and z- components of the total THz field are presented here. As mentioned above the THz emission from a single filament is radially polarized as E_θ is the only non-zero component of the THz field in spherical coordinate system (eq. (5.46)). In this case the three field components are defined by:

$$\begin{cases} E_x = -E_\theta \cos\theta \cos\phi, \\ E_y = -E_\theta \cos\theta \sin\phi, \\ E_z = E_\theta \sin\theta. \end{cases} \tag{5.50}$$

The x-, y- and z- components of the total THz field and the corresponding intensities are calculated and visualized in Figures 5.8(a) – 5.8(c). The radial polarization nature of the THz radiation is reflected in the symmetry of the x- and y- components presented respectively in Figures 5.8(a) and 5.8(b).
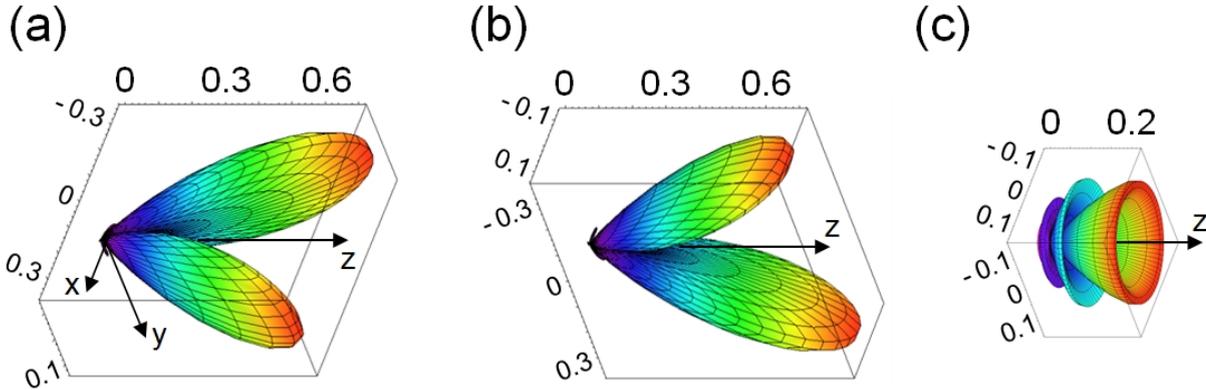

Figure 5.8: (a)-(c) Calculated THz radiation patterns for x-, y-, z- components of the polarization of the THz radiation from a single filament, respectively.

Chapter 6

Coherent synthesis of Terahertz radiation from femtosecond laser filaments in air

Electromagnetic radiation in the Terahertz (THz) domain has received much attention in the last two decades. Unfortunately, many applications which require illumination of a distant target are hampered by the poor transmission of THz radiation through atmosphere, due to the strong attenuation posed by water vapor. Recently, significant progress has been achieved in remote THz generation. To alleviate the strong attenuation in air, one can produce a THz emitting source close to the distant target. This can be readily achieved using intense infrared femtosecond laser pulses.

A first scheme consists in simply launching a short laser pulse in air. If the initial peak power exceeds a critical value $P_{cr} \equiv 3.72\lambda_0^2/8\pi n_0 n_2$, the pulse undergoes filamentation [Couairon 07] (see Chapter 1). Here, λ_0, n_0 and n_2 are the laser wavelength, the refractive index of air and the nonlinear refractive index of air, respectively. The plasma column created during this process is initially in an excited state of longitudinal oscillations; it produces a forward oriented, radially polarized conical THz emission (see the previous chapter). By simple manipulation of the initial laser beam, it is possible to place the ionized region, and hence the THz source, at a distance from the laser, which can reach hundreds of meters. This technique has poor energy conversion efficiency from IR to THz, on the order of 10^{-9} per filament [Houard 07]. However, the THz output can be increased by increasing the number of filaments. With a laser pulse of peak power $P \gg P_{cr}$, N parallel filaments are formed, where $N \sim P/Pcr$, adding their emission *incoherently*. For instance, a laser with terawatt power led to a THz radiation at 30 m from the laser with 40 times higher power than with a 12 gigawatt laser [D'Amico 07c]. Note that there is no obvious limit to the further scaling up in laser power since there is no optical element susceptible of being damaged in the path of the laser. Here we will show that the THz emission from multiple femtosecond laser filaments can interfere coherently, leading to a strong increase of the radiated THz energy.

6.1 THz emission from an array of parallel filaments

In this chapter, we describe the coherent synthesis of the THz radiation from N individual single-color filaments organized in an array. This demonstrates that there is a strong mutual coherence between the THz radiation pulses emitted by filaments created independently in air. We find that the THz intensity scales up with N^2 provided that proper filament separation and laser pulse temporal delays are chosen. Moreover, the THz radiation pattern can be controlled, which is a useful property for many applications. Calculations based on the transition-Cherenkov model of THz emission by filaments agree well with our observations.

Theoretical model

The THz field distribution in the far field from a single filament propagating along the z axis reads (see eq. (5.46)):

$$E_\theta = \frac{1}{4\pi}\sqrt{\frac{\mu_0}{\varepsilon_0}}j(\omega)\frac{e^{ikR}}{R}\sin\theta\frac{e^{ikL(1-\cos\theta)}-1}{1-\cos\theta}, \tag{6.1}$$

where ω, L, θ, k represent the frequency of the considered THz component, the length of the filament, the angle of the radiation and the THz wavenumber, respectively. R is the distance from the filament to the detector. The spectral current amplitude at frequency ω is given by (see eq. (5.26)):

$$j(\omega) = \varepsilon E_L \omega_{pe}\left(\frac{\omega + 2i\nu_e}{\omega^2 - \omega_{pe}^2 + i\nu_e\omega}\right)\frac{\sin(\omega\tau_L/2)}{1-(\omega\tau_L/2\pi)^2}e^{-i\omega\tau_L/2}, \tag{6.2}$$

where $E_L = e\omega_{pe}I_0/2m_e\varepsilon_0c^2\omega_0^2$ is the amplitude of the plasma wave, ω_{pe} is the electron plasma frequency, ω_0 is the laser circular frequency, ν_e is the electron collision frequency, I_0 is the laser intensity and τ_L is the laser pulse duration.

The model can be readily extended to the case of N identical filaments [Mitryukovskiy 13]. The interference between the THz fields from each independent filament yields

$$E_\theta^{total} = \frac{1}{4\pi}\sqrt{\frac{\mu_0}{\varepsilon_0}}j(\omega)\sum_{i=1}^{N}e^{i\xi_i}\frac{e^{ikR_i}}{R_i}\sin\theta_i\frac{e^{ikL(1-\cos\theta_i)}-1}{1-\cos\theta_i}, \tag{6.3}$$

where $\xi_i = \omega\tau_i$ is the accumulated phase difference of the ith THz field due to the temporal delay τ_i between the laser pulses, R_i is the distance from the ith filament emitter to the detector, and θ_i is the angle between the axis of ith filament and the direction from the filament to the detector.

Experimental data and calculation results

To verify the model, two IR femtosecond laser pulses of 46 fs duration, with equal energy of 1.1 mJ, obtained from a Mach-Zehnder interferometer were focused by two convex lenses ($f = 100$ cm) to form two 1-cm-long parallel filaments in ambient air [Mitryukovskiy 13]. The experimental setup is presented in Figure 6.1. The spatial separation and temporal delay of the two pulses could be controlled by a steering mirror of the interferometer and an integrated mechanical delay line. The forward THz radiation was detected by a heterodyne detector working at 91 GHz [Tzortzakis 02]. For the two parallel filaments in the horizontal plane, the detector was rotated in the YOZ and XOZ planes.
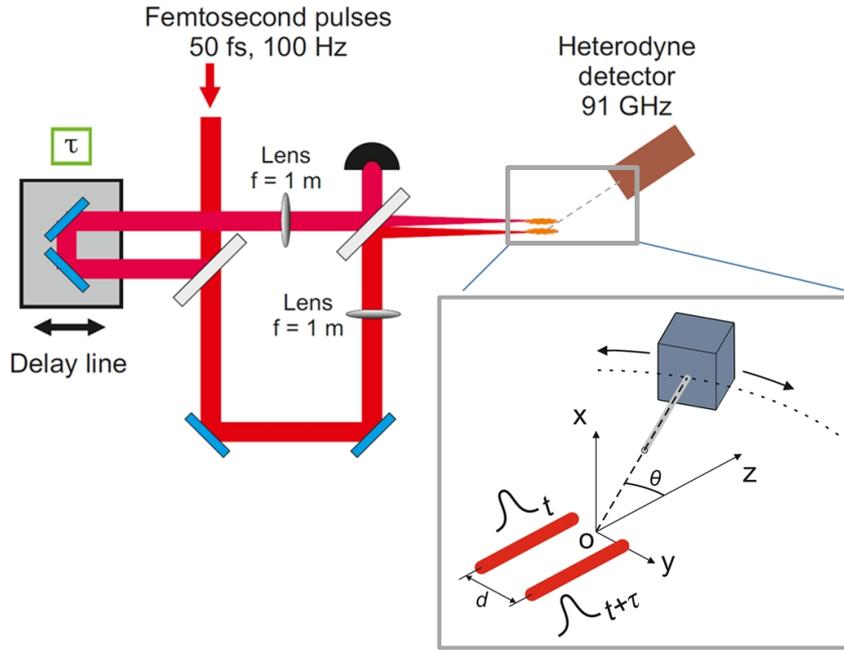
Figure 6.1: Scheme of the experimental setup.

The synthesized THz field intensity emitted in the YOZ plane is presented in Figure 6.2 for different spatial separations between the filaments and with zero temporal delay between the laser pulses. With the increase of the separation d from 0.5 mm to 3.4 mm, the THz radiation diminishes but remains symmetric. The emission in the XOZ plane for $d = 2.4$ mm is shown in Figure 6.2(d). Here (and in every further figure) the THz intensity is normalized to the peak THz intensity of a single filament.

The corresponding calculated 3D emission diagrams for several values of spatial separation d are presented in Figure 6.3. For small spatial separation between the filaments ($d = 0.5$ mm, as an example) the total THz radiation diagram has the distribution close to conical (Figure 6.3(a)). With further increase of the separation between the two filaments, a 'butterfly' wing pattern appears in the XOZ plane (see Figure 6.3(b)). Figures 6.2(b') and (d') are actually the cross section intensity distributions of this radiation pattern.

We note that there is a limited range of separation between the filaments for which our results apply. Filaments should not be closer than 200 μm because two filamentary plasmas at such distance influence each other [Liu 07b, Durand 10]. There is also an upper limit for the separation between the filaments: for the effective interference of THz fields at a frequency ν, d should be on the order of $\lambda = c/\nu$. Otherwise a highly modulated pattern is expected in the far field (see Figure 6.3(c), as an example).
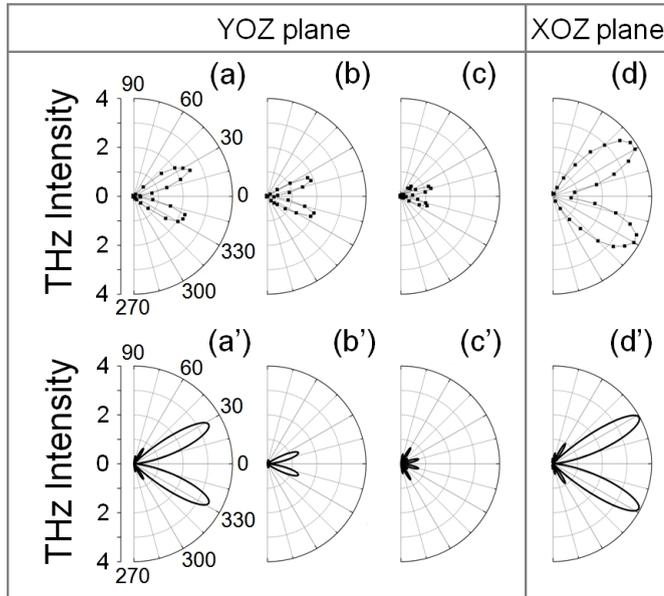
Figure 6.2: (a)-(c) Emission diagrams of the THz radiation at 91 GHz obtained in the YOZ plane from two filaments as a function of the spatial separation d between the filaments. Top row: experimental results. Bottom row: calculations. From (a) to (c), the lateral separation d is 0.5 mm, 2.4 mm and 3.4 mm, respectively. (d) Emission diagram of the THz radiation obtained in the XOZ plane from two filaments laying in the YOZ plane and separated by 2.4 mm.
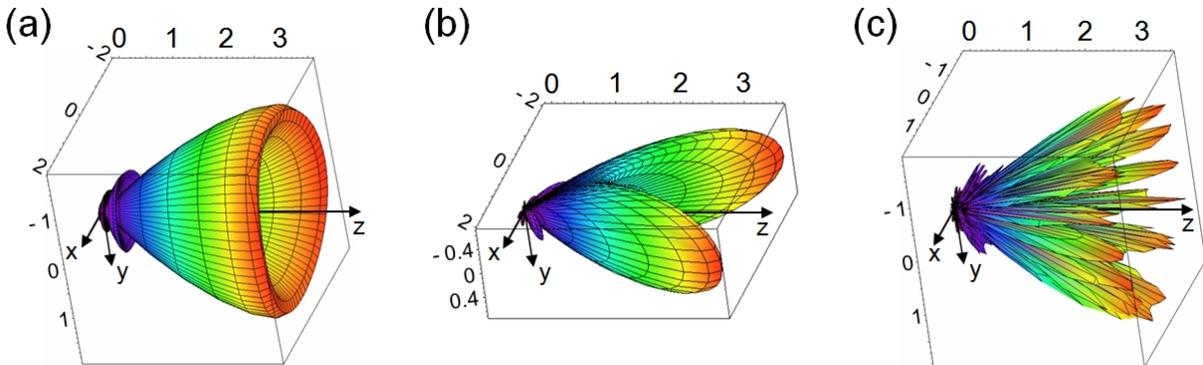


Figure 6.3: Calculated THz radiation diagrams for two parallel filaments spatially separated in YOZ plane by d with zero temporal delay between the filamentary pulses. Values of the lateral separation d: (a) 0.5 mm, (b) 2.4 mm and (c) 20 mm.

Next, we considered the interference of two synthesized THz fields for different values of temporal delay between the filament-forming laser pulses (τ_p) with a fixed spatial separation $d = 2.4$ mm between the two filaments. With variation of the temporal delay the radiation pattern undergoes significant changes (Figure 6.4). For zero temporal delay (Figure 6.4(a)) the THz radiation is symmetric with respect to XOZ and YOZ planes. Upon increase of the temporal delay the radiation pattern becomes asymmetric. With $\tau_p = 3.5$ ps (Figure 6.4(c)), the radiation is totally directed along a single lobe with an absolute maximum in the YOZ plane. The total THz radiation is now directed away from the laser propagation direction. This can prove interesting in applications where irradiation of targets with intense laser pulse should be avoided. With further delay (after $\tau_p = \lambda/2c \approx 5.5$ ps) another lobe starts to grow at the expense of the first one. For $\tau_p \approx 11$ ps ($\sim \lambda/c$), the radiation pattern becomes identical to that without temporal delay (Figure 6.4(i)).
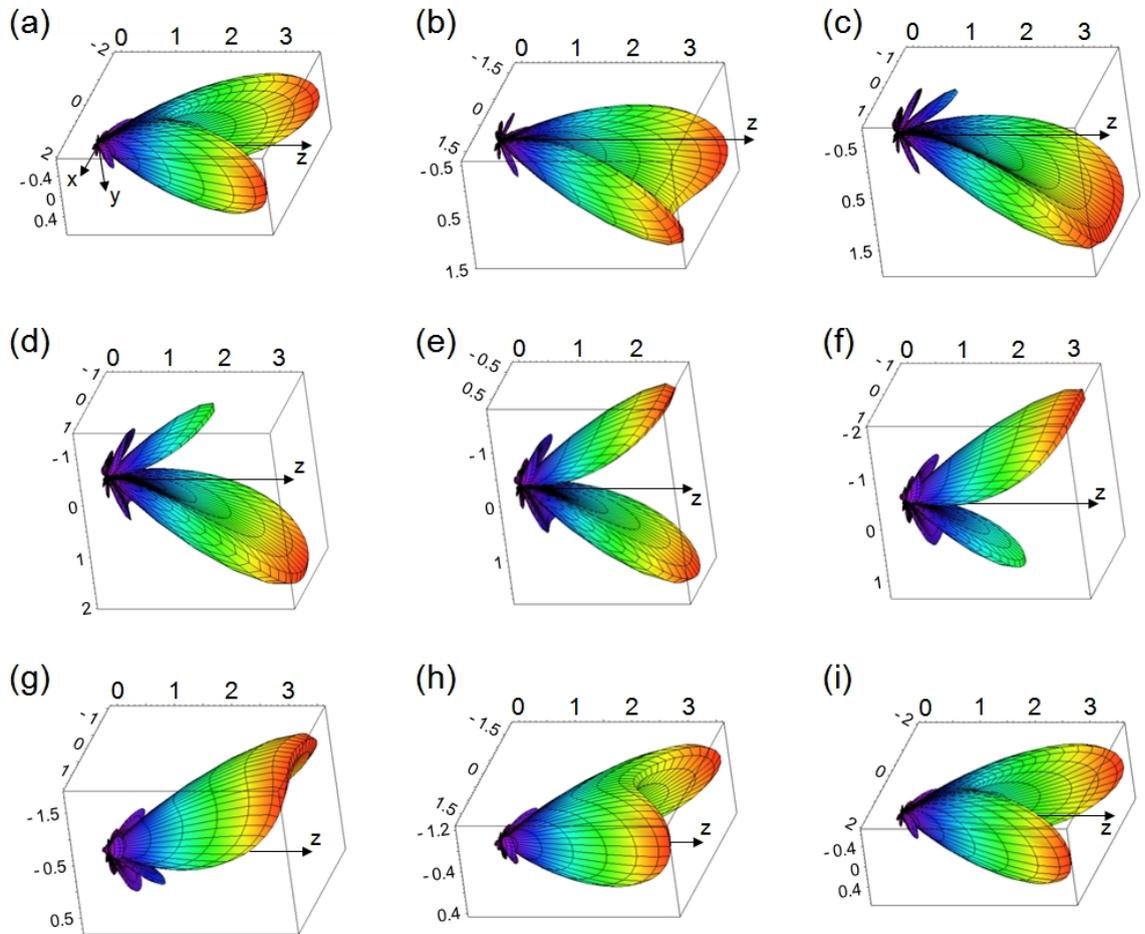
Figure 6.4: Evolution of the 3D emission diagram of the THz radiation from two parallel filaments as a function of the temporal delay between the two laser pulses (calculation). The filaments are separated by $d = 2.4$ mm. Values of the temporal delay τ_p: (a) 0 ps; (b) 2 ps; (c) 3.5 ps; (d) 4.6 ps; (e) 5.5 ps; (f) 6.5 ps; (g) 7.8 ps; (h) 9.5 ps; (i) 11 ps. THz intensity is normalized to the peak THz intensity of a single filament.

The experimentally observed evolution of the emission diagram of the THz radiation in the YOZ plane as a function of the temporal delay between the two laser pulses is presented in Figure 6.5. The good agreement between experimental observations and calculations validates the theoretical model and shows that a high degree of coherence exists between the THz radiation emitted by two independent filaments.
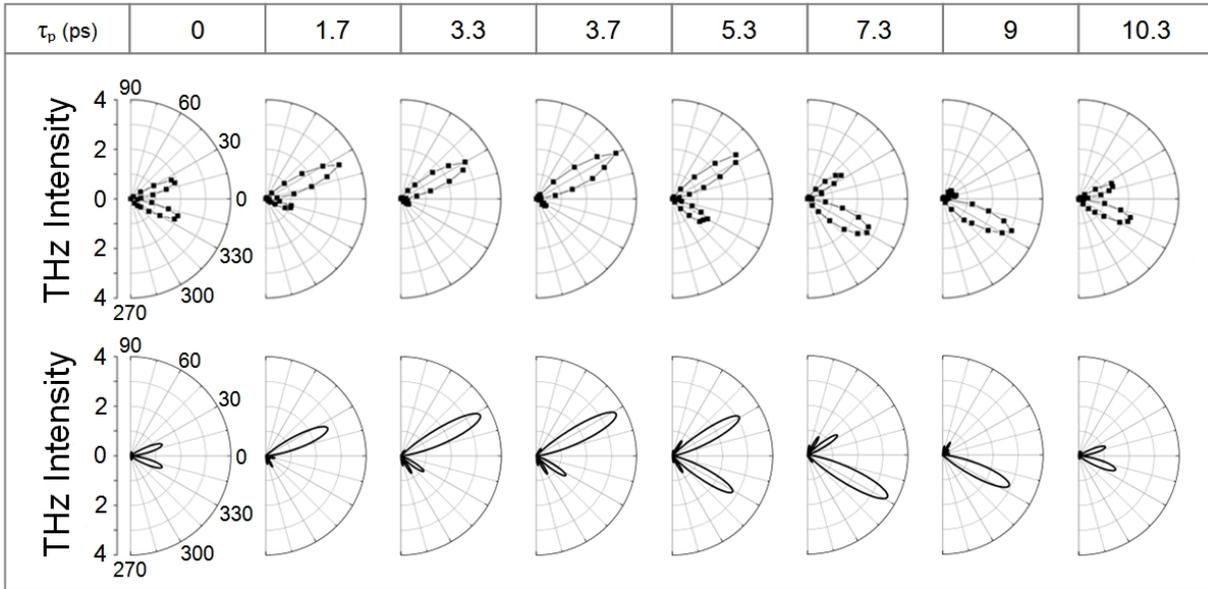

Figure 6.5: Evolution of the emission diagram of the THz radiation in the YOZ plane from two parallel filaments as a function of the temporal delay between the two laser pulses. The spatial separation between the filaments is $d = 2.4$ mm. Top row: experimental results. Bottom row: calculations.

Polarization of the total THz radiation

We have also considered the polarization components of the total THz field for the case of two parallel filaments with temporal delay $\tau_p = 3.5$ ps when the total THz radiation is directed along a single lobe off-axis of the laser direction. We used equations (5.50) to obtain x-, y- and z- components of the total THz field, assuming that the slight spatial separation between the two filaments may be considered insignificant in the far field. The calculated THz radiation patterns for x-, y- and z- components of the total THz field are presented in Figure 6.6. The emission lobe is mainly y-polarized, however x- and z-components are also present.
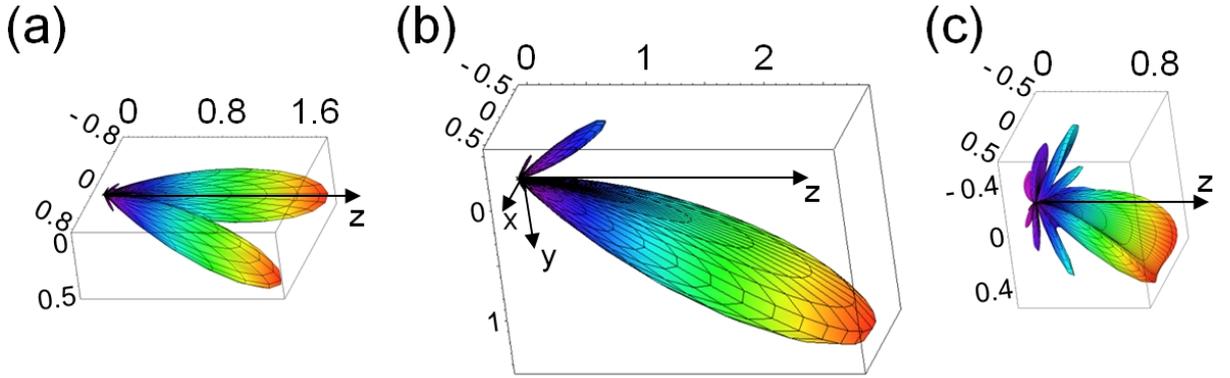
Figure 6.6: Calculated THz radiation patterns for (a) x-, (b) y- and (c) z-components of the total THz field radiated from two parallel filaments separated by $d = 2.4$ mm in the YOZ plane with temporal delay between the two filamentary pulses $\tau_p = 3.5$ ps (corresponding radiation diagram for the total THz intensity is presented in Figure 6.4(c).

Coherent THz synthesis at other frequencies

Figures 6.2 and 6.5 show the experimentally obtained and the calculated THz radiation patterns for the given spatial separations and temporal delays. Excellent agreement between the experimental results and calculation is found. We have considered theoretically the THz emission at a frequency of ~ 0.1 THz, because it corresponds to the spectral component measured by our detector. However the THz emission from filaments peaks at higher frequencies. In Figure 6.7 we show the temporal waveform of a THz pulse and the corresponding spectrum obtained from a 5-mm-long filament in air (induced by focusing 2 mJ, 50 fs, 800 nm laser pulses with an $f = 20$ cm lens). The THz waveform was obtained by the standard time domain THz spectroscopy system based on a 1-mm-thick ZnTe crystal [Wu 96] (see Appendix A for details). The THz power spectrum reaches a maximum around 0.5 THz. It is therefore instructive to calculate the emission pattern at other frequencies, which can be readily obtained from equations (6.2) and (6.3).
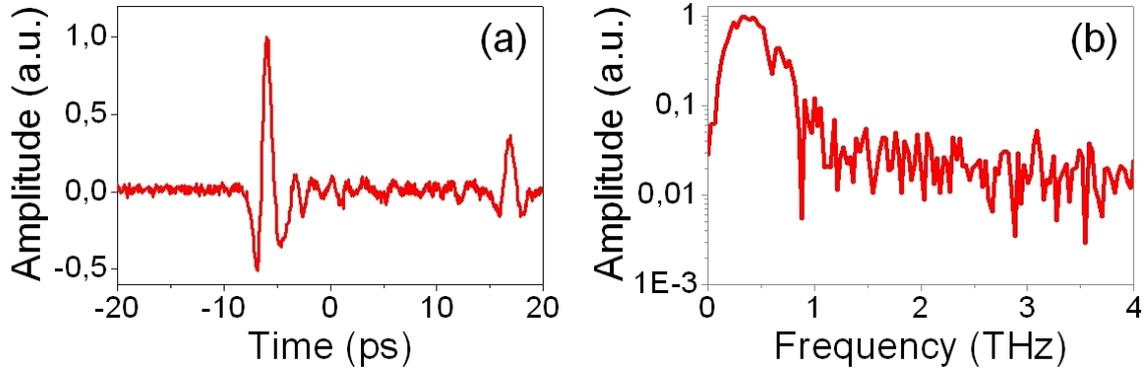
Figure 6.7: (a) Typical temporal waveform of a THz pulse emitted by a filament measured by the time domain THz spectroscopy system. (b) Corresponding spectrum of the THz field below 4 THz.

In Figures 6.8 (b) and (c) the result for 0.5 THz is presented for two parallel filaments separated by 0.5 mm in YOZ plane. Such spatial separation was chosen to keep the ratio d/λ on the same order as for 0.1 THz (d is the spatial separation between filaments, λ is the wavelength of the THz emission). Similar results to those shown in Figure 6.4 are obtained.
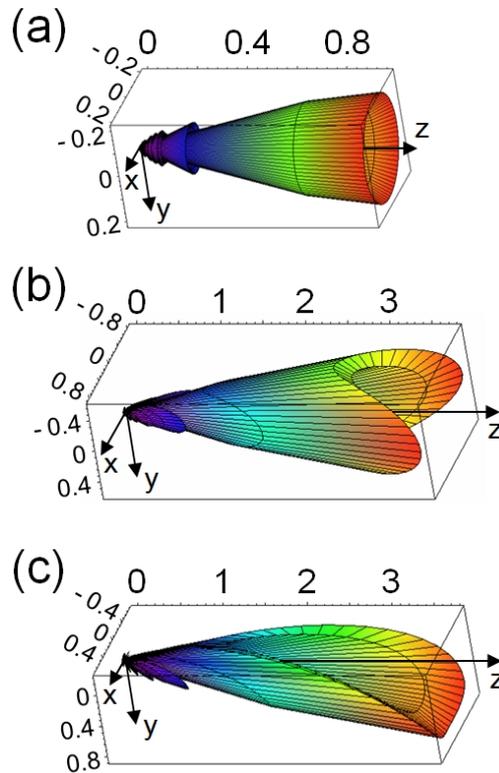
Figure 6.8: Calculated THz radiation diagrams for the frequency of 0.5 THz from (a) single filament, (b) two parallel filaments separated by 0.5 mm without temporal delay, (c) two parallel filaments separated by 0.5 mm with a temporal delay $\tau_p = 0.3$ ps.

Array of N parallel filaments

The good agreement between our experimental observations and calculations validates the theoretical model and permits to extrapolate the results to a higher number of filaments. It has been demonstrated that a large number of filaments can be organized in regular patterns by manipulation of the beam profile of a femtosecond laser pulse with $P \gg P_{cr}$ [Méchain 04b, Schroeder 04, Châteauneuf 08]. In this case, the onset of filamentation is no more ruled by the random fluctuations of the initial beam profile amplified by modulation instability (a process difficult to control), but they are rather imposed by the strong disturbance introduced by the mask. The onset of filamentation is therefore deterministic. We have calculated the THz radiation distribution for $N = 4$, 6, 8, 9, 12, 16 filaments organized in a square grid (see Figure 6.9). With certain combinations of filament delays, quite complicated radiation patterns can come up. With a properly optimized delay, the total THz energy can be channeled towards a preferential direction. The corresponding peak intensity scales almost like N^2, as shown in Figure 6.10.
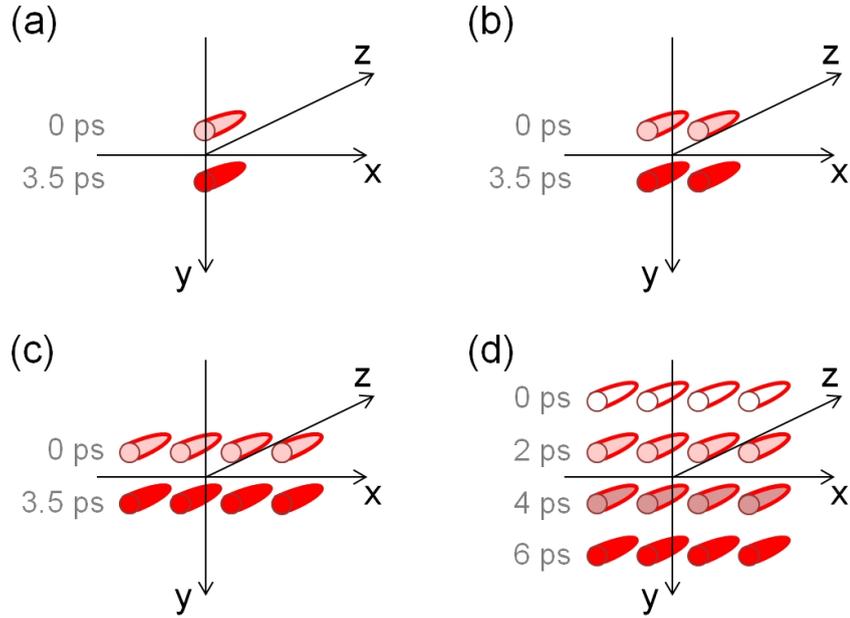
Figure 6.9: Spatial orientation of (a) 2, (b) 4, (c) 8, and (d) 16 filaments, used in our calculations. To obtain strong enhancement of the THz radiation the temporal delays τ_i between the filamentary laser pulses were optimised, the corresponding values of τ_i is shown near the filaments.

In Figure 6.11, we present the normalized three dimensional distribution of the optimized THz field for 2, 4, 8, and 16 filaments separated by $d = 2$ mm. For two filaments with $\tau_p = 3.5$ ps, a 'single-leaf' radiation pattern is obtained (Figure 6.11(a)). For a larger number of filaments, similar leaf-shape radiation pattern appears with properly chosen pulse delays. For example, the synthesized THz radiation from 16 filaments is presented in Figure 6.11(d), where its peak intensity is found to be ~ 250 times that of a single

filament. Recently, Châteauneuf, *et al.* have reported the generation of 10^3 filaments organized in a circle [Châteauneuf 08]. With proper phase control, it could lead to a 10^6 increase of THz peak intensity. We expect it would have an impact on remote THz delivery.
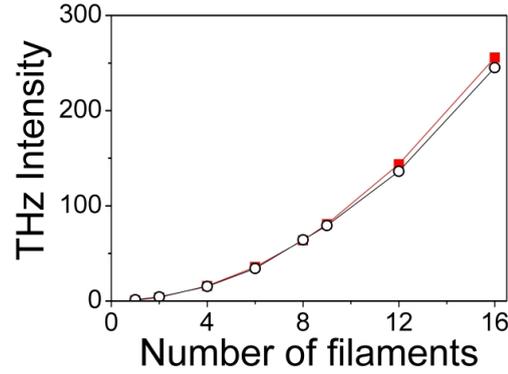
Figure 6.10: Dependence of peak THz intensity on the number of filaments N. Squares – theoretical upper limit (quadratic dependence), Circles – maximum value obtained in our calculations.
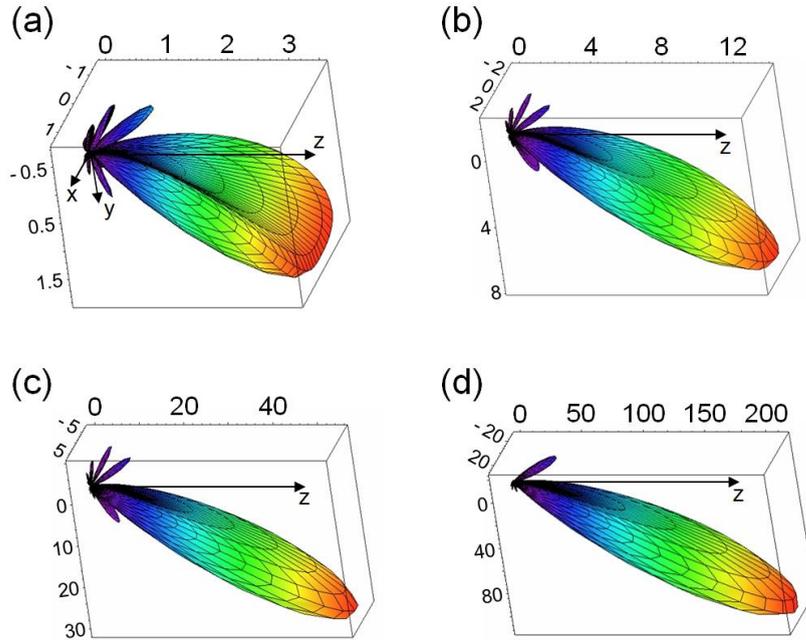
Figure 6.11: Calculated THz radiation diagrams from: (a) two parallel filaments separated by 2.4 mm with a temporal delay $\tau_p = 3.5$ ps; (b) a square matrix of 4 parallel filaments separated by 2 mm with 3.5 ps temporal delay between successive rows along y axis; (c) a (2×4) matrix of 8 parallel filaments separated by 2 mm with 3.5 ps time delay between successive rows along y axis; (d) a square matrix of 16 parallel filaments separated by 2 mm with 2 ps time delay between successive rows along y axis. The spatial orientations of filaments are presented in Figure 6.9.

6.2 THz emission from 'V-oriented' filaments

There is a large number of possible spatial orientations of filaments for coherent synthesis of THz radiation. We have studied experimentally and theoretically the emission from two non-parallel filaments forming the equivalent of a Vee antenna [Karr 01, Balanis 05] (see the scheme in Figure 6.12). The idea is the following: each independent filament emits THz radiation at a given frequency in a cone with an opening angle (2α) defined by the THz frequency and the filament length. If one places two filaments in one plane (YOZ) with an angle of 2α between them, then these two emission cones partially overlap (around the z-axis). If the temporal delay between the filamentary laser pulses is properly adjusted, an enhancement of the total THz radiation will occur due to the constructive interference of the THz fields. Moreover, varying the angle between the filaments one can select the frequency of the THz field to be enhanced.
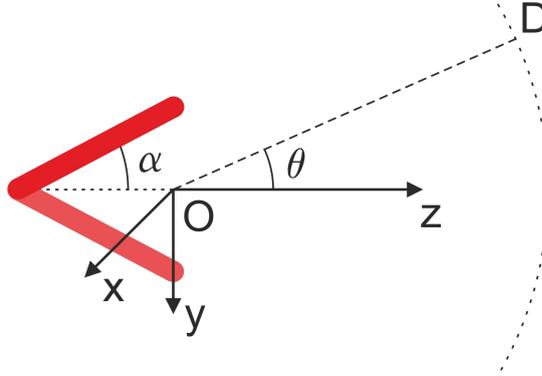
Figure 6.12: Scheme of the orientation of filaments. Two 'V-oriented' filaments with an angle 2α between the filament axes. The temporal delay τ_p between the two filamentary pulses can be adjusted.

Let us consider a filament forming an angle α with the z-axis. The direction of the filamentary laser pulses is defined in spherical coordinates by a polar angle α and an azimuthal angle β. The THz amplitude distribution in the far field from such filament is described by:

$$\begin{cases} E_x = E_\theta \dfrac{\sin\alpha\cos\beta - \sin\theta\cos\phi\cos\gamma}{(1 - \cos^2\gamma)^{1/2}}, \\[2mm] E_y = E_\theta \dfrac{\sin\alpha\sin\beta - \sin\theta\sin\phi\cos\gamma}{(1 - \cos^2\gamma)^{1/2}}, \\[2mm] E_z = E_\theta \dfrac{\cos\alpha - \cos\theta\cos\gamma}{(1 - \cos^2\gamma)^{1/2}}, \end{cases} \tag{6.4}$$

where E_θ is defined by equation (6.1), and

$$\cos\gamma = \sin\alpha\cos\beta\sin\theta\cos\phi + \sin\alpha\sin\beta\sin\theta\sin\phi + \cos\alpha\cos\theta. \tag{6.5}$$

For the case of N filaments 'V-oriented' around the z-axis, the total THz field distribution yields:

$$
\begin{cases}
E_x^{total} = \dfrac{1}{4\pi}\sqrt{\dfrac{\mu_0}{\varepsilon_0}}j(\omega)\displaystyle\sum_{i=1}^{N}e^{i\xi_i}\dfrac{e^{ikR_i}}{R_i}\sin\gamma_i\dfrac{e^{ikL(1-\cos\gamma_i)}-1}{1-\cos\gamma_i}\left(\dfrac{\sin\alpha_i\cos\beta_i-\sin\theta\cos\phi\cos\gamma_i}{\left(1-\cos^2\gamma_i\right)^{1/2}}\right), \\[2ex]
E_y^{total} = \dfrac{1}{4\pi}\sqrt{\dfrac{\mu_0}{\varepsilon_0}}j(\omega)\displaystyle\sum_{i=1}^{N}e^{i\xi_i}\dfrac{e^{ikR_i}}{R_i}\sin\gamma_i\dfrac{e^{ikL(1-\cos\gamma_i)}-1}{1-\cos\gamma_i}\left(\dfrac{\sin\alpha_i\sin\beta_i-\sin\theta\sin\phi\cos\gamma_i}{\left(1-\cos^2\gamma_i\right)^{1/2}}\right), \\[2ex]
E_z^{total} = \dfrac{1}{4\pi}\sqrt{\dfrac{\mu_0}{\varepsilon_0}}j(\omega)\displaystyle\sum_{i=1}^{N}e^{i\xi_i}\dfrac{e^{ikR_i}}{R_i}\sin\gamma_i\dfrac{e^{ikL(1-\cos\gamma_i)}-1}{1-\cos\gamma_i}\left(\dfrac{\cos\alpha_i-\cos\theta\cos\gamma_i}{\left(1-\cos^2\gamma_i\right)^{1/2}}\right),
\end{cases} \quad (6.6)
$$

where $\xi_i = \omega\tau_i$ is the accumulated phase difference of the THz fields due to the temporal delay τ_i between the laser pulses, α_i and β_i are the two angles which define the orientation of the ith filament with respect to the coordinate axes, and γ_i is defined as

$$\cos\gamma_i = \sin\alpha_i\cos\beta_i\sin\theta\cos\phi + \sin\alpha_i\sin\beta_i\sin\theta\sin\phi + \cos\alpha_i\cos\theta. \quad (6.7)$$

The total THz intensity in this case can be calculated as:

$$I_{THz}^{total} = \sqrt{(E_x^{total})^2 + (E_y^{total})^2 + (E_z^{total})^2}. \quad (6.8)$$

Figure 6.13 shows the calculated total THz emission pattern from two 1-cm-long 'V-oriented' filaments ($\alpha_1 = 28°$, $\beta_1 = 90°$ and $\alpha_2 = 28°$, $\beta_2 = 270°$) at a frequency of 91 GHz. With zero temporal delay (Figure 6.13(a)) no THz emission is observed along the z-axis. We remind that the THz radiation from a single filament is radially polarized,
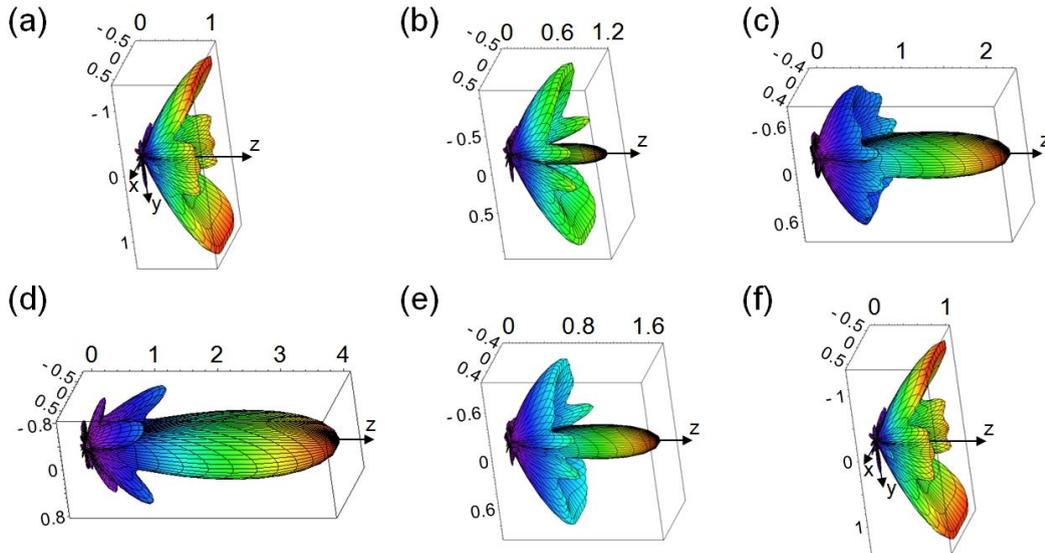
Figure 6.13: Evolution of the 3D emission diagram of the THz radiation from two 'V-oriented' filaments as a function of the temporal delay between the two laser pulses. The angle between the two filaments is $2\alpha = 56°$. Values of the temporal delay τ_p: (a) 0 ps; (b) 2 ps; (c) 3 ps; (d) 5.5 ps; (e) 8.5 ps; (f) 11 ps.

therefore the THz field directions are opposite for the two emission cones in the overlap area around the z-axis. As a consequence, complete destructive interference of the two THz fields is achieved along this direction. Upon increase of the delay τ_p the THz radiation in the z-direction becomes stronger, and for $\tau_p = \lambda/2c \approx 5.5$ ps a maximum is reached with a THz intensity 4 times stronger than for a single filament, due to the constructive interference between the two THz fields (Figure 6.13(d)).

To verify our calculations, we modified our previous experimental setup (Figure 6.1) to obtain two 'V-oriented' filaments crossed with an angle around 60°. In the top row of Figure 6.14, our results in the YOZ plane are shown. The laser beams propagate with angles of ±30° to the "0°-direction". With zero temporal delay between the filamentary pulses (Figure 6.14(a)) THz emission from the filaments interfere destructively and cancel in the "0°-direction". With a delay of $\tau_p = 5.5$ ps the THz intensity is enhanced by a factor close to 4, due to constructive interference (Figure 6.14(b)). Corresponding calculated THz emission diagrams are presented in the bottom row of Figure 6.14. Note that in the experiment we observed the existence of 4 small lobes in the emission pattern for zero temporal delay, in disagreement with just 2 small lobes obtained in the calculation. We attribute this to the fact that in the experiment the plane of detection and the plane of filaments were slightly misaligned. Another condition for the constructive interference on selected frequency which is difficult to satisfy in the experiment is the value of the angle between the filaments. These facts also explain the impossibility to experimentally achieve the THz intensity enhancement by a factor 4.
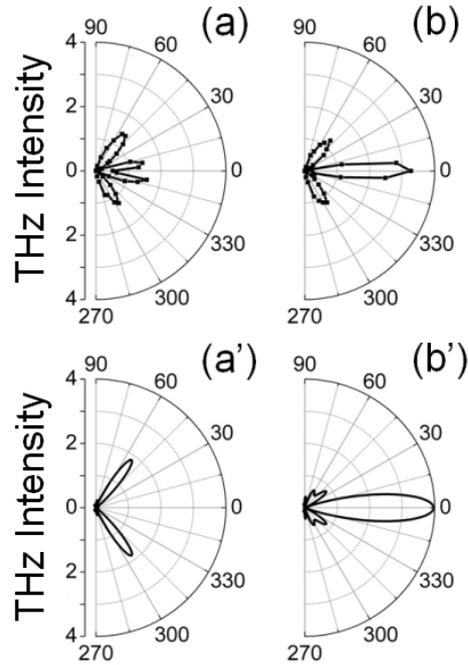
Figure 6.14: Emission diagrams of the THz radiation in the YOZ plane from two 'V-oriented' filaments without temporal delay (a) and with a temporal delay between the two filamentary pulses $\tau_p = 5.5$ ps (b). Top row: experimental results. Bottom row: calculations.
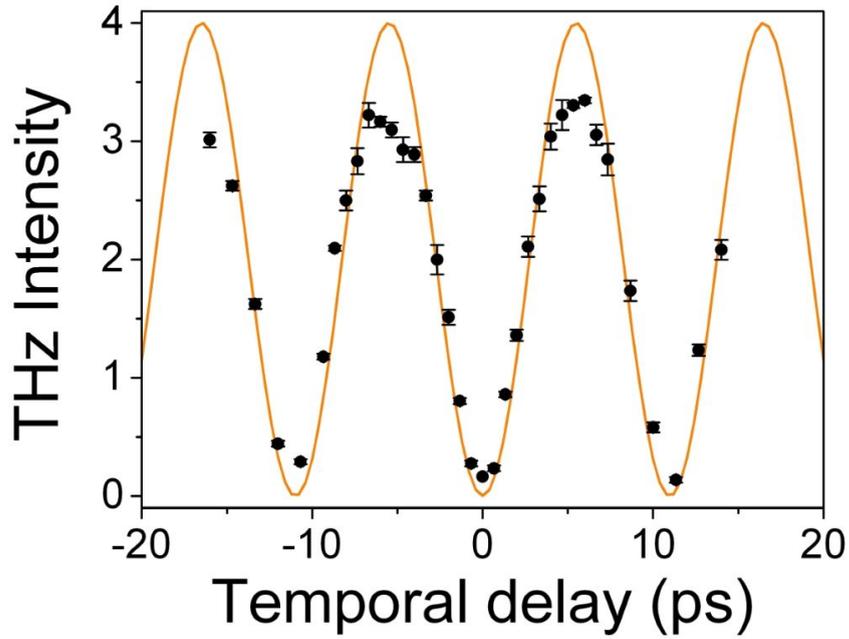
Figure 6.15: Evolution of the intensity of THz radiation in the OZ direction from two 'V-oriented' filaments as a function of the temporal delay between the two laser pulses. Black points: experimental results. Solid line: calculations.

Upon increase of the delay τ_p THz emission in the "0°-direction" changes periodically as shown in Figure 6.15. Good agreement of experimental data with calculation results also validates our model.

In practice it is complicated to organize multiple filaments in a form of 'Vee antenna' especially if it comes to a big number of filaments needed for strong total THz radiation. Nevertheless, we dwell below on two important properties of the THz emission from 'V-oriented' filaments, which are unique for such orientation of filaments: circularly polarized THz emission and THz frequency tuning.

Circularly polarized THz emission

First we consider the polarization components of the total THz field. The calculated THz radiation patterns for x-, y- and z- components of the total THz field from 'V-oriented' filaments in YOZ plane are presented in Figure 6.16. The temporal delay between the laser pulses is $\tau_p = 5.5$ ps which corresponds to the maximal THz intensity toward z-axis (see Figure 6.13(d)). The y-component (Figure 6.16(b)) of the total THz field is much higher than that for x- and z- components. Thus the total THz radiation from 'V-oriented' filaments may be considered to be linearly polarized in the y-direction. By using two pairs of such 'V-oriented' filaments in perpendicular planes (say one pair is in YOZ and another one in XOZ) one obtains the total THz field with two linearly polarized components orthogonal to each other (x- and y- components). Varying the temporal delay between filamentary laser pulses in each pair of filaments gives an opportunity to manipulate the polarization of the total THz field. It becomes possible to create linearly, elliptically and circularly polarized THz radiation by simple adjustment (tuning) of the phase differences between filament-forming laser pulses.
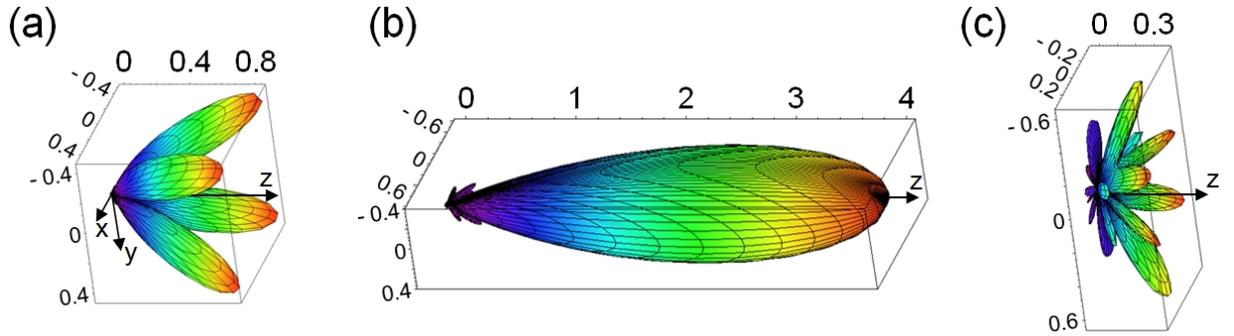
Figure 6.16: Calculated THz radiation patterns for (a) x-, (b) y- and (c) z- components of the total THz field radiated from two 'V-oriented' filaments lying in the YOZ plane. The angle between the two filaments is $2\alpha = 56°$. Temporal delay between the two filamentary pulses $\tau_p = 5.5$ ps (corresponding radiation diagram for the total THz intensity is presented in Figure 6.13(d)).

Enhancement of THz radiation at selected frequencies

So far, we have considered the THz radiation from filaments at a single, selected frequency. However, filaments emit radiation in a broad band of THz frequencies. Typically their radiation spectrum has a bandwidth of several THz with a maximum between $0.5 - 1$ THz, close to the value of the plasma natural oscillation frequency [Reimann 07, Liu 10] (also see Figure 6.8). The higher the frequency, the narrower the opening angle of the emission cone (2α) (see Figure 5.7(b)). For 1-cm-long filament the opening angle of the conical THz emission varies from $\sim 60°$ (for 0.1 THz) to $\sim 17°$ (for 1 THz). With two filaments in the form of 'Vee-antenna' the angle between the filaments defines which THz frequency component will be enhanced. We calculated the dependence of the total THz intensity from 'V-oriented' filaments with angle and with detection frequency to verify the possibility of THz enhancement at selected frequencies.

The dependence of the total THz signal with angle between two 'V-oriented' filaments is presented in Figure 6.17 for detection at 91 GHz, 0.2 THz, 0.5 THz and 1 THz. For each frequency the optimal temporal delay $\tau_p = 2/\nu$ between the filament-forming laser pulses was chosen to achieve the constructive interference between the two THz emissions. All curves in Figure 6.17 are normalized to the maximal THz intensity radiated from a single filament at the chosen frequency. The optimal value of the angle between the filaments for effective enhancement of the THz radiation at a desired frequency is clear from Figure 6.17 and presented in Table 6.1.
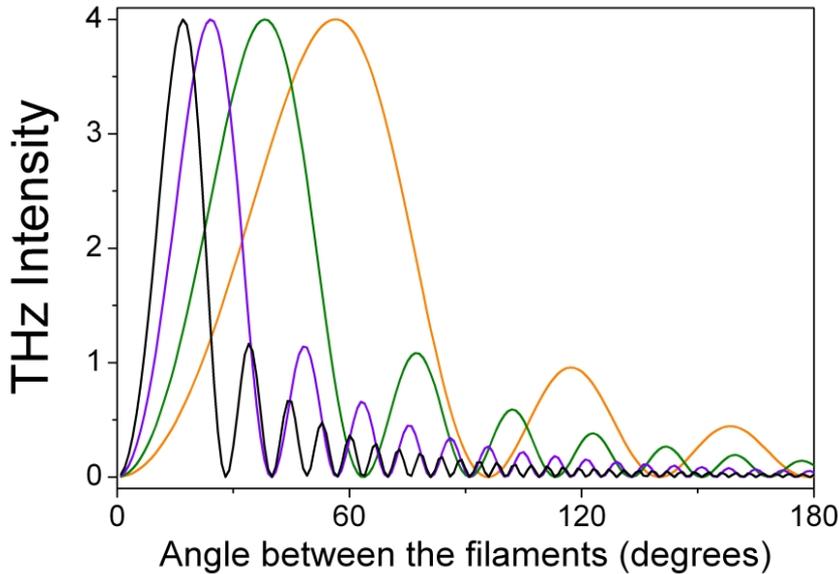
Figure 6.17: Intensity of the total THz emission radiated in the OZ direction by two 'V-oriented' filaments lying in the YOZ plane as a function of the angle between the filaments for selected values of the radiation frequency ν and the temporal delay $\tau_p = \lambda/2c = 2/\nu$ between the two filamentary pulses. Black line: $\nu = 1$ THz, $\tau_p = 0.5$ ps; Purple line: $\nu = 0.5$ THz, $\tau_p = 1$ ps; Green line: $\nu = 0.2$ THz, $\tau_p = 2.5$ ps; Orange line: $\nu = 91$ GHz, $\tau_p = 5.5$ ps. All the dependencies are normalized to the maximal THz intensity radiated from a single filament at the chosen frequency.

Table 6.1: Optimal values of the angle between the 'V-oriented' filaments and the temporal delay between the two laser pulses for the full constructive interference of the THz radiation at selected frequency.

Frequency of the THz radiation to be enhanced (THz)	Optimal delay τ_p (ps)	Optimal angle between the filaments 2α (°)
0.091	5.495	56.42
0.2	5	38.16
0.5	2.5	24.16
1	0.5	17.1

Next we studied how different THz spectral components (at 91 GHz, 0.2 THz, 0.5 THz and 1 THz) can be resolved for optimized sets of angle between the filaments and temporal delay $\tau_p = \lambda/2c = 2/\nu$. The result of the calculations is presented in Figure 6.18. This shows that filaments in a Vee arrangement provide a tool to deliver THz radiation at a desired frequency by simple selection of a proper angle between the filaments.
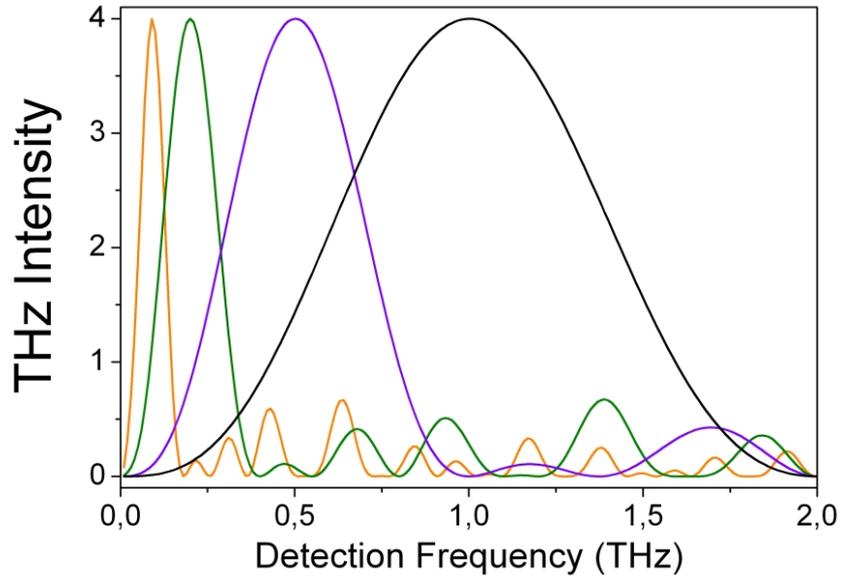
Figure 6.18: Spectrum intensity of the total THz emission radiated in the OZ direction by two 'V-oriented' filaments lying in the YOZ plane for selected values of the temporal delay $\tau_p = \lambda/2c = 2/\nu$ between the two filamentary pulses and the angle 2α between the filaments. Black line: $2\alpha = 17.1°$, $\tau_p = 0.5$ ps; Purple line: $2\alpha = 24.16°$, $\tau_p = 1$ ps; Green line: $2\alpha = 38.16°$, $\tau_p = 2.5$ ps; Orange line: $2\alpha = 56.42°$, $\tau_p = 5.5$ ps. All the dependencies are normalized to the maximal THz intensity radiated from a single filament.

We also compared the spectral selectivity of two 'V-oriented' filaments versus two parallel filaments. In the case of parallel filaments the total THz radiation is the superposition of the conical emission at different frequency components. By changing the temporal delay between the filament-forming laser pulses one can enhance the THz radiation at a selected frequency. The THz radiation in this case will be directed along some angle (α) to the filament axis. We calculated the intensity spectrum of THz radiation from two parallel filaments separated by $d = 0.5$ mm with the time delay $\tau_p = 0.325$ ps between the laser pulses. The maximum THz intensity is directed $\approx 12°$ away from the laser propagation direction. These conditions are optimal for the effective enhancement of THz radiation at 0.5 THz. The result of the calculation is presented as a dashed line in Figure 6.19. The corresponding result for the scheme of two 'V-oriented' filaments is presented in the same figure as a solid line. It shows that the Vee arrangement has a better spectral selectivity.
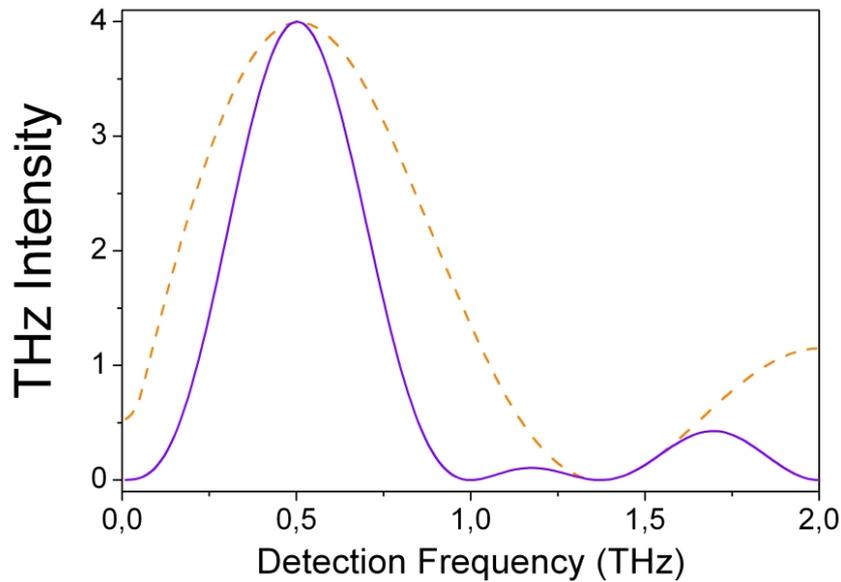
Figure 6.19: Solid line: spectrum intensity of the total THz emission radiated in the OZ direction from two 'V-oriented' filaments with an angle $2\alpha = 24.16°$ between them; Dashed line: spectrum intensity of the total THz emission radiated at angle $\alpha = 12.08°$ from the OZ axis from two parallel filaments separated by $d = 0.5$ mm. Such directions are optimal for the achievement of maximal THz intensity in these two configurations. The value of the temporal delay between the two filamentary pulses $\tau_p = 1$ ps is the same in the two schemes. Such temporal delay is optimal for effective enhancement of THz radiation at 0.5 THz in these schemes. The dependencies are normalized to the maximal intensity of the THz emission from a single filament.

6.3   Conclusion

In summary, we have discussed the coherent synthesis of the THz radiation from an array of N parallel femtosecond laser filaments. It provides a simple technique for scaling up the THz intensity with high power femtosecond laser since the total THz intensity is proportional to N^2. With appropriate delay between the filaments, the emission can be directed along preferential directions, which is of high interest for remote THz applications.

We have further considered the coherent synthesis of the THz radiation from another geometric configuration, where femtosecond laser filaments form an analogue of a 'Vee-antenna'. The polarization of the total THz radiation was examined, showing an interesting possibility for 'V-oriented' filaments to produce circularly polarized THz emission. A method of effective enhancement of a THz radiation at a selected frequency was discussed. It consists in optimizing the angle between two 'V-oriented' filaments.

Chapter 7

Effect of an external electric field on the coherent Terahertz emission from multiple filaments

7.1 Amplification of Terahertz radiation from femtosecond laser filaments in air

As discussed in Chapter 5, the THz radiation from a femtosecond laser filament is produced by the longitudinal plasma oscillations in the wake of the moving ionization front. These plasma oscillations are excited by the ponderomotive force of the laser pulse and are damped by electron collisions on a picosecond scale. The radiation is emitted by a dipole like structure moving at the speed of light; it is therefore a Cherenkov-like emission [D'Amico 07c]. A laser filament as a THz source has several unique advantages comparing to the traditional techniques for THz generation including photoconductive antenna and optical rectification with electro-optical crystal. Being a femtosecond filament a THz source can be positioned far away from the laser system, thereby avoiding the absorption of the THz field by water vapor during propagation in ambient air. At the same time, high energy laser pulses can be employed for THz generation without damage to the emitter, which is impossible with the traditional techniques. Unfortunately, the conversion efficiency of this method is very low. It has been measured to be on the order of 10^{-9} [Houard 07]. Several methods have been demonstrated to improve the conversion efficiency.

In a first approach, an external electric field is applied on the filament either longitudinally or transversely. A THz enhancement by 3 orders of magnitude was obtained with an applied longitudinal static field $E_{ext} \sim 10$ kV/cm (Figure 7.1). At the same time, the radiation pattern and polarization property of this amplified emission keep the same as that of the pure transition-Cherenkov THz radiation [Liu 08]. The amplification effect is explained by a higher longitudinal electron current in the wake driven by the external electric field. This amplified THz pulse is of particular significance since a radially polarized THz wave has been demonstrated to be compatible with the propagating mode of a metal wire THz waveguide [Wang 04]. Although, this method of enhancement suffers

101

from the fact that the electric field must be applied on the plasma region of the filament, not an easy task for stand-off THz applications.
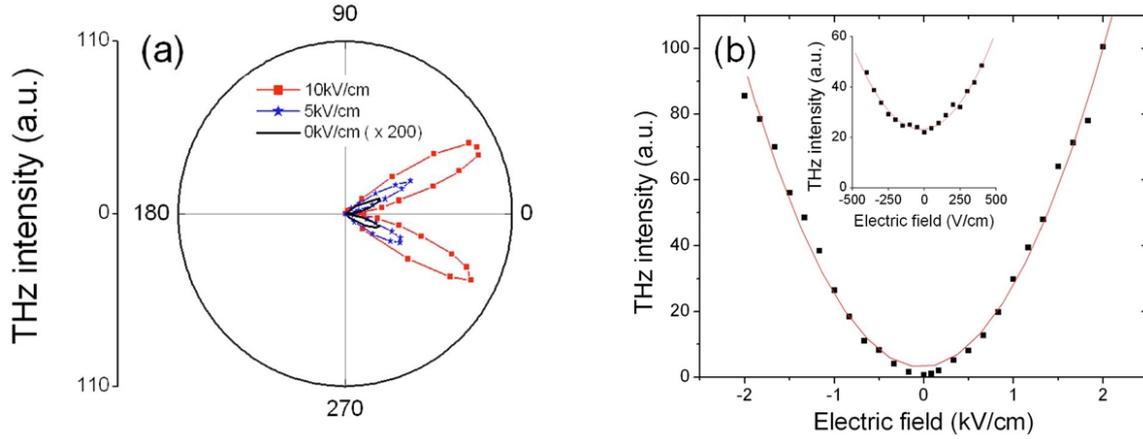
Figure 7.1: (a) Radiation pattern of the amplified THz emission from a filament in longitudinal electric field. The pure transition-Cherenkov THz emission ($E_{ext} = 0$ kV/cm) is multiplied by a factor of 200 for visibility. (b) Intensity of the amplified THz radiation as a function of the external electric field. The solid lines denote a quadratic fit. The figures are taken from [Liu 08].

Application of an external electric field perpendicularly to the filament axis induces a transverse electron current inside the filament [Houard 08c]. With the increase of the external electric field strength, the energy of the THz signal increases, while its peak gradually converges to the filament axis (see Figure 7.2). As a result, a THz beam with maximum intensity directed towards the laser propagation was obtained when E_{ext} exceeds 3 kV/cm. Moreover, with $E_{ext} = 9$ kV/cm the THz intensity was enhanced by 3 orders of magnitude with respect to the pure transition-Cherenkov THz without the external electric field. A quadratic dependence of the total THz energy on the external electric field was also observed in this case. In addition, the amplified THz emission was found to be linearly polarized and the polarization plane is dictated simply by the direction of the external field.
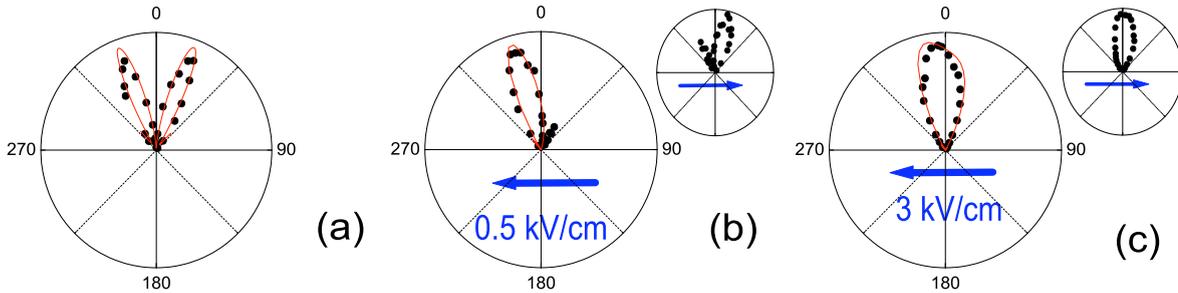
Figure 7.2: Angular dependence of the THz emission from a laser filament in the presence of increasing transverse electric field $E_{ext} = 0$ kV/cm (a), 0.5 kV/cm (b), and 3 kV/cm (c). The figure is taken from [Houard 08c].

Another method to amplify THz radiation from filaments is to use an oscillating transverse field, by combining a short IR pulse (at 800 nm) with its second harmonic generated in a thin BBO crystal. After the first demonstration of this two-color method [Cook 00], it has been extensively studied with a millimeter-scale-long plasma ($L \sim \lambda_{THz}$) [Xie 06, Thomson 07, Kim 07, Kim 08, Houard 08b, Liu 09]. It was found that the optical bias at second harmonic frequency can lead to a THz amplitude enhancement by two orders of magnitude compared to the air plasma driven by just 800 nm femtosecond laser pulses [Xie 06, Thomson 07]. The relative phase between the fundamental laser field and its second harmonic was found to be critical for the yield and polarity of the THz radiation [Xie 06, Liu 09]. Recently, this method was also extended to long air plasma ($L \gg \lambda_{THz}$) obtained in the filamentation regime [Wang 10, Daigle 12]. For such long filaments, it was confirmed that the two-color scheme is more efficient than the single-color one. However, the temporal separation of the 800 nm and 400 nm pulses during their propagation inside the long filaments due to group delay dispersion of air sets a limit of interaction length ($\sim$ 2 m) and results in a strong THz yield decrease for standoff THz generation [Daigle 12].

In the previous chapter, we have shown that it is possible to add coherently the THz emission from multiple filaments, leading to an increase of the radiated THz energy scaling like N^2, where N is the number of filaments. Here, we consider experimentally and theoretically the effect of a static electric field on the THz emission from multiple filaments.

7.2   Theoretical model

We first consider the effect theoretically. Because the longitudinal electric field merely increases the THz intensity without changing the radiation pattern [Liu 08] it is not necessary to consider it. We therefore focus our attention on the case of transverse electric field, where the action of the applied field leads to new emission patterns from filaments. The geometrical disposition of the filament, the electric field and the coordinate axes is shown in Figure 7.3.
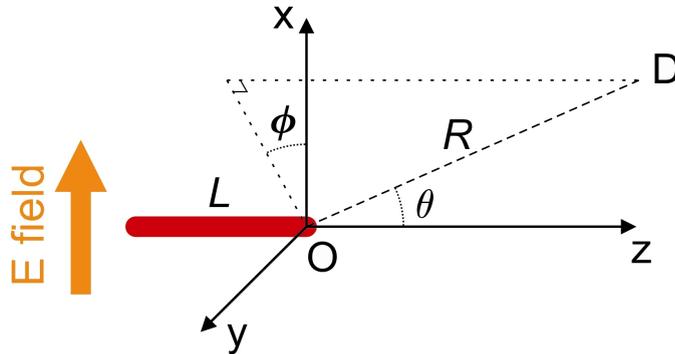
Figure 7.3: Schematic orientation of the filament and the coordinate axes. The transverse external electric field is applied in the direction parallel to the x-axis.

The distribution of the THz radiation from a filament in external transverse electric field can be obtained by the same procedure as in Chapter 5. We assume the external field to be high enough ($E_{ext} > 3$ kV/cm) and consider the electric current inside the filamentary plasma, which is directed mainly along the x-axis. Like in Chapter 5, we assume the distribution of the current to be the Dirac distribution, thus the current density can be written in the following form:

$$j_x(t) = j(t - nz/c)\delta(x)\delta(y). \tag{7.1}$$

Therefore, by taking the Fourier transform, one has:

$$\begin{cases} j_x(\omega) = j(\omega)\delta(x)\delta(y)e^{ikz}, \\ j_y(\omega) = 0, \\ j_z(\omega) = 0. \end{cases} \tag{7.2}$$

Here $j(\omega)$ represents a spectral component of the linear current density.

The equation (5.34) in the current case may be also solved using a convolution of the Green's function with the expression for the current density (7.2). One obtains the expression in the form of the Fresnel's diffraction integral:

$$A_\omega^{(x)}(\omega, x, y, z) =$$
$$= \frac{\mu_0}{4\pi} \int_{-\infty}^{\infty} \delta(x')dx' \int_{-\infty}^{\infty} \delta(y')dy' \int_0^L \frac{j(\omega)e^{ikz'}e^{ik\sqrt{(x-x')^2+(y-y')^2+(z-z')^2}}}{\sqrt{(x-x')^2 + (y-y')^2 + (z-z')^2}}dz'. \tag{7.3}$$

After the integration, one obtains:

$$\begin{cases} A_\omega^{(x)}(\omega, x, y, z) = \frac{\mu_0}{4\pi} \int_0^L \frac{j(\omega)e^{ikz'}e^{ik\sqrt{(x)^2+(y)^2+(z-z')^2}}}{\sqrt{(x)^2 + (y)^2 + (z - z')^2}}dz', \\ A_\omega^{(y)}(\omega, x, y, z) = 0, \\ A_\omega^{(z)}(\omega, x, y, z) = 0. \end{cases} \tag{7.4}$$

We can now calculate the components of electric and magnetic fields using the relations (5.29) and (5.35).

The approximation of the far field allows to simplify (7.4). We assume that the length of the filament (L) is much smaller than the distance to the detector (R), thus $A_x(\omega)$ may be rewritten as (in the same manner as in Chapter 5)

$$A_\omega^{(x)}(\omega, x, y, z) = \frac{\mu_0}{4\pi}j(\omega)\frac{e^{ikR}}{ikR}\frac{e^{ikL(1-\cos\theta)} - 1}{1 - \cos\theta}. \tag{7.5}$$

One can now write the components for the vector potential in the spherical coordinates (R, θ, ϕ) (see Figure 7.3):

$$\begin{cases} A_R = A_x \sin\theta \cos\phi, \\ A_\theta = A_x \cos\theta \cos\phi, \\ A_\phi = -A_x \sin\phi. \end{cases} \tag{7.6}$$

Using the equation (5.35)), one obtains:

$$V_\omega = -i\frac{\omega}{k^2}\frac{\partial A_x}{\partial x} \simeq i\omega\frac{\mu_0}{4\pi k^2}j(\omega)\frac{e^{ikR}}{R}\frac{e^{ikL(1-\cos\theta)}-1}{1-\cos\theta}\cos\phi\sin\theta, \tag{7.7}$$

where the terms $\sim 1/R^2$ are neglected.

Finally, using (5.29) we have the following expressions for the components of the emitted THz electric field, in the far field approximation.

$$\begin{cases} E_R = 0, \\ E_\theta = \dfrac{1}{4\pi}\sqrt{\dfrac{\mu_0}{\varepsilon_0}}j(\omega)\dfrac{e^{ikR}}{R}\cos\phi\cos\theta\dfrac{e^{ikL(1-\cos\theta)}-1}{1-\cos\theta}, \\ E_\phi = -\dfrac{1}{4\pi}\sqrt{\dfrac{\mu_0}{\varepsilon_0}}j(\omega)\dfrac{e^{ikR}}{R}\sin\phi\dfrac{e^{ikL(1-\cos\theta)}-1}{1-\cos\theta}. \end{cases} \tag{7.8}$$

The expressions for the magnetic field components can be found as well:

$$\begin{cases} B_R = 0, \\ B_\theta = \dfrac{1}{4\pi c}\sqrt{\dfrac{\mu_0}{\varepsilon_0}}j(\omega)\dfrac{e^{ikR}}{R}\sin\phi\dfrac{e^{ikL(1-\cos\theta)}-1}{1-\cos\theta}, \\ B_\phi = \dfrac{1}{4\pi c}\sqrt{\dfrac{\mu_0}{\varepsilon_0}}j(\omega)\dfrac{e^{ikR}}{R}\cos\phi\cos\theta\dfrac{e^{ikL(1-\cos\theta)}-1}{1-\cos\theta}. \end{cases} \tag{7.9}$$

In (7.8) and (7.9) ω, L, k represent the frequency of the considered THz component, the length of the filament, and the THz wavenumber, respectively. R is the distance from the filament to the detector, θ is the polar angle and ϕ is the azimuthal angle (spherical coordinates) (see Figure 7.3). The expression for the spectral current amplitude can be obtained similarly to that in the wake-field created by the laser ponderomotive force considered in Chapter 5 and reads ([Houard 08c]):

$$j(\omega) = \frac{\varepsilon_0 E_{ext}\omega_{pe}^2}{\omega^2 - \omega_{pe}^2 + i\nu_e\omega}, \tag{7.10}$$

where E_{ext} is the external static electric field, $\omega_{pe} = \sqrt{e^2 n_e/m_e\varepsilon_0}$ is the electron plasma frequency, ν_e is the electron collision frequency.

In the presence of an applied transverse field, the THz radiation pattern gradually evolves from a conical pattern to a single lobe forward oriented emission. A 3D emission diagram for the single filament is presented in Figure 7.4(a). We have verified the THz intensity angular dependence in experiment using a heterodyne detector operating at $\sim$ 0.1 THz, the corresponding data is presented in Figure 7.4(b) for the detector rotating in the XOZ plane, 30 cm away from a 1-cm-long filament.
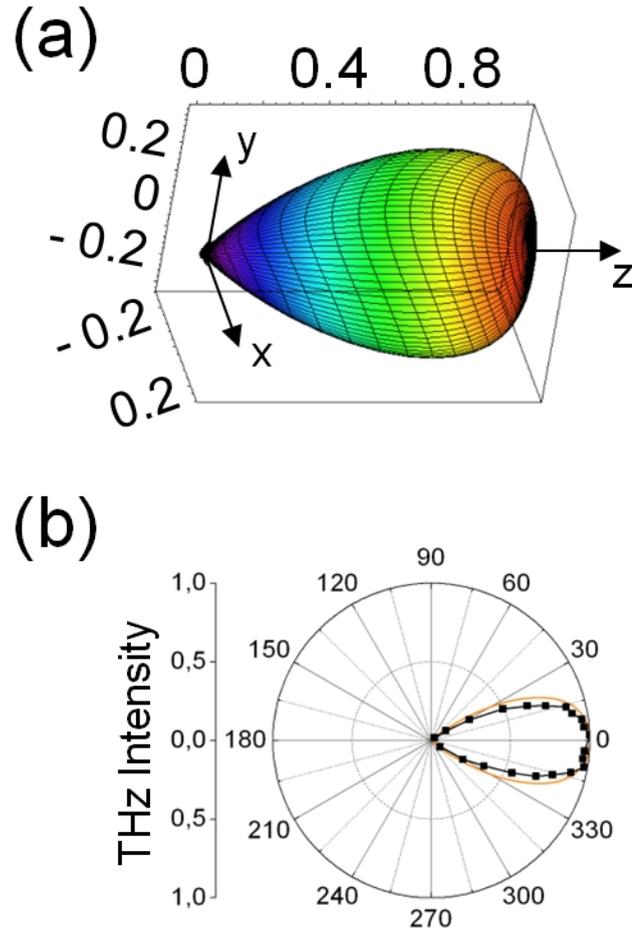
Figure 7.4: (a) Calculated THz radiation pattern at 91 GHz from a single 1-cm-long filament in transverse external electric field applied toward the x-axis. (b) Emission diagram of the THz radiation in the XOZ plane from a single filament in transverse external electric field (E_{ext} = 4 kV/cm). Black points: experimental results. Solid line: calculation.

The Poynting vector of the THz emission scales like:

$$
\begin{aligned}
\bar{S} =& \frac{1}{2\mu_0} \left(E_\theta B_\phi^* - B_\theta^* E_\phi \right) = \\
=& \frac{1}{128\pi^2} \sqrt{\frac{\mu_0}{\varepsilon_0}} \left(\frac{\cos^2\theta \cos^2\phi + \sin^2\phi}{(1-\cos\theta)^2} \right) \frac{1}{R^2} \sin^2 \left(\frac{L\omega}{2c}(1-\cos\theta) \right) \times |j(\omega)|^2 ,
\end{aligned}
\tag{7.11}
$$

therefore the intensity of THz emission depends on external electric field like E_{ext}^2. In [Houard 08c] the quadratic dependence of the energy of the THz radiation on external electric field has been verified experimentally.

Polarization of the THz emission

As mentioned above the THz emission from a single filament in transverse external electric field was observed to be linearly polarized in the direction of the applied external electric field [Houard 08c]. We have calculated the x-, y- and z- components of the total THz field in this case. The three field components are expressed by:

$$\begin{cases} E_x = -i\omega A_x(\cos^2\phi\sin^2\theta - 1), \\ E_y = -i\omega A_x\cos\phi\sin^2\theta\sin\phi, \\ E_z = -i\omega A_x\cos\phi\sin\theta\cos\theta, \end{cases} \qquad (7.12)$$

where A_x is defined by 7.5.

The x-, y- and z- components of the total THz field are calculated and the corresponding intensities are visualized in Figure 7.5. The x-component dominates among the three polarization components. The THz emission thus may be considered as linearly polarized in the direction parallel to the external electric field.
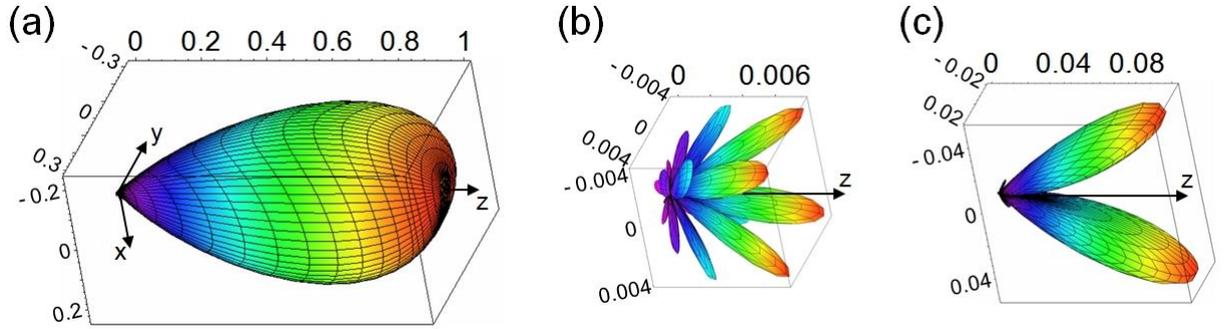
Figure 7.5: (a)-(c) Calculated THz radiation patterns for x-, y-, z- components of the polarization of the THz radiation from a single filament in transverse external electric field, respectively. The external electric field is applied toward the x-axis.

Multiple parallel filaments in transverse electric field

The model can be extended to the case of N identical filaments. The interference of the THz fields will give:

$$\bar{S}^{total} \simeq \left|\sum_{i=1}^{N} E_\theta(R_i,\theta_i,\phi_i)e^{i\xi_i}\right|^2 + \left|\sum_{i=1}^{N} E_\phi(R_i,\theta_i,\phi_i)e^{i\xi_i}\right|^2, \qquad (7.13)$$

where ξ_i is the accumulated phase difference of the THz field due to the temporal delay τ_i between the filamentary laser pulses and R_i is the distance from the ith filament emitter to the detector.

The normalized calculated 3D distribution of the THz field from two parallel filaments in transverse static electric field is presented in Figure 7.6. An enhancement of the THz intensity by a factor 4 is achieved comparing with the case of the single filament in the

presence of the same applied field (see Figures 7.4(a) and 7.6(a)). Note that varying of the temporal delay τ_p between the two filament-forming laser pulses leads to significant changes in the radiation diagram. For instance, the calculated result for two parallel filaments with temporal delay $\tau_p = 5.5$ ps is presented in Figure 7.6(b). The direction of the THz radiation is completely different from that of the laser pulses, forming two lobes on the two sides from the filament axes.
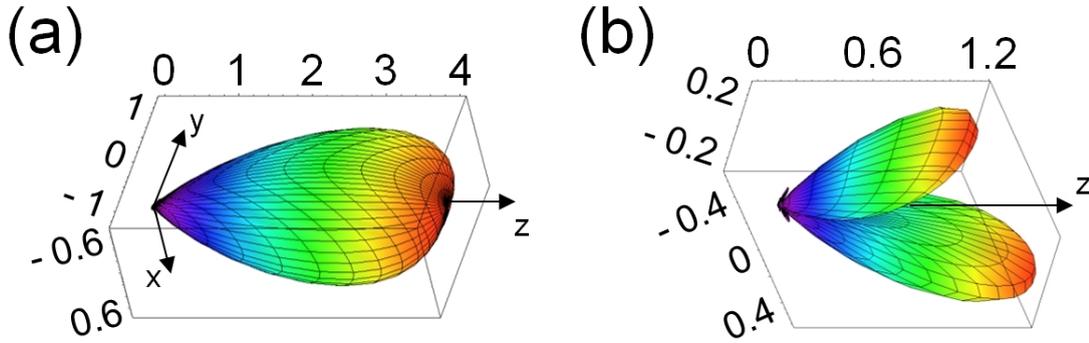
Figure 7.6: Calculated THz radiation diagrams at 91 GHz from two parallel filaments separated by 2 mm without temporal delay between the filamentary laser pulses (a) and with the temporal delay $\tau_p = 5.5$ ps (b).

7.3 Experimental results and discussion

We now compare our calculations with experimental measurements. We study experimentally how the THz emission depends on the variations of temporal delay τ_p and spatial separation d between two parallel filaments in the presence of a transverse electric field. In our experiments, a femtosecond laser system delivering 46 fs pulses with energy up to 12 mJ at 800 nm was employed. The experimental setup is similar to that described in the previous chapter (see Figure 6.1) except for the application of static transverse electric
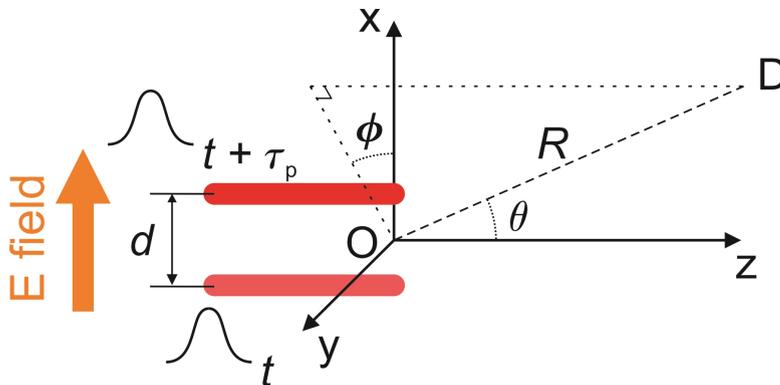
Figure 7.7: Scheme of spatial orientation of the two parallel filaments and the direction of the transverse electric field. The filaments are separated laterally by a variable distance d, and τ_p is the adjustable temporal delay between the two filamentary pulses.

field. We used a Mach-Zehnder interferometry scheme to obtain two parallel propagating laser pulses. The spatial separation and temporal delay of the two pulses could be controlled by a steering mirror of the interferometer and an integrated mechanic delay line. The two pulses with equal energy of 1.1 mJ were focused with two convex focusing lenses of $f = 100$ cm to form two 1-cm-long parallel, laterally separated filaments in ambient air. The forward THz radiation was detected by a heterodyne detector working at 91 GHz. The distance between the filaments and the detector was around 30 cm. In our experiment the detector measures only the component in the plane of the two filaments (which is the XOZ plane in the current case, see Figure 7.7). The static electric field was applied to the ionized region transversally by placing two electrodes around the filaments. The electrodes were square copper plates with dimensions of 5 cm $\times$ 5 cm. We have studied two cases: when the direction of the electric field is parallel (configuration A) or perpendicular (configuration B) to the plane defined by the filaments. The applied DC-electric field was 4 kV/cm.

We first studied the interference of two synchronized ($\tau_p = 0$) THz fields for different spatial separations in configuration A. The results are presented in Figure 7.8. Upon increase of the spatial separation d, the THz radiation pattern becomes narrower, but remains symmetric about the propagation direction of the laser pulses. Note that there is no decrease of the THz intensity within the range studied here. This differs from the results obtained in the absence of an electric field (see Figure 6.2), where the THz intensity starts to decrease with the increase of the spatial separation between filaments.
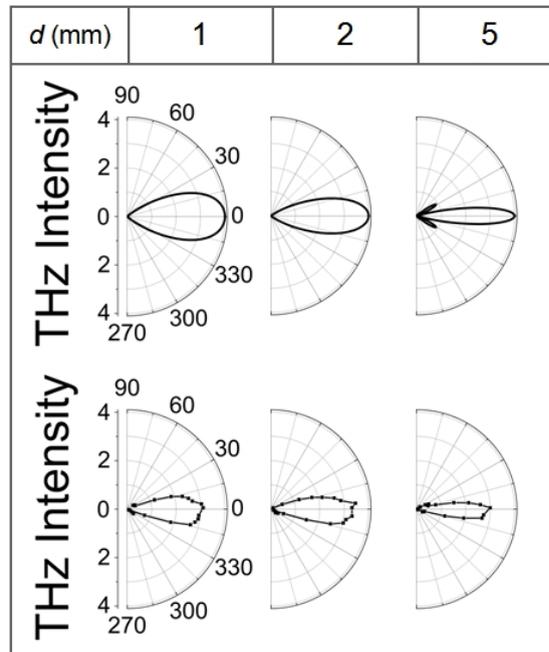
Figure 7.8: Emission diagrams of the THz radiation at 91 GHz obtained from two filaments as a function of lateral spatial separation d. The measurements were performed in the plane of the filaments (XOZ plane). Top row: calculations. Bottom row: experimental results. The THz intensity is normalized to the peak THz intensity of a single filament.

We attribute this to the different size of the intersection areas of two THz radiation patterns from each individual filament with and without external electric field. Without external electric field the THz emission from a filament has a narrow conical distribution, thus the overlap of the THz radiation patterns from two filaments is a sensitive function of separation between them. With the transverse electric field, the broader forward lobe allows larger filament separations while interference of the THz emissions is still present.

Next we studied the interference of two synthesized THz fields for different values of the temporal delay τ_p with a fixed spatial separation $d = 2$ mm between the two filaments, always in configuration A. The results are presented in Figure 7.9. Upon increase of the delay τ_p, the total radiation pattern becomes asymmetric, alternatively directed to either side of the filament propagation direction. The change in direction reflects the partial destructive interference between the THz fields due to the phase shift induced by the delay. At the same time, the total THz radiation decreases. Finally ($\tau_p = 5.5$ ps), the total THz radiation pattern comes to near complete cancelation of the THz field, keeping only two small lobes in the non-intersection area. Eventually, for $\tau_p = 11$ ps, the THz radiation recovers the value without the delay. Note that the strongest enhancement of THz radiation is always achieved with no temporal delay. By changing the temporal delay one can redirect the THz radiation along another direction that is not collinear with the laser beams. However, in most cases, the peak intensity decreases.
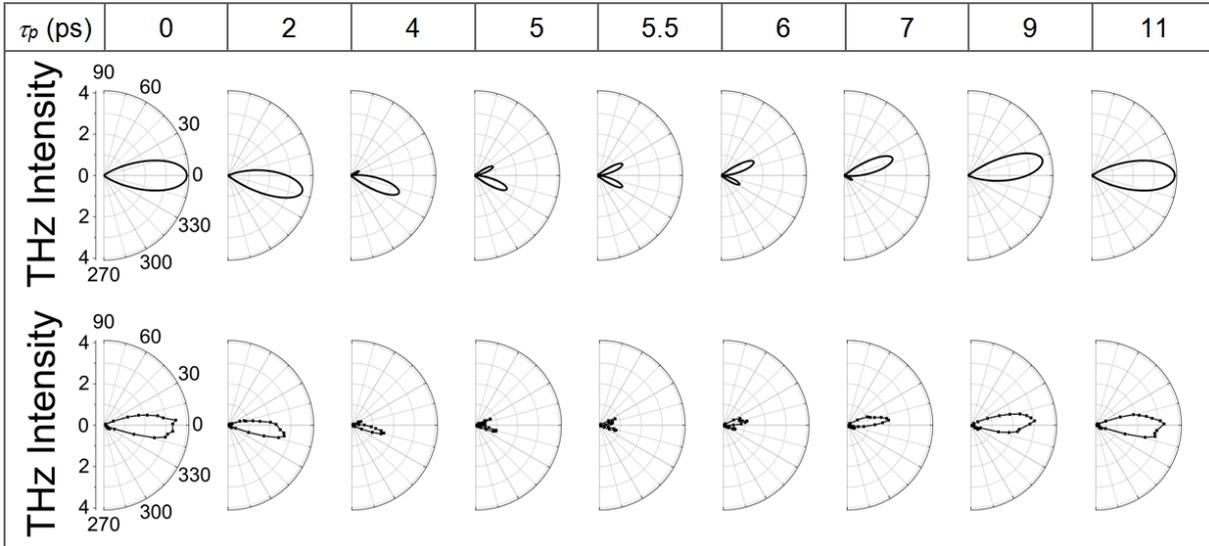
Figure 7.9: Evolution of the emission diagram of the THz radiation in the plane of filaments, as a function of the temporal delay between the two laser pulses. The two filaments are separated by $d = 2$ mm. Top row: calculations. Bottom row: experimental results.

We have also studied the case of configuration B, when the direction of the transverse external electric field is perpendicular to the plane of filaments and found results similar to the ones presented in Figures 7.8 and 7.9.

Extrapolation to the case of N parallel filaments

We have calculated the THz radiation distribution further for $N = 4, 8, 9, 12$ and 16 parallel filaments organized in a square grid in the presence of an external transverse electric field (see an example in Figure 7.10). THz emissions from individual filaments interfere constructively with each other if there is no temporal delay between the filamentary laser pulses. The total THz energy is channeled along the direction of the laser.
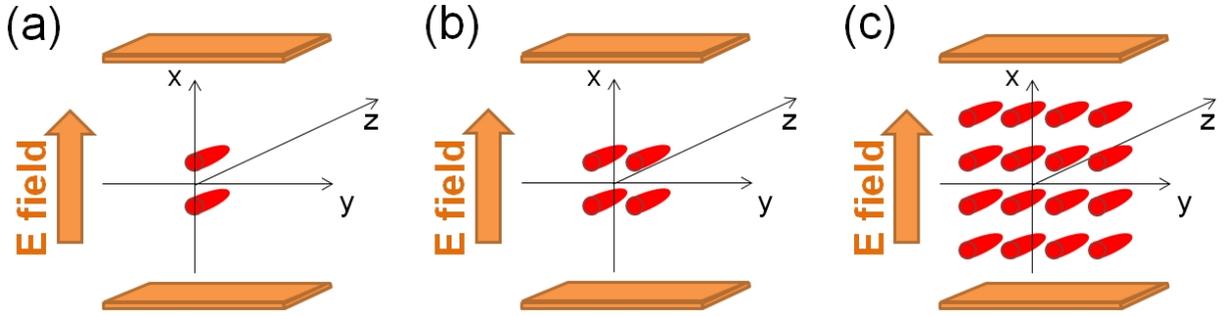
Figure 7.10: Spatial orientation of (a) 2, (b) 4, and (c) 16 filaments we used in our calculations.

The corresponding THz peak intensity scales like N^2, as shown in Figure 7.11. The 3D distribution of the THz radiation for 2, 4 and 16 parallel filaments is presented in Figures 7.12(a)-(c), respectively. The peak intensity in the case of 16 parallel filaments is found to be ~ 250 times larger than that of a single filament in the presence of the same external electric field and more than 10^5 times higher than that of a single filament without application of the external electric field. In principle, with a larger number of filaments, the THz peak intensity may be increased further.
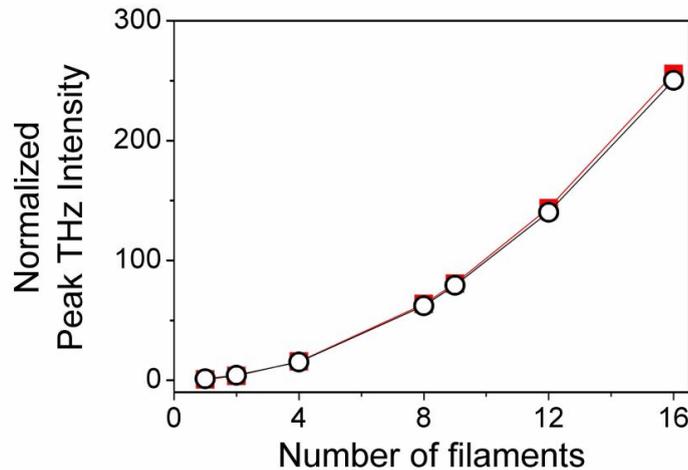
Figure 7.11: Dependence of the peak THz intensity on the number of filaments. Squares – theoretical upper limit (quadratic dependence), Circles – maximum value obtained in our calculations.
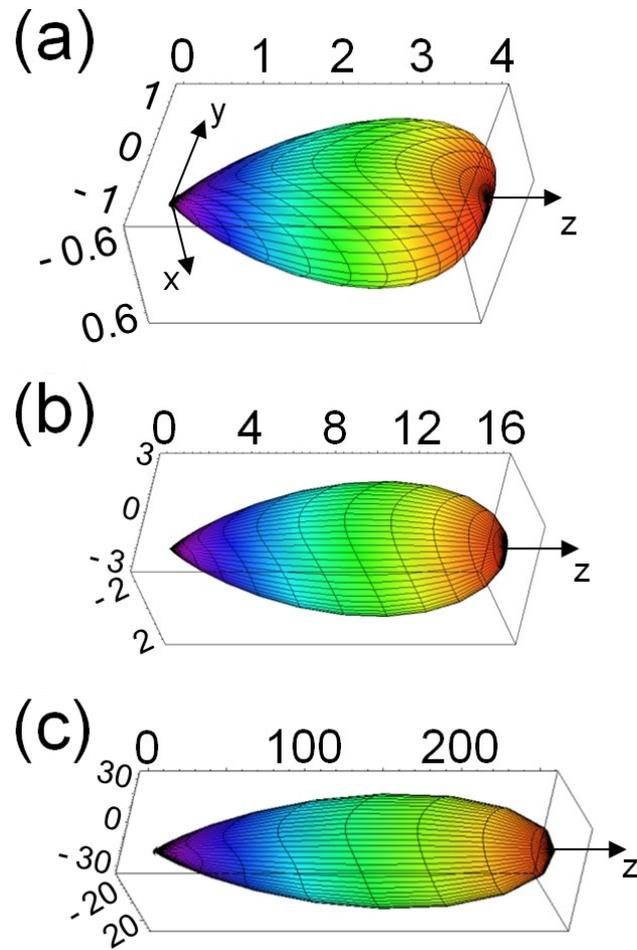
Figure 7.12: Calculated THz radiation diagrams at 91 GHz from: (a) two parallel filaments separated by 2 mm without temporal delay between the filamentary laser pulses, (b) a square matrix of 4 parallel filaments separated by 2 mm without temporal delay, (c) a square matrix of 16 parallel filaments separated by 2 mm without temporal delay. Spatial orientations of filaments is presented in Figure 7.10.

Simulations at other THz frequencies

Above, we have considered the THz emission at a frequency of ~ 0.1 THz, because it corresponds to the spectral component measured by our detector. However the THz emission from filaments peaks at higher frequencies. In Figure 7.13 we show the temporal waveform of a THz pulse and the corresponding spectrum obtained from a 5-mm-long filament in air in the presence of an external electric field of 8 kV/cm. The THz waveform was obtained by the standard time domain THz spectroscopy system based on a 1-mm-thick ZnTe crystal (see Appendix A). The maximum of the THz power spectrum is at 0.5 THz. We therefore calculated the emission pattern at this frequency. In Figure 7.14(b) the result for 0.5 THz is presented for two parallel filaments separated by 500 μm. Such spatial separation was chosen to keep the ratio d/λ on the same order as for 0.1 THz (d is the spatial separation between filaments, λ is the wavelength of the THz emission).
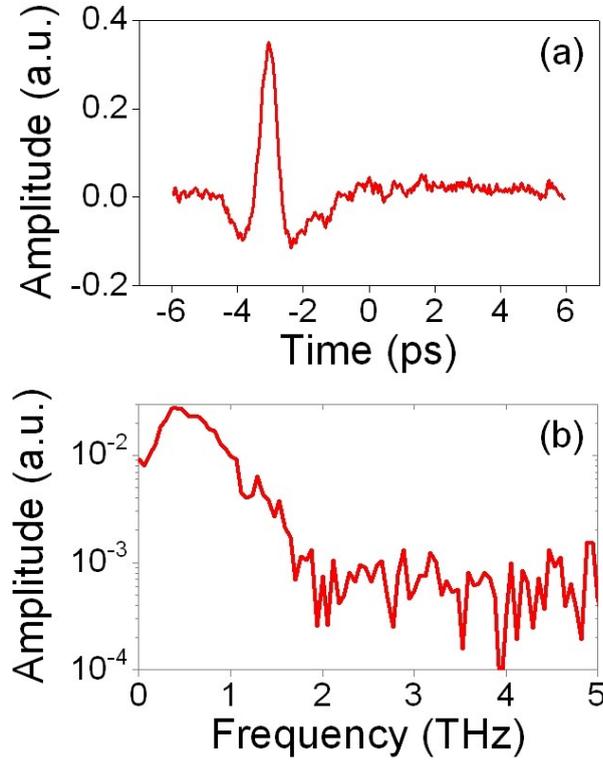
Figure 7.13: (a) Temporal waveform of a THz pulse, emitted by a filament in air in the presence of an external electric field of 8 kV/cm, measured by the time domain THz spectroscopy system. The filament was induced by focusing 2 mJ, 50 fs, 800 nm laser pulses with an $f = 20$ cm lens. (b) Corresponding spectrum of the THz field below 5 THz.

This parameter is important for the constructive interference. The THz radiation pattern becomes narrower with higher THz frequency and thus the intersection area of two THz emission from two filaments decreases, if the separation between the filaments is fixed. For $\tau_p = 0$ ps, the peak THz intensity is 4 times larger than that of a single filament with the same external field (see Figure 7.14(a)), showing again complete constructive interference when there is no temporal delay between the laser pulses. The behavior with an increasing temporal delay between the laser pulses is similar to that of the case presented in the Figure 7.9. It is periodic, but the period is different. The period corresponds to $1/\nu_d$, where ν_d is the considered THz frequency. In Figure 7.14(c) the result for $\tau_p = 1$ ps is presented as an example.

We have also calculated the THz radiation distribution at 0.5 THz from N parallel filaments, in Figure 7.14(d) the result for an array of 16 filaments is shown. We emphasize that the strong enhancement of THz emission from an array of parallel laser filaments in the presence of a transverse static electric field is achieved **for all THz frequencies at the same time** because the condition of zero temporal delay needed for the constructive interference applies at every frequency.
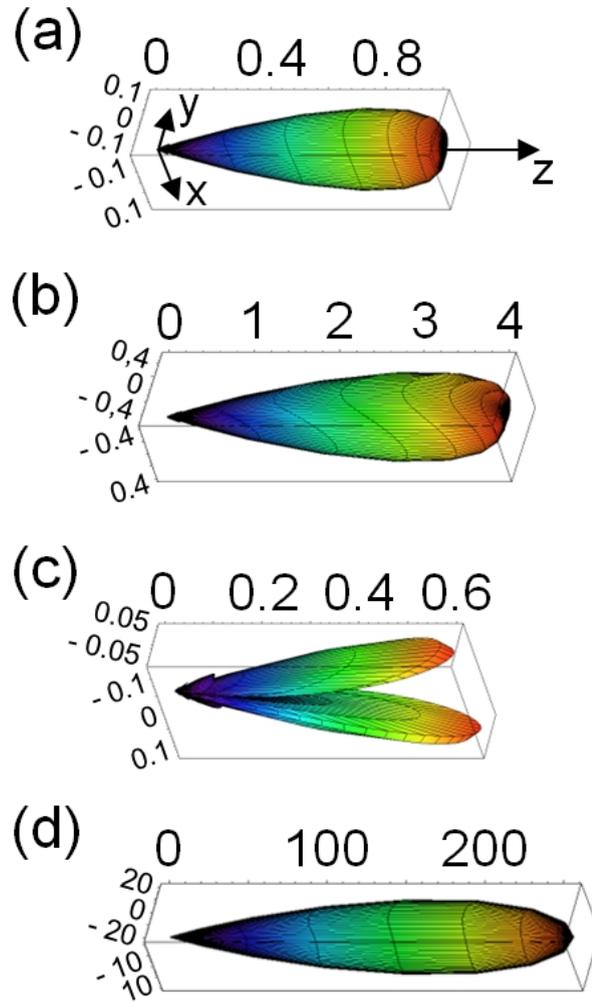
Figure 7.14: Calculated THz radiation diagrams for the frequency of 0.5 THz from: (a) single filament, (b) two parallel filaments separated by 500 μm without temporal delay between the filamentary laser pulses, (c) two parallel filaments separated by 500 μm with a time delay $\tau_p = 1$ ps, (d) a square matrix of 16 parallel filaments separated by 500 μm without temporal delay between the filamentary laser pulses.

7.4 Conclusion

In summary, we have discussed the THz emission from femtosecond laser filaments in air under the combination of two effects: the application of static electric field and the organization of filaments into an array. An enhancement of THz radiation is found, scaling like E_{ext}^2 in the presence of a static transverse electric field and scaling like N^2 with N laser filaments organized in an array. With no temporal delay between the laser pulses forming the filament array, the enhancement is the same at every THz frequency, leading to strong broadband THz radiation in the forward direction. It is also possible to direct the THz emission along preferential directions by playing with the time delay between the laser pulses.

General conclusion

In the thesis, the author's work performed at the Laboratoire d'Optique Appliquée of École Polytechnique during 3 years of the PhD enrollment is presented. It is mainly devoted to the study of the secondary radiation from femtosecond laser filaments: Ultraviolet luminescence, backward stimulated emission and Terahertz radiation emitted by plasma filaments. The obtained results are interesting in both points of view of fundamental science and potential applications.

In the first part, we have presented a simple technique for direct experimental determination of the laser fluence and intensity inside a plasma filament. It is based on the measurement of the laser energy transmitted through a variable diaphragm fabricated by a filament itself on a thin metallic foil with cumulative laser irradiation. Once the transmitted energy and the corresponding diaphragm size are measured, one can directly calculate the laser fluence inside the filament. With an additional measurement of the pulse duration, the intensity value can be estimated. A longitudinal scan along the filament provides a 2-dimensional characterization of the filamentary laser intensity. For a 1-mJ-energy laser pulse the peak intensity inside filament was measured to be $\approx 1.44 \times 10^{14}$ W/cm^2, 2-3 times larger than those previously reported for similar experimental conditions. We attribute this to an attainable spatial resolution of our method (≈ 50 μm) which is much less than the filament diameter (≈ 150 μm). The obtained value of the laser intensity inside filaments allowed us to explain our findings presented in the second part. Our simple technique could find application in other intense laser-matter interaction experiments where measurements of laser intensity distribution is desired, such as in high-order harmonic generation or laser surface ablation.

In the second part, we have concentrated on the plasma luminescence and the stimulated emission of laser filaments in air and nitrogen gas. We have demonstrated that the luminescence emitted by neutral and singly ionized nitrogen molecules depends strongly on the polarization state of the incident laser pulses. In the lower laser intensity regime ($I < 3 \times 10^{13}$ W/cm^2), the emission from both neutral and ionic N$_2$ molecules is found to be stronger with linearly polarized laser than with circular laser polarization. At higher laser intensity ($I = 1.45 \times 10^{14}$ W/cm^2), a circularly polarized laser pulse produces more luminescence signal from the excited neutral N$_2$ molecules while the luminescence of N$_2^+$ molecules is found to be insensitive to laser polarization. For lower laser intensity, the predominance of the luminescence from both species with linearly polarized pump is explained by the higher optical field ionization rate. At higher laser intensity, electron collision-assisted excitation routes become available, due to the presence of free electrons

with high kinetic energy left after the laser pulse. This collision-assisted mechanism leads to an increase of population in the excited triplet state through direct collision excitation from neutral molecules in the ground state with energetic electrons. For a laser intensity reaching 10^{14} W/cm^2, it is also believed to increase the population of the excited ionic state.

We have analyzed the fluorescence in the backward direction and obtained a strong stimulated radiation at 337 nm from plasma filaments in atmospheric-pressure nitrogen gas pumped by a circularly polarized 800 nm femtosecond laser pulses. Existence of the stimulated radiation is confirmed by the distinct dependence of the backward ultraviolet spectrum on the incident laser polarization and intensity, the observed beam profile, and the polarization property of the emission. We attribute the mechanism responsible for the population inversion to inelastic collision between electrons liberated by the laser and neutral nitrogen molecules. As in the case of plasma luminescence, this process is more efficient with circularly polarized laser pulses.

To further confirm the existence of population inversion, we have injected a seeding pulse (with a wavelength around 337 nm) in the opposite direction of the pump laser pulses. The enhancement of the backward radiation intensity by a factor of ~ 16 was observed. The amplified lasing radiation inherits the polarization property of the seeding pulse, and its divergence angle was found to be around 3.8 mrad, much less than that of the backward ASE. The critical role of the pump laser polarization was also observed in the seeded lasing regime, where intense lasing effect was only possible for circularly polarized pump pulses. We believe that our findings on the filamentary plasma luminescence as well as the proposed scheme for backward stimulated emission from filaments induced by the widely available 800 nm femtosecond laser pulses can find potential applications in remote sensing of atmosphere and characterization of electric field or THz radiation at a long distance.

In the third part of the thesis, we have discussed the coherent synthesis of THz radiation from an array of N parallel femtosecond filaments. This provides a simple technique to scale up the THz intensity with high power femtosecond laser since the total THz intensity is proportional to N^2. With appropriate temporal delay between the filamentary laser pulses, the THz emission can be directed along a preferential direction away from the laser propagation axis, which is of a high interest for remote THz applications. Our experimental results agree well with the numerical simulation. We have also examined another geometric configuration of filaments in the form of a 'Vee-antenna'. Such 'V-oriented' filaments exhibit an interesting property to produce circularly polarized THz emission.

Next, we have studied the effect of an external electric field (E_{ext}) on the coherent synthesis of the THz radiation from an array of parallel filaments. The THz radiation was shown to scale like E_{ext}^2 in the presence of a static transverse electric field along with a scaling up as N^2 for N parallel filaments organized in an array. With zero temporal delay between the filament-forming laser pulses, the enhancement is achieved at every THz frequency, leading to strong broadband THz radiation in the forward direction of the laser propagation axis. It is also possible to direct the THz emission along the preferential direction by tuning the temporal delay between the laser pulses.

Appendices

Appendix A

Detection of Terahertz radiation

During the PhD study, we have built and tested several methods for the THz detection. These schemes include the traditional heterodyne detection and the electro-optic sampling method, as well as the THz detection based on the second harmonic generation in air plasma. In this appendix the detailed results are presented.

THz detection schemes are largely classified as either coherent or incoherent techniques. The fundamental difference is that for incoherent detection of electro-magnetic radiation one measures the intensity of an electric field or an emitted energy, whereas coherent detection allows to measure both the amplitude and the phase of the electric field (and their temporal variations). Coherent detection techniques are closely associated with generation techniques in that they share underlying mechanisms and key components. In particular, optical techniques utilize the same light source for both generation and detection.

A.1 Incoherent detection with heterodyne detector

The detection of an electromagnetic radiation is called *incoherent* when one detects the intensity or the energy of the radiation. Commonly used systems of incoherent detection are based on the principles of electronics (Schottky diodes), opto-acoustics (Golay cell), calorimetry (Bolometer, pyroelectric detector).

The heterodyne detection is commonly used in telecommunications, astronomy and microwave domain. It permits to measure continuous monochromatic radiation with high sensitivity. In heterodyne detector, a signal of interest at a given frequency is non-linearly mixed with a reference "local oscillator" that is set to a close-by frequency. A Schottky diode mixer is commonly used for THz detection.

In the experiments we use a heterodyne detector operating at 91 GHz with a bandwidth of 4 GHz, it thus corresponds to the lower limit of the THz band. Only a linearly polarized component of the THz radiation is measured. The functioning of the heterodyne detector is described in more detail in [Tzortzakis 02]. The response time of the detector is on the $1-10$ nanosecond order, typical signal measured by the detector is presented in Figure

A.1(b). In our experiments the detector is placed on a specially designed rotation stage allowing the movement of the detector around a filament in the plane parallel to the optical table. The rotation of the detector around its axis is possible as well, this allows the THz polarization measurements.
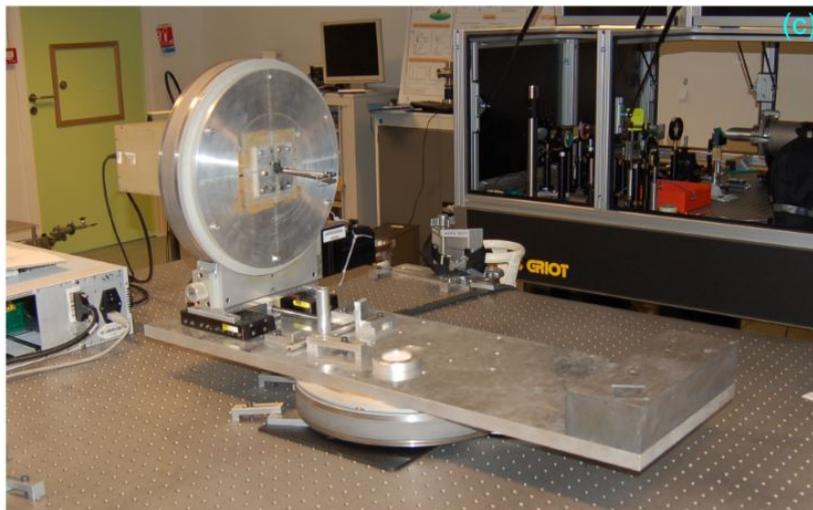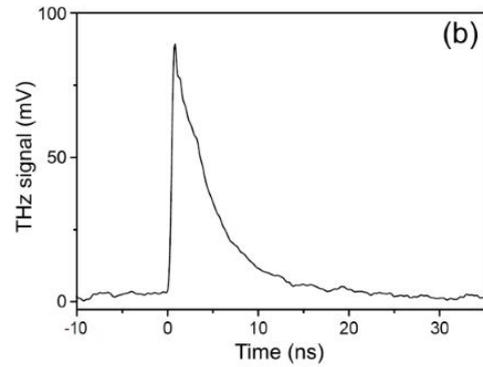

Figure A.1: (a) Photo of the heterodyne detector used in the experiments. (b) A typical THz signal measured by the detector. (c) Photo of the detector fixed on the rotation stage.

A.2 Coherent detection

The detection of the electric field of a coherent light pulse is a very important unique feature of the THz frequency range (no other method to measure the temporal variation of the electric field of the optical wave is yet available). For the coherent THz detection a non-linear effect proportional to the THz electric field should be induced on an ultrashort laser pulse. By characterization of the polarization modification of the laser pulse one obtains the amplitude of the temporally coincident THz field. A laser pulse with the duration of 50 fs is much shorter than a THz pulse (the order of 1 ps), and by tuning the temporal delay between the two pulses (with construction of a delay line) one obtains the total evolution of the field $E_{THz}(t)$.

Electro-optic sampling

Electro-optic sampling uses the Pockels effect [Pockels 94] (also called linear electro-optic effect), which describes the change in the refractive indices of a material proportional to the applied electric field. This effect occurs only in crystals without inversion symmetry [Yariv 89]. The detection of THz radiation by electro-optic sampling technique was presented for the first time in 1995 by Wu and Zhang [Wu 95]. After that time it was used in numerous studies. The most frequently used electro-optic crystal is zinc telluride (ZnTe) [Wu 96, Cai 98, Planken 01], it has the important feature that for frequencies around 1 THz the THz pulse velocity is equal to the group velocity of the radiation of the commonly used Ti:Sapphire laser (wavelength is around 800 nm), thus it is possible to use rather thick crystals yielding large signals. However, because of its optical phonon resonance, ZnTe can only be used for THz frequencies up to 4 THz and for frequencies above 8 THz. For a higher bandwidth (up to 8 THz) one can use gallium phosphide (GaP) [Wu 97, Bartel 05]. Other materials used in experiments are lithium niobate (LiNbO3) [Winnewisser 97], gallium arsenide (GaAs) [Cao 02, Nagai 04], diethylaminosulfur trifluoride (DAST) [Schneider 07], poled polymers [Cao 02], *etc.* The electro-optic effect may be described in the terms of the inverse dielectric tensor ϵ^{-1} [Reimann 07]. With the presence of an electric field changes from its no-field value $\epsilon^{-1}(0)$:

$$\epsilon^{-1}(\mathbf{E}) = \epsilon^{-1}(0) + r\mathbf{E}, \tag{A.1}$$

where r is the electro-optic tensor of a third rank, the form of which is determined by the crystal symmetry. For example, crystals with symmetry of the zinc-blende type (ZnTe, GaAs) have only one non-zero independent tensor component $r_{xyz} = r_{yzx} = \ldots$ (i.e. only the components with all different indices). Without an electric field the inverse dielectric tensor is the same as for an isotropic medium, an intense THz pulse induce an instant birefringence in the crystal which is directly proportional to the field $E_{THz}(t)$. For the crystal oriented for (110) one obtains the largest effect if the THz field is polarized parallel to $(1\bar{1}0)$ [Planken 01]. The inverse dielectric constant is different between the $(1\bar{1}\sqrt{2})$ and the $(\bar{1}1\sqrt{2})$ polarization directions. As soon as femtosecond laser pulse is send at the same time as the THz pulse, in the crystal it undergoes a phase delay $\Delta\phi$ between directions of

its polarization components. The delay is proportional to the THz field [Dragomar 04]:

$$\Delta\phi = \frac{2\pi d}{\lambda}n_0^3 r_{xyz}E_{THz}(t), \tag{A.2}$$

there λ is the vacuum wavelength of the laser pulse, n_0 is the refractive index at this wavelength, r_{xyz} is the electro-optic coefficient of the crystal and d is the thickness of the crystal. Note, that the equation (A.2) is valid only if the group velocity of the probe pulse v_g equals the phase velocity of the THz pulse v_p, this gives a limitation on the thickness of the crystal (it should be considerably less than the coherence length $l_{coh} = c\lambda_{THz}|v_p^{-1} - v_g^{-1}|$). The phase delay $\Delta\phi$ is most often measured with the setup presented in Figure A.2.
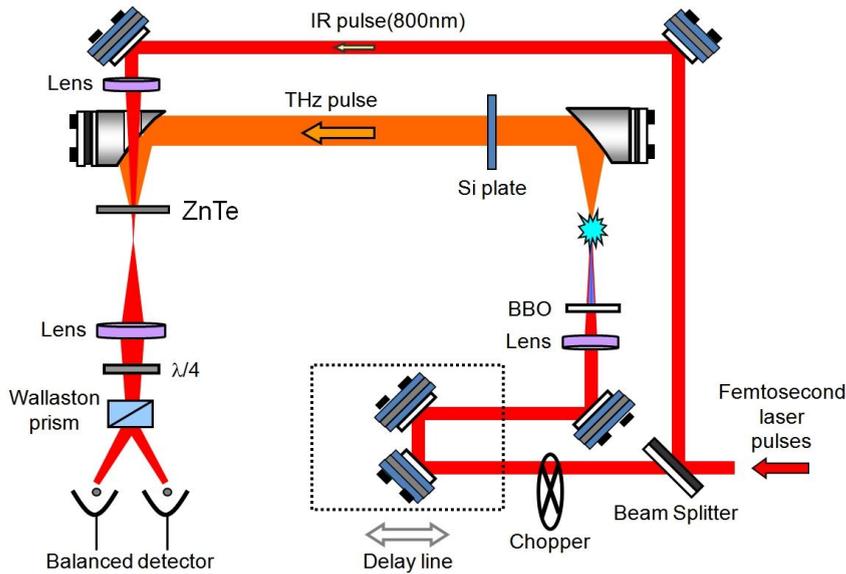
Figure A.2: Schematic layout of the electro-optic sampling system for THz measurements.

Passing through the crystal, polarization of the laser pulse remains linear without THz field. Next the pulse comes to the quarter-wave plate at 45°, which transforms the polarization to circular. After this, a Wallaston prism (WP) splits the horizontal and the vertical components of the polarization. The two beams from WP are detected by two photodiodes (PD). An electronic circuit measures precisely the difference of the signals on the two PDs. The difference equals zero without the THz field because the beam which comes to WP is circularly polarized. In the presence of THz field the crystal exhibits birefringence and the probe beam becomes elliptically polarized before entering the WP, so on the signal measured by one PD (I_1) becomes bigger than that measured by the second PD (I_2). Considering the phase difference of 90° induced by the quarter-wave plate, the difference of the signals of the two DPs is proportional to the sine of the phase difference $\Delta\phi$:

$$\frac{I_1 - I_2}{I_1 + I_2} = \sin(\Delta\phi). \tag{A.3}$$

THz detection via electro-optic sampling in ZnTe crystal

For our work we have built a new EO sampling system based on a 1-mm-thick (110) ZnTe crystal. The general layout of this system is presented in Figure A.2. This system was built on a 1000 mm × 1500 mm optical breadboard. Therefore, it can easily be moved from one laser system to another without complicated alignment requirement. A new data acquisition software has been developed by the engineer of our lab (Pierre Zaparucha), piloting the new stepping motor with a 20 nm resolution and the fast data acquisition card. Photography of the optical part of this system is shown in Figure A.3. To optimize the system, we always start with the THz generated by the two-color (800 nm and 400 nm) method. We have found that the two-color method typically produces ~ 100 times more intense THz field than that driven by a single 800 nm pulse.
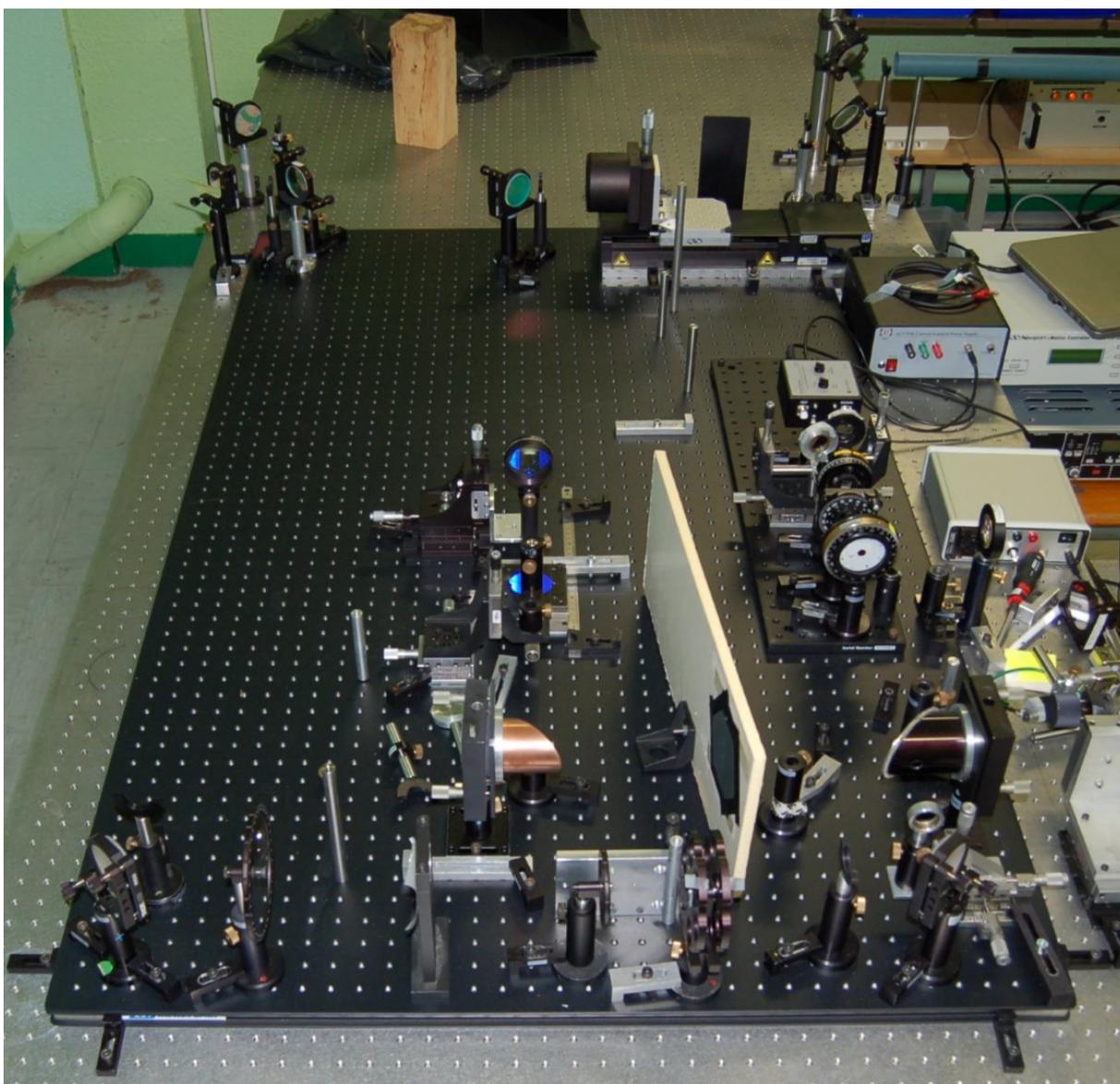
Figure A.3: Photo of the THz EO sampling setup built during the PhD study.

After optimization of the optical and electronic systems, we have obtained a THz signal with a signal to noise ratio (SNR) around 7000, as presented in Figure A.4. This data was obtained with a lock-in time constant of 300 ms with a 10 scans averaging. We note also that with the new stepping motor, one scan of 500 data points can be achieved in 2 minutes, so the data may be collected in a short time.
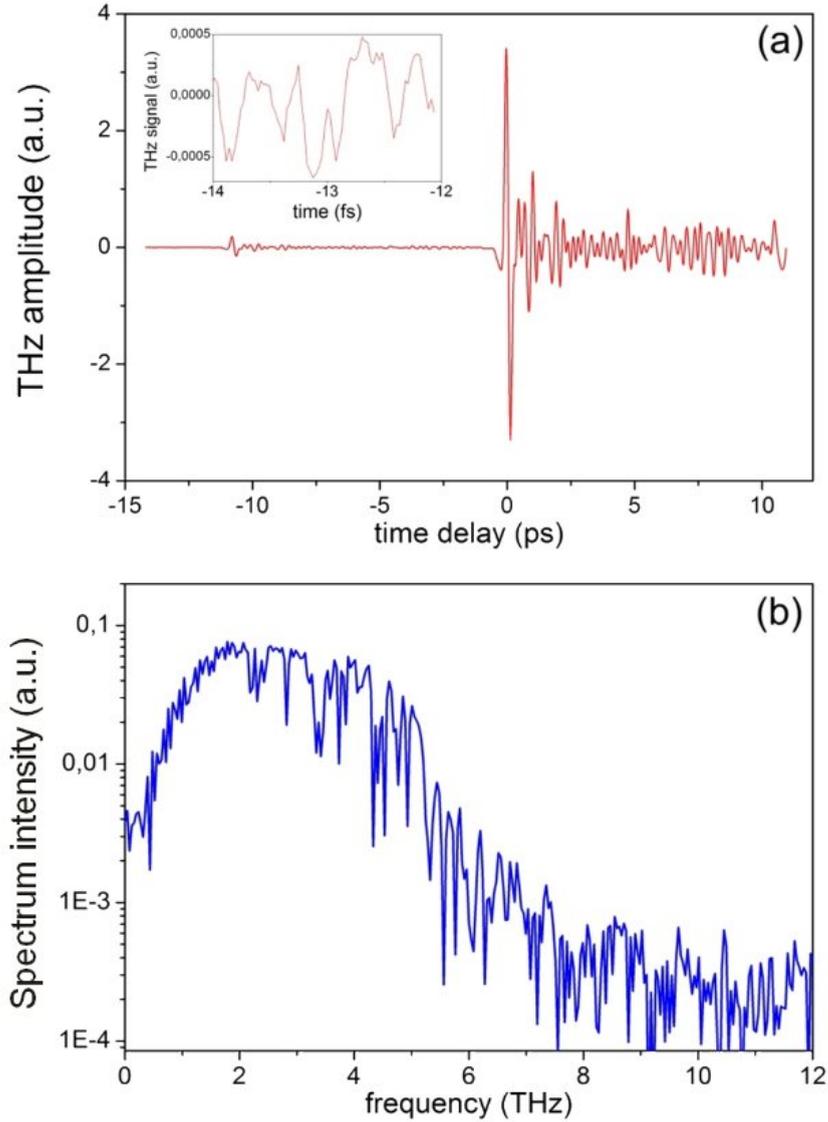
Figure A.4: (a) THz waveform obtained with our newly built THz EO sampling system. The inset shows the noise level between -14 ps and -12 ps. The weak peak around -11 ps is due to the presence of a pre-pulse in the laser system. (b) Corresponding spectrum obtained by Fourier transform. The cut-off observed around 5 THz is due to the intrinsic absorption of the ZnTe crystal.

Figure A.4(b) shows the THz spectrum obtained by taking the Fourier transform of the waveform in Figure A.4(a). The bandwidth of the detection extends up to around 4 THz, which is determined by the intrinsic phonon absorption of ZnTe crystal. To achieve higher bandwidth, other methods such as air plasma detector should be implemented.

The THz field strength can be estimated from the modulation depth of the optical signal detected by the balanced detector. In our experiment, we measured that the maximum modulation of the balanced photo-detector signal I_1 and I_2 measured at the peak THz field, i.e., $(I_1 - I_2)/(I_1 + I_2)$, is 0.11 with one Si attenuator. The calibration relationship between the optical modulation depth and the THz field strength can be expressed (using eq. (A.2) and (A.3)) as

$$\arcsin\left(\frac{I_1 - I_2}{I_1 + I_2}\right) = \frac{2\pi L}{\lambda}n_0^3 r_{41} t_{ZnTe} t_{Si} E_{THz}, \tag{A.4}$$

where $n_0 = 2.85$ is the refractive index of the ZnTe crystal for the THz radiation, r_{41} = 4 pV/m is the electro-optic coefficient and $L = 1$ mm is the thickness of the crystal. Fresnel transmission coefficients are $t_{ZnTe} = 0.46$ for the ZnTe crystal and $t_{Si}= 0.7$ for the Si wafer. Based on the above equation (A.4), we estimated the maximum THz field in our experiment to be $E_{THz} = 170$ kV/cm. We note that the maximum THz field is certainly underestimated since the real spectrum width of the THz pulse is much broader than the detection range of ZnTe crystal (as we will show in the next section).

THz detection based on second harmonic generation

As it is widely known, air plasma can emit THz radiation. In an inverse manner, it is possible to use air plasma as a THz detector. Several schemes have been demonstrated by the group of Prof. X.-C. Zhang of Rochester University in the past few years [Dai 06, Karpowicz 08a, Liu 10, Clough 13]. The advantages of this air plasma detector include its large bandwidth due to lack of intrinsic material absorption and its capacity for remote detection. We have tried to implement these different detection methods and to compare them with the traditional detection based on EO sampling in ZnTe crystal.

In 2006 Dai, *et al.* presented a THz detection technique based on the four-wave mixing mechanism in ionised air [Dai 06]. This method allows to measure the THz spectra spreading from 0.1 to 10 THz.

In this scheme, a probe pulse at the wavelength of 800 nm was mixed with the THz pulse emerging from the filament inside the plasma produced by the probe pulse itself ("plasma 2" in Figure A.5), yielding a signal at the second harmonic frequency, 400 nm. By measuring the harmonic signal as a function of the delay between the THz and the ultrashort infrared pulse, one determines the waveform of the THz field, giving access to the THz pulse duration and spectrum.
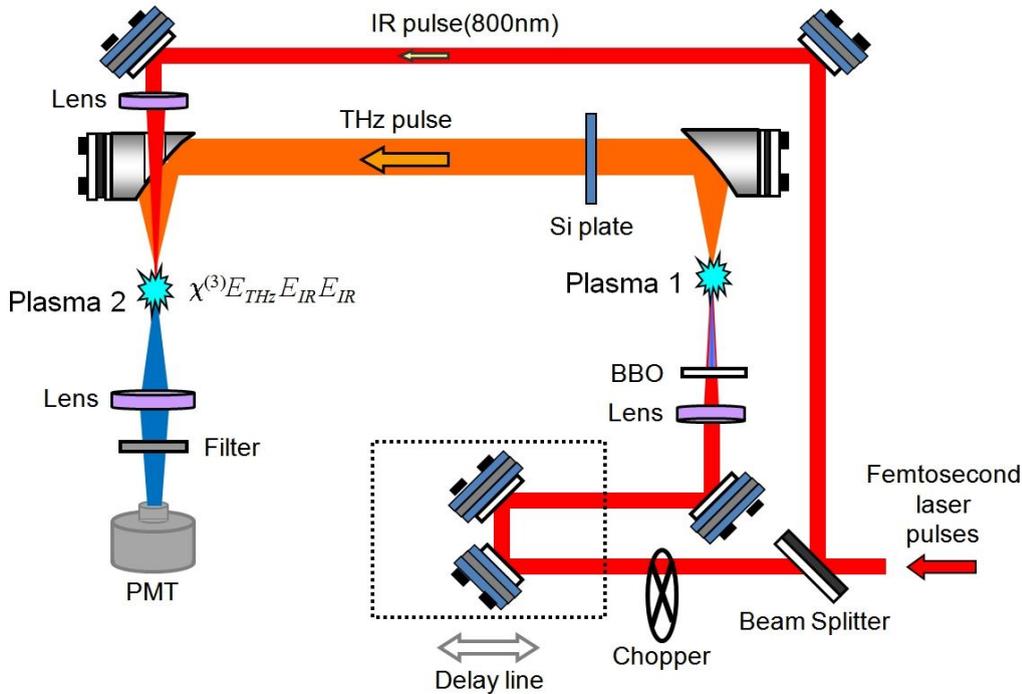
Figure A.5: Schematic setup for THz generation and detection based on the detection of the second harmonic signal. THz wave is generated by mixing the pump beam and its second harmonic from a thin type-I BBO crystal at the first air plasma point, or by applying a transverse DC electric field on the same plasma. The THz wave is detected by measuring the time-resolved SH signal produced by mixing the probe beam and the THz field at the position of the second plasma.

By focusing the THz pulse with the probe beam fundamental (ω) pulse, an optical field at the second harmonic frequency (2ω) is emitted, it is expressed as

$$E_{2\omega}^{signal} \propto \chi^{(3)} E_\omega E_\omega E_{THz}, \tag{A.5}$$

where $\chi^{(3)}$ is the third-order susceptibility of air. Since $E_{2\omega} \propto E_{THz}$, the intensity of the measured second harmonic signal is proportional to the intensity of the THz wave: $I_{2\omega} \propto I_{THz}$. However the phase information is missing and the detection is thus incoherent. To amend the analysis the second harmonic contribution generated inside the plasma by a laser pulse has to be included. This contribution may be considered as a local oscillator (LO) since it is independent from the THz field. One thus obtains the expression for the second harmonic intensity:

$$I_{2\omega} \propto (E_{2\omega})^2 = \left(E_{2\omega}^{signal} + E_{2\omega}^{LO} \right)^2 = (E_{2\omega}^{signal})^2 + (E_{2\omega}^{LO})^2 + 2 E_{2\omega}^{signal} E_{2\omega}^{LO} \cos(\phi), \tag{A.6}$$

where ϕ is the phase difference between the $E_{2\omega}^{signal}$ and $E_{2\omega}^{LO}$.

Using the equation (A.5) one obtains

$$I_{2\omega} \propto (\chi^{(3)} I_\omega)^2 I_{THz} + (E_{2\omega}^{LO})^2 + 2\chi^{(3)} I_\omega E_{2\omega}^{LO} E_{THz} \cos(\phi). \tag{A.7}$$

The second term is the DC contribution from the LO and can be filtered out through the use of a lock-in amplifier by modulating the THz beam (by installing a chopper to the pump beam). The equation, thus, can be rewritten as

$$I_{2\omega} \propto (\chi^{(3)} I_\omega)^2 I_{THz} + 2\chi^{(3)} I_\omega E_{2\omega}^{LO} E_{THz} \cos(\phi). \tag{A.8}$$

Equation (A.8) predicts that, when the probe intensity is lower than the air ionization threshold, the total second harmonic signal is dominated by the first term of the equation, leading to $I_{2\omega} \propto I_{THz}$. In this case the measured $I_{2\omega}(t)$ is unipolar, and the detection is incoherent. With the probe intensity much higher than the ionization threshold ($\approx 5 \times 10^{14}$ W/cm^2, see [Dai 06]), the last term dominates. $I_{2\omega}(t)$ is then proportional to the THz electric field with a bipolar waveform, and the detection becomes coherent.

We have tested the above detection principle and obtained the results presented in Figure A.6. The unipolar feature of the signal indicates that we were in the regime of incoherent detection. The underlying reason can be that our probe pulse was limited to less than 200 μJ. With a focal geometry of $f/40$, we cannot produce an intense plasma for detection.
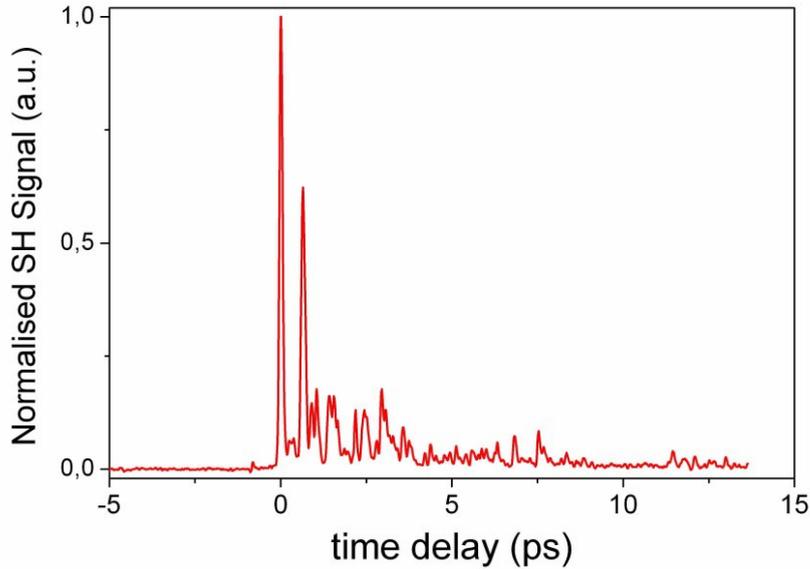
Figure A.6: Time-resolved second harmonic signal measured in air plasma.

THz detection based on second harmonic generation in a biased plasma

The detection based on the second harmonic generation in air plasma has several drawbacks: first of all, it is difficult to reach the same SNR as that of the EO sampling method, furthermore relatively high laser intensity is needed for the coherent detection by this method. To overcome the difficulties another method has been proposed by the group of Prof. Zhang: by using the heterodyne detection technique the SNR may be improved, the authors have presented the THz spectrum reaching 40 THz [Karpowicz 08a, Karpowicz 08b]. The basic principle is to apply an AC external electric field to the optical focus. A bias-field-induced second harmonic pulse, with field amplitude $E_{2\omega}^{LO}$ is generated. This additional second harmonic pulse mixes with the THz-field-induced second harmonic pulse $E_{2\omega}^{THz}$. The total second-harmonic intensity in terms of the time-dependent electric fields has the following form:

$$I_{2\omega} \propto \langle E_{2\omega}^2 \rangle = \langle (E_{2\omega}^{THz} + E_{2\omega}^{LO})^2 \rangle = \langle E_{2\omega}^{THz\,2} \rangle + \langle E_{2\omega}^{LO\,2} \rangle + 2\langle E_{2\omega}^{THz} E_{2\omega}^{LO} \rangle. \qquad (A.9)$$

The THz-field-induced and the AC-bias-induced second harmonic can be written as, respectively:

$$\begin{aligned} E_{2\omega}^{THz} &\propto \chi^{(3)} I_\omega E_{THz}, \\ E_{2\omega}^{LO} &\propto \chi^{(3)} I_\omega E_{bias}, \end{aligned} \qquad (A.10)$$

where E_{bias} is the bias electric field. Using eq. (A.9) and (A.10) one obtains

$$I_{2\omega} \propto \left(\chi^{(3)} I_\omega \right)^2 \left[(E_{THz})^2 + (E_{bias})^2 \pm 2 E_{bias} E_{THz} \right]. \qquad (A.11)$$

In this case the process can be interpreted in terms of heterodyne detection. With a lock-in amplifier, the term proportional to E_{THz} can be easily isolated and the measured second harmonic signal will be

$$I_{2\omega} \propto \left(\chi^{(3)} I_\omega(t)\right)^2 E_{bias} E_{THz}. \tag{A.12}$$

To check the validity of this approach the transverse AC electric field was applied to the "plasma 2" area with field amplitude of up to 17 kV/cm. Figure A.7 presents the measured THz temporal signal and the corresponding spectrum. Coherent detection is clearly achieved, in view of the positive and negative signal. Moreover, two features can be noticed. First, the measured spectrum extends up to 30 THz (Figure A.7(b)), which is much larger than that obtained with the ZnTe crystal. Second, a large number of sharp absorption lines can be observed in the spectrum. Most of these lines are due to absorption by water vapor since all experiments were performed in atmospheric air. With the conventional electro-optic detection, it is impossible to resolve all these absorption lines due to the limitation in the detection bandwidth.
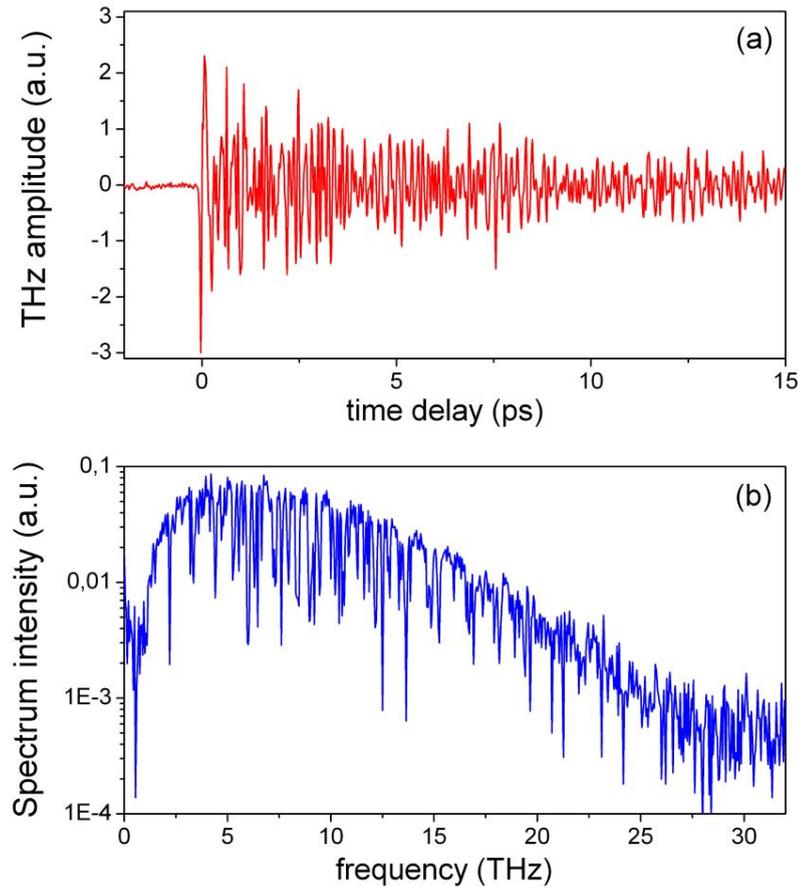
Figure A.7: THz signal (a) and corresponding spectrum (b) measured by means of the AC-electric-field-biased plasma (field amplitude is 15 kv/cm, frequency 500 Hz). The fast oscillations in (a) are due to the absorption lines of atmospheric water vapor, which is clearly revealed in the spectral domain.

To further verify the validity of the equation (A.12), we have measured the second harmonic signal as a function of the external bias electric field E_{bias} and of the laser intensity I_ω (assuming a linear dependence between the input energy and the intensity at the focus). Figure A.8(a) presents the linear dependence of the second harmonic signal as a function of the bias field, which confirms the linear dependence predicted by the equation (A.12). Figure A.8(b) shows that the measured second harmonic signal increase quadratically with the energy of the probe pulse. The good agreement between experiment and the fit confirms again the validity of the equation (A.12).
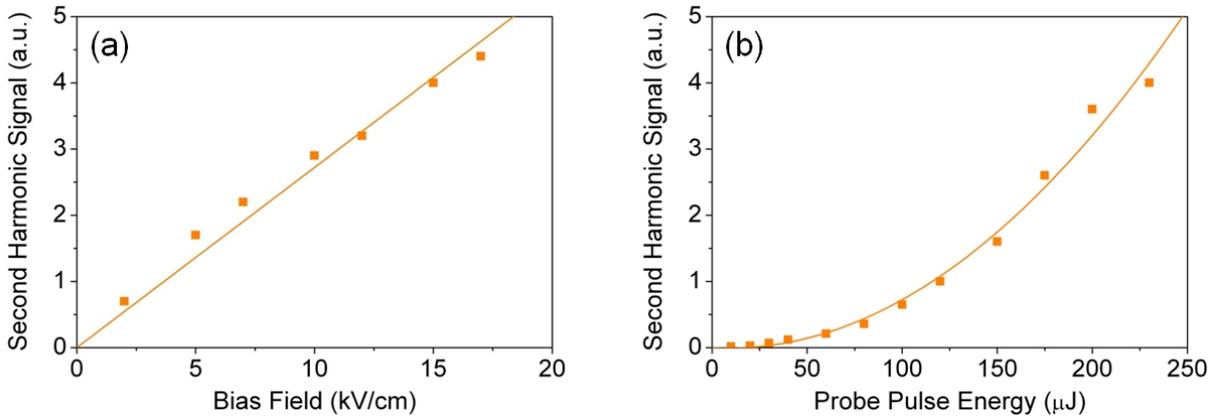
Figure A.8: Measured second harmonic signal as a function of biased field (a) and probe pulse energy (b). For the measurement in (a) the probe pulse energy was 200 μJ. The bias field was 15 kV/cm for the measurement in (b).

Appendix B

Personal references

Publications in peer-reviewed scientific journals

1. S. Mitryukovskiy, Y. Liu, A. Houard and A. Mysyrowicz, *Re-evaluation of the peak intensity inside a femtosecond laser filament in air*, Submitted to J. Phys. B

2. S. Mitryukovskiy, Y. Liu, P. Ding, A. Houard, A. Couairon and A. Mysyrowicz, *Plasma luminescence from femtosecond filaments in air: evidence for impact ionization with circularly polarized light pulses*, Submitted to Phys. Rev. Lett.

3. P. Ding, S. Mitryukovskiy, A. Houard, E. Oliva, A. Couairon, A. Mysyrowicz and Y. Liu, *Backward Lasing of Air plasma pumped by Circularly polarized femtosecond pulses for the saKe of remote sensing (BLACK)*, Opt. Express **22**, 29964 (2014)

4. S. I. Mitryukovskiy, Y. Liu, B. Prade, A. Houard and A. Mysyrowicz, *Coherent interaction between the THz radiation emitted by filaments in air*, Laser Phys. **24**, 094009 (2014)

5. S. Mitryukovskiy, Y. Liu, P. Ding, A. Houard and A. Mysyrowicz, *Backward stimulated radiation from filaments in nitrogen gas and air pumped by circularly polarized 800 nm femtosecond laser pulses*, Opt. Express **22**, 12750 (2014)

6. S. I. Mitryukovskiy, Y. Liu, B. Prade, A. Houard and A. Mysyrowicz, *Effect of an external electric field on the coherent terahertz emission from multiple filaments in air*, Appl. Phys. B **117**, 265 (2014)

7. G. Point, Y. Liu, Y. Brelet, S. Mitryukovskiy, P. Ding, A. Houard and A. Mysyrowicz, *Lasing of ambient air with microjoule pulse energy pumped by a multi terawatt IR femtosecond laser*, Opt. Lett. **39**, 1725 (2014)

8. S. I. Mitryukovskiy, Y. Liu, B. Prade, A. Houard and A. Mysyrowicz, *Coherent synthesis of terahertz radiation from femtosecond laser filaments in air*, Appl. Phys. Lett. **102**, 221107 (2013)

9. Y. Liu, Y. Brelet, Z. He, L. Yu, S. Mitryukovskiy, A. Houard, B. Forestier, A. Couairon and A. Mysyrowicz, *Ciliary white-light: Optical aspect of ultrashort laser ablation on transparent dielectrics*, Phys. Rev. Lett. **110**, 097601 (2013)

10. S. I. Mitryukovskiy, A. A. Nikulin, A. I. Stognij and T. V. Murzina, *Magneto- and electroinduced effects in optical second-harmonic generation from a planar Au/Co/Si nanostructure*, Appl. Phys. Lett. **103**, 151606 (2013)

Publications in peer-reviewed scientific books

1. Y. Liu, S. Mitryukovskiy, P. Ding, G. Point, Y. Brelet, A. Houard, A. Couairon and A. Mysyrowicz, *Backward lasing of femtosecond plasma filaments*, To appear in "Progress in Ultrafast Intense Laser Science XII", edited by K. Yamanouchi, Springer Series in Chemical Physics

References

[Ackermann 04]   R. Ackermann, K. Stelmaszczyk, P. Rohwetter, G. Méjean, E. Salmon, J. Yu, J. Kasparian, G. Méchain, V. Bergmann, S. Schaper, B. Weise, T. Kumm, K. Rethmeier, W. Kalkner, L. Wöste & J.-P. Wolf. *Triggering and guiding of megavolt discharges by laser-induced filaments under rain conditions.* Appl. Phys. Lett., vol. 85, no. 23, pages 5781–5783, 2004.

[Alam 90]   R. C. Alam, S. J. Fletcher, K. R. Wasserman & L. Hüwel. *Time-resolved emission spectroscopy in laser-generated nitrogen plasmas.* Phys. Rev. A, vol. 42, pages 383–390, 1990.

[Alfano 70]   R. R. Alfano & S. L. Shapiro. *Observation of self-phase modulation and small-scale filaments in crystals and glasses.* Phys. Rev. Lett., vol. 24, pages 584–587, 1970.

[Andrews 46]   D. H. Andrews, R. M. Milton & W. J. DeSorbo. *A fast superconducting bolometer.* J. Opt. Soc. Am., vol. 36, no. 9, pages 518–524, 1946.

[Arkadiewa 24]   A. Glagolewa-Arkadiewa. *Short electromagnetic waves of wave-length up to 82 microns.* Nature, vol. 113, no. 2844, page 640, 1924.

[Armstrong 83]   R. A. Armstrong, R. A. Lucht & W. T. Rawlins. *Spectroscopic investigation of laser-initiated low-pressure plasmas in atmospheric gases.* Appl. Opt., vol. 22, no. 10, pages 1573–1577, 1983.

[Arnold 12]   B. R. Arnold, S. D. Roberson & P. M. Pellegrino. *Excited state dynamics of nitrogen reactive intermediates at the threshold of laser induced filamentation.* Chem. Phys., vol. 405, pages 9–15, 2012.

[Askar'yan 62]   G. A. Askar'yan. *Effects of the gradient of a strong electromagnetic beam on electrons and atoms.* Sov. Phys. JETP, vol. 15, pages 1088–1090, 1962.

[Askar'yan 74]   G. A. Askar'yan. *The sef-focusing effect.* Sov. Phys. Usp., vol. 16, page 680, 1974.

[Auston 73]   D. H. Auston, A. M. Glass & P. Lefur. *Tunable far-infrared generation by difference frequency mixing of dye lasers in reduced (black) lithium niobate.* Appl. Phys. Lett., vol. 21, no. 1, pages 47–48, 1973.

[Auston 84]   D. H. Auston, K. P. Cheung & P. R. Smith. *Picosecond photoconducting Hertzian dipoles.* Appl. Phys. Lett., vol. 45, no. 3, pages 284–286, 1984.

[Auston 88]   D. H. Auston & M. C. Nuss. *Electrooptical generation and detection of femtosecond electrical transients.* IEEE J. Quant. Electron., vol. 24, no. 2, pages 184–197, 1988.

[Balanis 05]   K. A. Balanis. Antenna Theory: Analysis and Design. John Wiley & Sons, Inc., Hoboken, New Jersey, 3rd edition, 2005.

[Barnes 35]   R. B. Barnes, W. S. Benedict & C. M. Lewis. *The far infrared spectrum of H_2O.* Phys. Rev., vol. 47, pages 918–921, 1935.

[Bartel 05]   T. Bartel, P. Gaal, K. Reimann, M. Woerner & T. Elsaesser. *Generation of single-cycle THz transients with electric-field amplitudes.* Opt. Lett., vol. 30, page 2805, 2005.

[Bass 62]   M. Bass, P. A. Franken, J. F. Ward & G. Weinreich. *Optical rectification.* Phys. Rev. Lett., vol. 9, page 446, 1962.

[Becker 01]   A. Becker, A. D. Bandrauk & S. L. Chin. *S-Matrix analysis of non-resonant multiphoton ionisation of inner-valence electrons of the nitrogen molecule.* Chem. Phys. Lett., vol. 343, pages 345–350, 2001.

[Bergé 07]   L. Bergé, S. Skupin, R. Nuter, J. Kasparian & J.-P. Wolf. *Ultrashort filaments of light in weakly ionized, optically transparent media.* Rep. Prog. Phys., vol. 70, pages 1633–1713, 2007.

[Berlinger 46]   R. Berlinger. *The absorption of one-half centimeter electromagnetic waves in oxygen.* Phys. Rev., vol. 70, page 53, 1946.

[Bernhardt 08]   J. Bernhardt, W. Liu, F. Théberge, H. L. Xu, J.-F. Daigle, M. Châteauneuf, J. Dubois & S. L. Chin. *Spectroscopic analysis of femtosecond laser plasma filament in air.* Opt. Commun., vol. 281, pages 1268–1274, 2008.

[Bernstein 02]   A. C. Bernstein, T. S. Luk, T. R. Nelson, A. McPherson, J.-C. Diels & S. M. Cameron. *Asymmetric ultra-short pulse-splitting measured in air using FROG.* Appl. Phys. B, vol. 75, no. 1, pages 119–122, 2002.

[Bespalov 02]   V. G. Bespalov, S. A. Kozlov, Yu. A. Shpolyanskiy & I. A. Walmsley. *Simplified field wave equations for the nonlinear propagation of extremely short light pulses.* Phys. Rev. A, vol. 66, page 013811, 2002.

[Borghese 98]   A. Borghese & S. S. Merola. *Time-resolved spectral and spatial description of laser-induced breakdown in air as a pulsed, bright, and broadband ultraviolet–visible light source.* Appl. Opt., vol. 37, no. 18, pages 3977–3983, 1998.

[Bourayou 05]   R. Bourayou, G. Méjean, J. Kasparian, M. Rodriguez, E. Salmon, J. Yu, H. Lehmann, B. Stecklum, U. Laux, J. Eislöffel, A. Scholz, A. P. Hatzes, R. Sauerbrey, L. Wöste & J.-P. Wolf. *White-light filaments for multiparameter analysis of cloud microphysics.* J. Opt. Soc. Am. B, vol. 22, no. 2, pages 369–377, 2005.

[Boyle 59]   W. S. Boyle & K. F. Rogers. *Performance characteristics of a new low-temperature bolometer.* J. Opt. Soc. Am., vol. 49, pages 66–69, 1959.

[Brabec 97]   T. Brabec & F. Krausz. *Nonlinear optical pulse propagation in the single-cycle regime.* Phys. Rev. Lett., vol. 78, pages 3282–3285, 1997.

[Braun 95]   A. Braun, G. Korn, X. Liu, D. Du, J. Squier & G. Mourou. *Self-channeling of high-peak-power femtosecond laser pulses in air.* Opt. Lett., vol. 20, no. 1, pages 73–75, 1995.

[Bucksbaum 86]   P. H. Bucksbaum, M. Bashkansky, R. R. Freeman, T. J. McIlrath & L. F. DiMauro. *Suppression of multiphoton ionization with circularly polarized coherent light.* Phys. Rev. Lett., vol. 56, pages 2590–2593, 1986.

[Burrus 54]   C. A. Burrus & W. Gordy. *Submillimeter wave spectroscopy.* Phys. Rev., vol. 93, page 897, 1954.

[Cai 98]   Y. Cai, I. Brener, J. Lopata, J. Wynn, L. Pfeiffer, J. B. Stark, Q. Wu, X.-C. Zhang & J. F. Federici. *Coherent terahertz radiation detection: Direct comparison between free-space electro-optic sampling and antenna detection.* Appl. Phys. Lett., vol. 73, no. 4, pages 444–446, 1998.

[Cao 02]   H. Cao, T. F. Heinz & A. Nahata. *Electro-optic detection of femtosecond electromagnetic pulses by use of poled polymers.* Opt. Lett., vol. 27, no. 9, pages 775–777, 2002.

[Chamberlain 63] J. E. Chamberlain, J. E. Gibbs & H. A. Gebbie. *Refractometry in the far infra-red using a twobeam interferometer.* Nature, vol. 198, page 874, 1963.

[Châteauneuf 08] M. Châteauneuf, S. Payaur, J. Dubois & J.-C. Kieffer. *Microwave guiding in air by a cylindrical filament array waveguide.* Appl. Phys. Lett., vol. 92, page 091104, 2008.

[Cheng 01]   C.-C. Cheng, E. M. Wright & J. V. Moloney. *Generation of electromagnetic pulses from plasma channels induced by femtosecond light strings.* Phys. Rev. Lett., vol. 87, page 213001, 2001.

[Chiao 64]   R. Y. Chiao, E. Garmire & C. H. Townes. *Self-trapping of optical beams.* Phys. Rev. Lett., vol. 13, no. 15, pages 479–482, 1964.

[Chin 09]   S. L. Chin, H. L. Xu, Q. Luo, F. Théberge, W. Liu, J.-F. Daigle, Y. Kamali, P. T. Simard, J. Bernhardt, S. A. Hosseini, M. Sharifi, G. Méjean, A. Azarm, C. Marceau, O. Kosareva, V. P. Kandidov, N. Aközbek, A. Becker, G. Roy, P. Mathieu, J. R. Simard, M. Châteauneuf & J. Dubois. *Filamentation remote sensing of chemical and biological agents/pollutants using only one femtosecond laser source.* Appl. Phys. B, vol. 95, no. 1, pages 1–12, 2009.

[Chin 10]   S. L. Chin. Femtosecond Laser Filamentation. Springer, New York, 2010.

[Chiron 99]   A. Chiron, B. Lamouroux, R. Lange, J.-F. Ripoche, M. Franco, B. Prade, G Bonnaud, G. Riazuelo & A. Mysyrowicz. *Numerical simulations of the nonlinear propagation of femtosecond optical pulses in gases.* Eur. Phys. J. D, vol. 6, no. 3, pages 383–396, 1999.

[Chu 12] W. Chu, B. Zeng, J. Yao, H. Xu, J. Ni, G. Li, H. Zhang, F. He, C. Jing, Y. Cheng & Z. Xu. *Multiwavelength amplified harmonic emissions from carbon dioxide pumped by mid-infrared femtosecond laser pulses.* Europhys. Lett., vol. 97, no. 6, page 64004, 2012.

[Chu 14a] W. Chu, G. Li, H. Xie, J. Ni, J. Yao, B. Zeng, H. Zhang, C. Jing, H. Xu, Y. Cheng & Z. Xu. *A self-induced white light seeding laser in a femtosecond laser filament.* Laser Phys. Lett., vol. 11, no. 1, page 015301, 2014.

[Chu 14b] W. Chu, H. Li, J. Ni, B. Zeng, J. Yao, H. Zhang, G. Li, C. Jing, H. Xie, H. Xu, K. Yamanouchi & Y. Cheng. *Lasing action induced by femtosecond laser filamentation in ethanol flame for combustion diagnosis.* Appl. Phys. Lett., vol. 104, no. 9, page 091106, 2014.

[Clough 13] B. Clough, J. Liu & X.-C. Zhang. *Acoustic methods and systems for detecting terahertz radiation*, 2013. US Patent App. 13/643,871.

[Comtois 00] D. Comtois, C. Y. Chien, A. Desparois, F. Génin, G. Jarry, T. W. Johnston, J.-C. Kieffer, B. La Fontaine, F. Martin, R. Mawassi, H. Pépin, F. A. M. Rizk, F. Vidal, P. Couture, H. P. Mercure, C. Potvin, A. Bondiou-Clergerie & I. Gallimberti. *Triggering and guiding leader discharges using a plasma channel created by an ultrashort laser pulse.* J. Appl. Phys., vol. 76, no. 7, pages 819–821, 2000.

[Conti 03] C. Conti, S. Trillo, P. Di Trapani, G. Valiulis, A. Piskarskas, O. Jedrkiewicz & J. Trull. *Nonlinear electromagnetic X-waves.* Phys. Rev. Lett., vol. 90, no. 17, page 170406, 2003.

[Cook 00] D. J. Cook & R. M. Hochstrasser. *Intense terahertz pulses by four-wave rectification in air.* Opt. Lett., vol. 25, pages 1210–1212, 2000.

[Cook 05] K. Cook, A. K. Kar & R. A. Lamb. *White-light filaments induced by diffraction effects.* Opt. Express, vol. 33, no. 6, page 2025, 2005.

[Corkum 89] P. B. Corkum, N. H. Burnett & F. Brunel. *Above-threshold ionization in the long-wavelength limit.* Phys. Rev. Lett., vol. 62, pages 1259–1262, 1989.

[Corkum 93] P. B. Corkum. *Plasma perspective on strong field multiphoton ionization.* Phys. Rev. Lett, vol. 71, pages 1994–1997, 1993.

[Couairon 02a] A. Couairon & L. Bergé. *Light filaments in air for ultraviolet and infrared wavelengths.* Phys. Rev. Lett., vol. 88, no. 13, pages 135003 1–4, 2002.

[Couairon 02b] A. Couairon, S. Tzortzakis, L. Bergé, M. Franco, B. Prade & A. Mysyrowicz. *Infrared femtosecond light filaments in air: simulations and experiments.* J. Opt. Soc. Am. B, vol. 19, no. 13, pages 1117–1131, 2002.

[Couairon 07] A. Couairon & A. Mysyrowicz. *Femtosecond filamentation in transparent media.* Phys. Rep., vol. 441, no. 2-4, pages 47–189, 2007.

[Couairon 11] A. Couairon, E. Brambilla, T. Corti, O. de J. Ramírez-Góngora D. Majus and & M. Kolesik. *Practitioner's guide to laser pulse propagation models and simulation.* Europ. Phys. J. Spec. Topics, vol. 199, no. 1, pages 5–76, 2011.

[Crandall 74]   D. H. Crandall, W. E. Kauppila, R. A. Phaneuf, Paul O. Taylor & Gordon H. Dunn. *Absolute cross sections for electron-impact excitation of* N_2^+. Phys. Rev. A, vol. 9, pages 2545–2551, 1974.

[Crocker 64]   A. Crocker, H. A. Gebbie, M. F. Kimmitt & L. E. S. Mathias. *Stimulated emission in the far infra-red*. Nature, vol. 201, page 250, 1964.

[Dai 06]   J. Dai, X. Xie & X.-C. Zhang. *Detection of broadband Terahertz Waves with a laser-induced plasma in gases*. Phys. Rev. Lett., vol. 97, page 103903, 2006.

[Dai 11]   J. Dai, J. Liu & X.-C. Zhang. *Terahertz wave air photonics: terahertz wave generation and detection with laser-induced gas plasma*. IEEE J. Sel. Top. Quant. Electron., vol. 17, no. 1, pages 183–190, 2011.

[Daigle 08]   J.-F. Daigle, Y. Kamali, G. Roy & S. L. Chin. *Remote filament-induced fluorescence spectroscopy from thin clouds of smoke*. Appl. Phys. B, vol. 93, no. 4, pages 759–762, 2008.

[Daigle 12]   J.-F. Daigle, F. Théberge, M. Henriksson, T.-J. Wang, S. Yuan, M. Châteauneuf, J. Dubois, M. Piché & S. L. Chin. *Remote THz generation from two-color filamentation: long distance dependence*. Opt. Express, vol. 20, no. 6, pages 6825–6834, 2012.

[D'Amico 07a]   C. D'Amico. *Filamentation femtoseconde dans les milieux transparents passifs et amplificateurs, et étude de la filamentation comme source de radiation secondaire*. Thèse de doctorat, École Polytechnique, Palaiseau, France, 2007.

[D'Amico 07b]   C. D'Amico, A. Houard, M. Franco, B. Prade & A. Mysyrowicz. *Coherent and incoherent radial THz emission from femtosecond filaments in air*. Opt. Commun., vol. 15, no. 23, pages 15274–15279, 2007.

[D'Amico 07c]   C. D'Amico, A. Houard, M. Franco, B. Prade, A. Mysyrowicz, A. Couairon & V. T. Tikhonchuk. *Conical forward THz emission from femtosecond-laser-beam filamentation in air*. Phys. Rev. Lett., vol. 98, no. 23, 2007.

[D'Amico 08a]   C. D'Amico, A. Houard, S. Akturk, Y. Liu, J. Le Bloas, M. Franco, B. Prade, A. Couairon, V. T. Tikhonchuk & A. Mysyrowicz. *Forward THz radiation emission by femtosecond filamentation in gases: theory and experiment*. New J. Phys., vol. 10, page 013015, 2008.

[D'Amico 08b]   C. D'Amico, A. Houard, M. Pellet, Ch. Pichot & A. Mysyrowicz. *Dipolar-like antenna emission in the radiofrequency range by laser-produced plasma channels in air*. J. Phys. D: Appl. Phys., vol. 41, no. 24, page 245206, 2008.

[Dawes 69]   E. L. Dawes & J. H. Marburger. *Computer studies in self-focusing*. Phys. Rev., vol. 179, no. 3, pages 862–868, 1969.

[Diaw 08]   A. Diaw. Emission du raynnement électromagnétique Térahertz d'une impulsion laser auto-focalisée. Rapport de stage, Université Bordeaux 1, CELIA, Talence, 2008.

[Ding 14]   P. Ding, S. Mitryukovskiy, A. Houard, A. Couairon, A. Mysyrowicz & Y. Liu. *Externally seeded backward lasing radiation from femtosecond laser filament in nitrogen gas.* submitted to Opt. Express, 2014.

[Dogariu 11]   A. Dogariu, J. B. Michael, M. O. Scully & R. B. Miles. *High-gain backward lasing in air.* Science, vol. 331, no. 6016, pages 442–445, 2011.

[Dragomar 04]   D. Dragomar & M. Dragomar. *Terahertz fields and applications.* Prog. Quant. Electron., vol. 28, pages 1–66, 2004.

[Durand 10]   M. Durand, Y. Liu, A. Houard & A. Mysyrowicz. *Fine control of terahertz radiation from filamentation by molecular lensing in air.* Opt. Lett., vol. 35, no. 10, pages 1710–1712, 2010.

[Durand 13]   M. Durand, A. Houard, B. Prade, A. Mysyrowicz, A. Durécu, B. Moreau, D. Fleury, O. Vasseur, H. Borchert, K. Diener, R. Schmitt, F. Théberge, M. Chateauneuf, J.-F. Daigle & J. Dubois. *Kilometer range filamentation.* Opt. Express, vol. 21, no. 22, pages 26836–26845, 2013.

[Elias 84]   L. R. Elias, J. Hu & G. Ramian. *The UCSB electrostatic accelerator free electron laser: first operation.* Nucl. Instr. Meth., vol. 237, page 203–206, 1984.

[Faccio 06]   D. Faccio, M. Porras, A. Dubietis, F. Bragheri, A. Couairon & P. Di Trapani. *Conical emission, pulse splitting and X-wave parametric amplification in nonlinear dynamics of ultrashort light pulses.* Phys. Rev. Lett., vol. 96, page 193901, 2006.

[Faist 94]   J. Faist, F. Capasso, D. L. Sivko, C. Sirtori, A. L. Hutchinson & A. Y. Cho. *Quantum cascade laser.* Science, vol. 264, no. 5158, pages 553–556, 1994.

[Faist 04]   J. Faist, L. Ajili, G. Scalari, M. Giovannini, M. Beck, M. Rochat, H. Beere, G. Davies, E. H. Linfield & D. Ritchie. *Terahertz quantum cascade lasers.* Phil. Trans. R. Soc. Lond., vol. 362, pages 215–231, 2004.

[Fattinger 88]   C. Fattinger & D. Grischkowsky. *Point source terahertz optics.* Appl. Phys. Lett., vol. 53, no. 16, pages 1480–1482, 1988.

[Fattinger 89]   C. Fattinger & D. Grischkowsky. *Terahertz beams.* Appl. Phys. Lett., vol. 54, no. 6, pages 490–494, 1989.

[Fazio 79]   G. G. Fazio. *A review of infrared and submillimeter astronomy with ballon-borne telescopes.* Infrared Phys., vol. 19, pages 341–351, 1979.

[Federici 10]   J. Federici & L. Moeller. *Review of terahertz and subterahertz wireless communications.* J. Appl. Phys., vol. 107, no. 11, page 111101, 2010.

[Feit 74]   M. D. Feit & J. A. Fleck. *Effect of refraction on spot-size dependence of laser-induced breakdown.* Appl. Phys. Lett., vol. 24, no. 4, pages 169–172, 1974.

[Ferguson 02]   B. Ferguson & X.-C. Zhang. *Materials for terahertz science and technology.* Nat. Mater., vol. 1, pages 26–33, 2002.

[Fibich 00]   G. Fibich & A. L. Gaeta. *Critical power for self-focusing in bulk media and in hollow waveguides.* Opt. Lett., vol. 25, no. 5, pages 335–337, 2000.

[Filin 09]   A. Filin, R. Compton, D. A. Romanov & R. J. Levis. *Impact-ionization cooling in laser-induced plasma filaments.* Phys. Rev. Lett., vol. 102, page 155004, 2009.

[Fillippidis 12] G. Fillippidis, M. Massaouti, A. Selimis, E. J. Gualda, J. M. Manceau & S. Tzortzakis. *Nonlinear imaging and THz diagnostic tools in the service of Cultural Heritage.* Appl. Phys. A, vol. 106, pages 257–263, 2012.

[Fitzgerald 02] A. J. Fitzgerald, E. Berry, N. N. Zinovev, G. C. Walker, M. A. Smith & J. M. Chamberlain. *An introduction to medical imaging with coherent terahertz frequency radiation.* Phys. Med. Biol., vol. 47, page 67, 2002.

[Flyagin 77]   V. A. Flyagin, A. V. Gaponov, M. I. Petelin & V. K. Yulpatov. *The Gyrotron.* IEEE Trans. Microwave Th. Tech., vol. 25, pages 514–521, 1977.

[Fons 96]   J. T. Fons, R. S. Schappe & C. C. Lin. *Electron-impact excitation of the second positive band system ($C^3\Pi_u \to B^3\Pi_g$) and the $C^3\Pi_u$ electronic state of the nitrogen molecule.* Phys. Rev. A, vol. 53, pages 2239–2247, 1996.

[Gaeta 00]   A. L. Gaeta. *Catastrophic collapse of ultrashort pulses.* Phys. Rev. Lett., vol. 84, page 3582, 2000.

[Garmire 66]   E. Garmire, R. Y. Chiao & C. H. Townes. *Dynamics and characteristics of the self-trapping of intense light beams.* Phys. Rev. Lett., vol. 16, pages 347–349, 1966.

[Golay 47]   M. J. E. Golay. *Theoretical consideration in heat and infra-red detection, with particular reference to the pneumatic detector.* Rev. Sci. Instr., vol. 18, no. 5, pages 357–362, 1947.

[Golub 90]   I. Golub. *Optical characteristics of supercontinuum generation.* Opt. Lett., vol. 15, no. 6, page 305, 1990.

[Gravel 04]   J.-F. Gravel, Q. Luo, D. Boudreau, X. P. Tang & S. L. Chin. *Sensing of halocarbons using femtosecond laser-induced fluorescence.* Anal. Chem., vol. 76, no. 16, pages 4799–4805, 2004.

[Grimes 68]   C. C. Grimes, P. L. Richards, & S. Shapiro. *Josephson-effect far-infrared detector.* Appl. Phys., vol. 39, page 3905, 1968.

[Hamster 93]   H. Hamster, A. Sullivan, S. Gordon, W. White & R. W. Falcone. *Subpicosecond, electromagnetic pulses from intense laser-plasma interaction.* Phys. Rev. Lett., vol. 71, page 2725, 1993.

[Hamster 94]   H. Hamster, A. Sullivan, S. Gordon & R. W. Falcone. *Short-pulse terahertz radiation from high-intensity-laser-produced plasmas.* Phys. Rev. E, vol. 49, page 671, 1994.

[Hangyo 05]   M. Hangyo, M. Tani & T. Nagashima. *Terahertz time-domain spectroscopy of solids: a review.* Int. J. Infrared Millim. Waves, vol. 26, pages 1661–1690, 2005.

[Hemmer 11]   P. R. Hemmer, R. B. Miles, P. Polynkin, T. Siebert, A. V. Sokolov, P. Sprangle & M. O. Scully. *Standoff spectroscopy via remote generation of a backward-propagating laser beam.* Proc. Nat. Acad. Sci. U.S.A., vol. 108, no. 8, pages 3130–3134, 2011.

[Henin 11]   S. Henin, Y. Petit, P. Rohwetter, K. Stelmaszczyk, Z. Q. Hao, W. M. Nakaema, A. Vogel, T. Pohl, F. Schneider, J. Kasparian, K. Weber, L. Wöste & J.-P. Wolf. *Laser-induced water condensation in air.* Nat. Commun., vol. 2, page 456, 2011.

[Hirori 11]   H. Hirori, A. Doi, F. Blanchard & K. Tanaka. *Single-cycle terahertz pulses with amplitudes exceeding 1 MV/cm generated by optical rectification in LiNbO3.* Appl. Phys. Lett., vol. 98, no. 9, page 091106, 2011.

[Hosseini 03]   S. A. Hosseini, Q. Luo, B. Ferland, W. Liu, N. Aközbek, G. Roy & S. L. Chin. *Effective length of filaments measurement using backscattered fluorescence from nitrogen molecules.* Appl. Phys. B, vol. 77, no. 6-7, pages 697–702, 2003.

[Houard 07]   A. Houard, Y. Liu, A. Mysyrowicz & B. Leriche. *Calorimetric detection of the conical terahertz radiation from femtosecond laser filaments in air.* App. Phys. Lett., vol. 91, no. 24, page 241105, 2007.

[Houard 08a]   A. Houard. *Filamentation laser femtoseconde dans l'air et amplification au guidage de décharges électriques et à la géneration de rayonnement térahertz.* Thèse de doctorat, École Polytechnique, Palaiseau, France, 2008.

[Houard 08b]   A. Houard, Y. Liu, B. Prade & A. Mysyrowicz. *Polarization analysis of THz radiation generated by four wave mixing in air.* Opt. Lett., vol. 33, no. 11, pages 1195–1197, 2008.

[Houard 08c]   A. Houard, Y. Liu, B. Prade, V. T. Tikhonchuk & A. Mysyrowicz. *Strong enhancement of Terahertz radiation from laser filaments in air by a static electric field.* Phys. Rev. Lett., vol. 100, page 255006, 2008.

[Hu 95]   B. B. Hu & M. C. Nuss. *Imaging with terahertz waves.* Opt. Lett., vol. 20, no. 16, pages 1716–1718, 1995.

[Itikawa 06]   Y. Itikawa. *Cross sections for electron collisions with nitrogen molecules.* J. Phys. Chem. Ref. Data., vol. 35, no. 1, pages 31–53, 2006.

[Iwasaki 03]   A. Iwasaki, N. Aközbek, B. Ferland, Q. Luo, G. Roy, C. M. Bowden & S. L. Chin. *A LIDAR technique to measure the filament length generated by a high-peak power femtosecond laser pulse in air.* Appl. Phys B, vol. 76, no. 3, pages 231–236, 2003.

[Iwaszczuk 12] K. Iwaszczuk, A. Andryieuski, A. Lavrinenko, X.-C. Zhang & P. U. Jepsen. *Terahertz field enhancement to the MV/cm regime in a tapered parallel plate waveguide.* Opt. Express, vol. 20, no. 8, pages 8344–8355, 2012.

[Jackson 65]   J. D. Jackson. Classical Electrodynamics. Wiley, New York, 1965.

[Jackson 08]   J. B. Jackson, M. Mourou, J. F. Whitaker, I. N. Duling, S. L. Williamson, M. Menu & G. A. Mourou. *Terahertz imaging for non-destructive evaluation of mural paintings.* Opt. Commun., vol. 281, pages 527–532, 2008.

[Jamison 03]   S. P. Jamison, J. Shen, D. R. Jones, R. C. Issac, B. Ersfeld, D. Clark & D. A. Jaroszynski. *Plasma characterization with terahertz time-domain measurements.* J. Appl. Phys., vol. 93, no. 7, pages 4334–4336, 2003.

[Kamali 09]   Y. Kamali, J.-F. Daigle, F. Théberge, M. Châteauneuf, A. Azarm, Y. Chen, C. Marceau, S.C. Lessard, F. Lessard, G. Roy, J. Dubois & S.L. Chin. *Remote sensing of trace methane using mobile femtosecond laser system of T&T lab.* Opt. Commun., vol. 282, no. 10, pages 2062–2065, 2009.

[Kampfrath 11]   T. Kampfrath, A. Sell, G. Klatt, A. Pashkin, S. Mährlein, T. Dekorsy, M. Wolf, M. Fiebig, A. Leitenstorfer & R. Huber. *Coherent terahertz control of antiferromagnetic spin waves.* Nat. Photon., vol. 5, page 31–34, 2011.

[Kandidov 97]   V. P. Kandidov, O. G. Kosareva, A. Brodeur & S. L. Chin. *State-of-the-art of investigations into the filamentation of high-power subpicosecond laser pulses in gases.* Atmos. Oceanic Opt., vol. 10, no. 12, page 966, 1997.

[Kandidov 03]   V. P. Kandidov, O. G. Kosareva, I. S. Golubtsov, W. Liu, A. Becker, N. Aközbek, C. M. Bowden & S. L. Chin. *Self-transformation of a powerful femtosecond laser pulse into a white-light laser pulse in bulk optical media (or supercontinuum generation).* Appl. Phys. B, vol. 77, no. 2-3, pages 149–165, 2003.

[Kandidov 11]   V. P. Kandidov, V. Y. Fedorov, O. V. Tverskoi, O. G. Kosareva & S. L. Chin. *Intensity clamping in the filament of femtosecond laser radiation.* Quant. Electron., vol. 41, no. 4, page 382, 2011.

[Karpowicz 08a]   N. Karpowicz, J. Dai, X. Lu, Y. Chen, M. Yamaguchi, H. Zhao & X.-C. Zhang. *Coherent heterodyne time-domain spectroscopy covering the entire terahertz gap.* Appl. Phys. Lett., vol. 92, page 011131, 2008.

[Karpowicz 08b]   N. E. Karpowicz, J. Chen, T. Tongue & X.-C. Zhang. *Coherent millimetre wave to mid-infrared measurements with continuous bandwidth reaching 40 THz.* Electron. Lett., vol. 44, pages 544–545, 2008.

[Karr 01]   J. J. Karr. Practical Antenna Handbook. McGraw-Hill/TAB Electronics, 2001.

[Kartashov 12]   D. Kartashov, S. Ališauskas, G. Andriukaitis, A. Pugžlys, M. Shneider, A. Zheltikov, S. L. Chin & A. Baltuška. *Free-space nitrogen gas laser driven by a femtosecond filament.* Phys. Rev. A, vol. 86, page 033831, 2012.

[Kartashov 13]   D. Kartashov, S. Ališauskas, A. Baltuška, A. Schmitt-Sody, W. Roach & P. Polynkin. *Remotely pumped stimulated emission at 337 nm in atmospheric nitrogen.* Phys. Rev. A, vol. 88, page 041805, 2013.

[Kasparian 00]   J. Kasparian, R. Sauerbrey & S. L. Chin. *The critical laser intensity of self-guided light filaments in air.* Appl. Phys. B, vol. 71, page 877, 2000.

[Kasparian 03]   J. Kasparian, M. Rodriguez, G. Méjean, J. Yu, E. Salmon, H. Wille, R. Bourayou, S. Frey, Y.-B. André, A. Mysyrowicz, R. Sauerbrey, J.-P., Wolf & L. Wöste. *White light filaments for atmospheric analysis.* Science, vol. 301, page 61, 2003.

[Kasparian 08]   J. Kasparian & J.-P. Wolf. *Physics and applications of atmospheric nonlinear optics and filamentation.* Opt. Express, vol. 16, page 466, 2008.

[Keldysh 65]   L. V. Keldysh. *Ionization in the field of a strong electromagnetic wave.* Sov. Phys. JETP, vol. 20, no. 5, pages 1307–1314, 1965.

[Kelley 65]   P. L. Kelley. *Self-focusing of optical beams.* Phys. Rev. Lett., vol. 15, no. 26, pages 1005–1008, 1965.

[Kim 07]   K.-Y. Kim, J. H. Glownia, A. J. Taylor & G. Rodriguez. *Terahertz emission from ultrafast ionizing air in symetry-broken laser fields.* Opt. Express, vol. 15, page 4577, 2007.

[Kim 08]   K.-Y. Kim, A. J. Taylor, J. H. Glownia & G. Rodriguez. *Coherent control of THz supersontinuum generation in ultrafast laser-gas interactions.* Nat. Photon., vol. 2, pages 605 – 609, 2008.

[Kim 09]   K.-Y. Kim. *Generation of coherent terahertz radiation in ultrafast laser-gas interactions.* Phys. Plasmas, vol. 16, page 056706, 2009.

[Kimmitt 03]   M. F. Kimmitt. *Restrahlen to T-Rays – 100 years of Terahertz radiation.* J. Biol. Phys., vol. 29, pages 77–85, 2003.

[Kocharovsky 05]   V. Kocharovsky, S. Cameron, K. Lehmann, R. Lucht, R. Miles, Y. Rostovtsev, W. Warren, G. R. Welch & M. O. Scully. *Gain-swept superradiance applied to the stand-off detection of trace impurities in the atmosphere.* Proc. Nat. Acad. Sci. U.S.A., vol. 102, no. 22, pages 7806–7811, 2005.

[Kolesik 01]   M. Kolesik, J. V. Moloney & E. M. Wright. *Polarization dynamics of femtosecond pulses propagating in air.* Phys. Rev. E, vol. 64, page 046607, 2001.

[Kompfner 53]   R. Kompfner & N. T. Williams. *Backward-wave tubes.* Proc. IRE, vol. 41, pages 1602–1611, 1953.

[Kosareva 97]   O. G. Kosareva, V. P. Kandidov, A. Brodeur, C. Y. Chien & S. L. Chin. *Conical emission from laser-plasma interactions in the filamentation of powerful ultrashort laser pulses in air.* Opt. Lett., vol. 22, no. 17, pages 1332–1334, 1997.

[Kosareva 07]   O. G. Kosareva, I. N. Murtazin, N. A. Panov, A. B. Savel'ev, V. P. Kandidov & S. L. Chin. *Pulse shortening due to filamentation in transparent medium.* Laser Phys. Lett., vol. 4, no. 2, pages 126–132, 2007.

[Kosareva 08]   O. G. Kosareva, N. A. Panov, D. S. Uryupina, M. V. Kurilova, A. V. Mazhorova, A. B. Savel'ev, R. V. Volkov, V. P. Kandidov & S. L. Chin. *Optimization of a femtosecond pulse self-compression region along a filament in air.* Appl. Phys. B, vol. 91, no. 1, pages 35–43, 2008.

[Kossyi 92]   I. A. Kossyi, A. Yu. Kostinsky, A. A. Matveyev & V. P. Silakov. *Kinetic scheme of the non-equilibrium discharge in nitrogen-oxygen mixtures.* Plasma Sourc. Sci. Technol., vol. 1, no. 3, page 207, 1992.

[Krause 92]   J. L. Krause, K. J. Schafer & K. C. Kulander. *High-order harmonic generation from atoms and ions in the high intensity regime.* Phys. Rev. Lett., vol. 68, pages 3535–3538, 1992.

[Kress 04]   M. Kress, T. Löffler, S. Eden, M. Thomson & H. G. Roskos. *Terahertz pulse generation by photoionization of air with laser pulses composed of both fundamental and second-harmonic waves.* Opt. Lett., vol. 29, page 1120, 2004.

[Kulesa 11]   C. Kulesa. *Terahertz spectroscopy for astronomy: from comets to cosmology.* IEEE Trans. Terahertz Sci. Tech., vol. 1, no. 1, pages 232–240, 2011.

[Kunabenchi 84]   R. S. Kunabenchi, M. R. Gorbal & M. I. Savadatti. *Nitrogen lasers.* Prog. Quant. Electron., vol. 9, no. 4, pages 259–329, 1984.

[La Fontaine 99] B. La Fontaine, F. Vidal, Z. Jiang, C. Y. Chien, D. Comtois, A. Desparois, T. W. Johnston, J.-C. Kieffer & H. Pépin. *Filamentation of ultrashort pulse laser beams resulting from their propagation over long distances in air.* Phys. Plasmas, vol. 6, page 1615, 1999.

[Ladouceur 01]   H. D. Ladouceur, A. P. Baronavski, D. Lohrmann, P. W. Grounds & P. G. Girardi. *Electrical conductivity of a femtosecond laser generated plasma channel in air.* Opt. Commun., vol. 189, page 107, 2001.

[Lallemand 65]   P. Lallemand & N. Bloembergen. *Self-focusing of laser beams and stimulated Raman gain in liquids.* Phys. Rev. Lett., vol. 15, pages 1010–1012, 1965.

[Lange 98]   H.R. Lange, A. Chiron, J.F. Ripoche, A. Mysyrowicz, P. Breger & P. Agostini. *High-order harmonic generation and quasiphase matching in xenon using self-guided femtosecond pulses.* Phys. Rev. Lett., vol. 81, no. 8, pages 1611–1613, 1998.

[Langley 81]   S. P. Langley. *The Bolometer.* Nature, vol. 25, pages 14–16, 1881.

[Le Bloas 07]   J. Le Bloas. Emission Cherenkov d'une impulsion laser ultra courte. Rapport de stage, Université Bordeaux 1, CELIA, Talence, 2007.

[Lee 12]   Y.-K. Lee, S.-W. Choi, S.-T. Han, D. H. Woo & H. S. Chun. *Detection of Foreign Bodies in Foods Using Continuous Wave Terahertz Imaging.* J. Food Prot., vol. 75, no. 1, pages 179–183, 2012.

[Li 12]   M. Li, W. Li, Y. Shi, P. Lu, H. Pan & H. Zeng. *Verification of the physical mechanism of THz generation by dual-color ultrashort laser pulses.* Appl. Phys. Lett., vol. 101, no. 16, page 161104, 2012.

[Liu 03]   W. Liu, S. L. Chin, O. Kosareva, I. S. Golubtsov & V. P. Kandidov. *Multiple refocusing of a femtosecond laser pulse in a dispersive liquid (methanol)*. Opt. Commun., vol. 225, no. 1-3, pages 193–209, 2003.

[Liu 05]   J. Liu, Z. Duan, Z. Zeng, X. Xie, Y. Deng, R. Li, Z. Xu & S. L. Chin. *Time-resolved investigation of low-density plasma channels produced by a kilohertz femtosecond laser in air*. Phys. Rev. E, vol. 72, page 026412, 2005.

[Liu 07a]   H.-B. Liu, H. Zhong, N. Karpowicz, Y. Chen & X.-C. Zhang. *Terahertz spectroscopy and imaging for defense and security applications*. Proc. IEEE, vol. 95, no. 8, pages 1514–1527, 2007.

[Liu 07b]   Y. Liu, A. Houard, B. Prade, S. Akturk, A. Mysyrowicz & V. T. Tikhonchuk. *Terahertz radiation source in air based on bifilamentation of femtosecond laser pulses*. Phys. Rev. Lett., vol. 99, no. 13, 2007.

[Liu 08]   Y. Liu, A. Houard, B. Prade, A. Mysyrowicz, A. Diaw & V. T. Tikhonchuk. *Amplification of transition-Cherenkov terahertz radiation of femtosecond filament in air*. Appl. Phys. Lett., vol. 93, page 051108, 2008.

[Liu 09]   Y. Liu, A. Houard, M. Durand, B. Prade & A. Mysyrowicz. *Maker fringes in the Terahertz radiation produced by a 2-color laser field in air*. Opt. Express, vol. 17, no. 14, pages 11480–11485, 2009.

[Liu 10]   J. Liu, J. Dai, S. L. Chin & X.-C. Zhang. *Broadband terahertz wave remote sensing using coherent manipulation of fluorescence from asymmetrically ionized gases*. Nat. Photon., vol. 4, pages 627–631, 2010.

[Liu 13]   Y. Liu, Y. Brelet, G. Point, A. Houard & A. Mysyrowicz. *Self-seeded lasing in ionized air pumped by 800 nm femtosecond laser pulses*. Opt. Express, vol. 21, no. 19, pages 22791–22798, 2013.

[Löffler 00] T. Löffler, F. Jacob & H. G. Roskos. *Generation of terahertz pulse by photoionization of electrically biased air*. Appl. Phys. Lett., vol. 77, page 453, 2000.

[Löffler 02] T. Löffler & H. G. Roskos. *Gas-pressure dependence of terahertz-pulse generation in a laser-generated nitrogen plasma*. J. Appl. Phys., vol. 91, page 2611, 2002.

[Löffler 05] T. Löffler, M. Kress, M. Thomson, T. Hahn, N. Hasegawa & H. G. Roskos. *Comparative performace of terahertz emitters in amplified-laser-based systems*. Semicond. Sci. Technol., vol. 20, pages 134–141, 2005.

[Lofthus 77] A. Lofthus & P. H. Krupenie. *The spectrum of molecular nitrogen*. J. Phys. Chem. Ref. Data, vol. 6, no. 1, pages 113–307, 1977.

[Low 61]   F. J. Low. *Low temperature germanium bolometer*. J. Opt. Soc. Am., vol. 51, page 1300, 1961.

[Luo 03]   Q. Luo, W. Liu & S. L. Chin. *Lasing action in air induced by ultrafast laser filamentation*. Appl. Phys. B, vol. 76, pages 337–340, 2003.

[Luo 04]   Q. Luo, S. A. Hosseini, B. Ferland & S. L. Chin. *Backward time-resolved spectroscopy from filament induced by ultrafast intense Laser pulses*. Opt. Commun., vol. 233, pages 411–416, 2004.

[Luo 05]   Q. Luo, J. Yu, S. A. Hosseini, W. Liu, B. Ferland, G. Roy & S. L. Chin. *Long-range detection and length estimation of light filaments using extra attenuation of terawatt femtosecond laser pulses propagating in air*. Appl. Opt., vol. 44, no. 3, page 391, 2005.

[Luo 06]   Q. Luo, H. L. Xu, S. A. Hosseini, J.-F. Daigle, F. Théberge, M. Sharifi & S. L. Chin. *Remote sensing of pollutants using femtosecond laser pulse fluorescence spectroscopy*. Appl. Phys. B, vol. 82, no. 1, pages 105–109, 2006.

[Luther 94]   G. G. Luther, A. C. Newell, J. V. Moloney & E. M Wright. *Short pulse conical emission and spectral broadening in normally dispersive media*. Opt. Lett., vol. 19, no. 11, pages 789–791, 1994.

[Maine 88]   P. Maine, D. Strickland, P. Bado, M. Pessot & G. Mourou. *Generation of ultrahigh peak power pulses by chirped pulse amplification*. IEEE J. Quant. Electron., vol. 24, pages 398–403, 1988.

[Malevich 12]   P. N. Malevich, D. Kartashov, Z. Pu, S. Ališauskas, A. Pugžlys, A. Baltuška, L. Giniūnas, R. Danielius, A. A. Lanin, A. M. Zheltikov, M. Marangoni & G. Cerullo. *Ultrafast-laser-induced backward stimulated Raman scattering for tracing atmospheric gases*. Opt. Express, vol. 20, no. 17, pages 18784–18794, 2012.

[Manceau 10]   J.-M. Manceau, M. Massaouti & S. Tzortzakis. *Strong terahertz emission enhancement via femtosecond laser filament concatenation in air*. Opt. Lett., vol. 35, no. 14, pages 2424–2426, 2010.

[Marburger 75] J. H. Marburger. *Self-focusing: Theory*. Prog. Quant. Electron., vol. 4, pages 35–110, 1975.

[Martin 02]   F. Martin, R. Mawassi, F. Vidal, I. Gallimberti, D. Comtois, H. Pépin, J. C. Kieffer & H. P. Mercure. *Spectroscopic study of ultrashort pulse laser-breakdown plasmas in air*. Appl. Spectrosc., vol. 56, no. 11, pages 1444–1452, 2002.

[Matsubara 12] E. Matsubara, M. Nagai & M. Ashida. *Ultrabroadband coherent electric field from far infrared to 200 THz using air plusma induced by 10 fs pulses*. Appl. Phys. Lett., vol. 101, page 011105, 2012.

[Méchain 03]   G. Méchain, S. Tzortzakis, B. Prade, M. Franco, A. Mysyrowicz & B. Leriche. *Calorimetric detection of THz radiation from femtosecond filaments in air*. App. Phys. B, vol. 77, no. 8, pages 707–709, 2003.

[Méchain 04a]   G. Méchain, A. Couairon, Y.-B. André, C. D'Amico, M. Franco, B. Prade, S. Tzortzakis, A. Mysyrowicz & R. Sauerbrey. *Long range self-channeling of infrared laser pulses in air: a new propagation regime without ionization*. Appl. Phys. B, vol. 79, pages 379–382, 2004.

[Méchain 04b]   G. Méchain, A. Couairon, M. Franco, B. Prade & A. Mysyrowicz. *Organizing multiple femtosecond filaments in air.* Phys. Rev. Lett., vol. 93, no. 3, page 035003, 2004.

[Méchain 05]   G. Méchain, C. D'Amico, Y.-B. André, S. Tzortzakis, M. Franco, B. Prade, A. Mysyrowicz, A. Couairon, E. Salmon & R. Sauerbrey. *Range of plasma filaments created in air by a multi-terawatt femtosecond laser.* Opt. Commun., vol. 247, no. 1-3, pages 171–180, 2005.

[Mitryukovskiy 13]   S. I. Mitryukovskiy, Y. Liu, B. Prade, A. Houard & A. Mysyrowicz. *Coherent synthesis of terahertz radiation from femtosecond laser filaments in air.* Appl. Phys. Lett., vol. 102, no. 22, page 221107, 2013.

[Mitryukovskiy 14]   S. Mitryukovskiy, Y. Liu, P. Ding, A. Houard & A. Mysyrowicz. *Backward stimulated radiation from filaments in nitrogen gas and air pumped by circularly polarized 800 nm femtosecond laser pulses.* Opt. Express, vol. 22, no. 11, pages 12750–12759, 2014.

[Mlejnek 99]   M. Mlejnek, M. Kolesik, J. V. Moloney & E. M. Wright. *Optically turbulent femtosecond light guide in air.* Phys. Rev. Lett., vol. 83, no. 15, pages 2938–2941, 1999.

[Moloney 07]   J. V. Moloney & M. Kolesik. *Full vectorial, intense ultrashort pulse propagators: derivation and applications.* In Progress in Ultrafast Intense Laser Science II, volume 85 of *Springer Series in Chemical Physics*, pages 253–280. Springer Berlin Heidelberg, 2007.

[Moore 65]   W. J. Moore & H. Shenker. *A high-detectivity gallium-doped germanium detector for the 40–120 µm region.* Infrared Phys., vol. 5, page 99, 1965.

[Nagai 04]   M. Nagai, K. Tanaka, H. Ohtake, T. Bessho, T. Sugiura, T. Hirosumi & M. Yoshida. *Generation and detection of terahertz radiation by electro-optical process in GaAs using 1.56 µm fiber laser pulses.* Appl. Phys. Lett., vol. 85, no. 18, pages 3974–3976, 2004.

[Nagy 03]   O. Nagy. $X^2\Sigma_g^+(\nu''=0) \rightarrow B^2\Sigma_u^+(\nu'=0)$ *excitation cross-sections of* N_2^+ *molecular ion by electron impact and the vibrational energy levels of the three target states* N_2^+ *(*$X^2\Sigma_g^+$*,* $A^2\Pi_u$ *and* $B^2\Sigma_u^+$*).* Chem. Phys., vol. 286, no. 1, pages 109–114, 2003.

[Nahata 96]   A. Nahata, D. H. Auston & T. Heinz. *Coherent detection of freely propagating terahertz radiation by electro-optic sampling.* Appl. Phys. Lett., vol. 68, no. 2, pages 150–152, 1996.

[Ni 12]   J. Ni, W. Chu, H. Zhang, C. Jing, J. Yao, H. Xu, B. Zeng, G. Li, C. Zhang, S. L. Chin, Y. Cheng & Z. Xu. *Harmonic-seeded remote laser emissions in N_2-Ar, N_2-Xe and N_2-Ne mixtures: a comparative study.* Opt. Express, vol. 20, no. 19, pages 20970–20979, 2012.

[Ni 13]   J. Ni, W. Chu, C. Jing, H. Zhang, B. Zeng, J. Yao, G. Li, H. Xie, C. Zhang, H. Xu, S. L. Chin, Y. Cheng & Z. Xu. *Identification of the physical mechanism*

of generation of coherent N_2^+ emissions in air by femtosecond laser excitation. Opt. Express, vol. 21, no. 7, pages 8746–8752, 2013.

[Nibbering 96]   E. T. J. Nibbering, P. F. Curley, G. Grillon, B. S. Prade, M. A. Franco, F. Salin & A. Mysyrowicz. *Conical emission from self-guided femtosecond pulses in air.* Opt. Lett., vol. 21, no. 1, pages 62–64, 1996.

[Nibbering 97]   E. T. J. Nibbering, G. Grillon, M. A. Franco, B. S. Prade & A. Mysyrowicz. *Determination of the inertial contribution to the nonlinear refractive index of air, N_2, and O_2 by use of unfocused high-intensity femtosecond laser pulses.* J. Opt. Soc. Am. B, vol. 14, no. 3, pages 650–660, 1997.

[Nichols 97]   E. F. Nichols. *A method for energy measurements in the infrared spectrum and the properties of the ordinary ray in quartz for waves of great wavelength.* Phys. Rev., vol. 4, pages 297–313, 1897.

[Nichols 23]   E. F. Nichols & J. D. Tear. *Short electric waves.* Phys. Rev., vol. 21, pages 587–610, 1923.

[Nicolson 68]   A. M. Nicolson. *Broad-band microwave transmission characteristics from a single measurement of the transient response.* IEEE Transact. Instr. Meas., vol. 17, no. 4, pages 395–402, 1968.

[Nurhuda 02]   M. Nurhuda, A. Suda, M. Hatayama, K. Nagasaka & K. Midorikawa. *Propagation dynamics of femtosecond laser pulses in argon.* Phys. Rev. A, vol. 66, no. 2, page 023811, 2002.

[Odhner 10]   J. H. Odhner, D. A. Romanov & R. J. Levis. *Self-shortening dynamics measured along a femtosecond laser filament in air.* Phys. Rev. Lett., vol. 105, page 125001, 2010.

[Owada 13]   S. Owada, A. Azarm, S. Hosseini, A. Iwasaki, S. L. Chin & K. Yamanouchi. *Amplified spontaneous $C^3\Pi_u - B^3\Pi_g$ emission and rotational and vibrational state distributions in $C^3\Pi_u$ state of N_2 in femtosecond laser induced filament in air.* Chem. Phys. Lett., vol. 581, pages 21–25, 2013.

[Pereira 10]   L. Pereira, A. Morozov, M. M. Fraga, T. Heindl, R. Krücken, J. Wieser & A. Ulrich. *Temperature dependence of the quenching of $N_2(C^3\Pi_u)$ by $N_2(X)$ and $O_2(X)$.* Europ. Phys. J. D, vol. 56, no. 3, pages 325–334, 2010.

[Petit 11]   Y. Petit, S. Henin, J. Kasparian, J. P. Wolf, P. Rohwetter, K. Stelmaszczyk, Z. Q. Hao, W. M. Nakaema, L. Wöste, A. Vogel, T. Pohl & K. Weber. *Influence of pulse duration, energy, and focusing on laser-assisted water condensation.* Appl. Phys. Lett., vol. 98, no. 4, page 041105, 2011.

[Pickwell 06]   E. Pickwell & V. P. Wallace. *Biomedical applications of terahertz technology.* J. Phys. D: Appl. Phys., vol. 39, pages 301–310, 2006.

[Planken 01]   P. C. M. Planken, H.-K. Nienhuys, H. J. Bakker & T. Wenckebach. *Measurement and calculation of the orientation dependence of terahertz pulse detection in ZnTe.* J. Opt. Soc. Am. B, vol. 18, no. 3, pages 313–317, 2001.

[Pockels 94]   F. Pockels. *Ueber den einfluss des elektrostatischen feldes auf das optische verhalten piëzoelektrischer krystalle.* Abh. Gess. Wiss. Göttingen, vol. 39, pages 1–204, 1894.

[Point 14]   G. Point, Y. Liu, Y. Brelet, S. Mitryukovskiy, P. Ding, A. Houard & A. Mysyrowicz. *Lasing of ambient air with microjoule pulse energy pumped by a multiterawatt infrared femtosecond laser.* Opt. Lett., vol. 39, no. 7, pages 1725–1728, 2014.

[Proulx 00]   A. Proulx, A. Talebpour, S. Petit & S. L. Chin. *Fast pulsed electric field created from the self-generated filament of a femtosecond Ti:Sapphire laser pulse in air.* Opt. Commun., vol. 174, pages 305–309, 2000.

[Putley 60]   E. H. Putley. *Impurity Photoconductivity in n-type InSb.* Proc. Phys. Soc., vol. 76, page 802, 1960.

[Radziemski 83] L. J. Radziemski, T. R. Loree, D. A. Cremers & N. M. Hoffman. *Time-resolved laser-induced breakdown spectrometry of aerosols.* Anal. Chem., vol. 55, no. 8, pages 1246–1252, 1983.

[Randall 37]   H. M. Randall, D. M. Dennison, N. Ginsburg & L. R. Weber. *The far infrared spectrum of water vapor.* Phys. Rev., vol. 52, pages 160–174, 1937.

[Ranka 96]   J. K. Ranka, R. W. Schirmer & A. L. Gaeta. *Observation of pulse splitting in nonlinear dispersive media.* Phys. Rev. Lett., vol. 77, no. 18, pages 3783–3786, 1996.

[Reimann 07]   K. Reimann. *Table-top source of ultrashort THz pulses.* Rep. Prog. Phys., vol. 70, pages 1597–1632, 2007.

[Ripoche 97]   J.-F. Ripoche, G. Grillon, B. Prade, M. Franco, E. Nibbering, R. Lange & A. Mysyrowicz. *Determination of the time dependence of n_2 in air.* Opt. Commun., vol. 135, pages 310–314, 1997.

[Rodriguez 02]   M. Rodriguez, R. Sauerbrey, H. Wille, L. Wöste, T. Fujii, Y.-B. André, A. Mysyrowicz, L. Klingbeil, K. Rethmeier, W. Kalkner, J. Kasparian, E. Salmon, J. Yu & J.-P. Wolf. *Triggering and guiding megavolt discharges by use of laser-induced ionized filaments.* Opt. Lett., vol. 27, no. 9, pages 772–774, 2002.

[Rohwetter 08]   P. Rohwetter, M. Quiesser, K. Stelmaszczyk, M. Fechner & L. Wöste. *Laser multiple filamentation control in air using a smooh phase mask.* Phys. Rev. A, vol. 77, page 013812, 2008.

[Rohwetter 10]   P. Rohwetter, J. Kasparian, K. Stelmaszczyk, Z. Hao, S. Henin, N. Lascoux, W. M. Nakaema, Y. Petit, M. Queisser, R. Salamé, E. Salmon, L. Wöste & J.-P. Wolf. *Laser-induced water condensation in air.* Nat. Photon., vol. 4, pages 451–456, 2010.

[Roso-Franco 85] L. Roso-Franco. *Self-reflected wave inside a very dense saturable absorber.* Phys. Rev. Lett., vol. 55, pages 2149–2151, 1985.

[Rubens 93]   H. Rubens & B. W. Snow. *On the refraction of rays of great wavelength in rock salt, sylvine, and fluorite.* Phil. Mag., vol. 35, pages 35–45, 1893.

[Rubens 11]   H. Rubens & O. V. Baeyer. *On extremely long waves emitted by the quartz mercury lamp.* Phil. Mag., vol. 21, page 689–703, 1911.

[Salières 99]   P. Salières, A. l'Huillier, P. Antoine & M. Lewenstein. *Studies of the spatial and temporal coherence of high order harmonics.* Adv. At. Mol. Opt. Phys., vol. 41, page 83, 1999.

[Schillinger 99] H. Schillinger & R. Sauerbrey. *Electrical conductivity of long plasma channels in air generated by self-guided femtosecond laser pulses.* Appl. Phys. B, vol. 68, pages 753–756, 1999.

[Schneider 07]   A. Schneider & P. Günter. *Coherent detection of terahertz pulses based on two-photon absorption in a photodiode.* Appl. Phys. Lett., vol. 90, no. 12, 2007.

[Schroeder 04]   H. Schroeder, J. Liu & S. L. Chin. *From random to controlled small-scale filamentation in water.* Opt. Express, vol. 12, no. 20, pages 4768–4774, 2004.

[Sell 08]   A. Sell, A. Leitenstorfer & R. Huber. *Phase-locked generation and field-resolved detection of widely tunable terahertz pulses with amplitudes exceeding 100 MV/cm.* Opt. Lett., vol. 33, no. 23, pages 2767–2769, 2008.

[Shen 75]   Y. R. Shen. *Self-focusing: experimental.* Prog. Quantum Electron., vol. 4, pages 1–34, 1975.

[Shen 84]   Y. R. Shen. The Principles of Nonlinear Optics. Wiley-interscience, New York, 1984.

[Shneider 11]   M. N. Shneider, A. Baltuška & A. M. Zheltikov. *Population inversion of molecular nitrogen in an Ar:N_2 mixture by selective resonance-enhanced multiphoton ionization.* J. Appl. Phys., vol. 110, no. 8, page 083112, 2011.

[Siegel 04]   P. H. Siegel. *Terahertz technology in biology and medicine.* IEEE Trans. Microwave Theory Tech., vol. 52, pages 2438–2446, 2004.

[Smith 88]   P. R. Smith, D. H. Auston & M. C. Nuss. *Subpicosecond photoconductive dipole antennas.* IEEE J. Quant. Electron., vol. 24, no. 2, pages 255–260, 1988.

[Sprangle 02]   P. Sprangle, J. R. Peñano & B. Hafizi. *Propagation of intense short laser pulses in the atmosphere.* Phys. Rev. E, vol. 66, no. 4, page 046418, 2002.

[Sprangle 04]   P. Sprangle, J. R. Peñano, B. Hafizi & C. A. Kapetanakos. *Ultrashort laser pulses and electromagnetic pulse generation in air and on dielectric surfaces.* Phys. Rev. E, vol. 69, no. 6, page 066415, 2004.

[Sprangle 11]   P. Sprangle, J. Peñano, B. Hafizi, D. Gordon & M. Scully. *Remotely induced atmospheric lasing.* Appl. Phys. Lett., vol. 98, no. 21, page 211102, 2011.

[Steingrube 11]   D. S. Steingrube, E. Shulz, T. Binhammer, M. B. Gaarde, A. Couairon, U. Morgner & M. Kovačev. *High-order harmonic generation directly from a filament.* New J. Phys., vol. 13, page 043022, 2011.

[Stelmaszczyk 04] K. Stelmaszczyk, P. Rohwetter, G. Méjean, J. Yu, E. Salmon, J. Kasparian, R. Ackermann, J.-P. Wolf & L. Wöste. *Long-distance remote laser-induced breakdown spectroscopy using filamentation in air.* Appl. Phys. Lett., vol. 85, no. 18, pages 3977–3979, 2004.

[Strickland 85]   D. Strickland & G. Mourou. *Compression of amplified chirped optical pulses.* Opt. Commun., vol. 56, pages 219–221, 1985.

[Sugiyama 09]   K. Sugiyama, T. Fujii, M. Miki, M. Yamaguchi, A. Zhidkov, E. Hotta & K. Nemoto. *Laser-filament-induced corona discharges and remote measurements of electric fields.* Opt. Lett., vol. 34, no. 19, pages 2964–2966, 2009.

[Suzuki 12]   T. Suzuki & R. Shimano. *Exciton mott transition in Si revealed by terahertz spectroscopy.* Phys. Rev. Lett., vol. 109, page 046402, 2012.

[Takahashi 00]   T. Takahashi, Y. Shibata, K. Ishi, M. Ikezawa, M. Oyamada & Y. Kondo. *Observation of coherent Čerenkov radiation from a solid dielectric with short bunches of electrons.* Phys. Rev. E, vol. 62, page 8606, 2000.

[Talebpour 99]   A. Talebpour, S. Petit & S. L. Chin. *Re-focusing during the propagation of a focused femtosecond Ti:sapphire laser pulse in air.* Opt. Commun., vol. 171, pages 285–290, 1999.

[Talebpour 00]   A. Talebpour, A. Bandrauk & S. L. Chin. Multiphoton Processes, pages 508–516. AIP, New York, 2000.

[Talebpour 01]   A. Talebpour, M. Abdel-Fattah, A. D. Bandrauk & S. L. Chin. *Spectroscopy of the gases interacting with intense femtosecond laser pulses.* Laser Phys., vol. 11, pages 68–76, 2001.

[Théberge 06]   F. Théberge, W. Liu, P. T. Simard, A. Becker & S. L. Chin. *Plasma density inside a femtosecond laser filament in air: Strong dependence on external focusing.* Phys. Rev. E, vol. 74, page 036406, 2006.

[Thomson 07]   M. D. Thomson, M. Kress, T. Löffler & H. G. Roskos. *Broadband THz emission from gas plasma induced by femtosecond optical pulses: From fundamentals to applications.* Laser Photonics Rev., vol. 1, page 349, 2007.

[Ting 05a]   A. Ting, I. Alexeev, D. Gordon, R. Fischer, D. Kaganovich, T. Jones, E. Briscoe, J. Peñano, R. Hubbard & P. Sprangle. *Measurements of intense femtosecond laser pulse propagation in air.* Phys. Plasmas, vol. 12, page 056705, 2005.

[Ting 05b]   A. Ting, D. F. Gordon, E. Briscoe, J. Peñano & P. Sprangle. *Direct characterization of self-guided femtosecond laser filaments in air.* Appl. Opt., vol. 44, no. 8, page 1474, 2005.

[Tonouchi 07]   M. Tonouchi. *Cutting-edge terahertz technology.* Nat. Photon., vol. 1, pages 97–105, 2007.

[Trebino 00]   R. Trebino. *Frequency-Resolved Optical Gating: The Measurement of Ultrashort Laser Pulses.* Springer, New York, 2000.

[Tyte 64]   D. C. Tyte & R. W. Nicholls. *Identification Atlas of Molecular Spectra. 2. The* N_2 $C^3\Pi_u - B^3\Pi_g$ *Second Positive System.* Defense Technical Information Center, Univerity of Western Ontario, London, Ontario, 1964.

[Tyte 65]   D. C. Tyte & R. W. Nicholls. *Identification Atlas of Molecular Spectra. 3. The* N_2^+ $B^2\Sigma_u^+ - X^2\Sigma_g^+$ *First Negative System of Nitrogen.* Defense Technical Information Center, Univerity of Western Ontario, London, Ontario, 1965.

[Tzortzakis 99]   S. Tzortzakis, M. A. Franco, Y.-B André, A. Chiron, B. Lamouroux, B. S. Prade & A. Mysyrowicz. *Formation of a conducting channel in air by self-guided femtosecond laser pulses.* Phys. Rev. E, vol. 60, no. 4, Part A, pages 3505–3507, 1999.

[Tzortzakis 00]   S. Tzortzakis, B. Prade, M. Franco & A. Mysyrowicz. *Time-evolution of the plasma channel at the trail of a self-guided IR femtosecond laser pulse in air.* Opt. Commun., vol. 181, no. 1-3, pages 123–127, 2000.

[Tzortzakis 02]   S. Tzortzakis, G. Méchain, G. Patalano, Y.-B. André, B. Prade, M. Franco, A. Mysyrowicz, J.-M. Munier, M. Gheudin, G. Beaudin & P. Encrenaz. *Coherent subterahertz radiation from femtosecond infrared filaments in air.* Opt. Lett., vol. 27, no. 21, pages 1944–1946, 2002.

[Vidal 96]   F. Vidal & T. W. Johnston. *Electromagnetic beam breakup: Multiple filaments, single beam equilibria, and radiation.* Phys. Rev. Lett., vol. 77, no. 7, pages 1282–1285, 1996.

[Wang 04]   K. Wang & D. M. Mittleman. *Metal wires for terahertz wave guiding.* Nature, vol. 432, pages 376–379, 2004.

[Wang 10]   T.-J. Wang, S. Yuan, Y. Chen, J.-F. Daigle, C. Marceau, F. Théberge, M. Châteauneuf, J. Dubois & S. L. Chin. *Toward remote high energy terahertz generation.* Appl. Phys. Lett., vol. 97, no. 11, page 111108, 2010.

[Wang 12]   T.-J. Wang, H. Xu, J.-F. Daigle, A. Sridharan, S. Yuan & S. L. Chin. *Water vapor concentration measurement in air using filament-induced fluorescence spectroscopy.* Opt. Lett., vol. 37, no. 10, pages 1706–1708, 2012.

[Wang 13]   T.-J. Wang, J. Ju, J.-F. Daigle, S. Yuan, R. Li & S. L. Chin. *Self-seeded forward lasing action from a femtosecond Ti:sapphire laser filament in air.* Laser Phys. Lett., vol. 10, no. 12, page 125401, 2013.

[Waters 06]   J. W. Waters & *et al. The Earth Observing System Microwave Limb Sounder (EOS MLS) on the Aura satellite.* IEEE Trans. Geosci. Remote Sensing, vol. 44, pages 1075–1092, 2006.

[Winnewisser 97]   C. Winnewisser, P. Uhd Jepsen, M. Schall, V. Schyja & H. Helm. *Electro-optic detection of THz radiation in* $LiTaO_3$, $LiNbO_3$ *and* $ZnTe$. Appl. Phys. Lett., vol. 70, no. 23, pages 3069–3071, 1997.

[Wood 10]   R. W. Wood. *The echelette grating for the infrared.* Phil. Mag., vol. 20, pages 270–281, 1910.

[Wu 95]   Q. Wu & X.-C. Zhang. *Free-space electrooptic sampling of terahertz beams.* Appl. Phys. Lett., vol. 67, page 3523, 1995.

[Wu 96]   Q. Wu, M. Litz & X.-C. Zhang. *Broadband detection capability of ZnTe electro-optic field detectors.* Appl. Phys. Lett., vol. 68, no. 21, pages 2924–2926, 1996.

[Wu 97]   Q. Wu & X.-C. Zhang. *Terahertz broadband GaP electro-optic sensor.* Appl. Phys. Lett., vol. 70, page 1784, 1997.

[Xie 06]   X. Xie, J. Dai & X.-C. Zhang. *Coherent control of THz wave generation in ambient air.* Phys. Rev. Lett., vol. 96, page 075005, 2006.

[Xu 06]   H. L. Xu, J. F. Daigle, Q. Luo & S. L. Chin. *Femtosecond laser-induced nonlinear spectroscopy for remote sensing of methane.* Appl. Phys. B, vol. 82, pages 655–658, 2006.

[Xu 07]   H. L. Xu, Y. Kamali, C. Marceau, P. T. Simard, W. Liu, J. Bernhardt, G. Méjean, P. Mathieu, G. Roy, J.-R. Simard & S. L. Chin. *Simultaneous detection and identification of multigas pollutants using filament-induced nonlinear spectroscopy.* Appl. Phys. Lett., vol. 90, no. 10, page 101106, 2007.

[Xu 09]   H. L. Xu, A. Azarm, J. Bernhardt, Y. Kamali & S. L. Chin. *The mechanism of nitrogen fluorescence inside a femtosecond laser filament in air.* Chem. Phys., vol. 360, no. 1-3, pages 171–175, 2009.

[Xu 11a]   H. L. Xu, A. Azarm & S. L. Chin. *Controlling fluorescence from N_2 inside femtosecond laser filaments in air by two-color laser pulses.* Appl. Phys. Lett., vol. 98, no. 14, page 141111, 2011.

[Xu 11b]   H. L. Xu & S. L. Chin. *Femtosecond laser filamentation for atmospheric sensing.* Sensors, vol. 11, pages 32–53, 2011.

[Xu 12]   S. Xu, X. Sun, B. Zeng, W. Chu, J. Zhao, W. Liu, Y. Cheng, Z. Xu & S. L. Chin. *Simple method of measuring laser peak intensity inside femtosecond laser filament in air.* Opt. Express, vol. 20, no. 1, pages 299–307, 2012.

[Yablonovitch 72] E. Yablonovitch & N. Bloembergen. *Avalanche ionization and the limiting diameter of filaments induced by light pulses in transparent media.* Phys. Rev. Lett., vol. 29, no. 14, pages 907–910, 1972.

[Yang 71]   K. H. Yang, P. L. Richards & Y. R. Shen. *Generation of far-infrared radiation by picosecond light pulses in $LiNbO_3$.* Appl. Phys. Lett., vol. 19, page 320, 1971.

[Yang 84]   G Yang & Y. R. Shen. *Spectral broadening of ultrashort pulses in a nonlinear medium.* Opt. Lett., vol. 9, pages 510–512, 1984.

[Yang 02]   H. Yang, J. Zhang, Y. Li, J. Zhang, Y. Li, Z. Chen, H. Teng, Z. Wei & Z. Sheng. *Characteristics of self-guided laser-plasma channels generated by femtosecond laser pulses in air.* Phys. Rev. E, vol. 66, no. 1, page 016406, 2002.

[Yao 11]   J. Yao, B. Zeng, H. Xu, G. Li, W. Chu, J. Ni, H. Zhang, S. L. Chin, Y. Cheng & Z. Xu. *High-brightness switchable multiwavelength remote laser in air*. Phys. Rev. A, vol. 84, page 051802, 2011.

[Yao 13]   J. Yao, G. Li, C. Jing, B. Zeng, W. Chu, J. Ni, H. Zhang, H. Xie, C.Zhang, H. Li, H. Xu, S. L. Chin, Y. Cheng & Z. Xu. *Remote creation of coherent emissions in air with two-color ultrafast laser pulses*. New J. Phys., vol. 15, no. 2, page 023046, 2013.

[Yariv 89]   A. Yariv. Quantum Electronics. Wiley, New York, 3rd edition, 1989.

[You 12]   Y. S. You, T. I. Oh & K.-Y. Kim. *Off-axis phase-matched terahertz emission from two-color laser-induced plasma filaments*. Phys. Rev. Lett., vol. 109, page 183902, 2012.

[Yu 12]   C. Yu, S. Fan, Y. Sun & E. Pickwell-MacPherson. *The potential of terahertz imaging for cancer diagnosis: A review of investigations to date*. Quant. Imaging Med. Surg., vol. 2, no. 1, 2012.

[Yuan 14]   S. Yuan, T. Wang, P. Lu, S. L. Chin & H. Zeng. *Humidity measurement in air using filament-induced nitrogen monohydride fluorescence spectroscopy*. Appl. Phys. Lett., vol. 104, no. 9, page 091113, 2014.

[Zhang 10]   X.-C. Zhang & J. Xu. Introduction to THz Wave Photonics. Springer, New York, 2010.

[Zhang 13]   H. Zhang, C. Jing, G. Li, H. Xie, J. Yao, B. Zeng, W. Chu, J. Ni, H. Xu & Y. Cheng. *Abnormal dependence of strong-field-ionization-induced nitrogen lasing on polarization ellipticity of the driving field*. Phys. Rev. A, vol. 88, page 063417, 2013.

[Zhao 95]   X. M. Zhao, J.-C. Diels, C. Y. Wang & J. M. Elizondo. *Propagation dynamics of intense femtosecond pulses: multiple splittings, coalescence, and continuum generation*. IEEE J. Quant. Electron., vol. 31, page 599, 1995.

[Zhong 06]   H. Zhong, A. Redo-Sanchez & X.-C. Zhang. *Identification and classification of chemicals using terahertz reflective spectroscopic focal-plane imaging system*. Opt. Express, vol. 14, no. 20, pages 9130–9141, 2006.

[Zozulya 98]   A. A. Zozulya, S. A. Diddams & T. S. Clement. *Investigations of nonlinear femtosecond pulse propagation with the inclusion of Raman, shock, and third-order phase effects*. Phys. Rev. A, vol. 58, pages 3303–3310, 1998.

Rayonnements Secondaires Cohérents Émis lors de la Filamentation Laser Femtoseconde

Résumé

La filamentation laser est un phénomène optique non-linéaire qui apparaît spontanément au cours de la propagation d'une impulsion laser ultracourte intense dans un milieu transparent, quand sa puissance crête dépasse une valeur critique (quelques Gigawatts dans l'air). A un tel niveau d'intensité le faisceau a tendance à se contracter en raison de l'effet Kerr optique jusqu'à ce que l'intensité devienne suffisamment élevée pour ioniser le milieu, donnant naissance à un plasma de défocalisation. Par la suite, une compétition dynamique entre ces deux effets a lieu, produisant un canal de plasma mince et faiblement ionisé dans le sillage de l'impulsion. Depuis sa découverte en 1995, la filamentation laser femtoseconde dans l'air a suscité un intérêt considérable en raison de la physique riche impliquée dans ce processus et de la large gamme d'applications potentielles (détection à distance, conversion de fréquences optiques, contrôle atmosphérique par laser, génération d'ondes Térahertz, *etc.*).

Cette thèse est consacrée principalement à l'étude des rayonnements secondaires cohérents émis lors de la filamentation femtoseconde dans les gaz. Tout d'abord, je me suis intéressé à la luminescence ultraviolet des filaments de plasma, qui est associée à les transitions de l'azote moléculaire neutre et ionique dans un état excité. J'ai démontré que cette luminescence dépend fortement de l'état de polarisation des impulsions laser incidentes. J'ai ensuite décrit et interprété pour la première fois l'apparition d'un gain optique important observé vers l'arrière de la colonne de plasma dans l'azote. Ce gain apparait lorsque les impulsions laser femtoseconde à 800 nm sont polarisées circulairement et à pression atmosphérique. Cet effet constitue une étape importante vers la réalisation d'un "laser dans le ciel". La dernière partie de la thèse, porte sur la génération du rayonnement Térahertz par plusieurs filaments laser femtoseconde. Par la synthèse cohérente du rayonnement Térahertz d'un réseau de filaments, j'ai ainsi démontré la possibilité d'accroitre l'intensité Térahertz et de contrôler la directivité de ce rayonnement par l'organisation de filaments multiples.

Mots clefs : Optique non-linéaire, plasma, filamentation, effet laser, rayonnement Térahertz.

Coherent Secondary Radiation from Femtosecond Laser Filaments

Abstract

Laser filamentation is a nonlinear optical phenomenon which appears spontaneously during the propagation of an intense ultrashort laser pulse in a transparent medium, when the pulse peak power exceeds a critical value (several Gigawatts in air). At such an intensity level the beam tends to collapse due to the optical Kerr self-focusing effect until the intensity is high enough to ionize the medium, giving rise to a defocusing plasma. Thereafter, a dynamic competition between these two effects takes place, leaving a thin and weakly ionized plasma channel in the wake of the pulse. Following its discovery in 1995, femtosecond laser filamentation in air has attracted considerable interest because of the rich physics involved in the process and the wide range of potential applications (remote sensing, light frequency conversion, laser-based weather control, Terahertz generation, *etc.*).

This thesis is devoted to the study of the coherent secondary emission from femtosecond laser filaments in gases. First, the ultraviolet luminescence of plasma filaments, corresponding to transitions of excited neutral and ionic molecular Nitrogen, is studied. I demonstrate that this luminescence depends strongly on the polarization state of the incident laser pulses. I further report and interpret for the first time a strong optical gain in the backward direction from plasma filaments created by circularly polarized 800 nm femtosecond laser pulses at normal pressure. This effect is a significant step towards the realization of a "laser in the sky". In the last part of the thesis, I discuss the Terahertz generation from multiple femtosecond laser filaments in air. The coherent synthesis of the Terahertz radiation from an array of filaments is demonstrated, showing the capability for energy scaling up and directionality control of the Terahertz emission.

Keywords : Nonlinear optics, plasma, filamentation, lasing effect, Terahertz radiation.